Kristofer Leach

Modelling Force Transfer in Boundary Layers of Moving Walls for Compressible and Incompressible Turbulent Flows Across Multiple Scales

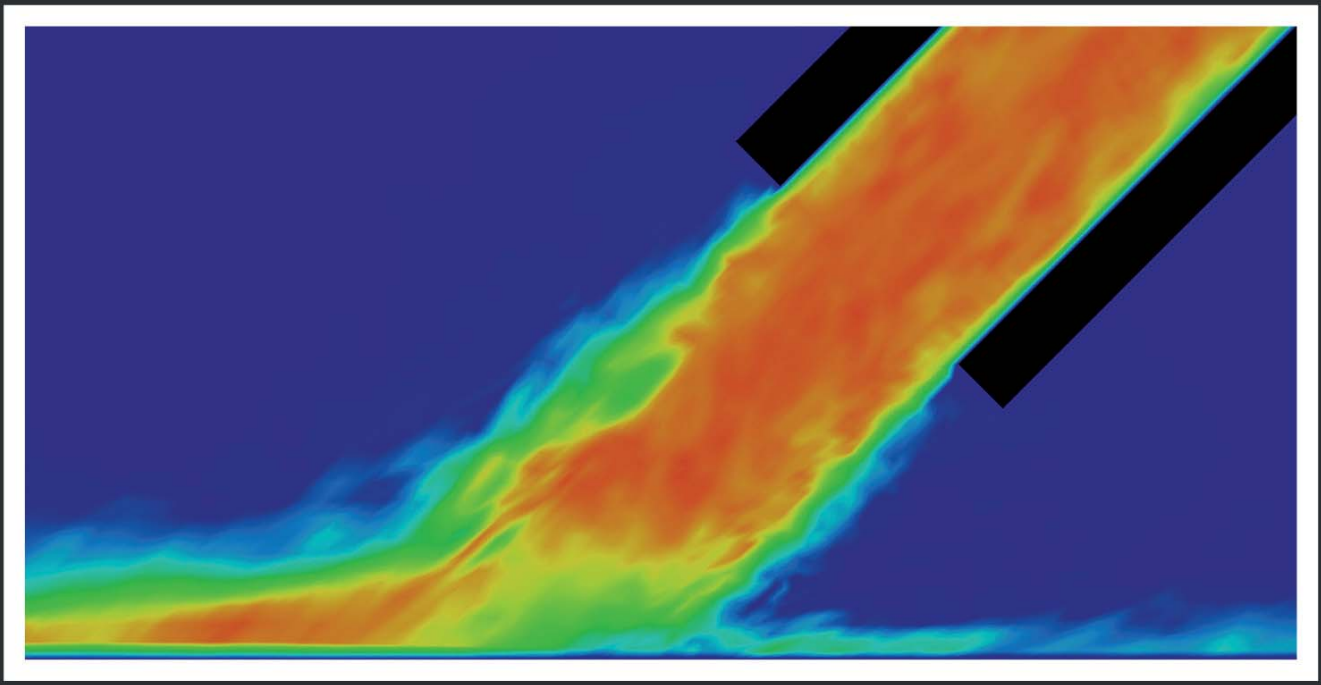

Cuvillier Verlag Göttingen
Internationaler wissenschaftlicher Fachverlag

Modelling Force Transfer in Boundary Layers of Moving Walls for Compressible and Incompressible Turbulent Flows Across Multiple Scales

Modelling Force Transfer in Boundary Layers of Moving Walls for Compressible and Incompressible Turbulent Flows Across Multiple Scales

Vom Fachbereich Produktionstechnik
der
Universität Bremen

zur Erlangung des Grades
Doktor-Ingenieur
genehmigte

Dissertation

von
M.Math. Kristofer Leach

Gutachter:
Prof. Dr. rer. nat. Claus Braxmaier
Prof. Dr. rer. nat. Thomas Schuster, Universität des Saarlandes

Tag der mündlichen Prüfung:
10. Dezember 2014

Bibliografische Information der Deutschen Nationalbibliothek
Die Deutsche Nationalbibliothek verzeichnet diese Publikation in der Deutschen Nationalbibliografie; detaillierte bibliografische Daten sind im Internet über http://dnb.d-nb.de abrufbar.

1. Aufl. - Göttingen: Cuvillier, 2014
Zugl.: Bremen, Univ., Diss., 2014

Nonnenstieg 8, 37075 Göttingen
Telefon: 0551-54724-0
Telefax: 0551-54724-21
www.cuvillier.de

1. Auflage, 2014
Gedruckt auf umweltfreundlichem, säurefreiem Papier aus nachhaltiger Forstwirtschaft

ISBN 978-3-95404-910-3
eISBN 978-3-7369-4910-2

Zusammenfassung

Die Entwicklung kleiner Werkzeugmaschinen zur Bearbeitung extrem kleiner Werkstücke ist u.a. auf den Gebieten der Mechantronik, der Optik oder der Medizin von zunehmend größerer Bedeutung. Das Miniaturisieren existierender Werkzeuge stößt allmählich an gewisse Grenzen und es ist nötig, neue Werkzeuge zu entwickeln, um einen Fortschritt zu erzielen.

Diese Arbeit beschreibt die Gestaltung einer neuartigen Schleifkugel, die magnetisch gelagert und von einer pressluftgetriebenen Strömung in Rotation versetzt wird. Es wird eine Parameterstudie durchgeführt, welche die optimale geometrische Auslegung eines Prototyps unter Einhaltung gewisser physikalischer Einschränkungen bestimmt. Die daraus hervorgehende optimale Auslegung wird im Anschluss detailliert untersucht, um festzustellen, welcher Belastung die elektromagnetische Lagerung standzuhalten hat und um die zum Schleifen verfügbare Kraft zu quantifizieren. Entgegen den Erwartungen zeigte die Untersuchung, dass Luft kein geeignetes Antriebsmedium darstellt und dass Öl an dessen Stelle treten muss um genügend Schleifkraft zu erzielen. Die bei der Entwicklung des Prototyps gesammelten Erfahrungen dienen als Grundlage für die Entwicklung eines kleineren funktionsfähigen Schleifwerkzeugs, welches unter Verwendung von hydraulischem Antrieb analysiert wird. Im Anschluss wird unter Verwendung von Luftantrieb eine skalenübergreifende Analyse der auf die Schleifkugel wirkenden Kräfte durchgeführt.

Machzahlen betragen bis zu 0,9, während Reynoldszahlen maximal 10^5 erreichen. Daher wird Large-Eddy-Simulation in Verbindung mit dem kompressiblen Smagorinsky Modell nach Furby eingesetzt. Geringe Temperaturvariation erlaubt die Annahme adiabater Wände. Fluid-Struktur Interaktion wird durch das logarithmische Wandgesetz für kompressible turbulente Strömungen modelliert. Die Parameterstudien untersuchen den Einfluss verschiedener Faktoren wie geometrische Eigenschaften und Viskosität des Antriebsmediums. Anschließend werden Simulationen unter einer Vielzahl verschiedener Normvolumenströme $\dot{V}_N$ und Kugelrotationsfrequenzen f durchgeführt.

Da die Schleifkraft des 40 mm Prototyps weniger als 0,04 N betrug, wurde für ein funktionstüchtiges 8 mm Schleifwerkzeug das Antriebsmedium durch ein Öl mit einer kinematischen Viskosität von $1{,}38 \cdot 10^4\,\mathrm{m^2\,s^{-1}}$ bei Raumtemperatur ersetzt. Zwei weitere Kanäle wurden hinzugefügt und vertikal angeordnet, um die Schleifkraft und die Anpresskraft zu erhöhen. So konnte ausreichend Schleifkraft von mehr als 0,1 N und Anpresskraft von mehr als 1 N erzielt werden. Im Anschluss wurden durch eine Skalenanalyse dimen-

sionslose Gleichungen für Normalkräfte, Schleifkraft sowie Anpresskraft aufgestellt. Diese konnten nicht nur genutzt werden um auf beliebige weitere Skalen schließen zu können, sondern auch um die beiden Antriebsmedien und die beiden Geometrien untereinander zu vergleichen.

Die in dieser Arbeit präsentierten Ergebnisse zeigen nicht nur wie die Kraftübertragung von Fluiden auf Festkörper skalenübergreifend modelliert werden kann und die Resultate zur Herleitung dimensionsloser Gleichungen, welche für beliebige Parameter gelten, genutzt werden, sondern bieten eine Grundlage für die Entwicklung eines neuartigen und bahnbrechenden Schleifwerkzeuges auf dem Gebiet des Mikroschleifens.

Abstract

Developing miniature tools used to machine parts that are themselves small in size is rapidly gaining importance in fields such as mechatronics, optics, or medicine. Miniaturising existing tools has its limitations and it is becoming ever more necessary to develop new tools in order make progress in this regard.

This thesis describes the design of a new kind of abrading sphere which is magnetically mounted inside a spherical gap and set in rotation pneumatically with air. A parametric study is performed in order to determine optimal geometric layout of a prototype while taking physical restrictions into account. The resulting optimal configuration is then examined in detail in order to determine demands to be met by the magnetic bearing and its computerised control, as well as to quantify the extent of force potentially available to the abrasion process. Contrary to expectation, the analysis showed that air is not a viable propulsion medium and that oil needs to take its place to yield sufficient grinding force. Using the knowledge gained from developing the prototype, a smaller working model is devised and analysed using hydraulic propulsion. Use of the tool with pneumatic propulsion is then subjected to a study across multiple length scales focusing on the forces acting on the grinding sphere.

Mach numbers range up to 0.9 with Reynolds numbers of up to 10^5. Hence, Large Eddy Simulation is performed in conjunction with the compressible Smagorinsky model according to Fureby. Minimal temperature variation allows for the assumption of adiabatic walls. Fluid-solid interaction is modelled using the law of the wall for compressible turbulent flow. Parametric studies investigate the influence of varying geometric factors and viscosities of the fluid used. Subsequently, simulations are conducted under a variety of standard volumetric flow rates $\dot{V}_N$ and rotation frequencies f.

The available grinding force determined for the 40 mm prototype using pneumatic propulsion was found not to exceed 0.04 N. For the working 8 mm model, the propulsion medium was thus changed to an oil with a kinematic viscosity of $1.38 \cdot 10^{-4}\,\mathrm{m^2\,s^{-1}}$ at room temperature. Two additional fluid ducts were added and introduced vertically from the top to increase grinding force and downward force. Sufficient grinding force in excess of 0.1 N and contact force exceeding 1 N could be achieved. In a subsequent study across multiple scales, non-dimensional relations governing normal forces, grinding force, as well as grinding power were established. These could not only be used to predict arbitrary scales, but also to compare the two propulsion media and geometric variations with each other.

The results presented in this thesis demonstrate how fluid-to-solid force transfer can be modelled across a multitude of scales and the results used to derive non-dimensional relations that hold true for arbitrary parameters. They also lay the foundation for the development of a novel and revolutionary grinding tool in the field of miniature precision machining.

Preface

I would like to extend my gratitude to my project supervisors the late Prof. Dr.-Ing. Hans J. Rath, Prof. Dr. Claus Braxmaier, and Dr.-Ing. Rodion Groll for their continued support and their valuable and inspiring guidance in the field of Fluid Mechanics and CFD. Also, I would like to thank Prof. Dr. Thomas Schuster, Prof. Dr.-Ing. Ekkard Brinksmeier, Prof. Dr.-Ing. Bernd Orlik, Dr.-Ing. Ralf Gläbe, Dr.-Ing. Lars Schönemann, Carla Brandao, Alexander Norbach, and all the members of SPP 1476 for their excellent cooperation and fruitful discussions while working on project *GrindBall*. Additionally, I would like to thank my colleagues at ZARM Stephan Reichel, Claudia Zimmermann, Torben Schadowski, Fabian Fastabend, Rico Schultz, and Želimir Marojević with whom I had inspiring scientific inter-exchange throughout my time there. I would especially like to thank the members of my family Barry, Helga, and Jennifer for their love and support.

Furthermore, many thanks are due to the German Research Foundation (DFG) for funding project *GrindBall* and the North-German Supercomputing Alliance (HLRN) for providing free access to their super-computing facilities, thereby enabling a quality of simulations that would not have been achievable by regular means.

Contents

Nomenclature

Scalar quantities are dented by normal italic symbols while vectors and tensors are presented in bold. To differentiate, vectors are underlined once while tensors receive double underlining. Alternatively, Einstein notation may be used to denote vector and tensor components. Unless stated otherwise, units and dimensions are presented according to the International System of Units, i.e. mass (M) in kg, length (L) in meters m, time (T) in seconds s, temperature (Θ) in Kelvin K, and amount of substance (N) in mol. Furthermore, the derived units Newton N=$\mathrm{kg\,m\,s^{-2}}$, Pascal Pa=$\mathrm{kg\,m^{-1}\,s^{-2}}$, Hertz Hz=$\mathrm{s^{-1}}$, Joule J=$\mathrm{kg\,m^2\,s^{-2}}$and Watt W=$\mathrm{J\,s^{-1}}$are employed.

Roman Symbols

Symbol	Description	Unit	Dimension
A	Area	$\mathrm{m^2}$	$\mathrm{L^2}$
A_S	Sutherland coefficient	$\mathrm{kg\,m^{-1}s^{-1}K^{-\frac{1}{2}}}$	$\mathrm{M\,L^{-1}T^{-1}\Theta^{-\frac{1}{2}}}$
$\underline{\mathbf{a}}$	Acceleration	$\mathrm{m\,s^{-2}}$	$\mathrm{L\,T^{-2}}$
a	Speed of sound	$\mathrm{m\,s^{-1}}$	$\mathrm{L\,T^{-1}}$
a	Arbitrary scalar		
B	Constant		
$\underline{\mathbf{b}}$	Body force vector	N	$\mathrm{M\,L\,T^{-2}}$
b	Blending coefficient		
C_{ij}	Clark tensor	$\mathrm{m^2s^{-2}}$	$\mathrm{L^2T^{-2}}$
C	Constant		
c_p	Specific heat at constant pressure	$\mathrm{J\,kg^{-1}K^{-1}}$	$\mathrm{L^2\Theta^{-1}T^{-2}}$
c_v	Specific heat at constant volume	$\mathrm{J\,kg^{-1}K^{-1}}$	$\mathrm{L^2\Theta^{-1}T^{-2}}$
d	Diameter	m	L
E	Energy	J	$\mathrm{M\,L^2T^{-3}}$
E_{tot}	Total energy per unit volume	$\mathrm{J\,m^{-3}}$	$\mathrm{M\,L^{-1}T^{-2}}$
$\underline{\mathbf{e}}_i$	Unit vector		
e	Internal energy per unit mass	$\mathrm{m^2s^{-2}}$	$\mathrm{L^2T^{-2}}$
$\underline{\mathbf{F}}$	Force	N	$\mathrm{M\,L\,T^{-2}}$
$\underline{\mathbf{f}}$	Force per volume	$\mathrm{N\,m^{-3}}$	$\mathrm{M\,L^{-2}T^{-2}}$
F_t	Abrasion force	N	$\mathrm{M\,L\,T^{-2}}$
f	Rotation frequency	Hz	$\mathrm{T^{-1}}$
f	Generic flux term		
f	Arbitrary function		
G	Convolution kernel		
$\underline{\mathbf{g}}$	Gravity vector	$\mathrm{m\,s^{-2}}$	$\mathrm{L\,T^{-2}}$
h	Enthalpy per unit mass	$\mathrm{m^2s^{-2}}$	$\mathrm{L^2T^{-2}}$

h	Height	m	L
$\mathbf{I}$	Identity tensor		
K	Constant		
K_B	Boltzmann Constant	$\mathrm{J\,K^{-1}}$	$\mathrm{M\,L^2\Theta^{-1}T^{-2}}$
k	Thermal conductivity	$\mathrm{W\,m^{-1}K^{-1}}$	$\mathrm{M\,L\,\Theta^{-1}T^{-3}}$
k_l	Characteristic length of wall roughness	m	L
k_{sgs}	Subgrid scale kinetic energy	$\mathrm{m^2s^{-2}}$	$\mathrm{L^2T^{-2}}$
L_{ij}	Leonard tensor	$\mathrm{m^2s^{-2}}$	$\mathrm{L^2T^{-2}}$
L	Characteristic length	m	L
$\underline{\mathbf{M}}$	Moment	$\mathrm{N\,m}$	$\mathrm{M\,L^2T^{-2}}$
M	Molecular weight	$\mathrm{kg\,mol^{-1}}$	$\mathrm{M\,N^{-1}}$
m	Mass	kg	M
$\dot{m}$	Mass flow rate	$\mathrm{kg\,s^{-1}}$	$\mathrm{M\,T^{-1}}$
$\underline{\mathbf{n}}$	Normal vector		
P	Power	W	$\mathrm{M\ L\ T^{-3}}$
p	Pressure	Pa	$\mathrm{M\,L^{-1}T^{-2}}$
Q	Source term		
Q	Heat per unit volume	$\mathrm{J\,m^{-3}}$	$\mathrm{M\,L^{-1}T^{-2}}$
$\underline{\mathbf{q}}$	Heat flux	$\mathrm{kg\,s^{-2}}$	$\mathrm{M\,T^{-3}}$
R_{ij}	Reynolds tensor	$\mathrm{m^2s^{-2}}$	$\mathrm{L^2T^{-2}}$
R	Specific gas constant	$\mathrm{J\,kg^{-1}K^{-1}}$	$\mathrm{L^2\Theta^{-1}T^{-2}}$
R_0	Universal gas constant	$\mathrm{J\,mol^{-1}K}$	$\mathrm{M\,L^2N^{-1}\Theta^{-1}T^{-2}}$
$\underline{\mathbf{r}}$	Spatial position vector		
r	Radial vector		
r	Radius	m	L
$\underline{\underline{\mathbf{S}}}$	Symmetric velocity gradient	$\mathrm{s^{-1}}$	$\mathrm{T^{-1}}$
s	Path length	m	L
$\underline{\underline{\mathbf{T}}}$	Arbitrary tensor		
$\underline{\underline{\mathbf{U}}}$	Arbitrary tensor		
T	Temperature	K	Θ
T_S	Sutherland constant	K	Θ
t	Time	s	T
U	Magnitude of velocity	$\mathrm{m\,s^{-1}}$	$\mathrm{L\,T^{-1}}$
$\underline{\mathbf{u}}$	Velocity vector	$\mathrm{m\,s^{-1}}$	$\mathrm{L\,T^{-1}}$
u_τ	Shear velocity	$\mathrm{m\,s^{-1}}$	$\mathrm{L\,T^{-1}}$
u_1, u_2, u_3	Velocity components	$\mathrm{m\,s^{-1}}$	$\mathrm{L\,T^{-1}}$
$\underline{\mathbf{v}}$	Arbitrary vector		
V	Volume	$\mathrm{m^3}$	$\mathrm{L^3}$
$\dot{V}$	Volumetric flow rate	$\mathrm{m^3s^{-1}}$	$\mathrm{L^3T^{-1}}$
$\underline{\mathbf{w}}$	Rate of work per unit area	$\mathrm{kg\,s^{-2}}$	$\mathrm{M\,T^{-3}}$
$\underline{\mathbf{w}}$	Arbitrary vector		

W	Work per unit volume	$\mathrm{J\,m^{-3}}$	$\mathrm{M\,L^{-1}T^{-2}}$
$\underline{\mathbf{x}}$	Spatial position vector		
$\hat{\mathbf{x}}$	Unit vector		
x	Standard variable		
x_1, x_2, x_3	Cartesian coordinates		
x, y, z	Cartesian coordinates		

Greek Symbols

Symbol	Description	Unit	Dimension
α	Thermal diffusivity	$\mathrm{Pa\,s}$	$\mathrm{M\,L^{-1}T^{-1}}$
α, β, γ	Direction cosines		
α, β	Angles		
β	Coefficient of thermal expansion	$\mathrm{K^{-1}}$	Θ^{-1}
Γ	Diffusion coefficient	$\mathrm{kg\,m^{-1}s^{-1}}$	$\mathrm{M\,L^{-1}T^{-1}}$
γ	Ratio of specific heats		
δ	Viscous sublayer thickness	m	L
δ_{ij}	Kronecker delta		
Δ	Difference		
$\overline{\Delta}$	Filter cutoff length	m	L
$\underline{\underline{\boldsymbol{\epsilon}}}$	Strain rate tensor	$\mathrm{s^{-1}}$	$\mathrm{T^{-1}}$
ϵ	Error		
$\overline{\epsilon}$	Extrapolated standard deviation		
θ	Angle		
κ	Von Kármán Constant		
λ	Coefficient of bulk viscosity	$\mathrm{Pa\,s}$	$\mathrm{M\,L^{-1}T^{-1}}$
λ	Interpolation factor		
μ	Dynamic viscosity	$\mathrm{Pa\,s}$	$\mathrm{M\,L^{-1}T^{-1}}$
ν	Kinematic viscosity	$\mathrm{m^2s^{-1}}$	$\mathrm{L^2T^{-1}}$
ξ	parameter		
ρ	Density	$\mathrm{kg\,m^{-3}}$	$\mathrm{M\,L^{-3}}$
$\underline{\underline{\boldsymbol{\sigma}}}$	Stress tensor	$\mathrm{kg\,m^{-1}s^{-2}}$	$\mathrm{M\,L^{-1}T^{-2}}$
σ	Standard deviation		
$\sigma(x)$	Sigmoid function		
$\underline{\underline{\boldsymbol{\tau}}}$	Sub-grid scale stress tensor	$\mathrm{m^2s^{-2}}$	$\mathrm{L^2T^{-2}}$
τ	Stress	$\mathrm{kg\,m^{-1}s^{-2}}$	$\mathrm{M\,L^{-1}T^{-2}}$
τ_w	Wall shear stress	$\mathrm{kg\,m^{-1}s^{-2}}$	$\mathrm{M\,L^{-1}T^{-2}}$
Φ	Dissipation function	$\mathrm{N\,s^{-1}}$	$\mathrm{M\,L\,T^{-3}}$
$\underline{\boldsymbol{\psi}}$	Arbitrary vector		
ψ	Arbitrary intensive property		

$\mathrm{d}\underline{\boldsymbol{\Omega}}$	Rotation vector		
Ω	Control volume	m^3	L^3
$\underline{\boldsymbol{\omega}}$	Vorticity	s^{-1}	T^{-1}

Dimensionless quantities

Symbol	Description	Definition
Co	Courant number	$\Delta t \sum_{i=1}^{3} \frac{u_i}{\Delta x_i}$
Pe	Péclet number	$\frac{\rho U \Delta x}{2\Gamma}$
Re	Reynolds number	$\frac{UL}{\nu}$
Re_w	Boundary Reynolds number	$\frac{u_\tau k_l}{\nu}$
u^+	Dimensionless velocity	$\frac{u}{u_\tau}$
u_τ	Shear velocity	$\sqrt{\frac{\tau_w}{\rho}}$
y^+	Wall distance	$\frac{y u_\tau}{\nu}$

Subscripts

Symbol	Description
0	Initial value
0	Zero value
d	Duct
eff	Effective quantity
g	Gap
l	Length related quantity
M	Mechanical
max	maximum
min	minimum
o	Offset
op	operating point
p	Pressure
s	Sphere
sgs	Sub-grid scale
t	Tangential
t	Turbulent
tot	Total
τ	Shear stress related quantity
v	Viscous
w	Wall related quantity

Superscripts

Symbol	Description
$+$	Wall coordinate
$*$	Deviatoric component
D	Dimensionless quantity
1mm	1 mm sphere
8mm	8 mm sphere
40mm	40 mm sphere
diff	diffusive
num	numerical
p	prototype
real	realistic
T	Transpose

Operations

Operation	Description	Definition
∇s	Gradient of s	$\frac{\partial s}{\partial x_i}\underline{\mathbf{e}}_i$
$\nabla\underline{\mathbf{v}}$	Gradient of $\underline{\mathbf{v}}$	$\frac{\partial v_i}{\partial x_j}\left(\underline{\mathbf{e}}_i \otimes \underline{\mathbf{e}}_j\right)$
$\nabla \cdot \underline{\mathbf{v}}$	Divergence of $\underline{\mathbf{v}}$	$\frac{\partial v_i}{\partial x_i}$
$\nabla^2 s$	Laplacian of s	$\frac{\partial}{\partial x_i}\frac{\partial s}{\partial x_i}$
$\underline{\mathbf{v}} \otimes \underline{\mathbf{w}}$	Outer product of $\underline{\mathbf{v}}$ and $\underline{\mathbf{w}}$	$T_{ij} = v_i w_j$
$tr(\underline{\underline{\mathbf{T}}})$	Trace of $\underline{\underline{\mathbf{T}}}$	T_{kk}
$\underline{\underline{\mathbf{T}}}^*$	Deviatoric component of $\underline{\underline{\mathbf{T}}}$	$T_{ij} - T_{ii}\delta_{ij}$
$\underline{\underline{\mathbf{T}}} : \underline{\underline{\mathbf{U}}}$	Double inner product of $\underline{\underline{\mathbf{T}}}$ and $\underline{\underline{\mathbf{U}}}$	$T_{ij}U_{ij}$

Abbreviations

Acronym	Description
1D	One-dimensional
2D	Two-dimensional
3D	Three-dimensional
CDS	Central differencing scheme
DNS	Direct Numerical Simulation
FDM	Finite Difference Method
FEM	Finite Element Method
FVM	Finite Volume Method
LES	Large Eddy Simulation

LHS	Left hand side
LUDS	Linear Upwind Differencing Scheme
RANS	Reynolds-averaged Navier-Stokes
RHS	Right hand side
sgs	Subgrid scale
rpm	Revolutions per minute
UDS	Upwind differencing scheme
w.r.t.	With respect to

List of Figures

List of Tables

Chapter 1

Introduction

Project *GrindBall* is an applied research project sponsored by the German Research Foundation (DFG) as part of the work-group *Small Machine Tools* (SPP 1476) involving simulation, electro-magnetic control, and manufacture of a miniature abrading device. The workload in this project is hence distributed across three institutes: computational simulation is conducted at the *Center of Applied Space Technology and Microgravity* (ZARM), the electro-magnetic control element is developed at the *Institute for Electrical Drives, Power Electronics and Devices* (IALB), and manufacture of the tool itself is undertaken by the *Laboratory for Precision Machining* (LFM).

1.1 Motivation

Miniaturisation is of great importance in many fields such as mechantronics, optics, or medicine as it enables new functionality or makes processes more economical [BRB+13]. Micro-grinding, for example, can be performed with extremely high precision. While this increasing precision [DMT06] has made it possible to produce smaller and smaller workpieces, the tools used to work on them have, for the most part, remained constant in size [WRK10]. The skewed ratio of tool size to workpiece size is creating a growing ecological, economic, and technical inefficiency regarding respective processes [WGKK12]. Until now, miniaturising existing tools has been performed in order to combat said skewed ratio. This approach is, however, reaching its limits regarding technical feasibility and usefulness [ASB10]. For this reason, new innovative concepts and tools need to be developed, which are specifically designed to cope with small workpieces and spatially confined environments, in order to make progress in production processes such as micro-machining and ultra precise machining. It has already been shown that new operating principles and technologies present innovative methods of miniaturisation that supersede a mere reduction in size of pre-existing tools [BRB+13, DMK12]. This field possesses a lot of potential in terms of research and development of new tools which will be capable of outperforming currently available technologies. Workspace utilisation and energy requirements can still be vastly improved upon. Furthermore, the tools' susceptib-

ility to thermal deformation effects can be greatly reduced as a result of their smaller size [BRB+13]. Further direct results of miniature tools are increased flexibility and design possibilities concerning the machining of small workpieces since micro-tools can quickly adapt to new production procedures.

Since the ratio of surface area to volume increases dramatically with increasing miniaturisation, one has, proportionally, far more functional surface to work with as volume decreases. This effect is extremely useful for abrasive tools because the control dynamics, for example, improve with decreasing tool size, thus also improving the tools ability to adapt to particular machining conditions [BRB+13]. Most abrasive tools used to create micro cavities suffer from the following problem: since the axis of rotation and its orientation to the workpiece are crucial in ensuring positive grinding results, aligning the axis of rotation is key when grinding a cavity. A grinding pencil, for instance, has its theoretical maximum effectiveness when the axis of rotation is parallel to the work piece. This, however, can often be difficult to achieve as the grinding pencil's mounting apparatus can touch down on to the work piece before maximum effectiveness can be reached. Also, should the axis of rotation be perpendicular to the workpiece, the grinding pencil's abrasion would tend to zero. This problem can be counteracted by tilting the apparatus slightly, however, this still delivers mediocre results because it does not maximise the tool's effectiveness. Figure 1.1 illustrates the problems stated along with a theoretical solution in which the axis of rotation is parallel to the workpiece at all times, thus maximising the tool's grinding efficiency. It is the goal of project *GrindBall* to develop a spherical grinding tool, which, in addition, combines propulsion and control into one single element. The intended result is a highly compact, precise, efficient, and adaptive miniature tool, which can be used as a desktop machine for processing non-magnetic workpieces such as glass or ceramic. Possible applications include manufacturing dentures or miniature camera lenses as are used in modern smart phones (which require extreme precision) to name just a few.

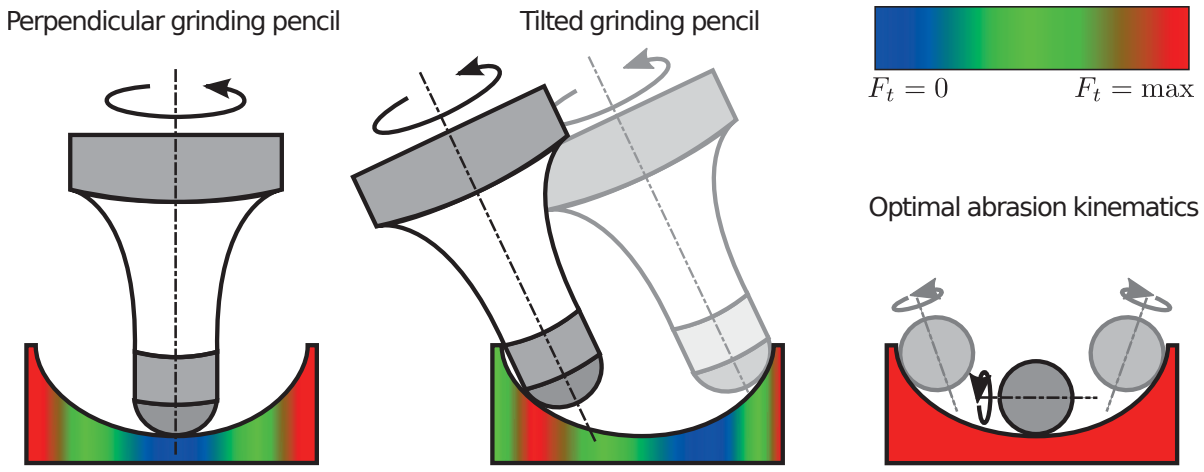

Figure 1.1: Grinding force depending on axis orientation

1.2 Basic setup

To achieve development of such a tool, fluid-driven propulsion is used in conjunction with a ferromagnetic sphere which is either covered in an abrasive coating or made entirely of abrasive material. It has already been shown that a variety of new production processes can achieve pleasing results concerning the manufacture of viable grinding spheres [BGB12, BRKB13]. In particular, injection moulding of micro-particle filled polymers has been shown to perform well in experiments conducted by the LFM and presents a viable option for use with the *GrindBall* [BRKB13].

Displacing forces are to be compensated by an adjustable opposing force, so that the sphere is held in a predefined position relative to the shaft at all times (as seen in Figure 1.2). Such displacing forces include gravity, vibration, forces resulting from the process of machining workpieces, and of course forces exerted by the fluid propulsion, all of which are to be counteracted. This task is performed by a magnetic bearing, which in addition to controlling the position of the grinding sphere, also defines an axis of rotation in combination with the flow. Experiments and simulations conducted by the IALB have shown that this concept can prove to meet the requirements demanded by this project and mathematical models were derived which aid in magnetically controlling and adjusting the position of the grinding sphere relative to the grinding shaft [Nor12, BOG+13].

The first prototype will utilise a sphere with a diameter of 40 mm. Throughout the duration of project *GrindBall*, this diameter is to be gradually scaled down to 1 mm with surrounding elements shrinking in proportion. The force necessary to achieve abrasion will be applied by the fluid flow. Due to the sphere having little mass and the resulting low moment of inertia, rotational frequencies in excess of 10,000 rpm and an extremely high control dynamic and accuracy are to be expected. Planning and construction of the *GrindBall* requires interdisciplinary cooperation between three branches of production technology: manufacturing engineering, electrical engineering, and fluid mechanics.

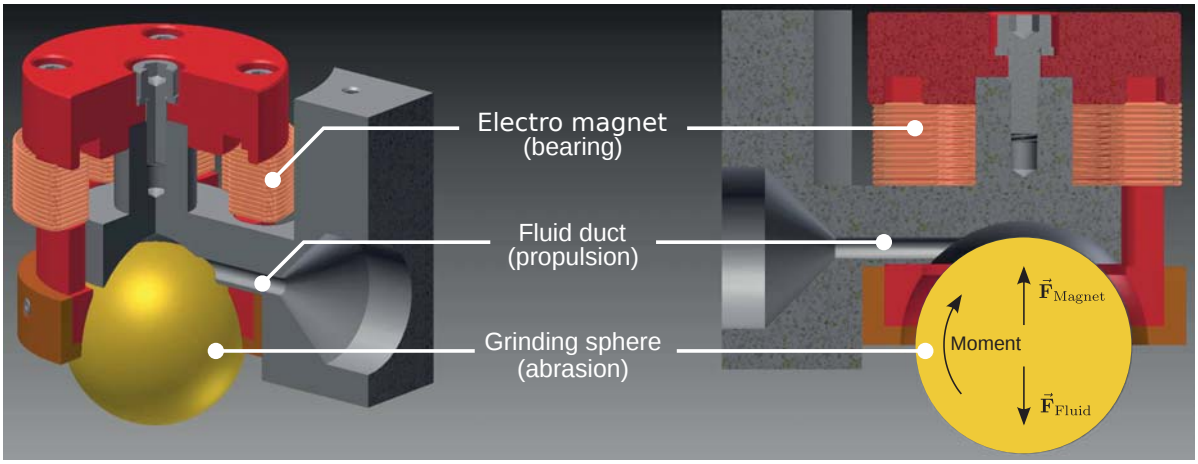

Figure 1.2: *GrindBall* - basic setup

1.3 Goals and limitations

This thesis begins by introducing the knowledge necessary to conduct computational simulations in the scope of this project, i.e. by deriving the equations governing fluid flow and stating common computational methods used in CFD simulations. Focus is drawn to the Finite Volume Method (FVM) and the modelling of turbulence using Large Eddy Simulation (LES). Throughout, the discussion is limited to sub-sonic flow and the use of adiabatic walls with uniform initial temperature distribution. Supersonic flow, heat-transferring walls, and temperature gradients on walls are best discussed once actual grinding trails have been performed and more data is available regarding the magnetic bearing's capabilities, material properties, and production of heat both by the bearing and the grinding process.

A parametric study is performed to determine the optimal configuration of a prototype tool with a 40 mm sphere using pneumatic propulsion (air). Once found, the optimal layout is subjected to a multitude of simulations under varying volumetric flow rates and spherical rotation frequencies, which ascertain the *GrindBall*'s possibilities and limitations. This includes identifying conditions for stable and efficient operation of the tool, quantifying acting forces, and deriving mathematical models which govern the force and power available to the abrasion process.

A fully functional version of the tool is devised with a spherical diameter of 8 mm using the knowledge gained from the development of the prototype. Parametric studies determine an optimal propulsion fluid and further improve the geometric layout. Forces and power are determined and discussed.

Simulation results - with specific focus on forces exerted by fluid impacting on to solid bodies - are validated by devising and performing an experiment with which to empirically confirm the presented findings. This is done using a setup consistent with the developed prototype. However, moving walls, which are analogous to a rotating grinding sphere, can not considered in the experimental setup.

Finally, a study is carried out using pneumatic propulsion which determines both forces and power for three different spherical diameters. These cover laminar, transitional, and fully turbulent flow. Using the resulting findings, non-dimensional relations are derived which govern forces and power depending on Reynolds number and a dimesionless spherical rotation frequency. Not only are the differences between laminar and turbulent flow made apparent, the need for further simulations with this geometry is eliminated as the resulting relations can be applied to arbitrary scales. Furthermore, it is shown that this type of analysis can be used both to compare different propulsion media and varying geometric layouts.

Knowledge of grinding force and power is extremely important when machining workpieces as it ensures that the rotation frequency and the cutting speed can be adapted

to particular materials, thereby ensuring accurate manufacturing of high quality cavities with smooth surfaces. The analyses conducted within this thesis pave the way for the development of a novel and revolutionary new grinding tool and demonstrate how fluid-to-solid force transfer can be modelled across a multitude of scales.

Chapter 2

Governing equations

The following section derives the equations which govern the flow of Newtonian compressible fluids and gives an overview of the concepts behind their derivations. Their incompressible equivalents are stated and specific models such as the perfect gas law and Sutherland's viscosity model are introduced.

2.1 Conservation of mass

Let ψ denote an arbitrary intensive property defined over a material control volume V. The Reynolds transport theorem[1] states that the rate of change of ψ within V must be equal to the sum of the flux of ψ over the volume boundaries δV and sources or sinks Q within V:

$$\frac{\mathrm{d}}{\mathrm{d}t}\int_V \psi \,\mathrm{d}V = -\int_{\delta V} \psi \underline{\mathbf{u}} \cdot \underline{\mathbf{n}} \,\mathrm{d}A + \int_V Q \,\mathrm{d}V. \tag{2.1}$$

Using the divergence theorem[1], the surface integral becomes a volume integral:

$$\frac{\mathrm{d}}{\mathrm{d}t}\int_V \psi \,\mathrm{d}V = -\int_V \nabla \cdot (\psi \underline{\mathbf{u}}) \,\mathrm{d}V + \int_V Q \,\mathrm{d}V. \tag{2.2}$$

Also the LHS can be written as

$$\frac{\mathrm{d}}{\mathrm{d}t}\int_V \psi \,\mathrm{d}V = \int_V \frac{\partial \psi}{\partial t} \,\mathrm{d}V \tag{2.3}$$

using Leibniz's integral rule[1]. Now the volume integrals may be combined into one single integral:

$$\int_V \frac{\partial \psi}{\partial t} + \nabla \cdot (\psi \underline{\mathbf{u}}) - Q \,\mathrm{d}V = 0. \tag{2.4}$$

[1] See Appendix A

Since this must hold for an arbitrary volume V, the integrand itself must equal zero. Hence,

$$\frac{\partial \psi}{\partial t} + \nabla \cdot (\psi \underline{\mathbf{u}}) - Q = 0. \tag{2.5}$$

This generic equation of continuity (eqn (2.5)) may be used to derive various conservation laws. The most basic such law is obtained by substituting the mass density ρ for ψ and assuming $Q = 0$, i.e. mass is neither created nor destroyed:

$$\frac{\partial \rho}{\partial t} + \nabla \cdot (\rho \underline{\mathbf{u}}) = 0. \tag{2.6}$$

This is known as the *mass continuity equation*, often also simply referred to as *the continuity equation* (cp. [Whi05]).

2.2 Conservation of momentum

In a similar yet somewhat less straight forward way, $\rho\underline{\mathbf{u}}$ may be substituted into eqn (2.5) to derive a relation for the rate of change of momentum. Note that Q is replaced by $\underline{\mathbf{f}}$, a vector representing sources and sinks of momentum, i.e. forces per unit volume:

$$\frac{\partial (\rho \underline{\mathbf{u}})}{\partial t} + \nabla \cdot (\rho \underline{\mathbf{u}} \otimes \underline{\mathbf{u}}) - \underline{\mathbf{f}} = 0. \tag{2.7}$$

Expanding the derivatives once yields

$$\frac{\partial \rho}{\partial t}\underline{\mathbf{u}} + \rho \frac{\partial \underline{\mathbf{u}}}{\partial t} + \nabla (\rho \underline{\mathbf{u}}) \cdot \underline{\mathbf{u}} + \rho \underline{\mathbf{u}} \nabla \cdot \underline{\mathbf{u}} = \underline{\mathbf{f}}, \tag{2.8}$$

which can be further decomposed into

$$\frac{\partial \rho}{\partial t}\underline{\mathbf{u}} + \rho \frac{\partial \underline{\mathbf{u}}}{\partial t} + \nabla (\rho)\, \underline{\mathbf{u}} \cdot \underline{\mathbf{u}} + \rho \nabla (\underline{\mathbf{u}}) \cdot \underline{\mathbf{u}} + \rho \underline{\mathbf{u}} \nabla \cdot \underline{\mathbf{u}} = \underline{\mathbf{f}}. \tag{2.9}$$

The following rearrangement highlights common factors ρ and $\underline{\mathbf{u}}$:

$$\underline{\mathbf{u}} \frac{\partial \rho}{\partial t} + \rho \frac{\partial \underline{\mathbf{u}}}{\partial t} + \underline{\mathbf{u}}\underline{\mathbf{u}} \cdot \nabla \rho + \rho \underline{\mathbf{u}} \cdot \nabla \underline{\mathbf{u}} + \rho \underline{\mathbf{u}} \nabla \cdot \underline{\mathbf{u}} = \underline{\mathbf{f}}, \tag{2.10}$$

which may be collected thusly:

$$\rho \left(\frac{\partial \underline{\mathbf{u}}}{\partial t} + \underline{\mathbf{u}} \cdot \nabla \underline{\mathbf{u}} \right) + \underline{\mathbf{u}} \left(\frac{\partial \rho}{\partial t} + \underline{\mathbf{u}} \cdot \nabla \rho + \rho \nabla \cdot \underline{\mathbf{u}} \right) = \underline{\mathbf{f}}. \tag{2.11}$$

At this point it is worth noting that the expression inside the second parenthesis on the LHS of eqn (2.11) is equal to the LHS of eqn (2.6), which is equal to zero. Hence, conservation of momentum is given by

$$\rho \frac{\partial \underline{\mathbf{u}}}{\partial t} + \rho \underline{\mathbf{u}} \cdot \nabla \underline{\mathbf{u}} = \underline{\mathbf{f}}. \tag{2.12}$$

$\underline{\mathbf{f}}$ is typically further divided into surface forces and body forces. Body forces are those which apply to the entire mass of the control volume. Such forces are usually gravitational or electromagnetic in nature. Here only gravity is considered, and thus

$$\underline{\mathbf{f}} = \underline{\mathbf{f}}_{\text{body}} + \underline{\mathbf{f}}_{\text{surface}} = \rho\underline{\mathbf{g}} + \underline{\mathbf{f}}_{\text{surface}}, \tag{2.13}$$

where $\underline{\mathbf{g}}$ is the vector acceleration of gravity.

Surface forces describe forces applied by external stresses on the sides of the volume element. These stresses consist of 9 components and are described by the tensor

$$\underline{\underline{\boldsymbol{\sigma}}} = \begin{pmatrix} \sigma_{xx} & \sigma_{xy} & \sigma_{xz} \\ \sigma_{yx} & \sigma_{yy} & \sigma_{yz} \\ \sigma_{zx} & \sigma_{zy} & \sigma_{zz} \end{pmatrix}. \tag{2.14}$$

$\underline{\underline{\boldsymbol{\sigma}}}$ is a symmetric tensor, i.e. $\sigma_{ij} = \sigma_{ji}$. Symmetry is required to satisfy equilibrium of moments about the three axes of the volume element and will be discussed in section 2.4. Note that the entries in the ith row of $\underline{\underline{\boldsymbol{\sigma}}}$ correspond to the forces acting on the surface facing in the direction of i. Entries in the jth column correspond to forces that act in the direction of j. Figure 2.1 shows individual components σ_{ij} acting on a control volume. Hence, the total force in each direction exerted by stress is given by

$$\begin{aligned} \mathrm{d}F_x &= \sigma_{xx}\mathrm{d}y\mathrm{d}z + \sigma_{yx}\mathrm{d}x\mathrm{d}z + \sigma_{zx}\mathrm{d}x\mathrm{d}y \\ \mathrm{d}F_y &= \sigma_{xy}\mathrm{d}y\mathrm{d}z + \sigma_{yy}\mathrm{d}x\mathrm{d}z + \sigma_{zy}\mathrm{d}x\mathrm{d}y \\ \mathrm{d}F_z &= \sigma_{xz}\mathrm{d}y\mathrm{d}z + \sigma_{yz}\mathrm{d}x\mathrm{d}z + \sigma_{zz}\mathrm{d}x\mathrm{d}y. \end{aligned}$$

In equilibrium, these forces would be balanced by equal and opposite forces on the back faces of the volume. However, if the element were to accelerate, stresses on the front and back would differ by differential amounts. In the direction of x, for example,

$$\sigma_{xx,\text{front}} = \sigma_{xx,\text{back}} + \frac{\partial\sigma_{xx}}{\partial x}\mathrm{d}x, \tag{2.15}$$

resulting in a net force on the volume element in the direction of x:

$$\mathrm{d}F_{x,\text{net}} = \left(\frac{\partial\sigma_{xx}}{\partial x}\mathrm{d}x\right)\mathrm{d}y\mathrm{d}z + \left(\frac{\partial\sigma_{yx}}{\partial y}\mathrm{d}y\right)\mathrm{d}x\mathrm{d}z + \left(\frac{\partial\sigma_{zx}}{\partial z}\mathrm{d}z\right)\mathrm{d}x\mathrm{d}y. \tag{2.16}$$

Or, dividing by $V = \mathrm{d}x\mathrm{d}y\mathrm{d}z$ and taking into account the symmetry of $\underline{\underline{\boldsymbol{\sigma}}}$:

$$f_x = \frac{\partial\sigma_{xx}}{\partial x} + \frac{\partial\sigma_{xy}}{\partial y} + \frac{\partial\sigma_{xz}}{\partial z}, \tag{2.17}$$

which is equivalent to taking the divergence of the vector composed of the top row of the stress tensor. Similarly, f_2 and f_3 are the divergences of the second and third row of $\underline{\underline{\boldsymbol{\sigma}}}$ respectively. Thus, the total vector surface force is

$$\underline{\mathbf{f}}_{\text{surface}} = \nabla\cdot\underline{\underline{\boldsymbol{\sigma}}} = \frac{\partial\sigma_{ij}}{\partial x_j}, \tag{2.18}$$

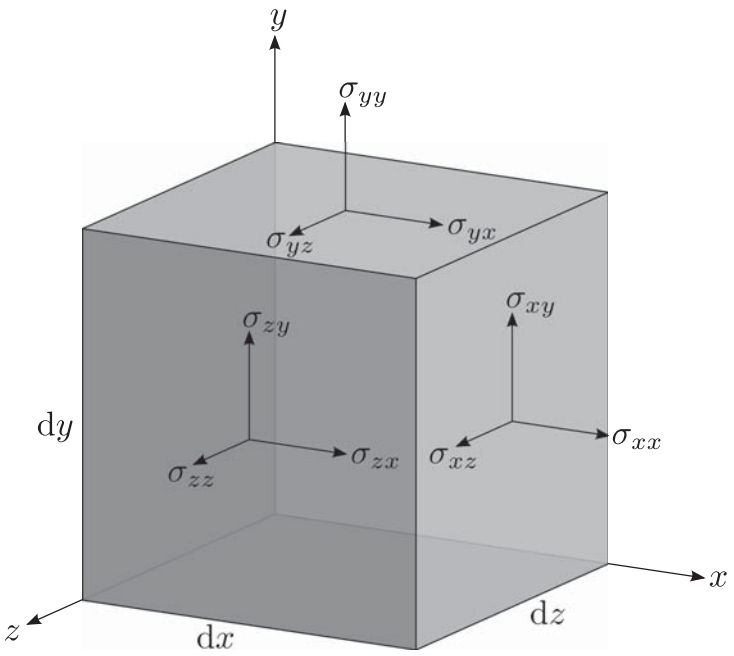

Figure 2.1: Stresses σ_{ij} acting on a control volume

where $\nabla \cdot \underline{\underline{\boldsymbol{\sigma}}}$ is to be interpreted in the tensor sense, resulting in a vector. Eqn (2.12) now becomes

$$\rho \frac{\partial \underline{\mathbf{u}}}{\partial t} + \rho \underline{\mathbf{u}} \cdot \nabla \underline{\mathbf{u}} = \nabla \cdot \underline{\underline{\boldsymbol{\sigma}}} + \rho \underline{\mathbf{g}} \tag{2.19}$$

and it remains to express $\underline{\underline{\boldsymbol{\sigma}}}$ in terms of the velocity $\underline{\mathbf{u}}$. In order to do this, the type of fluid must be taken into consideration. Here, only *Newtonian fluids* are examined, i.e. fluids in which stress is considered a linear function of rate of strain.

2.3 Motion and deformation of a fluid element

In fluid mechanics it is important to be able to describe and quantify motion, deformation, and rate of deformation of fluid elements. Four different types of motion and deformation typically exist: *translation*, *rotation*, *extensional strain* (*dilatation*), and *shear strain*. A 2D example of these four types can be seen in Figure 2.2. Point B is subject to translation as it has moved to the new position B'. The diagonal $\overline{BD}$ represented by the dashed line has been slightly rotated counter-clockwise to $\overline{B'D'}$. Dilatation can be seen in that the element has gained in size. Finally, the element has been subjected to shear strain as it is no longer square but now possesses a rhombic shape.

Now for a more analytical approach. Translation is defined using the displacements of the point B, namely $u\mathrm{d}t$ and $v\mathrm{d}t$. Hence, the rate of translation is simply u and v.

The rotation of $\overline{BD}$ is given by $\mathrm{d}\Omega_z = \theta + \mathrm{d}\alpha - \frac{\pi}{4}$. Noting the fact that $2\theta + \mathrm{d}\alpha + \mathrm{d}\beta = \frac{\pi}{2}$,

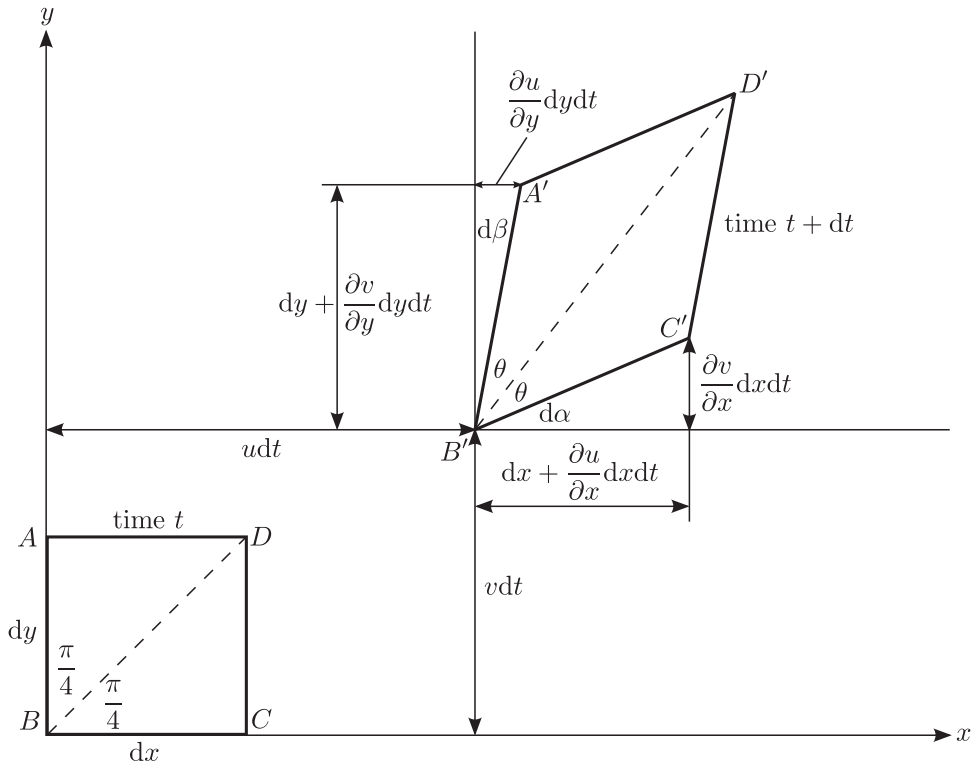

Figure 2.2: Distortion of a moving fluid element (as seen in [Whi05])

θ may be eliminated from the previous expression, leaving

$$\mathrm{d}\Omega_z = \frac{1}{2}\left(\mathrm{d}\alpha - \mathrm{d}\beta\right). \tag{2.20}$$

Both $\mathrm{d}\alpha$ and $\mathrm{d}\beta$ are linked to derivatives of velocity by

$$\begin{aligned}
\mathrm{d}\alpha &= \lim_{\mathrm{d}t\to 0}\left(\tan^{-1}\frac{\frac{\partial v}{\partial x}\mathrm{d}x}{\mathrm{d}x + \frac{\partial u}{\partial x}\mathrm{d}x\mathrm{d}t}\right)\mathrm{d}t = \frac{\partial v}{\partial x}\mathrm{d}t \\
\mathrm{d}\beta &= \lim_{\mathrm{d}t\to 0}\left(\tan^{-1}\frac{\frac{\partial u}{\partial y}\mathrm{d}y}{\mathrm{d}y + \frac{\partial v}{\partial y}\mathrm{d}y\mathrm{d}t}\right)\mathrm{d}t = \frac{\partial u}{\partial y}\mathrm{d}t,
\end{aligned} \tag{2.21}$$

which is valid for small angles. Eqn (2.21) may be substituted into (2.20) to yield the rate of rotation (also referred to as the *angular velocity)* about the z-axis:

$$\frac{\mathrm{d}\Omega_z}{\mathrm{d}t} = \frac{1}{2}\left(\frac{\partial v}{\partial x} - \frac{\partial u}{\partial y}\right). \tag{2.22}$$

Similarly, now for a 3D flow, the rates of rotation about the x and y axis are

$$\frac{\mathrm{d}\Omega_x}{\mathrm{d}t} = \frac{1}{2}\left(\frac{\partial w}{\partial y} - \frac{\partial v}{\partial z}\right) \qquad \frac{\mathrm{d}\Omega_y}{\mathrm{d}t} = \frac{1}{2}\left(\frac{\partial u}{\partial z} - \frac{\partial w}{\partial x}\right). \tag{2.23}$$

Since there is a factor $\frac{1}{2}$ in each of these 3 terms, the *vorticity* $\underline{\boldsymbol{\omega}}$ usually takes preference over $\frac{\mathrm{d}\underline{\boldsymbol{\Omega}}}{\mathrm{d}t}$, as it is equal to twice the angular velocity:

$$\underline{\boldsymbol{\omega}} = 2\frac{\mathrm{d}\underline{\boldsymbol{\Omega}}}{\mathrm{d}t} \tag{2.24}$$

Closer inspection of eqn (2.22) to eqn (2.24) shows their relation through vector calculus:

$$\underline{\boldsymbol{\omega}} = \nabla \times \underline{\mathbf{u}} \tag{2.25}$$

Hence, the vorticity is identically divergence free (or solenoidal):

$$\nabla \cdot \underline{\boldsymbol{\omega}} = \nabla \cdot (\nabla \times \underline{\mathbf{u}}) = 0 \tag{2.26}$$

On a side note, a flow with $\underline{\boldsymbol{\omega}} = 0$ is referred to as *irrotational* flow.

Shear strain can be thought of as the average decrease of the angle between two lines which are initially perpendicular to each other. Considering the lines $\overline{AB}$ and $\overline{BC}$ in Figure 2.2 as initial lines, the shear strain increment is $\frac{1}{2}(\mathrm{d}\alpha + \mathrm{d}\beta)$. Thus, making use of eqn (2.21), the shear strain rate is

$$\epsilon_{xy} = \frac{1}{2}\left(\frac{\mathrm{d}\alpha}{\mathrm{d}t} + \frac{\mathrm{d}\beta}{\mathrm{d}t}\right) = \frac{1}{2}\left(\frac{\partial v}{\partial x} + \frac{\partial u}{\partial y}\right) \tag{2.27}$$

Similarly,

$$\epsilon_{yz} = \frac{1}{2}\left(\frac{\partial w}{\partial y} + \frac{\partial v}{\partial z}\right) \qquad \epsilon_{zx} = \frac{1}{2}\left(\frac{\partial u}{\partial z} + \frac{\partial w}{\partial x}\right) \tag{2.28}$$

Note that shear strain rates are symmetric, i.e. $\epsilon_{ij} = \epsilon_{ji}$.

Finally, it remains to analytically define extensional strain (dilatation). Once again examining Figure 2.2, the extensional strain in direction of x is defined as the fractional increase in length of the horizontal side of the fluid element, given by

$$\epsilon_{xx}\mathrm{d}t = \frac{\left(\mathrm{d}x + \dfrac{\partial u}{\partial x}\mathrm{d}x\mathrm{d}t\right) - \mathrm{d}x}{\mathrm{d}x} = \frac{\partial u}{\partial x}\mathrm{d}t \tag{2.29}$$

with similar expressions for $\epsilon_{yy}\mathrm{d}t$ and $\epsilon_{zz}\mathrm{d}t$. Hence, the three dilatation strain rates are given by

$$\epsilon_{xx} = \frac{\partial u}{\partial x} \qquad \epsilon_{yy} = \frac{\partial v}{\partial y} \qquad \epsilon_{zz} = \frac{\partial w}{\partial z}. \tag{2.30}$$

These rates of strain form a second-order symmetric tensor

$$\underline{\underline{\boldsymbol{\epsilon}}} = \begin{pmatrix} \epsilon_{xx} & \epsilon_{xy} & \epsilon_{xz} \\ \epsilon_{yx} & \epsilon_{yy} & \epsilon_{yz} \\ \epsilon_{zx} & \epsilon_{zy} & \epsilon_{zz} \end{pmatrix}, \tag{2.31}$$

which will be shown to play a vital role in the derivation of the equation of motion.

2.4 Deformation law for a Newtonian fluid

In 1845, Sir George Gabriel Stokes postulated three assumptions which are valid for gases and most common fluids:

1. The fluid is continuous and its stress tensor σ_{ij} is at most a linear function of rates of strain ($\sigma_{ij} = f\left(\underline{\underline{\boldsymbol{\epsilon}}}\right)$).
2. The fluid is isotropic, i.e. its properties are independent of direction and therefore the deformation law is independent of the coordinate axes in which it is expressed.
3. When the strain rates are zero, the deformation law must reduce to the hydrostatic pressure condition $\sigma_{ij} = -p\delta_{ij}$.

The previous section shows that the tensor $\underline{\underline{\boldsymbol{\epsilon}}}$ is in fact symmetric, i.e. $\epsilon_{ij} = \epsilon_{ji}$. A property of symmetric tensors is that there exists one and only one set of axes for which the off-diagonal terms are zero. These are designated the *principal axes*, for which the strain rate tensor becomes

$$\underline{\underline{\boldsymbol{\epsilon}}}' = \begin{pmatrix} \epsilon'_{xx} & 0 & 0 \\ 0 & \epsilon'_{yy} & 0 \\ 0 & 0 & \epsilon'_{zz} \end{pmatrix}. \tag{2.32}$$

Condition 2 requires the principal strain axes be identical to the principal stress axes, which makes this a good basis from which to derive the deformation law. Let $\hat{\mathbf{x}}'$, $\hat{\mathbf{y}}'$, and $\hat{\mathbf{z}}'$ be the principal axes for which shear strain rates and shear stresses, i.e. the off-diagonal elements, are zero. Using these axes the deformation law can include at most three linear coefficients, for example

$$\sigma'_{xx} = -p + C_1\epsilon'_{xx} + C_2\epsilon'_{yy} + C_3\epsilon'_{zz}. \tag{2.33}$$

Note that $-p$ is added to satisfy condition 3. The condition of isotropy (condition 2) requires that $C_2 = C_3$, reducing the number of independent linear coefficients from three to two. Hence,

$$\sigma'_{xx} = -p + K\epsilon'_{xx} + C_2\left(\epsilon'_{xx} + \epsilon'_{yy} + \epsilon'_{zz}\right) = -p + K\epsilon'_{xx} + C_2\nabla\cdot\underline{\mathbf{u}}, \tag{2.34}$$

where $K = C_1 - C_2$, and the expression inside parentheses is the divergence of velocity. Eqn (2.34) may now be transformed to some arbitrary set of axes $\hat{\mathbf{x}}, \hat{\mathbf{y}}, \hat{\mathbf{z}}$ in which shear stresses are not equal to zero. Using directional cosines

$$\begin{array}{lll} \alpha_1 \equiv \hat{\mathbf{x}}'\cdot\hat{\mathbf{x}} & \beta_1 \equiv \hat{\mathbf{y}}'\cdot\hat{\mathbf{x}} & \gamma_1 \equiv \hat{\mathbf{z}}'\cdot\hat{\mathbf{x}} \\ \alpha_2 \equiv \hat{\mathbf{x}}'\cdot\hat{\mathbf{y}} & \beta_2 \equiv \hat{\mathbf{y}}'\cdot\hat{\mathbf{y}} & \gamma_2 \equiv \hat{\mathbf{z}}'\cdot\hat{\mathbf{y}} \\ \alpha_3 \equiv \hat{\mathbf{x}}'\cdot\hat{\mathbf{z}} & \beta_3 \equiv \hat{\mathbf{y}}'\cdot\hat{\mathbf{z}} & \gamma_3 \equiv \hat{\mathbf{z}}'\cdot\hat{\mathbf{z}} \end{array}$$

coordinates may be transformed from the arbitrary coordinate system to the principal coordinate system:

$$\hat{\mathbf{x}}' = \alpha_1\hat{\mathbf{x}} + \alpha_2\hat{\mathbf{y}} + \alpha_3\hat{\mathbf{z}}$$
$$\hat{\mathbf{y}}' = \beta_1\hat{\mathbf{x}} + \beta_2\hat{\mathbf{y}} + \beta_3\hat{\mathbf{z}}$$
$$\hat{\mathbf{z}}' = \gamma_1\hat{\mathbf{x}} + \gamma_2\hat{\mathbf{y}} + \gamma_3\hat{\mathbf{z}}$$

and vice-versa:

$$\hat{\mathbf{x}} = \alpha_1\hat{\mathbf{x}}' + \beta_1\hat{\mathbf{y}}' + \gamma_1\hat{\mathbf{z}}'$$
$$\hat{\mathbf{y}} = \alpha_2\hat{\mathbf{x}}' + \beta_2\hat{\mathbf{y}}' + \gamma_2\hat{\mathbf{z}}'$$
$$\hat{\mathbf{z}} = \alpha_3\hat{\mathbf{x}}' + \beta_3\hat{\mathbf{y}}' + \gamma_3\hat{\mathbf{z}}'.$$

By orthogonality of the coordinate system, it must hold that

$$\hat{\mathbf{x}}\cdot\hat{\mathbf{x}} = \hat{\mathbf{y}}\cdot\hat{\mathbf{y}} = \hat{\mathbf{z}}\cdot\hat{\mathbf{z}} = 1$$
$$\hat{\mathbf{x}}\cdot\hat{\mathbf{y}} = \hat{\mathbf{y}}\cdot\hat{\mathbf{z}} = \hat{\mathbf{z}}\cdot\hat{\mathbf{x}} = 0,$$

giving the identity

$$\alpha_l\alpha_m + \beta_l\beta_m + \gamma_l\gamma_m = \delta_{lm},$$

where δ_{lm} is the Kronecker delta. These definitions allow the following transformation rule for normal strain rates and stresses between the principal axes and the new arbitrary system:

$$\epsilon_{xx} = \epsilon'_{xx}\alpha_1^2 + \epsilon'_{yy}\beta_1^2 + \epsilon'_{zz}\gamma_1^2 \tag{2.35}$$
$$\sigma_{xx} = \sigma'_{xx}\alpha_1^2 + \sigma'_{yy}\beta_1^2 + \sigma'_{zz}\gamma_1^2 \tag{2.36}$$

Similarly, shear strain and stress can be expressed in terms of principal strain rates and stresses:

$$\epsilon_{xy} = \epsilon'_{xx}\alpha_1\alpha_2 + \epsilon'_{yy}\beta_1\beta_2 + \epsilon'_{zz}\gamma_1\gamma_2 \tag{2.37}$$
$$\sigma_{xy} = \sigma'_{xx}\alpha_1\alpha_2 + \sigma'_{yy}\beta_1\beta_2 + \sigma'_{zz}\gamma_1\gamma_2 \tag{2.38}$$

Now to eliminate σ'_{xx}, σ'_{yy}, and σ'_{zz} from eqn (2.36) by using eqn (2.34) in conjunction with eqn (2.35) and the fact that $\alpha_1^2 + \beta_1^2 + \gamma_1^2 = 1$:

$$\sigma_{xx} = -p + K\epsilon_{xx} + C_2\nabla\cdot\underline{\mathbf{u}}. \tag{2.39}$$

Similar expressions can be obtained for σ_{yy} and σ_{zz}. Also, σ'_{xx}, σ'_{yy}, and σ'_{zz} may be eliminated from eqn (2.38), resulting in

$$\sigma_{xy} = K\epsilon_{xy} \tag{2.40}$$

with analogous expressions for σ_{yz} and σ_{xz}. Note how the symmetry of ϵ_{ij} translates to σ_{ij}. For Newtonian fluids, K is typically equal to 2μ, twice the *ordinary coefficient*

of viscosity (usually called the *dynamic viscosity*, or simply the *viscosity*), and C_2, the *second coefficient of viscosity*, is usually referred to as the *coefficient of bulk viscosity* λ, as it is associated with volume expansion ($\nabla \cdot \underline{\mathbf{u}}$). Combining eqn (2.39) and eqn (2.40) yields a general deformation law for Newtonian viscous fluids:

$$\sigma_{ij} = -p\delta_{ij} + \mu\left(\frac{\partial u_i}{\partial x_j} + \frac{\partial u_j}{\partial x_i}\right) + \lambda\nabla \cdot \underline{\mathbf{u}}\delta_{ij}, \tag{2.41}$$

where the rates of strain ϵ_{ij} are now presented in terms of velocity gradients.

2.5 Mechanical and thermodynamic pressure

A direct consequence of eqn (2.41) was pointed out by Stokes in that he defined the mechanical pressure p_M as the average compression stress exerted on a control volume equal to $-\frac{1}{3}tr\left(\underline{\underline{\boldsymbol{\sigma}}}\right)$, which may also be expressed using (2.41). Hence,

$$p_M = -\frac{1}{3}\left(\sigma_{xx} + \sigma_{yy} + \sigma_{zz}\right) = p - \left(\frac{2}{3}\mu + \lambda\right)\nabla \cdot \underline{\mathbf{u}}. \tag{2.42}$$

This means that the average pressure in a viscous fluid under stress is not the same as the thermodynamic property called pressure. p_M also takes volume expansion into account, which exerts a force opposite to p. Stokes circumvented this problem in 1845 by assuming

$$\mu = -\frac{2}{3}\lambda \tag{2.43}$$

which is known as *Stokes' hypothesis*. Also, in incompressible fluids this problem vanishes as constant density implies $\nabla \cdot \underline{\mathbf{u}} = 0$. This is discussed later in Section 2.10.

2.6 The Navier-Stokes equations

The momentum equation for a Newtonian fluid is now obtained by substituting eqn (2.41) into eqn (2.12):

$$\begin{aligned}
\rho\frac{\mathrm{D}u}{\mathrm{D}t} &= \rho g_1 - \frac{\partial p}{\partial x} + \frac{\partial}{\partial x}\left(2\mu\frac{\partial u}{\partial x} + \lambda\nabla\cdot\underline{\mathbf{u}}\right) + \frac{\partial}{\partial y}\left[\mu\left(\frac{\partial u}{\partial y} + \frac{\partial v}{\partial x}\right)\right] \\
&\quad + \frac{\partial}{\partial z}\left[\mu\left(\frac{\partial u}{\partial z} + \frac{\partial w}{\partial x}\right)\right] \\
\rho\frac{\mathrm{D}v}{\mathrm{D}t} &= \rho g_2 - \frac{\partial p}{\partial y} + \frac{\partial}{\partial x}\left[\mu\left(\frac{\partial v}{\partial x} + \frac{\partial u}{\partial y}\right)\right] + \frac{\partial}{\partial y}\left(2\mu\frac{\partial v}{\partial y} + \lambda\nabla\cdot\underline{\mathbf{u}}\right) \\
&\quad + \frac{\partial}{\partial z}\left[\mu\left(\frac{\partial v}{\partial z} + \frac{\partial w}{\partial y}\right)\right] \\
\rho\frac{\mathrm{D}w}{\mathrm{D}t} &= \rho g_3 - \frac{\partial p}{\partial z} + \frac{\partial}{\partial x}\left[\mu\left(\frac{\partial w}{\partial x} + \frac{\partial u}{\partial z}\right)\right] + \frac{\partial}{\partial y}\left[\mu\left(\frac{\partial w}{\partial y} + \frac{\partial v}{\partial z}\right)\right] \\
&\quad + \frac{\partial}{\partial z}\left(2\mu\frac{\partial w}{\partial z} + \lambda\nabla\cdot\underline{\mathbf{u}}\right).
\end{aligned}$$

This can be expressed in a far more condensed manner using vector form:

$$\rho\frac{\partial\underline{\mathbf{u}}}{\partial t} + \rho\underline{\mathbf{u}}\cdot\nabla\underline{\mathbf{u}} = -\nabla p + \nabla\cdot\left(\mu\left(\nabla\underline{\mathbf{u}} + (\nabla\underline{\mathbf{u}})^T\right)\right) + \nabla\left(\lambda\nabla\cdot\underline{\mathbf{u}}\right) + \rho\underline{\mathbf{g}}. \tag{2.44}$$

For simplicity, eqn (2.44) is also presented using Einstein notation, while neglecting gravitational force, and assuming Stokes' hypothesis (eqn (2.43)):

$$\frac{\partial(\rho u_i)}{\partial t} + \frac{\partial(\rho u_j u_i)}{\partial x_j} = -\frac{\partial p}{\partial x_i} + \frac{\partial}{\partial x_j}\left[\mu\left(\frac{\partial u_i}{\partial x_j} + \frac{\partial u_j}{\partial x_i} - \frac{2}{3}\delta_{ij}\frac{\partial u_k}{\partial x_k}\right)\right] \tag{2.45}$$

with the associated mass continuity equation

$$\frac{\partial\rho}{\partial t} + \frac{\partial\left(\rho u_j\right)}{\partial x_j} = 0. \tag{2.46}$$

The Navier-Stokes equations were derived independently by Navier in 1823 and Stokes in 1845 and are of fundamental importance when studying the dynamics of a viscous fluid.

2.7 The energy equation

Rudolph Clausius states the first law of thermodynamics in [Cla50]: "*In a thermodynamic process, the increment in the internal energy of a system is equal to the difference between the increment of heat accumulated by the system and the increment of work done by it*". Based on this reasoning, the following equation must hold for a system:

$$\mathrm{d}E_{\mathrm{tot}} = \mathrm{d}Q + \mathrm{d}W, \tag{2.47}$$

where E_{tot} is the *total energy* of a system, Q is the *added heat*, and W is the *work done* to the system (not the work done by the system as stated by Clausius, hence the sign change). Thus, considering a fluid particle as such a system in motion results in:

$$E_{\text{tot}} = \Bigg(\underbrace{\rho e}_{\substack{\text{internal}\\ \text{energy}}} + \underbrace{\frac{1}{2}\rho U^2}_{\substack{\text{kinetic}\\ \text{energy}}} + \underbrace{\left(-\rho \underline{\mathbf{g}} \cdot \underline{\mathbf{x}}\right)}_{\substack{\text{potential}\\ \text{energy}}} \Bigg), \tag{2.48}$$

where e is the internal energy per unit volume, $U = (u^2 + v^2 + w^2)^{\frac{1}{2}}$ is the magnitude of $\underline{\mathbf{u}}$, and $\underline{\mathbf{x}}$ is the displacement of the fluid particle. Note that considering "the system" as a material control volume means that E_{tot}, Q, and W are now acting per unit volume. Eqn (2.47) may be differentiated using the material derivative following a particle in order to comply with the continuity equation and the equation of motion:

$$\frac{\mathrm{D}E_{\text{tot}}}{\mathrm{D}t} = \frac{\mathrm{D}Q}{\mathrm{D}t} + \frac{\mathrm{D}W}{\mathrm{D}t}. \tag{2.49}$$

Similarly, for eqn (2.48):

$$\frac{\mathrm{D}E_{\text{tot}}}{\mathrm{D}t} = \rho \left(\frac{\mathrm{D}e}{\mathrm{D}t} + U\frac{\mathrm{D}U}{\mathrm{D}t} - \underline{\mathbf{g}} \cdot \underline{\mathbf{u}} \right). \tag{2.50}$$

Eqn (2.47) and eqn (2.48) must now be linked by expressing Q and W in terms of fluid properties.

According to Fourier's law, the flow of heat is a direct result of temperature variation. Formally, this may be expressed in terms of heat flux and the temperature gradient:

$$\underline{\mathbf{q}} = -k\nabla T, \tag{2.51}$$

where $\underline{\mathbf{q}}$ is the *heat flow per unit area*, k is the *thermal conductivity*, and T denotes *temperature*. As seen in Figure 2.3, the heat flow entering the control volume through the left face is

$$q_x \mathrm{d}y\mathrm{d}z, \tag{2.52}$$

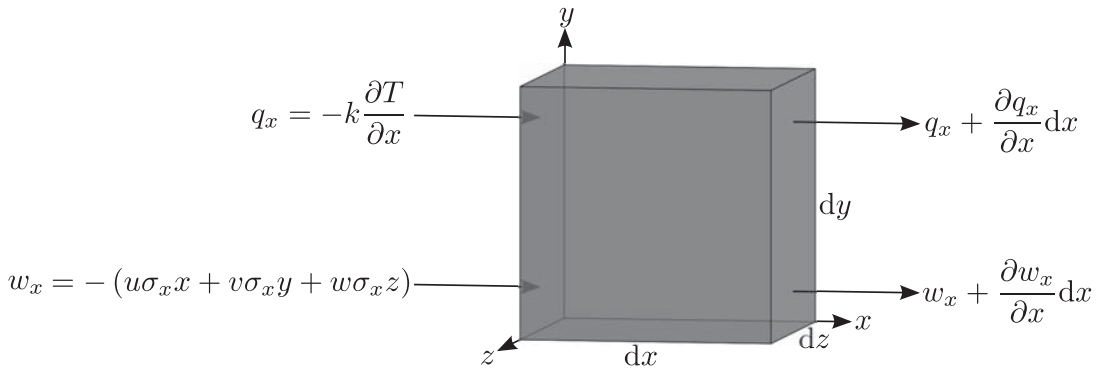

Figure 2.3: Exchange of heat and work done on $\mathrm{d}y\mathrm{d}z$ of a control volume [Whi05]

while the heat flow leaving the volume via the right face is

$$\left(q_x + \frac{\partial q_x}{\partial x}\mathrm{d}x\right)\mathrm{d}y\mathrm{d}z. \tag{2.53}$$

Similar expressions hold for q_y and q_z. Note that the net heat flow is now leaving the control volume. Hence, the heat transfer into the volume nets

$$-\left(\frac{\partial q_x}{\partial x} + \frac{\partial q_y}{\partial y} + \frac{\partial q_z}{\partial z}\right)\mathrm{d}x\mathrm{d}y\mathrm{d}z, \tag{2.54}$$

which may be divided by the volume $\mathrm{d}x\mathrm{d}y\mathrm{d}z$ to give the desired expression for heat transfer:

$$\frac{\mathrm{D}Q}{\mathrm{D}t} = -\nabla\cdot\underline{\mathbf{q}} = \nabla\cdot\left(k\nabla T\right). \tag{2.55}$$

It may be noted that internal heat generation is neglected here.

Considering once again Figure 2.3, this time in conjunction with Figure 2.1, the rate of work per unit area done to the control volume via the left face is

$$w_x = -\left(u\sigma_{xx} + v\sigma_{xy} + w\sigma_{xz}\right), \tag{2.56}$$

while the rate of work per unit area exerted by stresses acting on the right face is

$$-\left(w_x + \frac{\partial w_x}{\partial x}\mathrm{d}x\right) \tag{2.57}$$

with similar expressions for the other faces. In accordance with heat transfer, the net rate of work done to the control volume may now be expressed as

$$\begin{aligned}\frac{\mathrm{D}W}{\mathrm{D}t} = -\nabla\cdot\underline{\mathbf{w}} &= \frac{\partial}{\partial x}\left(u\sigma_{xx} + v\sigma_{xy} + w\sigma_{xz}\right)\\ &\quad+\frac{\partial}{\partial y}\left(u\sigma_{yx} + v\sigma_{yy} + w\sigma_{yz}\right)\\ &\quad+\frac{\partial}{\partial z}\left(u\sigma_{zx} + v\sigma_{zy} + w\sigma_{zz}\right)\\ &= \nabla\cdot\left(\underline{\mathbf{u}}\cdot\underline{\underline{\boldsymbol{\sigma}}}\right),\end{aligned} \tag{2.58}$$

which may be decomposed to read

$$\nabla\cdot\left(\underline{\mathbf{u}}\cdot\sigma_{ij}\right) = \underline{\mathbf{u}}\cdot\left(\nabla\cdot\sigma_{ij}\right) + \sigma_{ij}\frac{\partial u_i}{\partial x_j} \tag{2.59}$$

while making use of Einstein notation for terms involving $\underline{\underline{\boldsymbol{\sigma}}}$. The first term on the RHS of eqn (2.59) is linked to the momentum equation

$$\nabla\cdot\sigma_{ij} = \rho\left(\frac{\mathrm{D}\underline{\mathbf{u}}}{\mathrm{D}t} - \underline{\mathbf{g}}\right), \tag{2.60}$$

and thus,

$$\underline{\mathbf{u}} \cdot (\nabla \cdot \sigma_{ij}) = \rho \left(U \frac{\mathrm{D}U}{\mathrm{D}t} - \underline{\mathbf{g}} \cdot \underline{\mathbf{u}} \right), \tag{2.61}$$

the RHS of which is the same as the kinetic and potential energy terms presented in eqn (2.50). Now, equating eqn (2.49) and eqn (2.50), while taking into consideration eqn (2.55) and eqn (2.59), results in:

$$\rho \frac{\mathrm{D}e}{\mathrm{D}t} = \nabla \cdot (k \nabla T) + \sigma_{ij} \frac{\partial u_i}{\partial x_j}. \tag{2.62}$$

This form of the first law of thermodynamics for fluid motion is very common, however, it may also be expressed using *fluid enthalpy*

$$h = e + \frac{p}{\rho}. \tag{2.63}$$

To achieve this, the stress tensor σ_{ij} is split into pressure terms and viscous terms using eqn (2.41):

$$\sigma_{ij} \frac{\partial u_i}{\partial x_j} = \sigma'_{ij} \frac{\partial u_i}{\partial x_j} - p \nabla \cdot \underline{\mathbf{u}}. \tag{2.64}$$

Multiplying the continuity equation (eqn (2.6)) by pressure p results in the following expression for $p \nabla \cdot \underline{\mathbf{u}}$:

$$p \nabla \cdot \underline{\mathbf{u}} = -\frac{p}{\rho} \frac{\mathrm{D}\rho}{\mathrm{D}t} = \rho \frac{\mathrm{D}}{\mathrm{D}t} \left(\frac{p}{\rho} \right) - \frac{\mathrm{D}p}{\mathrm{D}t}. \tag{2.65}$$

Combining the above three equations with eqn (2.62) yields the following expression containing the enthalpy h:

$$\rho \frac{\mathrm{D}h}{\mathrm{D}t} = \frac{\mathrm{D}p}{\mathrm{D}t} + \nabla \cdot (k \nabla T) + \sigma'_{ij} \frac{\partial u_i}{\partial x_j}, \tag{2.66}$$

the *energy equation* in terms of enthalpy.

2.8 The perfect gas

Common gases tend to follow the *perfect gas law* (often also referred to as the *ideal gas law*)

$$p = \rho R T \tag{2.67}$$

within a reasonably small margin of error, where

$$R = \frac{k_B}{m} \tag{2.68}$$

is the ratio of Boltzmann's constant $k_B = 1.3806 \cdot 10^{-23}\,\mathrm{J\,K^{-1}}$to the mass m of a single molecule. Alternatively, R may also be expressed specific to a certain gas in terms of specific molecular weight M_{gas}:

$$R = \frac{R_0}{M_{\mathrm{gas}}}, \tag{2.69}$$

where $R_0 = 8.314\,\mathrm{J\,mol^{-1}\,K^{-1}}$ is the universal gas constant. Mixtures of gases may also be treated using eqn (2.67) and eqn (2.69) by defining the molecular weight of the mixture as

$$M_{\mathrm{mix}} = \frac{1}{\sum_i \frac{C_i}{M_i}}, \tag{2.70}$$

where $C_i = \frac{\rho_i}{\rho}$ are mass fractions and M_i are the molecular weights of the individual components. Or, regarding M_i in terms of mole fractions x_i, i.e. the number of moles of species i per mole of the mixture:

$$M_{\mathrm{mix}} = \sum_i x_i M_i. \tag{2.71}$$

As an example, air consisting of 78% nitrogen N_2, 21% oxygen O_2, and 1% argon Ar has molecular weight

$$\begin{aligned} M_{\mathrm{air}} &= 0.78 \cdot 28.016\,\mathrm{g\,mol^{-1}} + 0.21 \cdot 32.000\,\mathrm{g\,mol^{-1}} + 0.01 \cdot 39.944\,\mathrm{g\,mol^{-1}} \\ &= 28.97\,\mathrm{g\,mol^{-1}} \\ &= 28.97 \cdot 10^{-3}\,\mathrm{kg\,mol^{-1}}, \end{aligned}$$

which implies the following specific gas constant for air:

$$R_{\mathrm{air}} = \frac{8.314\,\mathrm{J\,mol^{-1}\,K}}{28.97 \cdot 10^{-3}\,\mathrm{kg\,mol^{-1}}} = 287\,\mathrm{J\,kg^{-1}\,K^{-1}}.$$

These are commonly used values for air at room temperature.

It is also useful to define the specific heats c_p and c_v at constant pressure and volume respectively:

$$c_p = \left(\frac{\partial h}{\partial T}\right)_p \qquad c_v = \left(\frac{\partial e}{\partial T}\right)_v. \tag{2.72}$$

Note that despite their names, these are not actually heats as such, but rather rates of change of energy. Another useful parameter is the ratio of specific heats

$$\gamma = \frac{c_p}{c_v}, \tag{2.73}$$

which ranges from 1.0 to 1.7 for all fluids. Furthermore, it is often helpful to observe the speed of sound a in a given fluid which is defined as the propagation of infinitesimal pressure pulses:

$$a^2 = \frac{\mathrm{d}p}{\mathrm{d}\rho} = \gamma \left(\frac{\partial p}{\partial \rho}\right)_T = \gamma \frac{p}{\rho} = \gamma R T. \tag{2.74}$$

It is due to great simplicity combined with reasonable accuracy that the ideal gas law is widely accepted and used in fluid mechanics.

2.9 Sutherland's viscosity model

William Sutherland proposed the following temperature dependent relation for the dynamic viscosity in [Sut93]:

$$\mu = \mu_0 \left(\frac{T}{T_0}\right)^{\frac{3}{2}} \frac{T_0 + T_S}{T + T_S}, \tag{2.75}$$

where μ_0 is the *reference viscosity* measured at temperature T_0, and T_S is the *Sutherland constant* which is characteristic of the gas considered. Note that eqn (2.75) may also be rearranged to give a slightly more condensed version of the model:

$$\mu = \frac{A_S \sqrt{T}}{1 + \frac{T_S}{T}}, \tag{2.76}$$

with

$$A_S = \mu_0 \frac{T_0 + T_S}{T_0^{\frac{3}{2}}}. \tag{2.77}$$

Consider, for example, air with a reference viscosity of $\mu_0 = 1.8325 \cdot 10^{-5}\,\mathrm{kg\,m^{-1}\,s^{-1}}$, measured at a reference temperature of $23^\circ\,\mathrm{C} = 296.15\,\mathrm{K}$ (see [Bir45]). The Sutherland constant for air is taken to be $T_S = 120\,\mathrm{K}$, resulting in

$$A_S = 1.8325 \cdot 10^{-5}\,\mathrm{kg\,m\,s^{-1}}\,\frac{296.15\,\mathrm{K} + 120\,\mathrm{K}}{296.15^{\frac{3}{2}}\,\mathrm{K}^{\frac{3}{2}}} = 1.496 \cdot 10^{-6}\,\mathrm{kg\,m^{-1}\,s^{-1}\,K^{-0.5}}. \tag{2.78}$$

Now to calculate the viscosity of air at, say, $20^\circ\,\mathrm{C} = 293.15\,\mathrm{K}$:

$$\mu = \frac{1.496 \cdot 10^{-6}\,\mathrm{kg\,m^{-1}\,s^{-1}\,K^{-\frac{1}{2}}} \cdot \sqrt{293.15\,\mathrm{K}}}{1 + \frac{120\,\mathrm{K}}{293.15\,\mathrm{K}}} = 1.817 \cdot 10^{-5}\mathrm{kg\,m^{-1}\,s^{-1}}. \tag{2.79}$$

While the Sutherland transport model is usually only valid for gases made up of a single substance, it can nevertheless be applied to air because of the nearly identical nature of oxygen and nitrogen molecules. The properties of argon molecules may be neglected due to its extremely low concentration. This allows the model to deliver fairly good results for this particular mixture.

2.10 Incompressible flow

While gases usually have a density that can vary greatly with pressure, most liquids have very little, or even negligible density variation. Water, for example, assuming constant temperature, undergoes a change of less than 5% in density when increasing pressure from atmospheric conditions by a factor of 1000. Hence, a special type of flow may

be considered when assuming constant density in both time and space. The continuity equation (eqn (2.6)) reduces to

$$\nabla \cdot \underline{\mathbf{u}} = 0, \tag{2.80}$$

leaving the divergence of $\underline{\mathbf{u}}$ to equal zero. Note that this does not have a great effect on the momentum equation (eqn (2.44)), apart from the obvious elimination of the $\nabla \cdot \underline{\mathbf{u}}$ term, thus also removing λ. However, if the dynamic viscosity μ is additionally assumed to be constant, several terms vanish, leaving the following *incompressible Navier-Stokes equations* for a fluid flow of constant viscosity and density:

$$\rho \frac{\mathrm{D}\underline{\mathbf{u}}}{\mathrm{D}t} = -\nabla p + \mu \nabla^2 \underline{\mathbf{u}} + \rho \underline{\mathbf{g}}, \tag{2.81}$$

where ∇^2 is the Laplace operator.

The energy equation may also be simplified in the limit of incompressible flow. Starting from the thermodynamic relation estimating the pressure dependence of enthalpy

$$\mathrm{d}h = c_p \mathrm{d}T + (1 - \beta T) \frac{\mathrm{d}p}{\rho} \tag{2.82}$$

known as the Boussinesq approximation (see [Whi05]), where

$$\beta = -\frac{1}{\rho} \left(\frac{\partial \rho}{\partial T} \right)_p \tag{2.83}$$

is the coefficient of thermal expansion, the energy equation (eqn (2.66)) may be written as

$$\rho c_p \frac{\mathrm{D}T}{\mathrm{D}t} = \beta T \frac{\mathrm{D}p}{\mathrm{D}t} + \nabla \cdot (k \nabla T) + \sigma'_{ij} \frac{\partial u_i}{\partial x_j}. \tag{2.84}$$

Considering constant density, i.e. $\beta = 0$, and neglecting dissipative terms leaves

$$\rho c_p \frac{\mathrm{D}T}{\mathrm{D}t} \approx \nabla \cdot (k \nabla T). \tag{2.85}$$

Now assuming constant thermal conductivity k:

$$\rho c_p \frac{\mathrm{D}T}{\mathrm{D}t} \approx k \nabla^2 T, \tag{2.86}$$

which is known as the *incompressible heat convection equation.*

2.11 Summary

In summary, there are three main laws that must be considered when discussing motion of a Newtonian fluid. These are conservation of mass

$$\frac{\partial \rho}{\partial t} + \nabla \cdot (\rho \underline{\mathbf{u}}) = 0, \tag{2.6}$$

conservation of momentum in form of the Navier-Stokes equations

$$\frac{\partial(\rho u_i)}{\partial t} + \frac{\partial(\rho u_j u_i)}{\partial x_j} = - \underbrace{\frac{\partial p}{\partial x_i}}_{\substack{\text{pressure} \\ \text{gradient}}} + \underbrace{\frac{\partial}{\partial x_j}\left[\mu\left(\frac{\partial u_i}{\partial x_j} + \frac{\partial u_j}{\partial x_i} - \frac{2}{3}\delta_{ij}\frac{\partial u_k}{\partial x_k}\right)\right]}_{\text{diffusive terms}}, \tag{2.45}$$

and conservation of energy

$$\rho\frac{\mathrm{D}h}{\mathrm{D}t} = \underbrace{\frac{\mathrm{D}p}{\mathrm{D}t}}_{\substack{\text{pressure} \\ \text{term}}} + \underbrace{\nabla\cdot(k\nabla T)}_{\substack{\text{diffusive} \\ \text{term}}} + \underbrace{\sigma'_{ij}\frac{\partial u_i}{\partial x_j}}_{\substack{\text{dissipative} \\ \text{term}}}. \tag{2.66}$$

These three equations involve seven variables, three of which are taken as primary ($\underline{\mathbf{u}}$, p, and T). The remaining variables are assumed to be known and related to one or more of the three main variables. These relations can stem from empirical evaluation or formulas derived from kinetic theory. Conservation laws are rather general and are subject to only a few restrictions (cp. [Whi05]):

1. the fluid forms a (mathematical) continuum
2. the particles are essentially in thermodynamic equilibrium
3. the only effective body forces are due to gravity
4. heat conduction follows Fourier's law
5. there are no internal heat sources

Here, the following relations are used for ρ, μ, h, and k: pressure is linked to density and temperature through the ideal gas law

$$p = \rho R T, \tag{2.67}$$

by which the change of enthalpy is given by

$$\mathrm{d}h = c_p \mathrm{d}T. \tag{2.87}$$

Sutherland's viscosity model governs the temperature dependence of viscosity

$$\mu = \mu_0 \left(\frac{T}{T_0}\right)^{\frac{3}{2}} \frac{T_0 + T_S}{T + T_S}. \tag{2.75}$$

Finally, heat conduction may also be approximated using Sutherland's formula [Whi05]:

$$k \approx k_0 \left(\frac{T}{T_0}\right)^{\frac{3}{2}} \frac{T_0 + T_S}{T + T_S}, \tag{2.88}$$

with k_0 and T_S stemming from tables. This, however, will be discussed with slightly more detail in the next chapter.

Chapter 3

Computational methods

This chapter deals with transforming the equations and relations derived in the previous chapter in a way that makes them viable for use in a computational simulation. Discretisation methods are introduced along with a selection of required spacial and temporal interpolation schemes. Treatment of pressure terms is shown to be of particular importance and the turbulence model *Large Eddy Simulation* is presented.

3.1 Discretisation methods

As described in the previous section, the equations governing a flow typically form a system of coupled, non-linear partial differential equations. In most cases these cannot be solved analytically. Hence, it is necessary to employ numerical methods in order to reach a solution. This can be achieved by *discretising* differential equations into algebraic equations, which are much easier to solve.

A typical transport equation for an arbitrary flow property ψ may be expressed as

$$\underbrace{\frac{\partial \rho\psi}{\partial t}}_{\substack{\text{local time}\\ \text{derivative}}} + \underbrace{\frac{\partial \rho u_j \psi}{\partial x_j}}_{\text{convection}} = \underbrace{\frac{\partial}{\partial x_j}\left(\Gamma \frac{\partial \psi}{\partial x_j}\right)}_{\text{diffusion}} + \underbrace{Q_\psi}_{\text{source terms}} \quad , \tag{3.1}$$

where Γ is the *diffusion coefficient* belonging to ψ and Q_ψ represents sources and sinks of ψ (cp. [Nol93]).

Several methods exist with which to perform discretisation of an equation such as eqn (3.1). In the field of numerical flow simulation the currently most prominent methods are the *Finite Difference Method* (*FDM*), the *Finite Volume Method* (*FVM*), and the *Finite Element Method* (*FEM*). In all three of these methods a *computational grid* is used within the computational domain in which ψ is determined at discrete points referred to as *computational nodes*. These nodes can be vertices of individual grid cells or centre points of grid cells. Hence, analytical solutions to the differential transport equations are replaced by numerical solutions to their discretised counter-parts, whereby the algebraic relations required to reach a numerical solution are dictated by the chosen method of discretisation.

The following will discuss FDM, FVM, and FEM as well as differences between these methods. Special attention will be given to FVM as it is the method utilised within this project besides being the most popular method in modern computational fluid dynamics.

3.1.1 Finite Difference Method

The Finite Difference Method uses Taylor series to approximate the derivatives occurring in transport equations. For a computational grid with constant distances between individual grid points this would imply

$$\psi_i = \psi_{i+1} - \Delta x \left(\frac{\partial \psi}{\partial x}\right)_{i+1} + \frac{1}{2}\Delta x^2 \left(\frac{\partial^2 \psi}{\partial x^2}\right)_{i+1} - ... \tag{3.2}$$

$$\psi_{i+2} = \psi_{i+1} + \Delta x \left(\frac{\partial \psi}{\partial x}\right)_{i+1} + \frac{1}{2}\Delta x^2 \left(\frac{\partial^2 \psi}{\partial x^2}\right)_{i+1} + ..., \tag{3.3}$$

here regarding the x-direction only as illustrated in Figure 3.1.

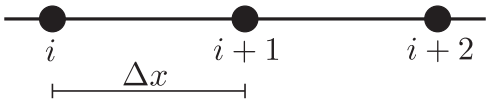

Figure 3.1: Discretisation on a computational grid in x-direction (cp. [Nol93])

Various terms occurring in partial differential equations (PDEs) can be approximated through algebraic manipulation or combination of these calculation models. Eqn (3.2) may be used to derive the *backward differencing scheme* (BDS):

$$\left(\frac{\partial \psi}{\partial x}\right)_{i+1} = \frac{\psi_{i+1} - \psi_i}{\Delta x} + \mathcal{O}(\Delta x^2), \tag{3.4}$$

where $\mathcal{O}(\Delta x^2)$ means that the terms neglected by truncating the Taylor series (the *approximation error*) are a function depending on Δx^n, where $n \geq 2$. Furthermore, the *central differencing scheme* (CDS) can be derived by subtracting eqn (3.2) from eqn (3.3):

$$\left(\frac{\partial \psi}{\partial x}\right)_{i+1} = \frac{\psi_{i+2} - \psi_i}{2\Delta x} + \mathcal{O}(\Delta x^2), \tag{3.5}$$

while addition of the two results in

$$\left(\frac{\partial^2 \psi}{\partial x^2}\right)_{i+1} = \frac{\psi_i + \psi_{i+2} - 2\psi_{i+1}}{\Delta x^2} + \mathcal{O}(\Delta x). \tag{3.6}$$

These are but a few examples of the possible ways to approximate individual terms.

The Finite Differece Method approximates the derivative terms in differential transport equations with discrete algebraic relations. The discretisation error describes the discrepancy between the results obtained on a finite computational grid and theoretical results

obtained on an infinitely fine grid (or an analytical solution). This error can be reduced by taking into account terms of higher order before truncating the Taylor series or by using a finer computational grid.

Finite Difference is a very simple and effective method of calculating flows on simple geometries and it is easy to develop higher order methods for regular computational grids. The FD method, however, is not suitable for more complex problems. Furthermore, it is not inherently conservative which makes it necessary to introduce additional conditions to satisfy conservation, thereby increasing computational cost.

3.1.2 Finite Volume Method

The Finite Volume Method subdivides the entire computational domain into a finite number of computational cells (control volumes). Computational nodes are taken to be centres of control volumes (see Figure 3.2). The coordinates x, y, and z are defined by the control volume and are not related to the entire domain. Nodes could also be taken to be the vertices of grid cells, with control volume borders taken to lie between adjacent grid points. Both options provide a computational grid consisting of non-overlapping control volumes, however, only the former is discussed here.

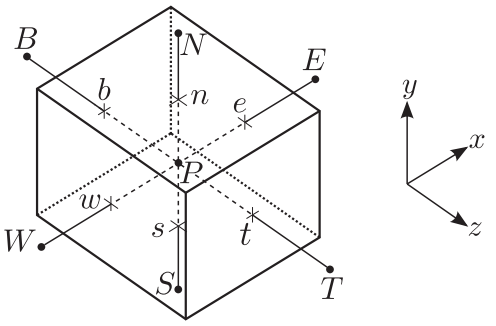

Figure 3.2: FVM control volume (cp. [Nol93])

In contrast to FDM, the FV method integrates transport equations over each control volume, meaning that transport equations need to be considered in integral form rather than differential form. Using vector notation, the general stationary transport equation

$$\nabla \cdot (\rho \underline{\mathbf{u}} \psi) = \nabla \cdot (\Gamma \nabla \psi) + Q_\psi \tag{3.7}$$

becomes

$$\int_V \nabla \cdot (\rho \underline{\mathbf{u}} \psi)\, \mathrm{d}V = \int_V \nabla \cdot (\Gamma \nabla \psi)\, \mathrm{d}V + \int_V Q_\psi\, \mathrm{d}V \tag{3.8}$$

when integrated over a control volume V. Using the divergence theorem, volume integrals

are replaced by surface integrals over the borders of the control volume:

$$\int_A \rho\psi\,(\underline{\mathbf{u}}\cdot \mathrm{d}\underline{\mathbf{A}}) = \int_A \Gamma\,(\nabla\psi\cdot \mathrm{d}\underline{\mathbf{A}}) + \int_V Q_\psi \mathrm{d}V. \tag{3.9}$$

Now, assuming that ρ, Γ, $\underline{\mathbf{u}}$, and ψ are evenly distributed on each of the control borders, integrals may be replaced by sums:

$$\sum_j \left[\,(\rho\psi)_j\, u_j A_j\right] = \sum_j \left[\Gamma_j\,(\nabla\psi)_j\, A_j\right] + \int_V Q_\psi\,\mathrm{d}V, \tag{3.10}$$

where the index j refers to the individual borders comprising the control volume. Figure 3.2 shows a control volume enclosed by six cell faces which are represented by the surfaces A_j for $j \in [1,6]$. u_j is the velocity component perpendicular to the surface A_j. Similarly, $(\nabla\psi)_j$ is the component of the gradient perpendicular to A_j.

When discussing FVM, it is customary to use compass notation as seen in Figure 3.2. The node lying inside the control volume under observation is designated P (point). Nodes lying in the control volumes above and below (in y-direction) are named N (north) and S (south) respectively, whereas nodes lying to the left and right (in x-direction) are called W (west) and E (east). Nodes neighbouring in the z-direction are named T (top) and B (bottom). Cell borders are given the according lower-case descriptions n, s, w, e, t, and b.

Using this notation, one may, for example, describe purely diffusive transport of the arbitrary property ψ based on the differential equation

$$\frac{\partial}{\partial x_j}\left(\Gamma\frac{\partial\psi}{\partial x_j}\right) + Q_\psi = 0 \tag{3.11}$$

in 3D for the node P as

$$\begin{aligned}&\left\{\Gamma\frac{\partial\psi}{\partial x}\right\}_e - \left\{\Gamma\frac{\partial\psi}{\partial x}\right\}_w + \left\{\Gamma\frac{\partial\psi}{\partial y}\right\}_n - \left\{\Gamma\frac{\partial\psi}{\partial y}\right\}_s + \\ &\left\{\Gamma\frac{\partial\psi}{\partial z}\right\}_t - \left\{\Gamma\frac{\partial\psi}{\partial z}\right\}_b + \int_V Q_\psi\,\mathrm{d}V = 0.\end{aligned} \tag{3.12}$$

Assuming linear distribution of ψ between grid points, i.e. for example $\psi_e = \psi_E - \psi_P$ and hence $\left\{\frac{\partial\psi}{\partial x}\right\}_e = \frac{\psi_E-\psi_P}{\Delta x_e}$, eqn (3.12) becomes

$$\begin{aligned}&\frac{\psi_E-\psi_P}{\Delta x_e}\Gamma_e A_e - \frac{\psi_P-\psi_E}{\Delta x_w}\Gamma_w A_w + \\ &\frac{\psi_N-\psi_P}{\Delta y_n}\Gamma_n A_n - \frac{\psi_P-\psi_S}{\Delta y_s}\Gamma_s A_s + \\ &\frac{\psi_T-\psi_P}{\Delta z_t}\Gamma_t A_t - \frac{\psi_P-\psi_B}{\Delta z_b}\Gamma_b A_b + \overline{Q}_\psi V = 0,\end{aligned} \tag{3.13}$$

where the volume integral over the source term Q_ψ has been approximated by $\overline{Q}_\psi V$. $\overline{Q}_\psi$ is a representative value of Q_ψ at node P. For simplicity, eqn (3.13) can be expressed in form of a general difference equation:

$$a_P \psi_P = \sum_i (a_i \psi_i) + b \qquad i = E, W, N, S, T, B, \tag{3.14}$$

where

$$\begin{aligned}
a_E &= \frac{\Gamma_e A_e}{\Delta x_e} \quad a_W = \frac{\Gamma_w A_w}{\Delta x_w} \quad a_N = \frac{\Gamma_n A_n}{\Delta y_n} \quad a_S = \frac{\Gamma_s A_s}{\Delta y_s} \quad a_T = \frac{\Gamma_t A_t}{\Delta z_t} a_B = \frac{\Gamma_b A_b}{\Delta z_b} \\
a_P &= \frac{\Gamma_e A_e}{\Delta x_e} + \frac{\Gamma_w A_w}{\Delta x_w} + \frac{\Gamma_n A_n}{\Delta y_n} + \frac{\Gamma_s A_s}{\Delta y_s} + \frac{\Gamma_t A_t}{\Delta z_t} + \frac{\Gamma_b A_b}{\Delta z_b} \\
&= a_E + a_W + a_N + a_S + a_T + a_B = \sum_i a_i \\
b &= \overline{Q}_\psi V.
\end{aligned}$$

The a_i's are coefficients that describe the influence neighbouring nodes (the values at points $E, W, N,$ ...) have on the value of ψ at point P. The general difference equation (eqn (3.14)) can be linear or non-linear. Non-linearity occurs when the initial differential equations themselves are also non-linear, as is the case for the Navier-Stokes equations.

Unlike the FD method, the Finite Volume Method is also suitable for complex geometries. Since it is constructed using fluxes over control borders, the FVM will always obey conservation as long as the fluxes of two control volumes sharing a border are equal. It's simplicity and intuitive design is what makes it the most popular method in modern flow computation.

It does, however, have the disadvantage that it can be very difficult to develop discretisation schemes of order higher than 2 in 3D. This is due to the fact that not only is interpolation required in the approximation, but also integration over the cell boundaries. Typically though, using schemes of order 2 delivers very good results as long as the computational grid is fine enough.

3.1.3 Finite Element Method

The *Finite Element Method* (FEM) is rather similar to the FV method. The computational grid (or the *mesh*) is made up of a finite number of control volumes (elements) which, unlike those used in the afore mentioned methods, tend to be unstructured. This makes mesh generation easier and less time consuming as well as making this method suitable for extremely complicated geometries.

The main difference between FEM and FVM is that in the former, equations are multiplied by a weight function before they are integrated over the whole domain. See [FP96] for slightly more detail on the FE method, as well as a list of literature for further reading.

FEM is widely used in solid body mechanics where it can aid in determining factors such as stresses or displacements. This can, for example, be very helpful in determining the behaviour of a car during a crash. For fluid dynamics, the FV method, however, is more than sufficient and delivers very good results at reasonable computational cost.

3.2 Interpolation schemes

It has been shown that the finite volume approximation of integrals over the control volumes and over their borders requires not only the values of variables at computational nodes, but also their values on control volume borders. These can be obtained by interpolation of nodal values. There exist a wide variety of interpolation schemes capable of delivering adequate results, two of which will be discussed in the following.

3.2.1 Upwind interpolation scheme

Consider ψ_e, the value if ψ on the border between the two nodes ψ_P and ψ_E. Using the *upwind differencing scheme* (UDS), the value of ψ_e is simply taken to be the same as the value of the node located upstream (or upwind) of the border e. Hence, depending on the direction of the flow, this can be formally described as

$$\psi_e = \begin{cases} \psi_P & \text{if } u_e > 0 \\ \psi_E & \text{if } u_e < 0 \end{cases}, \tag{3.15}$$

where u_e corresponds to the velocity u_1 of the flow evaluated at the boundary e. See Figure 3.3 for an illustration of the scheme.

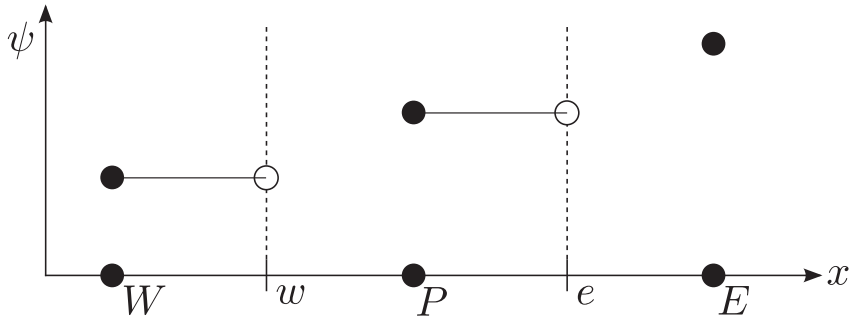

Figure 3.3: UDS for $u_w > 0$ and $u_e > 0$ (cp. [Nol93])

While UDS will always deliver non-oscillatory results, it does have the draw-back of introducing numerical diffusion. Considering the Taylor series expansion about the node P yields

$$\psi_e = \psi_P + (x_e - x_P)\left(\frac{\partial \psi}{\partial x}\right)_P + \frac{(x_e - x_P)^2}{2}\left(\frac{\partial^2 \psi}{\partial x^2}\right)_P + \mathcal{O}\left(x_e^3\right). \tag{3.16}$$

It is easily seen that this scheme is of first order since it uses only the first term on the RHS, leaving a truncation error of $\mathcal{O}(x_e)$ which closely resembles diffusive flux:

$$f_e^{\text{diff}} = \Gamma_e \left(\frac{\partial \psi}{\partial x} \right)_e , \tag{3.17}$$

where $\Gamma_e = \Gamma_e^{\text{real}} + \Gamma_e^{\text{num}}$, and the numerical diffusion coefficient is $\Gamma_e^{\text{num}} = \frac{1}{2}(\rho u)_e \Delta x$ ([FP96]). Should the direction of the flow be oriented at an angle to a multi-dimensional computational grid, numerical diffusion is increased even further since diffusion occurs both perpendicular to the flow as well as in the direction of flow. Sudden peaks or heavy variations tend to be smoothed out by UDS, and very fine grids are required to obtain satisfying results as the scheme is only of first order.

3.2.2 Linear upwind interpolation scheme

UDS may be expanded to a second order method by considering two upstream data points [VM07]. The resulting *linear upwind differencing scheme* (LUDS) uses the UDS estimate ψ_P (for $u_e > 0$) which is then corrected by an upwind-biased gradient $(\psi_P - \psi_W)/(x_P - x_W)$ multiplied by $x_e - x_P$, the distance between the node P and the east face. For equidistant grids $x_P - x_W = \Delta x$ and $x_e - x_P = \frac{1}{2}\Delta x$, yielding:

$$\psi_e = \begin{cases} \psi_P + \frac{1}{2}(\psi_P - \psi_W) & \text{if } u_e > 0 \\ \psi_E + \frac{1}{2}(\psi_E - \psi_{EE}) & \text{if } u_e < 0 \end{cases} . \tag{3.18}$$

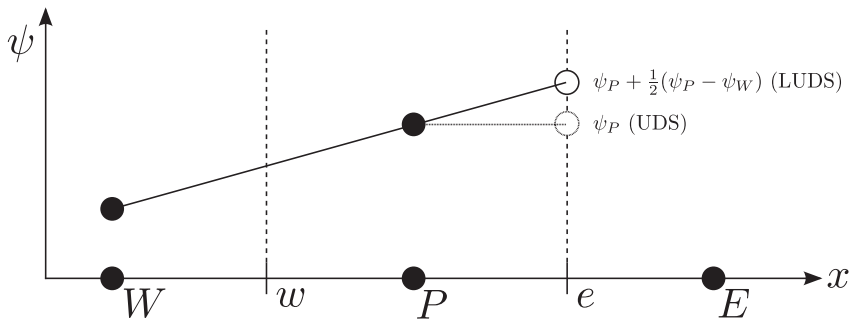

Figure 3.4: LUDS for $u_e > 0$

3.2.3 Linear interpolation scheme

The *linear interpolation scheme*, usually abbreviated CDS as it is equivalent to the central differencing scheme for the first derivative in FDM, is a very simple and intuitive way of

approximating values on control borders. Again considering the border e, the value ψ_e is taken to be a weighted average of its neighbouring values:

$$\psi_e = \lambda_e \psi_E + (1 - \lambda_e)\, \psi_P. \tag{3.19}$$

Figure 3.5 shows an illustration of the scheme. The interpolation factor λ_e takes into account the distance between the border e and the nodes P and E:

$$\lambda_e = \frac{x_e - x_P}{x_E - x_P}. \tag{3.20}$$

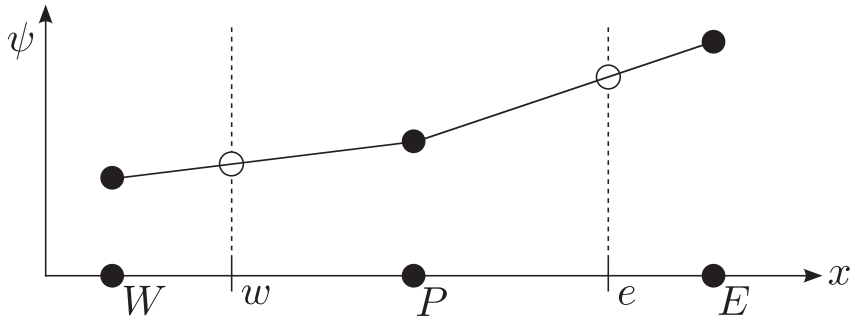

Figure 3.5: CDS for ψ on the control borders w and e (cp. [Nol93])

It can be shown by constructing the Taylor series of ψ_E about the point x_P and using the result to eliminate the first derivative of ψ in eqn (3.16) that

$$\psi_e = (1 - \lambda_e)\, \psi_P + \lambda_e \psi_E - \frac{(x_e - x_P)\,(x_E - x_e)}{2} \left(\frac{\partial^2 \psi}{\partial x^2}\right)_P + \mathcal{O}\left(x^2\right). \tag{3.21}$$

The LHS in conjunction with the first two terms on the RHS comprises the linear interpolation scheme, leaving a truncation error of order 2. Furthermore, since a linear profile of ψ is assumed between the nodes P and E, the gradient may also be approximated in a manner equivalent to eqn (3.19):

$$\left(\frac{\partial \psi}{\partial x}\right)_e \approx \frac{\psi_E - \psi_P}{x_e - x_P}. \tag{3.22}$$

A Taylor expansion around ψ_e can be used to show that the approximation error for the gradient is

$$\begin{aligned} \epsilon \;=\; & \frac{(x_E - x_e)^2 - (x_P - x_e)^2}{2\,(x_E - x_P)} \left(\frac{\partial^2 \psi}{\partial x^2}\right)_e + \\ & \frac{(x_E - x_e)^3 + (x_e - x_P)^3}{6\,(x_E - x_P)} \left(\frac{\partial^3 \psi}{\partial x^3}\right)_e + \mathcal{O}\left(x^4\right). \end{aligned} \tag{3.23}$$

For uniform grids this becomes a second order approximation since the coefficient of the second derivative in the truncation error cancels out. On non-uniform grids this method,

albeit being first order, behaves similarly to a second order approximation given that the grid is fine enough. See [FP96] for greater detail.

CDS is the simplest and most widely used second order interpolation scheme. It delivers very good results, thereby eliminating the need for higher order schemes and thus keeping computational cost at acceptable levels.

3.2.4 Other interpolation schemes

While the afore mentioned interpolation schemes suffice for most problems, there do exist several other schemes that deliver more exact results. *Quadratic Upwind Interpolation for Convective Kinematics* (QUICK) uses not two, but three nodal values to estimate the border value ψ_e by constructing a parabola through ψ_W, ψ_P, and ψ_E. On a uniform grid this would lead to

$$\psi_e = \frac{6}{8}\psi_P + \frac{3}{8}\psi_E - \frac{1}{8}\psi_W, \tag{3.24}$$

which has a truncation error of order 3. While this method brings with it the obvious advantage of a more exact solution, the difference to CDS is only minute. Hence, the increased computational cost is seldom justified.

It is also possible to construct hybrid methods that switch between two or more interpolation schemes. For example, one could use CDS, but switch to UDS in the case where CDS would produce an oscillatory solution. One could also use hybrid schemes to reduce computational cost by switching to higher order schemes only when absolutely necessary.

For the purposes of this thesis, UDS, LUDS, and CDS are sufficient and no further attention will be given to higher order or hybrid approximations.

3.3 Boundary conditions

Borders of control volumes that lie on the edge of the computational domain present a special case since they do not have a node on either side from which to extrapolate boundary values. Fluxes across these boundaries must either be given in the form of a boundary condition, or extrapolated from interior values and boundary information.

Inlet conditions are typically given by mass or volumetric flux for compressible and incompressible flow respectively. For outlets it usually suffices to use UDS. Impenetrable walls set the convective flux to zero, while relying on a zero gradient condition for pressure and density. Zero gradient simply takes the boundary value to be the same as that of the corresponding node. While much like upwind, this method is independent of the direction of the flow. Walls may also be given a specific flux condition for diffusive fluxes such as heat transfer, where zero heat flux corresponds to an adiabatic wall. If the gradient at

the wall is specified, it can be used to calculate the flux over the boundary, as well as an approximation for the value of the variable on the boundary.

Sensible boundary conditions are essential for simulating fluid flow. Incorrect, or even slightly inaccurate BCs can lead to anything from minor discrepancies between simulated and expected results, to an utterly unrealistic outcome. Even a complete failure of the simulation is possible. Thus, great care and consideration must be given toward the choice of correct boundary conditions prior to beginning a simulation.

3.4 Unsteady problems

So far, only spacial discretisation has been discussed. However, there is an additional coordinate that must be considered and discretised: time. This can be done either in the sense of FDM by using discrete points, or using the FV method by considering "temporal control volumes". Unlike spacial coordinates, time can obviously only influence the flow in one direction, which means that no conditions can be imposed on solutions once the calculation has begun, boundary conditions being the only exception. Methods for solving unsteady problems progress in a step-by-step fashion and bear great similarity to methods used for solving initial value problem ODEs.

The following basic first order initial value problem aids in discussing several solution methods:

$$\frac{\mathrm{d}\psi}{\mathrm{d}t} = f\left(t, \psi t\right), \qquad \psi\left(t_0\right) = \psi^0. \tag{3.25}$$

ψ is known at t_0 and the challenge lies in determining a solution at a later time. This becomes an iterative process as the new solution ψ^1 at time $t_1 = t_0 + \Delta t$ is taken as the new initial value used to calculate ψ^2. Note that here ψ^n refers to $\psi\left(t_n\right)$.

Integrating eqn (3.25) from t_n to t_{n+1} is a good basis from which to construct a solution method:

$$\int_{t_n}^{t_{n+1}} \frac{\mathrm{d}\psi}{\mathrm{d}t}\,\mathrm{d}t = \psi^{n+1} - \psi^n = \int_{t_n}^{t_{n+1}} f\left(t, \psi\left(t\right)\right)\mathrm{d}t. \tag{3.26}$$

The RHS of eqn (3.26) involves unknowns meaning exact solutions cannot be found. Hence, an approximation must be used. The mean value theorem states that there exists a point $\tau \in [t_n, t_{n+1}]$ for which the integral is exactly equal to $f\left(\tau, \psi\left(\tau\right)\right)\Delta t$. Since τ is not known, the integral must be approximated in some way, for example by a quadrature. Four such numerical quadrature methods are presented here.

Using the value of the integrand at the initial value is known as the *forward Euler method* (also *explicit Euler method*):

$$\psi^{n+1} = \psi^n + f\left(t_n, \psi^n\right)\Delta t. \tag{3.27}$$

Similarly one could use the other limit of integration, resulting in the *backward Euler method*:

$$\psi^{n+1} = \psi^n + f\left(t_{n+1}, \psi^{n+1}\right)\Delta t. \tag{3.28}$$

This is also known as the *implicit Euler method* as it involves the unknown value of f at time t_{n+1}.

The *midpoint rule* is yet another method that evaluates f at the point half way between t_n and t_{n+1}:

$$\psi^{n+1} = \psi^n + f\left(t_{n+\frac{1}{2}}, \psi^{n+\frac{1}{2}}\right)\Delta t. \tag{3.29}$$

The final method presented here utilises a straight line between $f(t_n)$ and $f(t_{n+1})$ to approximate the integral:

$$\psi^{n+1} = \psi^n + \frac{1}{2}\left[f\left(t_n, \psi^n\right) + f\left(t_{n+1}, \psi^{n+1}\right)\right]\Delta t. \tag{3.30}$$

This is called the *trapezoid rule*.

There are several definitions regarding the *stability* of these types of method. One such definition describes a method as stable if it produces a bounded solution provided the solution to the underlying differential equation is bounded as well. For the explicit Euler method, the following condition must be satisfied in order to guarantee a stable solution:

$$\left|1 + \Delta t \frac{\partial f\left(t, \psi\left(t\right)\right)}{\partial \psi}\right| < 1. \tag{3.31}$$

Allowing for complex values, this means that the second term on the LHS is restricted to a circle with radius 1 around -1 on the real axis. Such a condition makes this method *conditionally stable*.

As for accuracy, it can be shown using Taylor series that the explicit Euler method delivers a solution with an error proportional to $(\Delta t)^2$ at time $t_n + \Delta t$. However, the number of time steps needed to reach a solution at some time $t = t_0 + \sum_{n=1}^{N} t_n$ is inversely proportional to Δt. As an error is introduced at each time step, the overall truncation error of the method is proportional to Δt, making this method a first order method. Similarly, the implicit method is also a first order method, while the midpoint and trapezoid rule methods are of second order.

The other three methods are *unconditionally stable* for any Δt, provided $\frac{\partial f(t,\psi(t))}{\partial \psi} < 1$. The implicit Euler method has the additional advantage that it produces smooth (non-oscillating) solutions, even for very large time steps.

All of these methods are *two-level methods* because they use two points to calculate the unknown variable. In fact, it can be shown that second order is the highest achievable by two-level methods. Figure 3.6 illustrates these methods graphically. Methods requiring more than two points (*multipoint methods*) also exist. Naturally, they require more computational effort, but they also provide greater accuracy. Generally it can be said

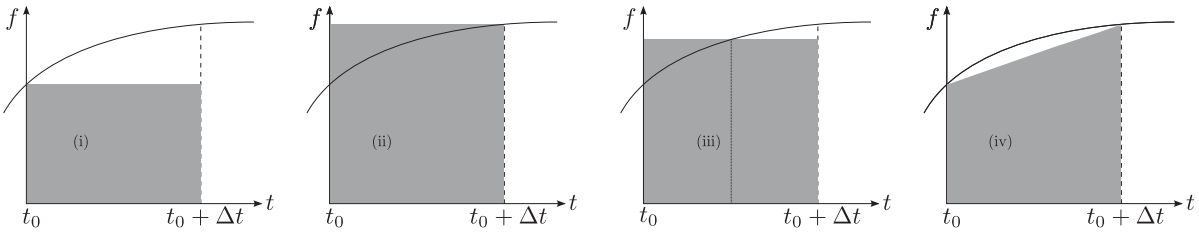

Figure 3.6: Approximation of $f(t)$ integrated over Δt. (i) explicit Euler, (ii) implicit Euler, (iii) midpoint rule, (iv) trapezoidal rule. (cp. [FP96])

that greater accuracy usually leads to decreased stability, meaning the simulation is more likely to diverge as a result of too coarse a mesh or complicated geometric features. Here, two-level methods are sufficient and the following will discuss four particular methods.

Temporal discretisation is now applied to the generic transport equation eqn (3.1). Terms that require spacial discretisation may be treated in the same way as has been previously discussed. The question that remains is at which point in time they are to be evaluated.

To make the generic transport equation more in keeping with eqn (3.26), convective, diffusive, and source terms are all collected on the RHS so they may be represented by $f(t, \psi(t))$:

$$\frac{\partial \rho\psi}{\partial t} = -\nabla \cdot (\rho\psi\underline{\mathbf{u}}) + \nabla \cdot (\Gamma \nabla\psi) + Q_\psi = f(t, \psi(t)). \tag{3.32}$$

When using explicit methods, the RHS need only be evaluated at t_n, for which the solution is already known. Implicit methods require the RHS to be evaluated at times for which the solution is not yet known, thereby introducing a new set of algebraic equations that need to be solved. This set of equations is different to the one obtained for steady problems.

3.4.1 Explicit (forward) Euler Method

The explicit Euler method is the simplest way of tackling unsteady problems. The only unknown is the value of ψ^{n+1} at the node in question and it is calculated in terms of neighbouring values which are evaluated at t_n and are thus already known.

The following simplified transport equation, in 1D, with constant velocity, constant fluid properties, and without source terms is used to demonstrate the explicit Euler method:

$$\frac{\partial \psi}{\partial t} = -u\frac{\partial \psi}{\partial x} + \frac{\Gamma}{\rho}\frac{\partial^2 \psi}{\partial x^2}. \tag{3.33}$$

Spacial derivatives are discretised according to CDS and the mesh is taken to be uniform in the direction of x. These assumptions deliver the same results for ψ_i^{n+1} using both FDM and FVM:

$$\psi_i^{n+1} = \psi_i^n + \left[-u\frac{\psi_{i+1}^n - \psi_{i-1}^n}{2\Delta x} + \frac{\Gamma}{\rho}\frac{\psi_{i+1}^n + \psi_{i-1}^n - 2\psi_i^n}{(\Delta x)^2}\right]\Delta t. \tag{3.34}$$

This may be expressed in a more condensed manner:

$$\psi_i^{n+1} = (1-2d)\,\psi_i^n + \left(d - \frac{Co}{2}\right)\psi_{i+1}^n + \left(d + \frac{Co}{2}\right)\psi_{i-1}^n, \tag{3.35}$$

where

$$d = \frac{\Gamma \Delta t}{\rho\,(\Delta x)^2} \tag{3.36}$$

and

$$Co = \frac{u \Delta t}{\Delta x} \tag{3.37}$$

are dimensionless parameters. The former, d, is the ratio of the time step to the characteristic diffusion time, i.e. the time it takes for a disturbance to be transported by diffusion over a spacial distance Δx. The latter, Co, is the ratio of time step to the characteristic convection time, unsurprisingly, the time it takes for a disturbance to be convected a distance Δx. Co is known as the *Courant number* and is a key parameter in CFD.

Inspection of eqn (3.35) shows that it is possible for the coefficients of ψ_i^n and ψ_{i+1}^n to become negative. This can lead to oscillating solutions which in turn can lead to non-physical behaviour or even instability of the simulation.

This is easily circumvented by imposing the following demands on the coefficients: $d < 0.5$ and $Co < 2d$. For the time step Δt this means

$$\Delta t < \frac{\rho\,(\Delta x)^2}{2\Gamma} \tag{3.38}$$

from the first condition. The second condition relates convection to diffusion:

$$\frac{\rho u \Delta x}{\Gamma} = Pe < 2, \tag{3.39}$$

where Pe is the *Péclet number* of the computational grid cell under investigation.

This method inherits its order from both the CDS approximation as well as the the explicit Euler method. Thus, it is said to be of second order in space and first order in time.

There is another way to combat this problem. The more the flow is dominated by convection, the more likely it becomes for the coefficient of ψ_{i+1}^n to become negative. A simple fix would be to use UDS for the convection term only, leading to

$$\psi_i^{n+1} = \psi_i^n + \Delta t \left[-u \frac{\psi_i^n - \psi_{i-1}^n}{2\Delta x} + \frac{\Gamma}{\rho} \frac{\psi_{i+1}^n + \psi_{i-1}^n - 2\psi_i^n}{(\Delta x)^2} \right], \tag{3.40}$$

resulting in

$$\psi_i^{n+1} = (1 - 2d - Co)\,\psi_i^n + d\psi_{i+1}^n + \left(d + \frac{Co}{2}\right)\psi_{i-1}^n. \tag{3.41}$$

The only restriction required is

$$\Delta t < \frac{1}{\frac{2\Gamma}{\rho\left(\Delta x\right)^2} + \frac{u}{\Delta x}} \tag{3.42}$$

to ensure a positive coefficient of ψ_i^n. The other coefficients are all unconditionally positive. For negligible convection, eqn (3.38) is once again obtained. Negligible diffusion yields

$$\Delta t < \frac{\Delta x}{u}. \tag{3.43}$$

In other words $Co < 1$. This is what is known as the *Courant–Friedrichs–Lewy condition* published in [CFL28] in 1928. Should both convection and diffusion be present, the criterion for stability becomes more complicated. A simple workaround is to satisfy both eqn (3.38) and eqn (3.43) individually. This may be a little more restrictive, but it provides a safe and easy alternative.

Due to the introduction of UDS, this approximation is no longer of second order in space, but rather of first order in both space in time. As a result, Δx and Δt must be kept small to prevent large errors from being introduced. This may become troublesome when simulating long time intervals as the required computation time can be dramatically increased.

3.4.2 Implicit (backward) Euler Method

A more versatile and stable method for solving unsteady problems is presented by the implicit Euler method. As the name suggests, the solution is no longer calculated explicitly, but approached iteratively because the algebraic equations use the unknown itself to calculate the next time step. Applying eqn (3.28) to eqn (3.33) while once again using CDS for spacial discretisation yields

$$\psi_i^{n+1} = \psi_i^n + \Delta t \left[-u \frac{\psi_{i+1}^{n+1} - \psi_{i-1}^{n+1}}{2\Delta x} + \frac{\Gamma}{\rho} \frac{\psi_{i+1}^{n+1} + \psi_{i-1}^{n+1} - 2\psi_i^{n+1}}{\left(\Delta x\right)^2} \right], \tag{3.44}$$

which may be expressed as

$$\left(1 + 2d\right)\psi_i^{n+1} + \left(\frac{Co}{2} - d\right)\psi_{i+1}^{n+1} + \left(-\frac{Co}{2} - d\right)\psi_{i-1}^{n+1} = \psi_i^n \tag{3.45}$$

using the same dimensionless parameters as before. In fact, the resulting system of algebraic equations are very similar to their steady counterparts. Rewriting the above as

$$a_P \psi_i^{n+1} = a_W \psi_{i-1}^{n+1} + a_E \psi_{i+1}^{n+1} + Q_P, \tag{3.46}$$

where

$$\begin{aligned} a_W &= +\tfrac{\rho u}{2\Delta x} + \tfrac{\Gamma}{(\Delta x)^2}, \quad a_E = \tfrac{\Gamma}{(\Delta x)^2} - \tfrac{\rho u}{2\Delta x}, \\ a_P &= -\left(a_E + a_W\right) + \tfrac{\rho}{\Delta t}, \quad Q_P = \tfrac{\rho}{\Delta t}\psi_i^n \end{aligned}$$

shows that the only difference to the steady version is the additional unsteady contribution to the coefficient a_P and the source term Q_P.

This method is of first order in time and requires a lot more computational effort due to the process of iteration. Increased stability and the possibility of using larger time steps is, however, often worth it. As previously stated, the implicit Euler method produces a smooth solution. Nevertheless, oscillatory solutions can occur for large Péclet numbers, yet this is easily counteracted by choosing the mesh fine enough.

This method's compatibility with non-linear equations as well as the fact that it does not depend on the size of the time step makes it a very efficient way of solving the unsteady portion of the Navier-Stokes equations and is also the reason it is used here.

3.4.3 Crank-Nicolson Method

Both Euler methods are first order methods in time which is sometimes not accurate enough for certain simulations. Crank and Nicolson proposed a way of combining both Euler methods in [CN47]. This method adds implicit and explicit Euler methods and divides by 2, thereby creating a second order method in a similar way as the midpoint rule:

$$F_{\text{Crank-Nicolson}} = \frac{1}{2}\left(F_{\text{explicit Euler}} + F_{\text{implicit Euler}}\right) \tag{3.47}$$

Discretising eqn (3.33) in this manner yields:

$$\begin{aligned}\psi_i^{n+1} &= \psi_i^n + \frac{\Delta t}{2}\left[-u\frac{\psi_{i+1}^n - \psi_{i-1}^n}{2\Delta x} + \frac{\Gamma}{\rho}\frac{\psi_{i+1}^n + \psi_{i-1}^n - 2\psi_i^n}{(\Delta x)^2}\right.\\ &\quad \left. -u\frac{\psi_{i+1}^{n+1} - \psi_{i-1}^{n+1}}{2\Delta x} + \frac{\Gamma}{\rho}\frac{\psi_{i+1}^{n+1} + \psi_{i-1}^{n+1} - 2\psi_i^{n+1}}{(\Delta x)^2}\right],\end{aligned} \tag{3.48}$$

which can be expressed as

$$(1+d)\left(\psi_i^{n+1} - \psi_i^n\right) = \frac{1}{2}\left[\left(d - \frac{Co}{2d}\right)\left(\psi_{i+1}^{n+1} + \psi_{i+1}^n\right) + \left(d + \frac{Co}{2d}\right)\left(\psi_{i-1}^{n+1} + \psi_{i-1}^n\right)\right]. \tag{3.49}$$

This method is second order accurate in both space and time and thus provides greater accuracy at the cost of decreased stability. Should stability become an issue it can be increased by blending this method with the implicit Euler method [Ope13c]:

$$F_{\text{Crank-Nicolson}}^{\text{blended}} = \frac{b}{2}\left(F_{\text{explicit Euler}} + F_{\text{implicit Euler}}\right) + (1-b)\,F_{\text{implicit Euler}}. \tag{3.50}$$

$b = 1$ corresponds to pure Crank-Nicolson and $b = 0$ to pure implicit Euler. Should pure Crank-Nicolson fail to produce a stable solution, b can be lowered to introduce blending. This way the loss of accuracy is not as great as switching straight to implicit Euler and it provides a sensible alternative for simulations that require high accuracy (such as Large Eddy Simulation discussed in Section 3.6) on complex geometries.

3.4.4 Other methods

Several other methods exist which can be used to tackle unsteady problems. Such methods can be of higher order or use more than two points to calculate values at a given time. Often both is the case. As with spatial methods, higher order temporal methods deliver far greater accuracy in exchange for decreased stability. Thus, complex geometries may not always be suitable and require that the order of the method used be lowered in order to perform a stable and converging simulation. Higher order temporal schemes are mostly applied when the spatial scheme is also of higher order. See [FP96] for more detail on higher order methods for unsteady problems.

3.5 Solving the Navier-Stokes equations

So far discretisation techniques have only been applied to generic conservation equations. This shall now be extended to the actual continuity and momentum equations, i.e. the Navier-Stokes equations. Both unsteady and advection terms are of the same form as the generic equations previously discussed. Hence, they can be treated in the same way using any of the methods presented in this chapter.

The viscous term in the momentum equation is equivalent to the diffusive term in the generic equation and can, for the most part, be treated in the same way. Special care, however, needs to be taken to account for spacial variability of dynamic viscosity, as well as having to account for bulk viscosity in compressible flow. This will not be discussed further but suffice to say discretisation of viscous terms is fairly straight forward.

One term that does not appear anywhere in the generic transport equation is pressure. Since there is no explicit transport equation for p, pressure must be determined using another method. In a compressible flow it is possible to use the continuity equation to obtain ρ, and then use an equation of state to determine p. Another approach would be to use the fact that mass must always be conserved. Hereby the velocity is first obtained from the momentum equation upon which a pressure field is constructed in a way that the continuity equation is also satisfied. Such pressure-velocity coupling techniques are usually derived for incompressible flow, but they may also be extended for the compressible case.

The following will give an overview over three such techniques for incompressible flow and state their compressible equivalents.

3.5.1 SIMPLE

Beginning with a solution for u_i that satisfies both the continuity equation

$$\frac{\partial \rho u_{i,P}^n}{\partial x_i} = 0 \tag{3.51}$$

and the momentum equation

$$\frac{\partial u_{i,P}^n}{\partial t} + \frac{\partial \rho u_{i,P}^n}{\partial x_j} = -\frac{1}{\rho}\frac{\partial p^n}{\partial x_i} + Q_i^n \tag{3.52}$$

at time n, one can advance to the next time step using any of the previously discussed methods for unsteady problems to obtain u_i^{n+1}. It should be noted at this point that u_i^{n+1} no longer satisfies the continuity equation which is why it must be corrected to ensure that mass is still conserved. The *Semi-Implicit Method for Pressure-Linked Equations* (SIMPLE) uses the pressure term to achieve this correction. Two types of iterations are performed within each time step. *Outer iterations* are those in which coefficient and source matrices of eqn (3.53) are updated and *inner iterations* are performed on the same equations but with source and coefficient matrices held constant while the pressure and velocity is corrected.

$$A_P u_{i,P}^{m*} + \sum_L A_L u_{i,L}^{m*} = -\frac{\partial p^{m-1}}{\partial x_i} + Q_i^{m-1}, \tag{3.53}$$

where the notation of u_i^{n+1} has been changed to u_i^{m*}. The asterisk indicates that it does not yet satisfy the continuity equation and an outer iteration counter m has been introduced. Rearranging yields the following expression for $u_{i,P}^{m*}$:

$$u_{i,P}^{m*} = -\frac{1}{A_P}\frac{\partial p^{m-1}}{\partial x_i} + \frac{1}{A_P}\left(Q_i^{m-1} - \sum_L A_L u_{i,L}^{m*}\right) \tag{3.54}$$

and the (at this point) hypothetical velocity u_i^m that satisfies continuity is given by

$$u_{i,P}^{m} = -\frac{1}{A_P}\frac{\partial p^{m}}{\partial x_i} + \frac{1}{A_P}\left(Q_i^{m} - \sum_L A_L u_{i,L}^{m}\right). \tag{3.55}$$

Subtracting eqn (3.54) from eqn (3.55) yields

$$u_{i,P}^{m} - u_{i,P}^{m*} = -\frac{1}{A_P}\frac{\partial}{\partial x_i}\left(p^m - p^{m-1}\right) - \frac{1}{A_P}\left(\sum_L A_L\left(u_{i,L}^{m} - u_{i,L}^{m*}\right)\right), \tag{3.56}$$

where the difference $Q_i^m - Q_i^{m-1}$ between source terms in each outer iteration is neglected. Furthermore, the SIMPLE method neglects the final term on the RHS of eqn (3.56)

entirely which is why it does not always converge quickly. Substituting eqn (3.56) into the continuity equation results in

$$\frac{\partial \rho u_{i,P}^{m}}{\partial x_i} - \frac{\partial \rho u_{i,P}^{m*}}{\partial x_i} = -\frac{\partial}{\partial x_i}\left(\frac{\rho}{A_P}\frac{\partial p'}{\partial x_i}\right). \tag{3.57}$$

Note that $p' = p^m - p^{m-1}$. Also, the first term on the LHS is equal to zero since it satisfies continuity, resulting in an equation that can be implicitly solved for p':

$$\frac{\partial \rho u_{i,P}^{m*}}{\partial x_i} - \frac{\partial}{\partial x_i}\left(\frac{\rho}{A_P}\frac{\partial p'}{\partial x_i}\right) = 0. \tag{3.58}$$

Now that p' is known it can be used to correct $u_{i,P}^{m*}$ to deliver a velocity that satisfies continuity:

$$u_{i,P}^{m} = u_{i,P}^{m*} - \frac{1}{A_P}\frac{\partial p'}{\partial x_i}. \tag{3.59}$$

This completes one outer iteration. This process is repeated by using $u_{i,P}^{m}$ and p^m as new starting estimates for $u_{i,P}^{n+1}$ and p^{n+1} until the correcting terms p' and $u' = u_{i,P}^{m} - u_{i,P}^{m*}$ are negligibly small upon which the next time step may be considered.

A compressible version of the SIMPLE method also exists. Rather than deriving this method from scratch, the incompressible method is used as a basis and then modified to account for variable density. This means that not only are velocity and pressure corrected, but density is also used as a correcting factor. This is done using

$$\rho' = \frac{\partial \rho}{\partial p} p' \tag{3.60}$$

where

$$\frac{\partial \rho}{\partial p} = \frac{1}{a^2} \tag{3.61}$$

and a is the speed of sound. Note that for incompressible flow, i.e. for infinitely large a, ρ' vanishes. No further details will be presented here. See [DLP93] for more information on the compressible equivalent of this method.

3.5.2 PISO

As was noted for the SIMPLE method, the last term on the RHS of eqn (3.56) is neglected entirely, leading to slow convergence and possibly even instability. This can be improved upon in a variety of ways, one of them being the *Pressure-Implicit Solution by Split-Operator* (PISO) method.

The first step is essentially a SIMPLE iteration:

$$u_{i,P}^{m*} = -\frac{1}{A_P}\frac{\partial p^{m-1}}{\partial x_i} + \frac{1}{A_P}\left(Q_i^{m-1} - \sum_L A_L u_{i,L}^{m*}\right) \tag{3.62}$$

is the initial velocity that fails to satisfy continuity and

$$u_{i,P}^{m**} = -\frac{1}{A_P}\frac{\partial p^{m-\frac{1}{2}}}{\partial x_i} + \frac{1}{A_P}\left(Q_i^{m-\frac{1}{2}} - \sum_L A_L u_{i,L}^{m**}\right) \tag{3.63}$$

satisfies continuity. Note that the double asterisk implies that this is not the final velocity and the superscript $m-\frac{1}{2}$ denotes that only "half" an outer iteration has been performed to reach this step. In other words a second part is required to complete an outer iteration. Subtracting the two previous equations yields

$$u_{i,P}^{m**} - u_{i,P}^{m*} = -\frac{1}{A_P}\frac{\partial}{\partial x_i}\left(p^{m-\frac{1}{2}} - p^{m-1}\right) - \frac{1}{A_P}\left(\sum_L A_L\left(u_{i,L}^{m**} - u_{i,L}^{m*}\right)\right), \tag{3.64}$$

which can be used to reach an implicit solution for $p' = p^{m-\frac{1}{2}} - p^{m-1}$ as before while once again neglecting the last term on the RHS of eqn (3.64):

$$\frac{\partial \rho u_{i,L}^{m*}}{\partial x_i} - \frac{\partial}{\partial x_i}\left(\frac{\rho}{A_P}\frac{\partial p'}{\partial x_i}\right) = 0. \tag{3.65}$$

The procedure up to this point is identical to the SIMPLE method apart from the different choice of nomenclature and results in a velocity that satisfies continuity:

$$u_{i,P}^{m**} = u_{i,P}^{m*} - \frac{1}{A_P}\frac{\partial p'}{\partial x_i}. \tag{3.66}$$

The second step of the PISO method compensates for having neglected the term $u' = u_{i,P}^{m**} - u_{i,P}^{m*}$ in the first step. Similarly to before the "initial" velocity

$$u_{i,P}^{m**} = -\frac{1}{A_P}\frac{\partial p^{m-\frac{1}{2}}}{\partial x_i} + \frac{1}{A_P}\left(Q_i^{m-\frac{1}{2}} - \sum_L A_L u_{i,L}^{m*}\right) \tag{3.67}$$

and the "final" velocity

$$u_{i,P}^{m} = -\frac{1}{A_P}\frac{\partial p^{m}}{\partial x_i} + \frac{1}{A_P}\left(Q_i^{m} - \sum_L A_L u_{i,L}^{m**}\right) \tag{3.68}$$

are subtracted from one another (again neglecting the difference of the two source terms)

$$u_{i,P}^{m} - u_{i,P}^{m**} = -\frac{1}{A_P}\frac{\partial}{\partial x_i}\left(p^{m} - p^{m-\frac{1}{2}}\right) - \frac{1}{A_P}\left(\sum_L A_L\left(u_{i,L}^{m**} - u_{i,L}^{m*}\right)\right) \tag{3.69}$$

and used to derive an implicit equation for $p'' = p^m - p^{m-\frac{1}{2}}$:

$$\frac{\partial}{\partial x_i}\left(\frac{\rho}{A_P}\frac{\partial p''}{\partial x_i}\right) = -\frac{\partial}{\partial x_i}\left(\frac{\rho}{A_P}\sum_L A_L u'_{i,L}\right) \tag{3.70}$$

where $\sum_L A_L u'_{i,L}$ can be determined using u'_i which can be calculated simply by rearranging the previously obtained eqn (3.66). Finally, the corrected velocity is given by:

$$u^m_{i,P} = u^{m**}_{i,P} - \frac{1}{A_P}\left(\frac{\partial p''}{\partial x_i} + \sum_L A_L u'_{i,L}\right) \tag{3.71}$$

together with the corresponding corrected pressure

$$p^m = p^{m-\frac{1}{2}} + p'' = p^{m-1} + p' + p''. \tag{3.72}$$

This method, while computationally more demanding, delivers greater stability and faster convergence since it does not simply neglect u'_i as the SIMPLE method does. Both methods are very similar and can be summarised into 6 basic steps:

1. Use u^n_i and p^n to advance to time $n+1$ according to the chosen temporal discretisation method
2. Obtain u^{m*}_i by solving the discrete momentum equations
3. Obtain p' by solving the pressure-correction equation
4. Use p' to obtain corrected velocity and pressure.
   If using the PISO algorithm, solve the second pressure-correction equation and correct velocity and pressure a second time
5. Repeat the procedure from step 2 onwards until all correction terms become negligible
6. Proceed to step one and repeat the loop for the text time step

As with the SIMPLE algorithm, PISO can be extended to the case of compressible flow but because the basic principle governing SIMPLE and PISO has already been presented here, no further attention will be given to the subject. See [Bre01] for more detail regarding the compressible equivalent of this algorithm.

3.5.3 PIMPLE

The PIMPLE method is an amalgamation of the SIMPLE and PISO methods. Essentially, inner iterations are performed using the SIMPLE method, while outer iterations are done with PISO [Ope13b]. SIMPLE can be used in this way because time does not progress within inner iterations and the flow can be locally treated as intransient. Results from the inner iterations are passed on to the outer iteration which then performs a PISO loop. Criteria for advancing to the next time step can either be sufficiently small corrections as mentioned before, or simply be done after a given amount of PISO loops. The latter is more convenient in practice as the former may dramatically increase computation time. In fact, the number of pressure-correction loops within each SIMPLE loop is usually also predetermined for the same reason. This means, however, that one needs to

carefully choose the number of iterations to ensure stability. The correct choice depends largely on geometry and complexity of the calculation.

As a result, this algorithm delivers even greater stability than the PISO method and also enables the use of larger time steps. PIMPLE, like PISO, is also capable of accurately solving transient flows, whereas the SIMPLE algorithm is more suited for steady state solutions. The increase in computational cost is usually well worth the improved accuracy of the result and stability of the calculation. Computational cost may even be lower than that of the previous two methods if the geometry allows for large enough time steps to be chosen without compromising stability.

3.6 Large Eddy Simulation

Turbulence in fluids is regarded as a very difficult subject in fluid dynamics. In fact, Lesieur mentions in [Les08] that turbulence even proves difficult to unequivocally define. Everyday life gives many different examples of turbulence: cigarette smoke being advected by its surrounding air. Sudden and abrupt changes in direction and velocity of wind affect not only air travel but also influence conditions on land and at sea. Fluid rapidly flowing around an obstacle creates a turbulent wake which increases the drag exerted on the object. Turbulent atmospheric and oceanic currents make the weather very hard to accurately predict. The list goes on, however, the common ground of all these different examples of turbulence is that they are disordered in time and space. This is, of course, no precise mathematical definition. Turbulent flow seems to be able to mix transported quantities more rapidly than molecular diffusion could do on its own. Hence, Lesieur introduces the following definition for turbulent flow:

- "*Firstly, a turbulent flow must be unpredictable, in the sense that a small uncertainty as to its knowledge at a given initial time will amplify so as to render impossible a precise deterministic prediction of its evolution*"
- "...[it] *has to satisfy the increased mixing property defined above*"
- "...[it] *must involve a wide range of spatial wave lengths*"

The uncertainties stated in the above definition require a statistical model in order to mimic turbulent behaviour in a numerical simulation. Despite only dealing with fluids in the Newtonian sense, it has so far not been possible to derive a generally accepted model. Instead, there exist a wide variety of models that all have varying accuracy and computational demand. One such turbulence model - *Large Eddy Simulation* (LES) [Frö06, Sag98] - is presented in the following.

The basic principle in LES is to differentiate between large and small frequency scales. The former, also referred to as *resolved scales*, are those which are directly calculated by the governing equations while the latter, also referred to as *subgrid scales*, are included by means of a statistical model. A generic property ψ is split into two separate components

$$\psi = \overline{\psi} + \psi', \tag{3.73}$$

with

$$\overline{\psi\left(\underline{\mathbf{x}}, t\right)} = \int_{-\infty}^{\infty}\int_{-\infty}^{\infty} \psi\left(\underline{\mathbf{r}}, t'\right) G\left(\underline{\mathbf{x}} - \underline{\mathbf{r}}, t - t'\right) \mathrm{d}t' \mathrm{d}\underline{\mathbf{r}}, \tag{3.74}$$

where the overbar indicates the expected value of ψ (the resolved part), calculated by means of a convolution, and the prime indicates a fluctuation (modelled quantity). This is what is known as *Reynolds filtering*. G is the convolution kernel associated with the filtering method used and t' is a dummy variable. Note also that $\overline{\psi'} = 0$.

A special method of density-weighted filtering is utilised for compressible flow called *Favre filtering* (see [Fav83]):

$$\psi = \widetilde{\psi} + \psi'', \tag{3.75}$$

with

$$\widetilde{\psi} = \frac{\overline{\rho\psi}}{\overline{\rho}}. \tag{3.76}$$

ψ'' is again a fluctuation but denoted with two primes to emphasise the different filtering method. Note also that $\widetilde{\rho\psi''} = 0$ but $\widetilde{\psi''} \neq 0$. This prevents having to model additional terms. Consider for example Reynolds filtering of ρu_i:

$$\overline{\rho u_i} = \overline{\overline{\rho}\left(\overline{u}_i + u_i'\right)} = \overline{\overline{\rho}\,\overline{u}_i} + \overline{\overline{\rho} u_i'} = \overline{\rho}\,\overline{u}_i + \overline{\overline{\rho} u_i'}, \tag{3.77}$$

whereas Favre filtering results in

$$\overline{\rho u_i} = \overline{\overline{\rho}\left(\tilde{u}_i + u_i''\right)} = \overline{\overline{\rho}\,\tilde{u}_i} + \overline{\overline{\rho} u_i''} = \overline{\rho}\tilde{u}_i. \tag{3.78}$$

Note that density fluctuations ρ' and ρ'' as well as pressure variations p' and p'' are generally neglected. Thus, $\widetilde{\rho} = \overline{\rho}$ and $\widetilde{p} = \overline{p}$.

In order to properly define scale separation, a cutoff length k_c needs to be determined which serves as a boundary between large and small scales. Figure 3.7 shows this decomposition. Another way of viewing scale separation would be that the information lost during the filtering process is subsequently modelled to compensate. In theory, the filtered quantity $\overline{\psi}$ is obtained by means of a convolution as seen above. In practise, however, this is not very helpful since ψ is unknown to begin with. Hence, the filter is taken to be the individual cells of the computational grid. Scales large enough to be calculated directly on the grid are taken as resolved scales, while scales too small to be captured by the grid are modelled. Thus, the cutoff length (or *filter width*) is easily defined as the characteristic length of a grid cell $k_c = \overline{\Delta}$. Calculated and modelled values of ψ are then summed to obtain a more accurate estimate than the calculated value alone.

The following subsections give an overview over the application of a filter to the Navier-Stokes equations and introduce a method for modelling subgrid scales. Furthermore, treatment of flow near a boundary layer (such as a rigid wall) is briefly discussed.

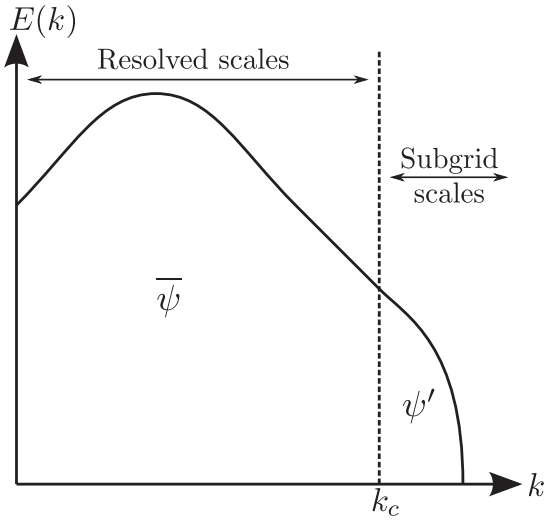

Figure 3.7: Symbolic representation of the energy spectrum decomposition in Large Eddy Simulation where k is the wave number and $E(k)$ is the associated energy

3.6.1 Filtered Navier-Stokes equations

Applying the Favre filter to the compressible momentum equation eqn (2.45) serves as a basis for deriving a suitable momentum equation for LES:

$$\frac{\partial \overline{\rho u_i}}{\partial t} + \frac{\partial \overline{\rho u_j u_i}}{\partial x_j} = -\frac{\partial \overline{p}}{\partial x_i} + \frac{\partial}{\partial x_j}\left(2\mu \widetilde{S}^*_{ij}\right), \tag{3.79}$$

where the dissipative terms have been combined into

$$\widetilde{S}^*_{ij} = \frac{1}{2}\left(\frac{\partial \tilde{u}_i}{\partial x_j} + \frac{\partial \tilde{u}_j}{\partial x_i}\right) - \frac{1}{3}\frac{\partial \tilde{u}_k}{\partial x_k}\delta_{ij}. \tag{3.80}$$

Note that the first term on the LHS of eqn (3.79) is, by eqn (3.78), simply decomposed into

$$\overline{\rho u_i} = \overline{\rho}\,\tilde{u}_i. \tag{3.81}$$

The second term, however, requires more careful consideration as it has two velocity components:

$$\begin{aligned}
\overline{\rho u_j u_i} = \overline{\rho}\widetilde{u_j u_i} = \quad &= \quad \overline{\rho}(\tilde{u}_i + \widetilde{u''_i})\left(\tilde{u}_j + u''_j\right) \\
&= \quad \overline{\rho}\big(\tilde{u}_i\tilde{u}_j + \tilde{u}_i\widetilde{u''_j} + \widetilde{\tilde{u}_j u''_i} + u''_i u''_j\big) \\
&= \quad \overline{\rho}\left(\widetilde{\tilde{u}_i\tilde{u}_j} + \widetilde{\tilde{u}_i u''_j} + \widetilde{\tilde{u}_j u''_i} + \widetilde{u''_i u''_j}\right).
\end{aligned} \tag{3.82}$$

All the terms that require modeling because they cannot be resolved on the grid are represented by the *subgrid tensor* τ_{ij}:

$$\tau_{ij} = \widetilde{u_j u_i} - \widetilde{\tilde{u}_i\tilde{u}_j} = C_{ij} + R_{ij}, \tag{3.83}$$

where the *Clark tensor* $C_{ij} = \widetilde{\tilde{u}_i u_j''} + \widetilde{\tilde{u}_j u_i''}$ represents interactions between resolved and subgrid scales, and the *Reynolds tensor* $R_{ij} = \widetilde{u_i'' u_j''}$ represents interactions purely among resolved scales. Additionally, $\widetilde{\tilde{u}_i \tilde{u}_j}$ may be further decomposed into

$$\begin{aligned} \widetilde{\tilde{u}_i \tilde{u}_j} &= \left(\widetilde{\tilde{u}_i \tilde{u}_j} - \tilde{u}_i \tilde{u}_j \right) + \tilde{u}_i \tilde{u}_j \\ &= L_{ij} + \tilde{u}_i \tilde{u}_j, \end{aligned} \tag{3.84}$$

where the *Leonard tensor* $L_{ij} = \widetilde{\tilde{u}_i \tilde{u}_j} - \tilde{u}_i \tilde{u}_j$ represents interactions among resolved scales. Using this notation the subgrid tensor becomes

$$\tau_{ij} = \widetilde{u_j u_i} - \tilde{u}_i \tilde{u}_j = C_{ij} + R_{ij} + L_{ij}. \tag{3.85}$$

This procedure is commonly referred to as *Leonard decomposition* and results in the following filtered momentum equations for compressible flow:

$$\frac{\partial \overline{\rho} \tilde{u}_i}{\partial t} + \frac{\partial \overline{\rho} \tilde{u}_j \tilde{u}_i}{\partial x_j} = -\frac{\partial \overline{p}}{\partial x_i} + \frac{\partial}{\partial x_j} \left(2\mu \widetilde{S}_{ij}^* \right) - \frac{\partial \overline{\rho} \tau_{ij}}{\partial x_j}. \tag{3.86}$$

Using eqn (3.78) the associated continuity equation simply becomes

$$\frac{\partial \overline{\rho}}{\partial t} + \frac{\partial \overline{\rho} \tilde{u}_i}{\partial x_i} = 0. \tag{3.87}$$

The filtered Navier-Stokes equations for incompressible flow are easily derived from the above by assuming constant density and using the resulting fact that $\widetilde{\psi} = \overline{\psi}$:

$$\frac{\partial \overline{u}_i}{\partial t} + \frac{\partial}{\partial x_j} \left(\overline{u}_i \overline{u}_j \right) = -\frac{1}{\rho} \frac{\partial \overline{p}}{\partial x_i} + \nu \frac{\partial^2 \overline{u}_i}{\partial x_j \partial x_j} - \frac{\partial \tau_{ij}}{\partial x_j} \tag{3.88}$$

and

$$\frac{\partial \overline{u}_i}{\partial x_i} = 0. \tag{3.89}$$

3.6.2 Smagorinsky model

It now remains to model the subgrid tensor τ_{ij}. Several models exist that can perform this task. Only one will be discussed here and that is the Smagorinsky Model based on [Fur96]. It uses information obtained by computing the large scales in order to model the small scales. See [Sag98] for more detail on other methods for modelling turbulence.

The Smagorinsky model conveniently assumes that τ_{ij} is a function of $\widetilde{S}_{ij}^*$. Specifically that

$$-\overline{\rho} \tau_{ij} = 2\mu_{\text{sgs}} \widetilde{S}_{ij}^*, \tag{3.90}$$

resulting in the following modification to eqn (3.86)

$$\frac{\partial \overline{\rho} \tilde{u}_i}{\partial t} + \frac{\partial \overline{\rho} \tilde{u}_j \tilde{u}_i}{\partial x_j} = -\frac{\partial \overline{p}}{\partial x_i} + \frac{\partial}{\partial x_j} \left(2 \left(\mu + \mu_{\text{sgs}} \right) \widetilde{S}_{ij}^* \right). \tag{3.91}$$

The subgrid scale viscosity μ_{sgs} is calculated according to

$$\mu_{\text{sgs}} = C_k \rho \Delta \sqrt{k_{\text{sgs}}}, \tag{3.92}$$

where C_k is a constant, $\Delta = |\underline{\boldsymbol{\Delta}}_1 \cdot (\underline{\boldsymbol{\Delta}}_2 \times \underline{\boldsymbol{\Delta}}_3)|^{\frac{1}{3}}$ is the cube root of the grid cell's volume (the preferred method for calculating the characteristic length of the grid cell in this project), and k_{sgs} represents the subgrid scale kinetic energy. k_{sgs} is in turn modelled by solving the following quadratic equation

$$-\frac{C_e}{\Delta}x^2 + \frac{2}{3}\widetilde{S}_{ii}x + 2C_k\Delta\widetilde{S}_{ij}\widetilde{S}^*_{ij} = 0, \tag{3.93}$$

in which C_e is a constant and

$$x = \frac{-b + \sqrt{b^2 - 4ac}}{2a} \tag{3.94}$$

$$a = -\frac{C_e}{\Delta} \tag{3.95}$$

$$b = \frac{2}{3}\widetilde{S}_{ii} \tag{3.96}$$

$$c = 2C_k\Delta\widetilde{S}_{ij}\widetilde{S}^*_{ij} \tag{3.97}$$

$$k_{\text{sgs}} = x^2. \tag{3.98}$$

Note that for incompressible flow, i.e. $\widetilde{S}_{ii} = \overline{S}_{ii} = 0$, $b = 0$ and $\widetilde{S}^*_{ij} = \overline{S}_{ij}$ and eqn (3.93) reduces to

$$k_{\text{sgs}} = 2\frac{C_k}{C_e}\Delta^2 \left|\overline{S}_{ij}\right|^2. \tag{3.99}$$

Plugging k_{sgs} into eqn (3.92) yields

$$\mu_{\text{sgs}} = \rho(C_S\Delta)^2 \left|\overline{S}_{ij}\right|, \tag{3.100}$$

where $C_S^2 = \sqrt{2}C_k^{1.5}C_e^{-0.5}$ is the Smagorinsky constant.

Finally, the transport equation for enthalpy [Ope13b] is given by

$$\frac{\partial\overline{\rho}\widetilde{h}}{\partial t} + \frac{\partial\overline{\rho}\widetilde{u}_j\widetilde{h}}{\partial x_j} - \frac{\partial}{\partial x_j}\left((\alpha + \alpha_{\text{sgs}})\frac{\partial\widetilde{h}}{\partial x_j}\right) = \frac{\partial\overline{p}}{\partial t} + \tilde{u}_j\frac{\partial\overline{p}}{\partial x_j}, \tag{3.101}$$

where

$$\alpha = \frac{k}{c_p} \tag{3.102}$$

$$\alpha_{\text{sgs}} = \frac{\mu_{\text{sgs}}}{Pr_{\text{sgs}}}. \tag{3.103}$$

Note that k here is the thermal conductivity and Pr_{sgs} the *subgrid scale Prandtl number*.

3.6.3 Dynamic Smagorinsky model for incompressible flow

The Smagorinsky model delivers good results with constant C_S. The model can be improved, however, by adjusting the constant according to flow properties as presented in [LMC05]. This mainly improves upon the model's behaviour near walls, especially if no wall law (Section 3.6.4) is used.

A second filter - the *test-filter* - is applied on top the Reynolds filter with a larger filter width, say $\alpha\Delta$ with $\alpha > 1$. This second filtering operation is denoted by $\widehat{\psi}$ and the product of both filters (double filter) by $\widehat{\overline{\psi}}$. The subgrid scale tensor for the double filtered Navier-Stokes equations is

$$\tau_{ij} = \widehat{\overline{u_i u_j}} - \widehat{\overline{u}}_i \widehat{\overline{u}}_j. \tag{3.104}$$

Considering $\overline{u}_i$ as the instantaneous field, the Leonard tensor may be expressed as

$$L_{ij} = \widehat{\overline{u}_i \overline{u}_j} - \widehat{\overline{u}}_i \widehat{\overline{u}}_j. \tag{3.105}$$

Applying the test filter to the incompressible version of eqn (3.83) yields

$$\widehat{\tau}_{ij} = \widehat{\overline{u_i u_j}} - \widehat{\overline{u}_i \overline{u}_j}. \tag{3.106}$$

Adding the previous two equations and then using eqn (3.104) results in Germano's identity:

$$L_{ij} = \tau_{ij} - \widehat{\tau}_{ij}. \tag{3.107}$$

The Leonard tensor can be directly calculated by applying the test filter to $\overline{u}_i$ whereas τ_{ij} and $\widehat{\tau}_{ij}$ must be modelled. Using the Smagorinsky model and applying the test filter yields

$$\widehat{\tau}_{ij} - \frac{1}{3}\widehat{\tau}_{ii}\delta_{ij} = 2\widehat{A_{ij}C}, \tag{3.108}$$

where $C = 2C_S^2$ and

$$A_{ij} = -\Delta^2 \left|\overline{S}_{ij}\right| \overline{S}_{ij}. \tag{3.109}$$

The stress from the filter product τ_{ij} is also determined using the Smagorinsky model:

$$\tau_{ij} - \frac{1}{3}\tau_{ii}\delta_{ij} = 2B_{ij}C, \tag{3.110}$$

where

$$B_{ij} = -(\alpha\Delta)^2 \left|\widehat{\overline{S}}_{ij}\right| \widehat{\overline{S}}_{ij}. \tag{3.111}$$

Subtracting eqn (3.108) from eqn (3.110) and using Germano's identity leads to

$$L_{ij} - \frac{1}{3}L_{ii}\delta_{ij} = 2B_{ij}C - 2\widehat{A_{ij}C}, \tag{3.112}$$

which relates C to the resolved stresses. Next C is removed from the filter, giving

$$L_{ij} - \frac{1}{3}L_{ii}\delta_{ij} = 2CM_{ij}, \tag{3.113}$$

with $M_{ij} = B_{ij} - \widehat{A}_{ij}$. This is now an overdetermined problem with five equations for one unknown. Germano proposes in [Ger92] to multiply eqn (3.113) by $\overline{S}_{ij}$, giving

$$C = \frac{1}{2}\frac{L_{ij}\overline{S}_{ij}}{M_{ij}\overline{S}_{ij}}. \tag{3.114}$$

Note that $S_{ii} = 0$ due to incompressibility. Using eqn (3.114), the problem may arise that the denominator tends to zero which can cause instabilities. Lilly proposes a different approach in [Lil92] using the least squares method:

$$C = \frac{1}{2}\frac{L_{ij}M_{ij}}{M_{ij}M_{ij}}. \tag{3.115}$$

While removing the instability arising from a vanishing denominator, eqn (3.115) allows for negative values of C. This can be an advantage in that it allows for local backscattering, however, very large negative values can cause numerical instability by introducing an unrealistic growth in the resolved scales' energy. To combat this, C can be averaged over space, time, or both. Although this may counter the intent of a dynamic model, it provides a stable method with which the constant C remains somewhat related to the properties of the flow. Another solution is to cap the local effective viscosity in case of large negative values for C, e.g. $\nu_{\text{eff}} = max(0, \nu + \nu_{\text{sgs}})$. This method is more dynamic as it allows for some local backscatter within the magnitude of ν while at the same time tending to zero near walls where the velocity gradient vanishes. The latter method combined with Lilly's approach for determining C is used for incompressible LES in this project.

3.6.4 Law of the Wall

The *Law of the Wall* (cp. [Spu06]) states that the mean velocity at a given point in a turbulent flow is proportional to the logarithm of the distance between the point in question and the nearest wall or boundary layer:

$$u^+ = \frac{1}{\kappa} ln(y^+) + B, \tag{3.116}$$

where $u^+ = u/u_\tau$ is a dimensionless velocity, $u_\tau = \sqrt{\tau_w/\rho}$ is the *shear velocity* and τ_w is the wall *shear stress*. Furthermore, $y^+ = yu_\tau/\nu$ is a dimensionless distance from the wall where y is the actual wall distance, made dimensionless by u_τ and the kinematic viscosity ν. B is a constant of integration and κ is the *Von Kármán constant*, typically equal to 0.41. The law does not hold in close proximity to the wall. In the region $y^+ < 5$, known as the *viscous sublayer*, the velocity displays linear behaviour: $u^+ = y^+$. The law of the wall does not set in until $y^+ > 30$. The region $5 < y^+ < 30$ is referred to as the *transition layer* or *buffer layer*. Here the law relies on an approximation that smoothly combines both layers with each other (see Figure 3.8).

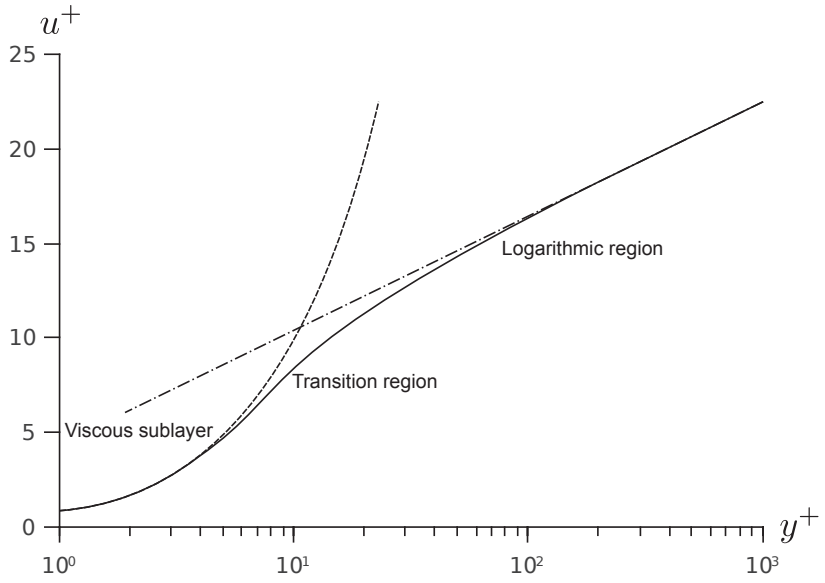

Figure 3.8: Law of the wall: layer transitions

With dimensions, the law of the wall may be written as

$$u = u_\tau \frac{1}{\kappa} ln \left(\frac{y}{y_0} \right). \tag{3.117}$$

Note that the constant of integration is now inside the logarithm and denotes the distance from the wall y_0 at which the mean velocity given by the law of the wall is zero. This distance is non-zero since the law of the wall ceases to hold before the wall is reached. Let k_l denote the characteristic length of roughness on the wall and δ be the thickness of the viscous sublayer. The flow is said to be *smooth* for $k_l < \delta$, for $k_l > \delta$ the flow is termed as *rough*, and for $k_l \approx \delta$ the flow is considered *transitional*. It seems intuitive that rough elements which only reside inside the viscous sublayer have a completely different effect on the flow than do rough elements which reach past the viscous sublayer. In terms of the boundary Reynolds number $Re_w = k_l u_\tau / \nu$, the flow is said to be smooth if $Re_w \leq 3$ and rough if $Re_w \geq 100$. For smooth flow $y_0 = \nu / 9u_\tau$ and for rough flow $y_0 = k/30$. For transitional flow, y_0 needs to be evaluated empirically or calculated analytically (see [LR02] for an example).

Wall roughness is of particular interest for future considerations of this project since the *GrindBall* is an abrasive tool with a rough surface. Different surface coatings may have varying effects on the flow, and a correlation between momentum transfer and roughness of the surface could be observed. For now, however, only smooth surface coating will be considered. Should experimental measurements display a non-negligible influence this will be taken into account at a later stage.

3.7 Summary

A large variety of numerical methods have been introduced in this chapter and comments made about stability and accuracy for each one. The simulations described in the following chapters are performed on highly complex geometries. Nonetheless, they require a high level of accuracy (i.e. higher order) and, furthermore, parametric studies require that a large number of simulations be conducted. Hence, numerical methods must be chosen to provide high accuracy at a low computational cost while remaining stable at all times.

The Finite Volume Method (FVM) introduced in Section 3.1.2 is used throughout, as it is the only method suited to the analyses within this project. Spacial interpolation is performed with second order methods to guarantee accuracy either using CDS (Section 3.2.3 or LUDS (Section 3.2.2) depending on which proves more stable. UDS (Section 3.2.1) is employed only in simulations in which accuracy is of lesser importance, e.g. precursor simulations or initial parametric studies, thus saving time.

Since all simulated cases are unsteady in nature, temporal interpolation must also be used. This is done either with the Implicit Euler Method (Section 3.4.2) or the Crank-Nicolson Method (Section 3.4.3). While the latter provides greater accuracy, it does not always produce sufficient stability and so the former must be used instead on some cases.

All simulations use the PIMPLE algorithm (Section 3.5.3) to solve the Navier-Stokes equations. Its ability to yield good stability in combination with relatively high time-step sizes for unsteady problems make it an ideal choice here.

Finally, turbulence must be modelled for cases with high Reynolds numbers. Large Eddy Simulation (Section 3.6) is the preferred method in conjunction with the Smagorinsky model. The "static" Smagorinsky model (Section 3.6.2) is chosen for compressible flow, while incompressible cases employ the dynamic Smagorinsky model (Section 3.6.3). All turbulent cases also require the Law of the Wall (Section 3.6.4) to adequately model the flow's behaviour near walls, thereby ensuring that fluid-solid interaction can be correctly quantified. Laminar cases ($Re < 2000$) require neither the modelling of turbulence, nor the Law of the Wall.

The methods and models employed, as well as further details such as boundary conditions, fluids properties, etc. are listed for each individual set of cases in Appendix D.

Chapter 4

Developing a prototype grinding tool

The previously discussed knowledge is now applied to a specific case - a pneumatically powered abrading sphere referred to as the *GrindBall*. A parametric study is conducted in order to identify the ideal configuration for the diameter of the duct h_d, its offset h_o, as well as the height of the spherical gap h_g as outlined in Section 1.2. The resulting optimal setup is subsequently simulated and analysed to determine demands to be met by the magnetic bearing and the force available to the abrasion process, as well as to derive a mathematical function governing the behaviour of the available grinding force.

4.1 Parametric study

The goal of this parametric study is to make the *GrindBall* as efficient as possible while abiding to certain practical and physical restrictions. The sphere's predetermined diameter of 40 mm is considered fixed and will not be varied here. Furthermore, air is the only considered medium of pneumatic propulsion. An important physical restriction is the fact that the height of the spherical gap should not exceed 3 mm as the resulting heat transfer of the magnetic bearing on to its surroundings would impair prolonged use of the tool. Force transfer on to the sphere should be maximised under these conditions while also maintaining acceptable pressure forces which can be easily countered by the magnetic control element. It should furthermore be noted that the magnetic bearing consists of five individual magnets, four of which can exert force on the sphere horizontally, and one of which can exert force in an upward direction (see Figure 4.1). Hence, the bearing relies on the weight of the sphere itself should the sphere be required to lower its position. The grinding sphere, which weighs 0.25 kg, exerts a force approximately equal to 2.5 N in a downward direction, a force which should not be overcome by any upward force resulting from effects the flow might have. Should this occur, the sphere could not be lowered without adjusting the flow, a condition which would render the tool inoperable. Thus, it is vital that the total vertical force always acts downwards within a reasonable margin. Also, a rotating sphere will not be considered during the parametric study as it is not a necessary factor when comparing individual geometries.

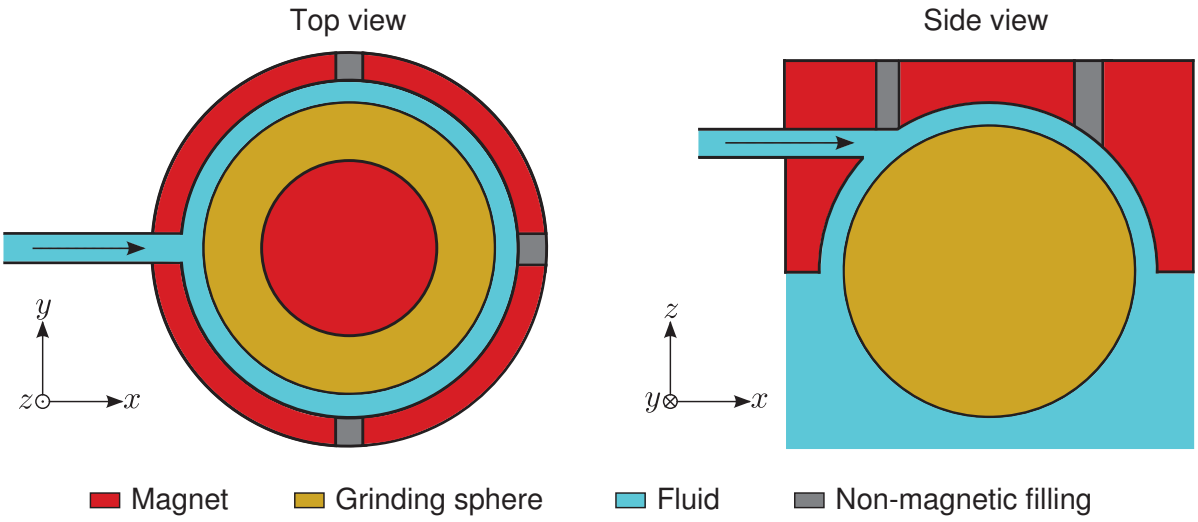

Figure 4.1: Magnetic bearing aligned around the grinding sphere

4.1.1 Variable parameters

Essentially, there are three main variable factors considered here. These are the height of the spherical gap h_g in which the abrading sphere is mounted and where most of the force transfer on to the sphere takes place, the diameter of the duct h_d which is responsible for introducing the pneumatic propulsion medium into the spherical gap, as well as the offset h_o of the duct relative to the top of the spherical gap. See Figure 4.2 for a graphic overview. The length of the duct as well as the diameter of the hose used to lead the medium into the duct are a result of practicality and of physical demands brought forth by the process of manufacture and operation of the tool. Hence, they are not included as parameters in this study.

Gap heights of 2 mm, 3 mm, and 4 mm are examined with duct diameters also ranging from 2-4 mm. Offset is taken as equal to gap height for this first run. Neglecting cases in which duct diameter is less than the height of the gap results in 6 individual cases to be considered (see Table 4.1). The 4 mm gap height case is considered here purely as a means of comparison since the maximum physically possible gap height is 3 mm as stated previously.

Offset of the duct relative to the top of the spherical gap is then examined using the optimum configuration obtained from the first run for the following values: 50%, 75%, 125%, 150%, 175%, and 200%, where the percentage refers to the offset's value relative to gap height.

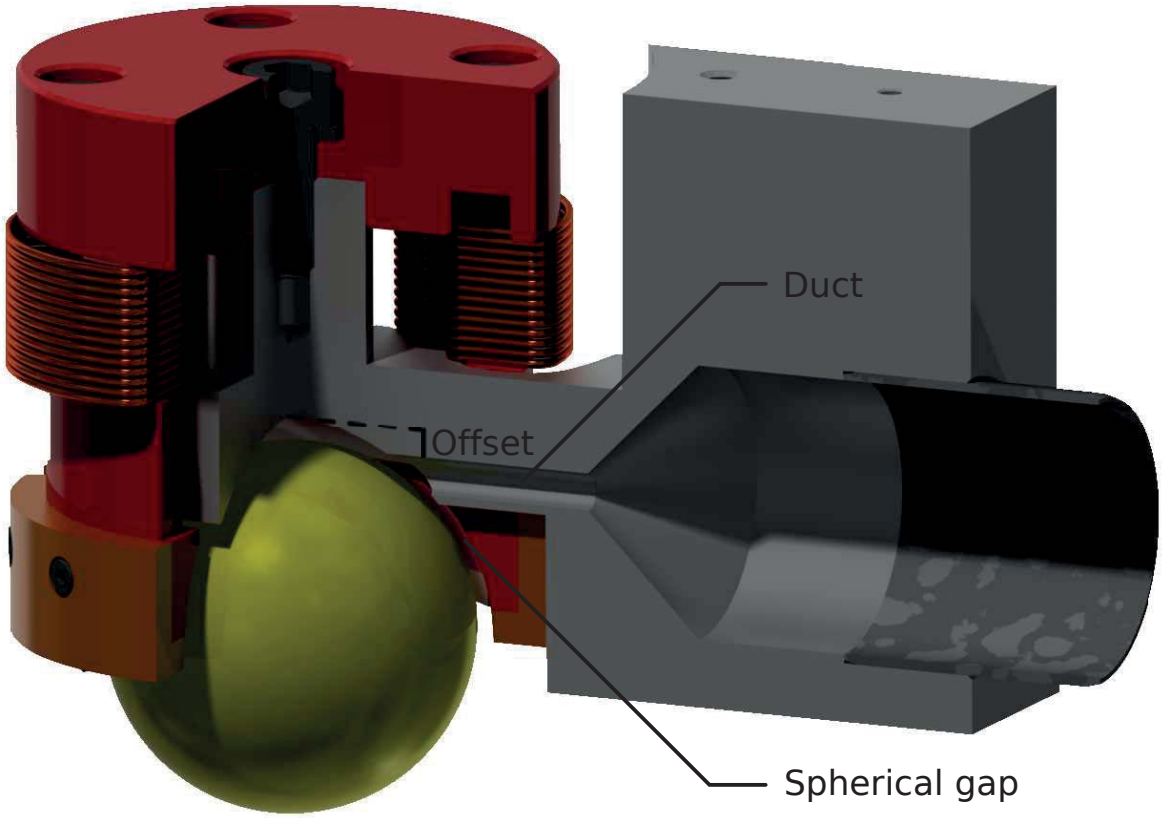

Figure 4.2: Variable parameters for the parametric study

4.1.2 Simulation setup

Simulations are conducted using the open source package for numerical computation `OpenFOAM-2.1.x` (Open Field Operation and Manipulation) [Ope13a].

The solver used is `rhoPimpleFoam` which is a pressure based compressible finite volume solver that utilises the PIMPLE algorithm (Section 3.5.3) and is capable of turbulence modelling. Large Eddy Simulation (discussed in Section 3.6) is the preferred method of incorporating turbulence in conjunction with the compressible Smagorinsky model introduced in Section 3.6.2. Spacial discretisation is performed using the linear interpolation scheme (CDS) presented in Section 3.2.3 and temporal discretisation is done using the

	2 mm duct	3 mm duct	4 mm duct
2 mm gap	√	√	√
3 mm gap		√	√
4 mm gap			√

Table 4.1: Cases considered while examining duct diameter and spherical gap height

implicit Euler method seen in Section 3.4.2. Pressure is linked to density via the perfect gas law (Section 2.8) and the viscosity's temperature dependence is determined according to Sutherland's viscosity model (Section 2.9). Fluid-solid interaction is modelled using the Law of the Wall for smooth walls stated in Section 3.6.4.

Inlet

Boundary conditions for the inlet are set as follows: each simulation has a fixed mass flow rate $\dot{m}$ which determines the amount of air entering the system. The variability of the duct's diameter must be taken into consideration when determining $\dot{m}$ since the flow should not be permitted to become super-sonic and the duct is the narrowest region in the system (resembling a laval nozzle). Hence, the mass flow rate is determined according to

$$\dot{m} = \rho \overline{U} A \tag{4.1}$$

given that

$$\overline{U} = \frac{\dot{m}}{\rho_d A_d} = const = 230\,\mathrm{m\,s^{-1}}, \tag{4.2}$$

where the density of air at the duct's exit is estimated as $\rho_d = 1.1\,\mathrm{kg\,m^{-3}}$ and A_d is the cross-sectional area of the duct. A value as low as $\overline{U} = 230\,\mathrm{m\,s^{-1}}$ for the mean velocity ensures sub-sonic flow even if the estimate for ρ_d is inaccurate. Table 4.2 gives an overview over the mass flow rates used for individual cases. Velocity $\underline{\mathbf{u}}$ at the inlet is calculated based on the mass flow rate. This approach is preferred over setting a fixed uniform value for $\underline{\mathbf{u}}$ across the inlet as it results in a realistic flow profile along the inlet. The boundary condition for pressure p is set to `zeroGradient`. Temperature T is set to 293.15 K, i.e. room temperature. This value was obtained by measurements of air travelling through the disconnected hose at different mass flow rates [Bra]. Values for μ_{sgs} and α_{sgs} are determined using `zeroGradient`.

Outlet

Boundary conditions for the velocity, the temperature, as well as μ_{sgs} and α_{sgs} at the outlet are set to `zeroGradient`. A fixed pressure condition called `totalPressure` is used to govern pressure where the total pressure is defined as $p_{\mathrm{tot}} = \left(1 + \frac{\gamma-1}{2} Ma^2\right)^{(\gamma-1)/\gamma}$ [Bal07]

	2 mm duct	3 mm duct	4 mm duct
2 mm gap	$7.9 \cdot 10^{-4}$	$1.8 \cdot 10^{-3}$	$3.1 \cdot 10^{-3}$
3 mm gap		$1.8 \cdot 10^{-3}$	$3.1 \cdot 10^{-3}$
4 mm gap			$3.1 \cdot 10^{-3}$

Table 4.2: Mass flow rates used for the parametric study [$\mathrm{kg\,s^{-1}}$]

which is set equal to atmospheric pressure of 101,325 Pa. Note that for incompressible flow $p_{\text{tot}} = p + \frac{1}{2}\rho U^2$ [Kü01].

Stationary walls

Boundary conditions for stationary walls are simply `zeroGradient` for pressure and temperature. A value of zero for the velocity ensures a no-slip condition. The special boundary conditions `muSgsUSpaldingWallFunction` and `alphaSgsWallFunction` ensure that the Law of the Wall presented in Section 3.6.4 is used by applying it via the modelled quantities μ_{sgs} and α_{sgs}.

Table 4.3 gives a brief overview of boundary conditions with descriptions as they are used in `OpenFOAM`.

	inlet	outlet	stationary wall
$\underline{\mathbf{u}}$	`timeVaryingFlow-RateInletVelocity`	`zeroGradient`	`fixedValue`
p	`zeroGradient`	`totalPressure`	`zeroGradient`
T	`fixedValue`	`zeroGradient`	`zeroGradient`
μ_{sgs}	`zeroGradient`	`zeroGradient`	`muSgsUSpalding-WallFunction`
α_{sgs}	`zeroGradient`	`zeroGradient`	`alphaSgsWallFunction`

Table 4.3: Boundary conditions used for the parametric study

Mesh

The mesh used consists of approximately 900,000 hexahedral cells and is comprised of 4 main areas. The first one is the inlet basin, which introduces the flow into the system through a 30 mm wide hose and leads up to the duct via a 90° constriction. The diameter of the hose is chosen so that the velocity of the flow is low enough as to be able to neglect the length of the hose and only simulate a small part of it. The constriction angle of 90° is preferred over the alternative 118° as it provides a smoother transition leading into the duct. These two angles stem from drilling heads available to the manufacturing process.

The second area is the duct, which is responsible for transporting the flow into the spherical gap. Its length is variable depending on its own diameter and the offset. The x-coordinate of the transition from constriction to duct, however, is fixed at -36.4 mm, again a requirement of the construction process. Note that coordinates are relative to the origin at the centre of the abrading sphere. See Figures 4.3 and 4.4 for clarification.

The spherical gap is the third area. This is where the flow transfers its force on to the abrading sphere. As this is the most important area in the simulation domain, special attention is given to ensuring that cell shapes are as close as possible to that of a cube. This ensures best possible results since the Smagorisnky model assumes isotropic turbulence. This also means that the amount of cells along the height of the gap must be adapted depending on the absolute height of the gap for each case.

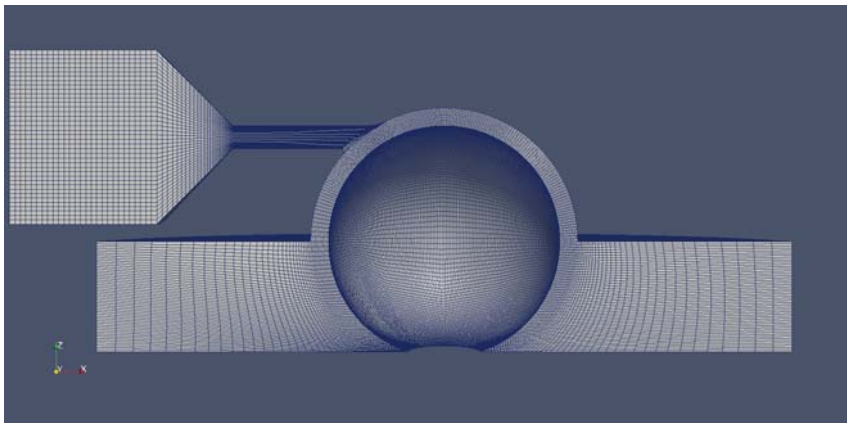

Figure 4.3: Side view of the mesh used for the parametric study (clipped along $y = 0$)

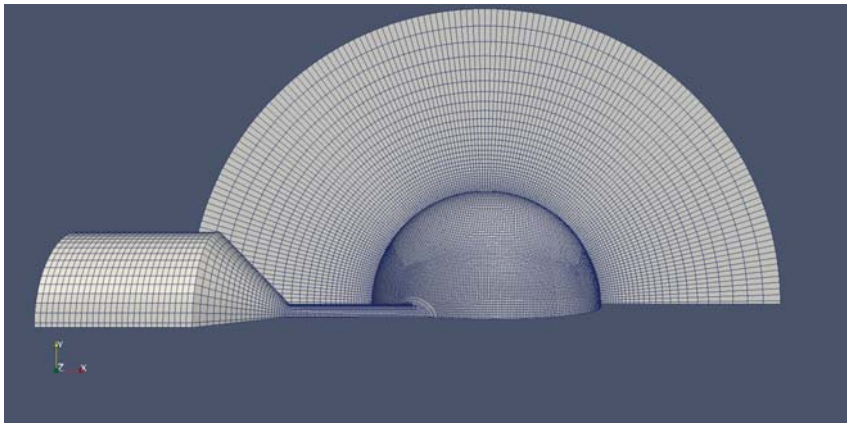

Figure 4.4: Top view of the mesh used for the parametric study (clipped along $y = 0$)

Finally, the outlet basin serves as the area where the flow can expand and slow down before exiting the system. It is vital that this area is sufficiently large as the total pressure boundary condition may not deliver physically accurate results if the outlet boundary is too close to areas in which the flow still has a large momentum or pressure conditions have not begun to converge to an atmospheric value as is imposed on the outlet boundary. The importance of cell shapes as well as cell sizes in this region decreases with distance to the sphere, thus allowing for a low number of cells in the basin and a subsequently low computational cost. Figures 4.3 and 4.4 give an overview over the entire mesh, while Figure 4.5 focuses on the individual domains.

While the amount of cells may seem somewhat low considering the extent of the geometry, the goal of this parametric study is not to deliver final results that can be used for operating the *GrindBall*. Instead, the objective here is to compare the effects of different parameters and determine which configuration delivers best performance by comparison. Once this is done, the resulting optimum is investigated more carefully in Section 4.2.

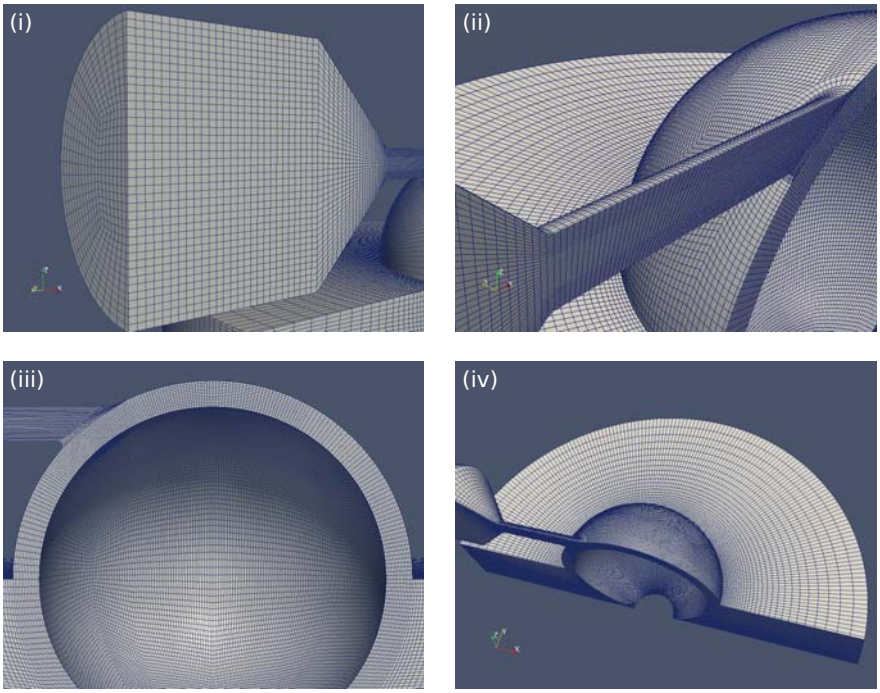

Figure 4.5: The four main mesh domains: (i) inlet basin, (ii) duct, (iii) spherical gap, (iv) outlet basin (clipped along $y = 0$)

Simulation Timeline

To avoid non-physical behaviour, the mass flow rate is initially set to zero and linearly increased over 0.005 s of simulated time using a ramp function. Beyond 0.005 s a constant value is maintained. The simulations are then allowed to continue up to 0.04 s where they are halted. Since the flow needs time to reach its equilibrium, results are not averaged before the simulations reach 0.025 s. Note that since these simulations involve turbulence modelling, the term "equilibrium" does not refer to a steady-state solution, but rather a state in which the flow is fluctuating about an average steady-state. Averages are thus taken over the interval of time between 0.025 s and 0.04 s. See Figure 4.6 for a graphic overview.

Variable time step size must be taken into account when averaging over this interval.

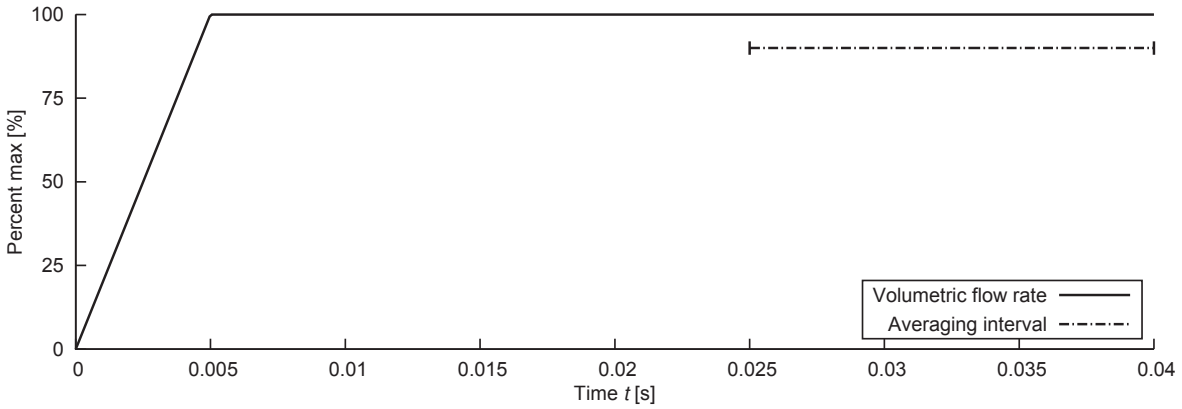

Figure 4.6: Timeline for simulations in the parametric study

Using the midpoint rule, the average for an arbitrary quantity ψ is defined as

$$\overline{\psi} = \frac{1}{\Delta T} \sum_{i=1}^{n-1} \frac{1}{2} \left(\psi_i + \psi_{i+1}\right) \left(t_{i+1} - t_i\right), \tag{4.3}$$

where n is the number of time steps in the interval and $\Delta T = 0.04\,\mathrm{s} - 0.025\,\mathrm{s} = 0.015\,\mathrm{s}$ is the length of the interval.

4.1.3 Forces

The main criterion, not only for this parametric study, but for all simulations in this project are forces and moments acting on the sphere. How these forces are calculated is described in the following.

Pressure p is calculated in each cell adjacent to the sphere and multiplied by the surface normal belonging to the corresponding cell face making up part of the sphere's surface. The sum of the resulting vectors yields the total pressure force acting on the sphere:

$$\underline{\mathbf{F}}_p = \sum_{i=1}^{n} p_i \underline{\mathbf{n}}_i, \tag{4.4}$$

where $\underline{\mathbf{n}}_i$ is the surface normal vector of the individual sphere boundary face i, and n is the total number of cell faces on the sphere. This is the discrete equivalent of integrating pressure over the entire surface.
Pressure moment is calculated by taking the cross product of the vector $\underline{\mathbf{r}}_i$, which points to the cell face centre from the origin at the centre of the sphere, and the pressure force defined previously:

$$\underline{\mathbf{M}}_p = \sum_{i=1}^{n} \underline{\mathbf{r}}_i \times p_i \underline{\mathbf{n}}_i. \tag{4.5}$$

Viscous forces are calculated using the part of stress tensor $\underline{\underline{\widetilde{\mathbf{S}}}}$ defined in eqn (3.80) that acts on the cell face:

$$\underline{\mathbf{F}}_v = \sum_{i=1}^{n} \underline{\mathbf{n}}_i \cdot 2\left[\mu + \mu_{\text{sgs}}\right]_i \underline{\underline{\widetilde{\mathbf{S}}}}_i, \tag{4.6}$$

where the dot product of a vector with a tensor is defined as $\underline{\mathbf{v}} \cdot \underline{\underline{\mathbf{T}}} = v_j T_{ji} \underline{\mathbf{e}}_i$.
Similarly to the pressure moment, the viscous moment is calculated thusly:

$$\underline{\mathbf{M}}_v = \sum_{i=1}^{n} \underline{\mathbf{r}}_i \times \left(\underline{\mathbf{n}}_i \cdot 2\left[\mu + \mu_{\text{sgs}}\right]_i \underline{\underline{\widetilde{\mathbf{S}}}}_i\right). \tag{4.7}$$

Note that since the surface examined here is a sphere centred at the origin, $\underline{\mathbf{r}}_i$ and $\underline{\mathbf{n}}_i$ are parallel for all i, resulting in $\underline{\mathbf{M}}_p = 0$. Furthermore, the total force exerted is obtained by adding pressure force and viscous force resulting in

$$\underline{\mathbf{F}}_{\text{tot}} = \underline{\mathbf{F}}_p + \underline{\mathbf{F}}_v, \tag{4.8}$$

which will henceforth simply be referred to as $\underline{\mathbf{F}}$, with individual vector components F_x, F_y, and F_z. Also,

$$F_n = -F_z \tag{4.9}$$

denotes the *contact force* with which the flow pushes the sphere down on to the workpiece. Additionally, considering the weight of the sphere, total contact force is given by

$$F_{n,\text{tot}} = -F_z + m_s g, \tag{4.10}$$

where m_s is the grinding sphere's mass and g is the negative z-component of the earth's gravitational acceleration $\underline{\mathbf{g}} = (0, 0, -g) = (0, 0, -9.81)\,\text{m}\,\text{s}^{-2}$.

Total moment is obtained by

$$\underline{\mathbf{M}}_{\text{tot}} = \underline{\mathbf{M}}_p + \underline{\mathbf{M}}_v = \underline{\mathbf{M}}_v, \tag{4.11}$$

henceforth referred to as $\underline{\mathbf{M}}$ with individual vector components M_x, M_y, and M_z representing the moments about the respective axes. Force exerted by a moment is obtained by dividing the moment by the length of the moment arm. Since the *GrindBall*'s sphere rotates purely about the y-axis, M_x and M_z can be neglected and the tangential force available to the grinding process is given by

$$F_t \approx \frac{M_y}{r}, \tag{4.12}$$

where $r = 0.02\,\text{m}$ is the sphere's radius in this case. Since the tangential force transferred on to the sphere by the flow is equal to the force available for grinding, F_t may also be referred to as *force transfer* or *available grinding force*. This approximation has an error of $\sim$0.5% for a grinding angle of 10°[1]. $\underline{\mathbf{F}}$ and $\underline{\mathbf{M}}$ are calculated and written to a file in each time step of the simulation and averaged in post-processing according to eqn (4.3).

[1]See Appendix A for further details on how to obtain an exact solution if the grinding angle is known

4.1.4 Evaluation

Part 1

The results from the first part of the parametric study can be seen in Table 4.4 and a graphical representation is given in Figure 4.7.

	2 mm gap 2 mm duct	2 mm gap 3 mm duct	2 mm gap 4 mm duct	3 mm gap 3 mm duct	3 mm gap 4 mm duct	4 mm gap 4 mm duct
F_t	$1.28 \cdot 10^{-2}$	$2.76 \cdot 10^{-2}$	$4.60 \cdot 10^{-2}$	$1.85 \cdot 10^{-2}$	$3.16 \cdot 10^{-2}$	$3.04 \cdot 10^{-2}$
$\sigma(F_t)$	$1.03 \cdot 10^{-3}$	$0.99 \cdot 10^{-3}$	$1.05 \cdot 10^{-3}$	$1.07 \cdot 10^{-3}$	$1.12 \cdot 10^{-3}$	$2.82 \cdot 10^{-3}$
F_x	$6.17 \cdot 10^{-2}$	$1.30 \cdot 10^{-1}$	$1.22 \cdot 10^{-1}$	$7.87 \cdot 10^{-2}$	$8.53 \cdot 10^{-2}$	$7.50 \cdot 10^{-2}$
$\sigma(F_x)$	0.30	0.22	0.20	0.09	0.12	0.13
F_y	$-2.45 \cdot 10^{-3}$	$-5.51 \cdot 10^{-3}$	$3.01 \cdot 10^{-3}$	$2.30 \cdot 10^{-3}$	$-3.34 \cdot 10^{-3}$	$-2.77 \cdot 10^{-3}$
$\sigma(F_y)$	0.44	0.36	0.32	0.09	0.10	0.11
F_z	$1.58 \cdot 10^{-1}$	$3.29 \cdot 10^{-1}$	$5.79 \cdot 10^{-1}$	$2.97 \cdot 10^{-1}$	$5.06 \cdot 10^{-1}$	$4.94 \cdot 10^{-1}$
$\sigma(F_z)$	0.17	0.18	0.34	0.09	0.16	0.15

Table 4.4: Results in *Newton* [N] from the first part of the parametric study: Tangential forces F_t as well as pressure and viscous forces F_x, F_y, and F_z

Clearly the case with a 2 mm gap and a 4 mm duct delivers the best results in terms of tangential force. The 3/4 mm case follows, with 4/4 mm and 2/3 mm closely behind. 3/3 mm and 2/2 mm deliver a rather poor performance by comparison. Forces in x-direction all display a similar average ranging from 0.06 N to 0.13 N. What is more interesting here are the large differences among standard deviations. From here on, only the top three cases are considered, bearing in mind that that the 4/4 mm case is not practically feasible. The 3/4 mm case's $\sigma(F_x)$ is approximately half of that seen in the cases 2/4 mm and 2/3 mm. This means that the former would deliver a much smoother performance as the force exerted does not oscillate as heavily about its mean. Similar observations can be made for F_y and F_z. Forces F_y all display an extremely low average as is to be expected since the geometry is symmetric about $y = 0$ and the flow's main direction is perpendicular to the y-axis. Standard deviations again display varying results. Here the cases 2/3 mm and 2/4 mm both deliver a $\sigma(F_y)$ more than 3 times as large as the 0.1 N seen in the 3/4 mm case. The force F_z is not quite in keeping with F_x and F_y: 2/3 mm delivers the best result with the lowest upward force of $F_z = 0.33$ N and a standard deviation of $\sigma(F_z) = 0.18$ N. 3/4 mm and 2/4 mm both show values around 0.5 N for F_z. The standard deviation, however, of 0.34 N for 2/4 mm is more than double the deviation of 0.16 N seen in the 3/4 mm case.

Despite having the largest tangential force, the 2/4 mm case displays such high standard deviations for force that is not a practical choice. The high upward force F_z combined with a large standard deviation $\sigma(F_z)$ make this configuration particularly problematic.

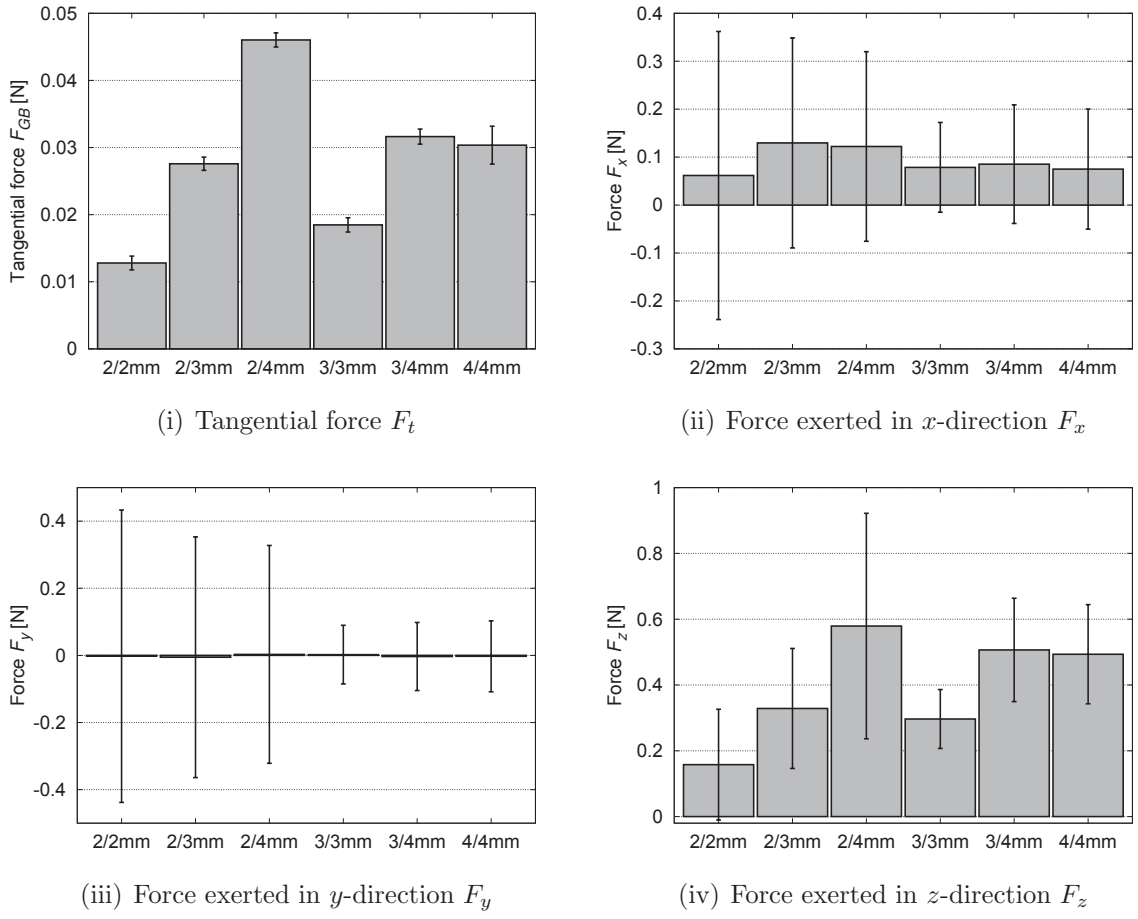

(i) Tangential force F_t

(ii) Force exerted in x-direction F_x

(iii) Force exerted in y-direction F_y

(iv) Force exerted in z-direction F_z

Figure 4.7: Results from the first part of the parametric study: Tangential force F_t and normal forces F_x, F_y, and F_z

Comparing 2/3 mm and 3/4 mm sees 3/4 mm as the far better choice. While 2/3 mm shows a lower F_z with comparable values for $\sigma(F_z)$, the standard deviations of F_x and F_y are simply too high by comparison. Such highly fluctuating forces could cause strong vibrations which would in turn cause the magnetic bearing to emit more heat while trying to compensate. This may impair prolonged use of the tool.

In general, it can be said that forces F_t, F_x, and F_z increase with increasing gap height for cases in which duct diameter is equal to gap height. Furthermore, these forces increase with increasing duct diameter for constant gap height. Standard deviations of F_t show little difference across all cases. Forces F_x, F_y, and F_z, however, display large variations in their standard deviations. The standard deviations seen for all cases using 2 mm gap height are far greater than those seen using a 3 mm or 4 mm gap. Gap heights of 3 mm and 4 mm are similar regarding $\sigma(\underline{\mathbf{F}})$. A smaller gap seems to promote heavier vibration of the sphere while a larger gap enables "smoother" operation. Varying the duct diameter at constant gap height shows similar results for standard deviations in all cases.

Figure 4.8 shows a comparison of velocity profiles for the dimensionless velocity

$$\hat{U} = \overline{U}/\overline{U}_0, \tag{4.13}$$

where $\overline{U}$ is the mean velocity averaged from $t = 0.025\,\mathrm{s}$ to $t = 0.04\,\mathrm{s}$, and $\overline{U}_0 = 230\,\mathrm{m\,s^{-1}}$. There are no distinct differences in velocity distribution among cases, all showing a typical mean velocity profile for turbulent flow inside the duct. Once the flow enters the spherical gap and impacts the sphere, velocity profiles shift toward the sphere, causing high velocity gradients near the sphere's surface and lower gradients near the top of the gap. This effect is observed for all cases, however, it appears to be more prominent in cases where the ratio of duct diameter to gap height is larger. Also, higher duct-to-gap ratios cause the flow to maintain high speeds inside the gap over longer distances, explaining higher tangential force in these cases. Furthermore, it is clear that the amount of mass impacting the sphere increases with duct diameter, which explains higher forces in general for larger ducts, i.e. higher flow rates.

Figure 4.9 compares dimensionless pressure distributions

$$\hat{p} = \overline{p}/p_0, \tag{4.14}$$

where $\overline{p}$ is the average pressure and $p_0 = 101{,}325\,\mathrm{Pa}$. Larger ducts show bigger areas of high pressure at the flow's main point of impact on the sphere, which is a direct consequence of higher flow rates. Varying gap height at constant duct diameter has no apparent influence on this factor. Low pressure areas at the top of the sphere behind the point of impact explain upward force acting on the sphere. These areas become more apparent for high duct-to-gap ratios, which is in keeping with the results for F_z. They do, however, also rise with flow rate, which is made apparent by comparing cases in which duct diameter and gap height are equal. In fact, these low-pressure zones correspond to the flow maintaining high speeds, as discussed above, which appears to be the cause of the pressure drop. Finally, there appear to be small areas of low pressure at the point in which the duct and the gap merge. They become more apparent for both higher flow rates and duct-to-gap ratios, however, they seem to have no noticeable influence on the flow, nor are they close enough to the sphere to exert any lifting force on it.

Figure 4.10 shows a comparison of Mach numbers between cases. Little variation is observed as is to be expected due to the way in which the fixed mass flow rate is defined at the inlet according to eqns (4.1) and (4.2). In general, there is no indication of significant increase in Mach numbers at the end of the duct or anywhere inside the gap. Instead, Mach numbers are homogeneously distributed throughout the vital areas of the geometry. However, they are high enough - in fact up to 0.7 in these cases - to justify the use of a compressible simulation model, which becomes necessary at $Ma > 0.3$ [Gra01, Whi09].

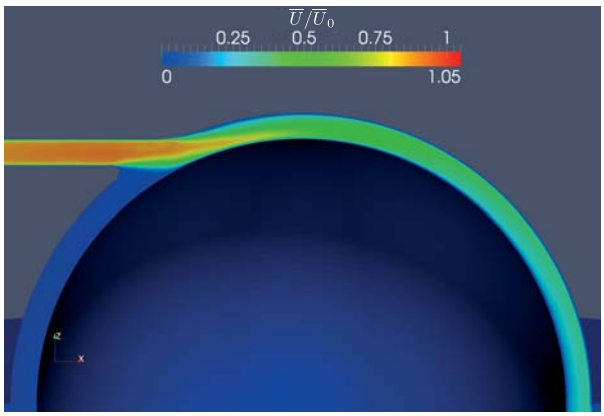

(i) 2 mm gap, 2 mm duct

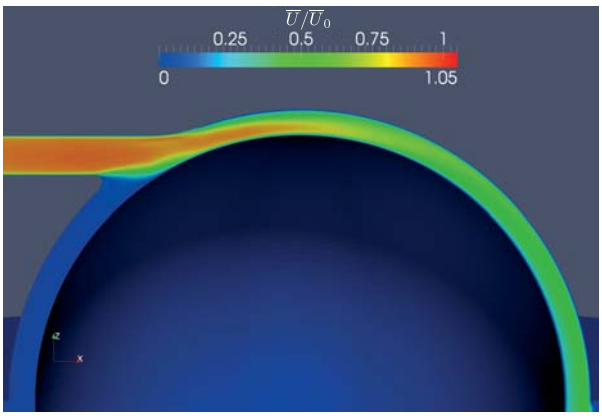

(ii) 2 mm gap, 3 mm duct

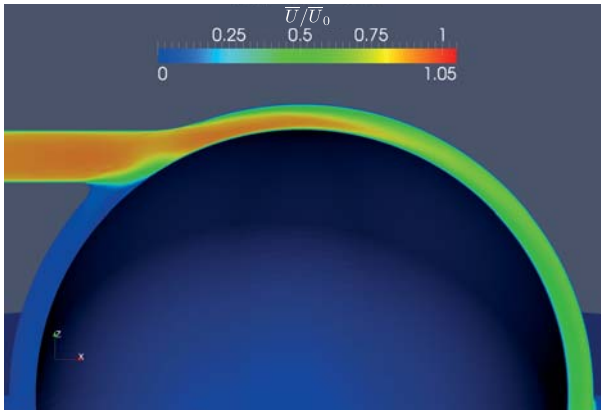

(iii) 2 mm gap, 4 mm duct

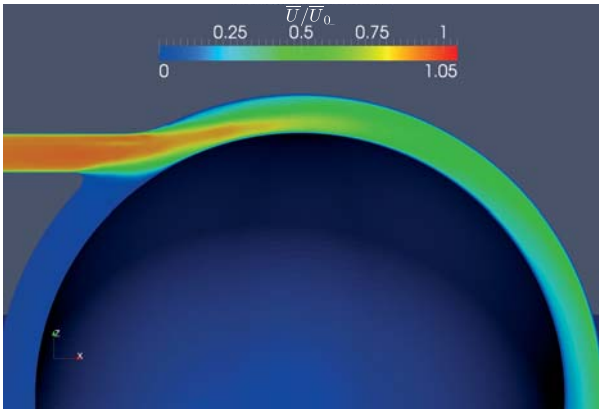

(iv) 3 mm gap, 3 mm duct

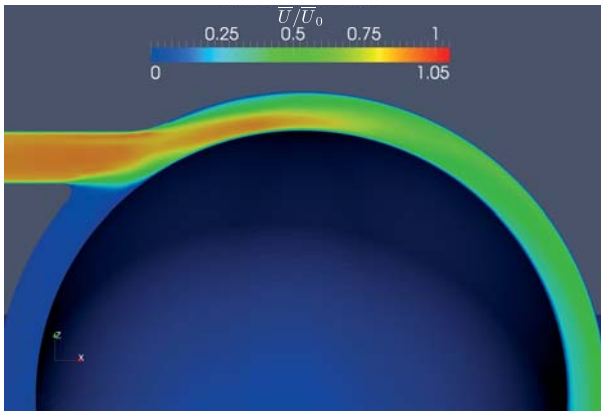

(v) 3 mm gap, 4 mm duct

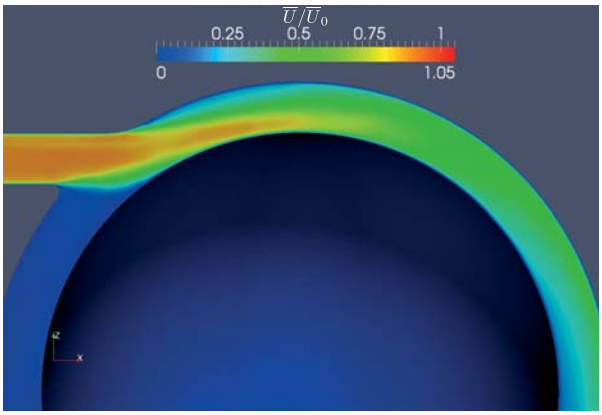

(vi) 4 mm gap, 4 mm duct

Figure 4.8: Dimensionless velocity profiles for individual cases in part one of the parametric study

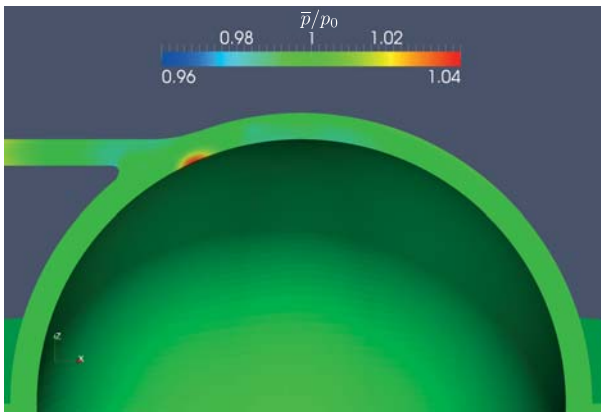

(i) 2 mm gap, 2 mm duct

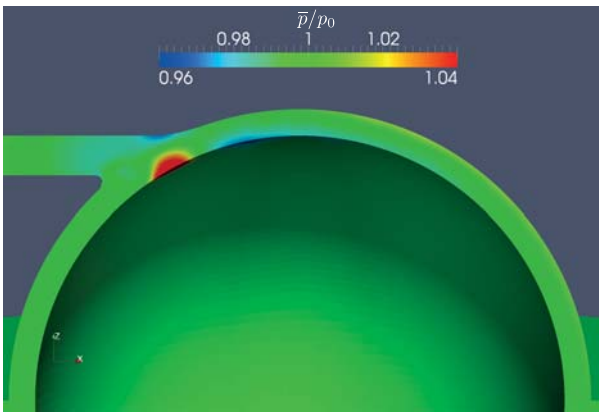

(ii) 2 mm gap, 3 mm duct

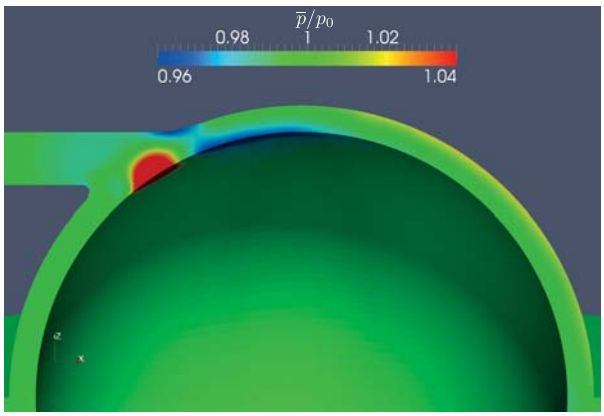

(iii) 2 mm gap, 4 mm duct

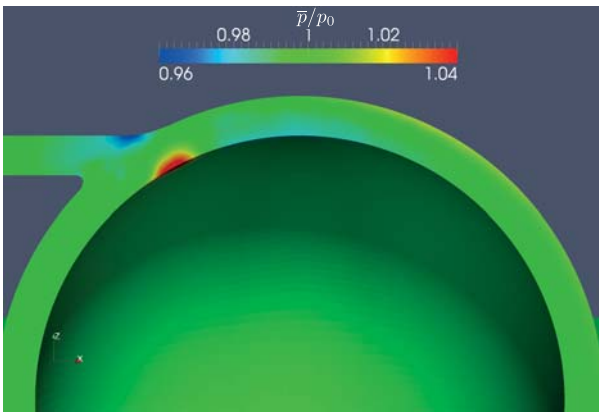

(iv) 3 mm gap, 3 mm duct

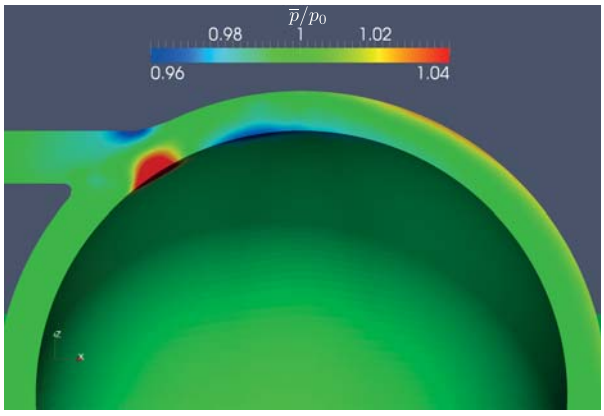

(v) 3 mm gap, 4 mm duct

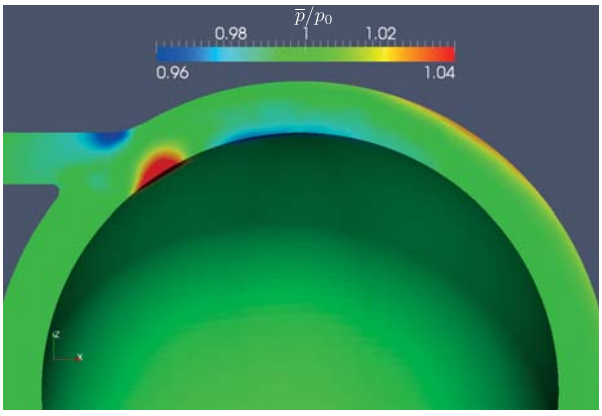

(vi) 4 mm gap, 4 mm duct

Figure 4.9: Dimensionless pressure distribution for individual cases in part one of the parametric study

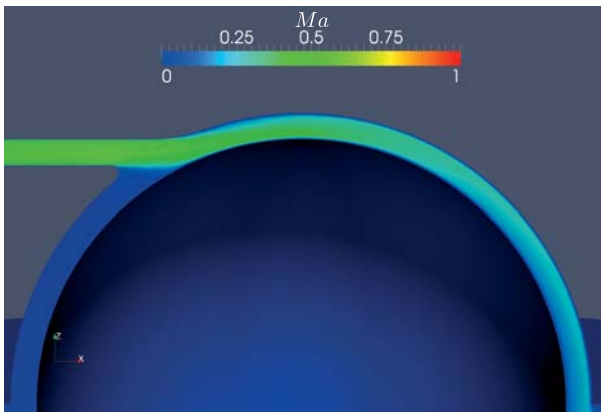

(i) 2 mm gap, 2 mm duct

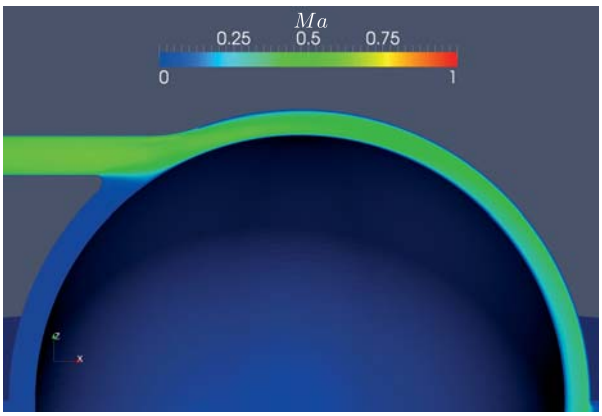

(ii) 2 mm gap, 3 mm duct

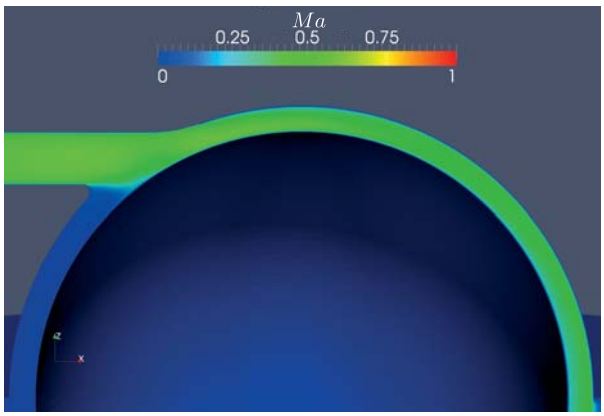

(iii) 2 mm gap, 4 mm duct

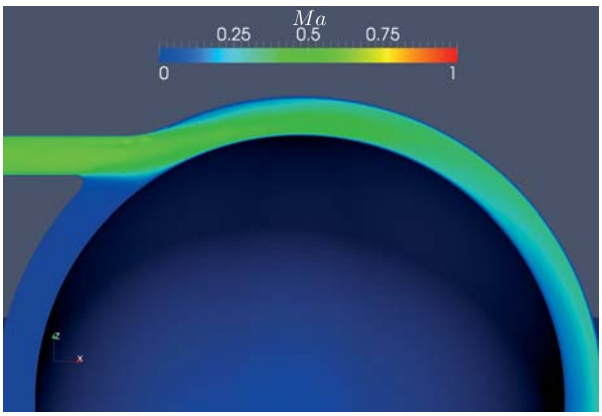

(iv) 3 mm gap, 3 mm duct

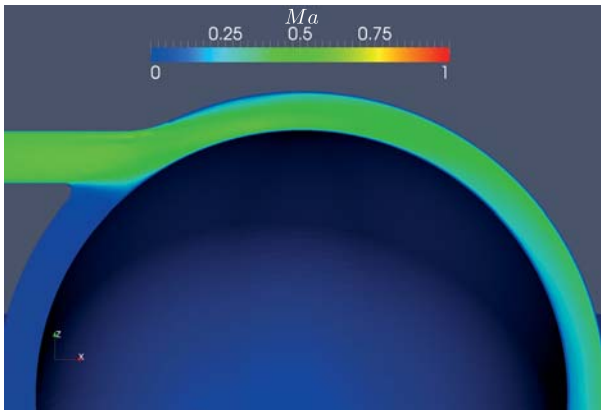

(v) 3 mm gap, 4 mm duct

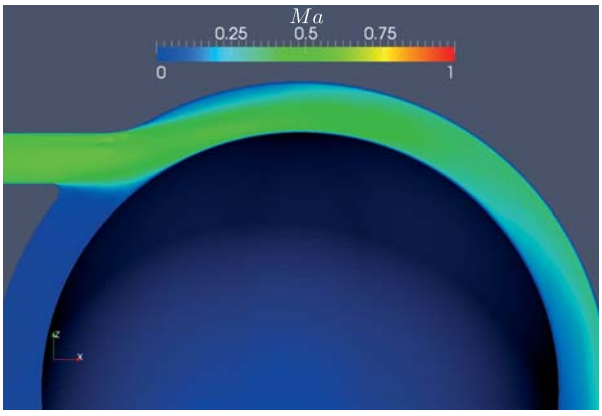

(vi) 4 mm gap, 4 mm duct

Figure 4.10: Mach number distribution for individual cases in part one of the parametric study

Part 2

The optimum case from the first part of the study with a 3 mm gap height h_g and a 4 mm duct diameter h_d is now subjected to a second study with varying offset. The offset h_o is given as a percentage of h_g and is measured as the vertical distance between the top of the gap and the highest point of the duct (see Figure 4.2). Cases investigated are for $h_o \in \{50\%, 75\%, 100\%, 125\%, 150\%, 175\%, 200\%\}$. An offset higher than 200% cannot be considered since the hose would penetrate the outlet basin, making multiple grid cells occupy the same space. Again, the goal here is to maximise F_t while maintaining acceptable values for $\underline{\mathbf{F}}$ and $\sigma(\underline{\mathbf{F}})$. Boundary conditions are identical to those used previously. The mass flow rate $\dot{m} = 0.0031\,\mathrm{m^3h^{-1}}$ is the same used for 4 mm ducts.

Table 4.5 shows results of the study and Figure 4.11 provides a graphic representation. Standard deviations for the individual forces are relatively uniform across all cases compared to the first study. Hence, the absolute values of the forces and how they compare across cases are the focus of this second study. It is easily seen that the tangential force

	50%	75%	100%	125%	150%	175%	200%
F_t	$2.30 \cdot 10^{-2}$	$2.70 \cdot 10^{-2}$	$3.16 \cdot 10^{-2}$	$3.40 \cdot 10^{-2}$	$3.63 \cdot 10^{-2}$	$3.86 \cdot 10^{-2}$	$4.04 \cdot 10^{-2}$
$\sigma(F_t)$	$1.47 \cdot 10^{-6}$	$2.05 \cdot 10^{-6}$	$1.26 \cdot 10^{-6}$	$1.24 \cdot 10^{-6}$	$1.17 \cdot 10^{-6}$	$1.18 \cdot 10^{-6}$	$1.08 \cdot 10^{-6}$
F_x	$1.26 \cdot 10^{-1}$	$1.10 \cdot 10^{-1}$	$8.53 \cdot 10^{-2}$	$5.82 \cdot 10^{-2}$	$2.3 \cdot 10^{-2}$	$-1.22 \cdot 10^{-2}$	$-4.06 \cdot 10^{-2}$
$\sigma(F_x)$	$2.41 \cdot 10^{-2}$	$3.66 \cdot 10^{-2}$	$1.53 \cdot 10^{-2}$	$1.98 \cdot 10^{-2}$	$1.09 \cdot 10^{-2}$	$1.84 \cdot 10^{-2}$	$1.50 \cdot 10^{-2}$
F_y	$1.67 \cdot 10^{-3}$	$-3.60 \cdot 10^{-4}$	$-3.34 \cdot 10^{-3}$	$5.06 \cdot 10^{-3}$	$8.02 \cdot 10^{-4}$	$7.28 \cdot 10^{-3}$	$-5.28 \cdot 10^{-4}$
$\sigma(F_y)$	$7.26 \cdot 10^{-3}$	$1.34 \cdot 10^{-2}$	$1.03 \cdot 10^{-2}$	$1.68 \cdot 10^{-2}$	$7.82 \cdot 10^{-3}$	$3.96 \cdot 10^{-2}$	$2.27 \cdot 10^{-2}$
F_z	$4.32 \cdot 10^{-1}$	$4.72 \cdot 10^{-1}$	$5.06 \cdot 10^{-1}$	$5.39 \cdot 10^{-1}$	$5.57 \cdot 10^{-1}$	$5.78 \cdot 10^{-1}$	$5.86 \cdot 10^{-1}$
$\sigma(F_z)$	$3.02 \cdot 10^{-2}$	$2.36 \cdot 10^{-2}$	$2.47 \cdot 10^{-2}$	$4.14 \cdot 10^{-2}$	$1.28 \cdot 10^{-2}$	$4.46 \cdot 10^{-2}$	$2.96 \cdot 10^{-2}$

Table 4.5: Results in Newton [N] from the second part of the parametric study: Tangential forces F_t as well as pressure and viscous forces F_x, F_y, and F_z

F_t increases with higher offsets. This can be explained by the fact that the angle at flow's point of impact on the sphere between the flow's main direction and the surface of the sphere becomes larger as offset increases. Greater viscous forces are a direct consequence of this. Although a maximum offset of 200% could not be exceeded, it seems intuitive that there must exist an optimum offset beyond which tangential force starts to drop. Should the afore mentioned angle become perpendicular, viscous forces vanish, cancelling each other out as they are distributed uniformly in all directions. This intuition is supported by inspecting tangential forces in Figure 4.11. Regarding F_t as a function of offset h_o, there is a clear decrease in the slope of the function as offset increases. Assuming $F_t \approx 0$ for $h_o = 23\,\mathrm{mm}$, the slope must become negative somewhere between $h_o = 2h_g$ and $h_o = 23\,\mathrm{mm}$. While this is not of particular importance here, this can be further investigated in the future for different geometries that allow for higher offsets. Forces F_x in x-direction clearly display a reduction with increasing offset. Forces are minimal for $h_o = 1.5h_g$ and $h_o = 2h_g$. Forces F_y in y-direction are similar across all cases while

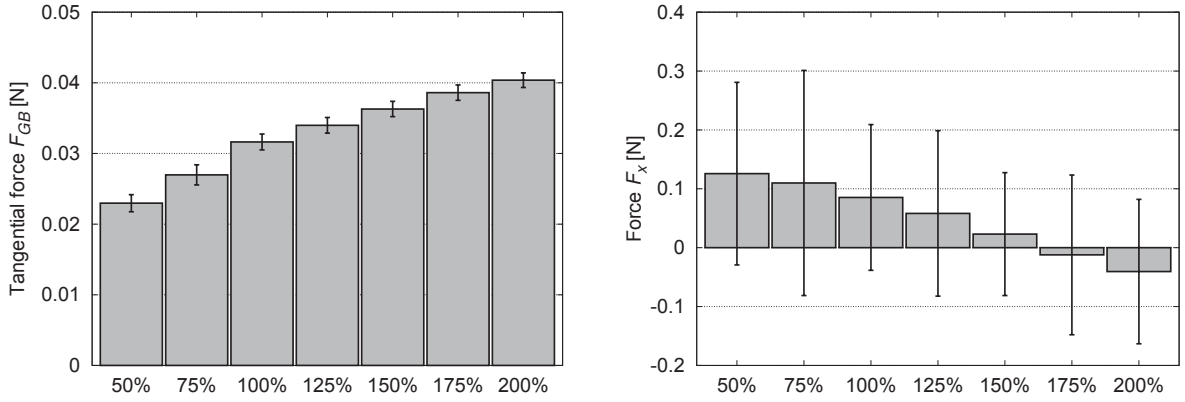

(i) Tangential force F_t

(ii) Force exerted in x-direction F_x

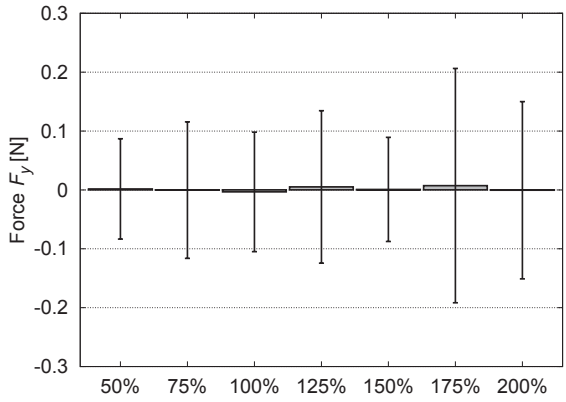

(iii) Force exerted in y-direction F_y

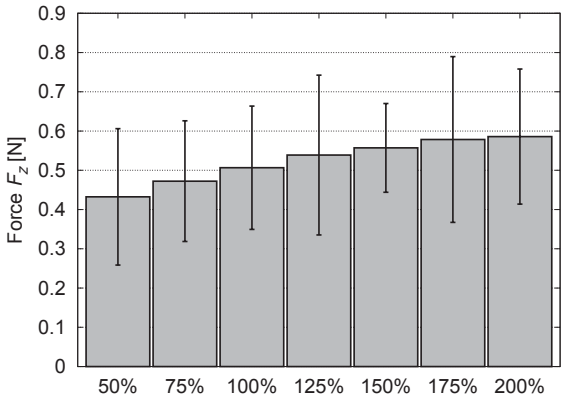

(iv) Force exerted in z-direction F_z

Figure 4.11: Results from the second part of the parametric study: Tangential force F_t and normal forces F_x, F_y, and F_z

F_z shows increasing upward force with increasing offset. Forces F_z, nonetheless, only vary between 0.43 N and 0.58 N. Based on this data, the optimal value for the offset is $h_o = 1.5h_g = 4.5\,\text{mm}$. While only in third place for tangential force, it delivers the lowest standard deviation across all directional forces F_x, F_y, and F_z. Furthermore, the force F_x is comparatively small. Hence, the sphere is subjected to the least amount of vibration with this setup, causing the magnetic bearing to emit less heat.

Unfortunately, a tight manufacturing schedule did not permit for the second study to reach completion on time. Consequently, only results from the first parametric study could be considered which is why the following deals with a setup consisting of $h_g = 3\,\text{mm}$, $h_d = 4\,\text{mm}$, and $h_o = 3\,\text{mm}$.

4.2 Computational results

The optimum configuration determined in Section 4.1 composed of $h_g = 3\,\text{mm}$, $h_d = 4\,\text{mm}$, and $h_o = 3\,\text{mm}$ is now simulated using a variety of rotation frequencies and mass flow rates (see Table 4.6). Flow properties, forces F_x, F_y, and F_z as well as tangential force F_t are investigated. Finally, a relation is established which states the dependency of tangential force F_t on rotation frequency f and on standard volumetric flow rate $\dot{V}_N$. Note that

$$\dot{V}_N = \frac{\dot{m}}{\rho_N}, \tag{4.15}$$

where $\rho_N = 1.293\,\text{kg}\,\text{m}^{-3}$ is the standard density of air at 0°C and atmospheric pressure. This representation is preferred over the mass flow rate $\dot{m}$ as it is a more common quantification and is also the unit employed by the flow meter used in the actual setup.

Flow rates [m^3h^{-1}]	1	2	3	4	5	6	7	8	9	10
Frequencies [Hz]	0	0	0	0	0	0	0	0	0	0
	50	75	25	50	75	50	50	50	50	200
			100	100	150	100	100	100	100	400
						200	250	300	350	

Table 4.6: Case configurations simulated for the *GrindBall* prototype

4.2.1 Simulation Setup

The setup is very similar to that used for the parametric study described in Section 4.1.2. Therefore, this section will only deal with differences in setup between the parametric study and that which is used for simulating the prototype.

Boundary conditions

Special attention must be given to the sphere which is now no longer a stationary wall but rotating at a given speed. The boundary condition for velocity is hence set using `rotatingWallVelocity` which determines the tangential velocity of each cell face based on a given rotation frequency about a given axis of rotation. All other boundary conditions are adopted from those used for stationary walls. See Table 4.7 for an overview of the boundary conditions used here.

	inlet	outlet	rigid wall	rotating wall
$\underline{\mathbf{u}}$	timeVaryingFlow-RateInletVelocity	zeroGradient	fixedValue	rotatingWall-Velocity
p	zeroGradient	totalPressure	zeroGradient	zeroGradient
T	fixedValue	inletOutlet	zeroGradient	zeroGradient
μ_{sgs}	zeroGradient	zeroGradient	muSgsUSpalding-WallFunction	muSgsUSpalding-WallFunction
α_{sgs}	zeroGradient	zeroGradient	alphaSgs-WallFunction	alphaSgs-WallFunction

Table 4.7: Boundary conditions used for the *GrindBall* prototype

Mesh

Two separate meshes are used for simulating the prototype, a coarse mesh consisting of 1.8 million cells, and a fine mesh with 4.5 million cells. The reason for this being that computational effort is reduced by first running the simulation on a coarse mesh until the flow has reached equilibrium. The results are then mapped on to a fine mesh where the computation is continued. The fine mesh is based on the coarse mesh with each cell inside the spherical gap split once along each edge. Hence, each coarse cell transforms into eight fine cells inside the gap. Figure 4.12 gives an overview of the entire mesh as well as side-views of both the coarse and the refined spherical gaps. This method cost-effectively

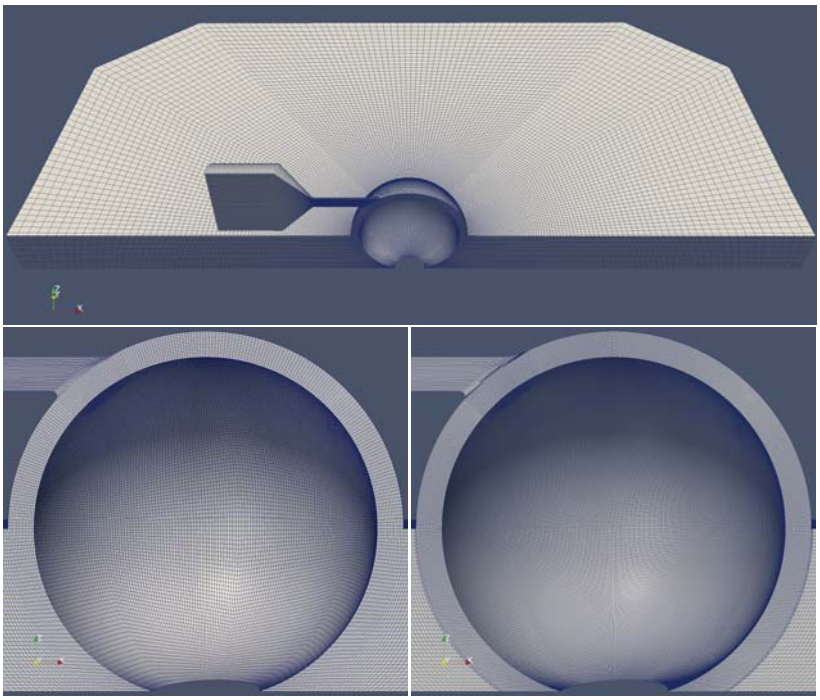

Figure 4.12: Mesh refinement inside the spherical gap (clipped along $y = 0$)

delivers detailed resolution of the flow's behaviour near the surface of the grinding sphere. Thus, forces $\underline{\mathbf{F}}$ and moments $\underline{\mathbf{M}}$ can be determined with high precision. Note also that the outlet basin is larger in size compared to the mesh used in the parametric study as higher mass flow rates lead to higher flow velocities, which implies that more space is required so that the flow may converge to atmospheric pressure before exiting the system.

Simulation timeline

For each case the mass flow rate is initially set to zero and linearly increased over 0.005 s of simulated time beyond which the simulation runs up to 0.03 s. Transition to the fine mesh occurs at this point and the simulation is continued up to 0.05 s where it is then halted. To save additional computational cost, the part of the simulation on the coarse mesh is done using the upwind interpolation scheme (UDS) introduced in Section 3.2.1. This is possible because obtaining accurate results on the coarse mesh is of no interest. The only goal here is for the flow to become fully developed. Results are once again averaged in post processing according to eqn (4.3) with $\Delta T = 0.05\,\mathrm{s} - 0.035\,\mathrm{s} = 0.015\,\mathrm{s}$. Note that the averaging interval is chosen to begin at $t = 0.035\,\mathrm{s}$ at which point any fluctuations caused by the mesh transition have subsided. See Figure 4.13 for a graphic representation of the simulation timeline.

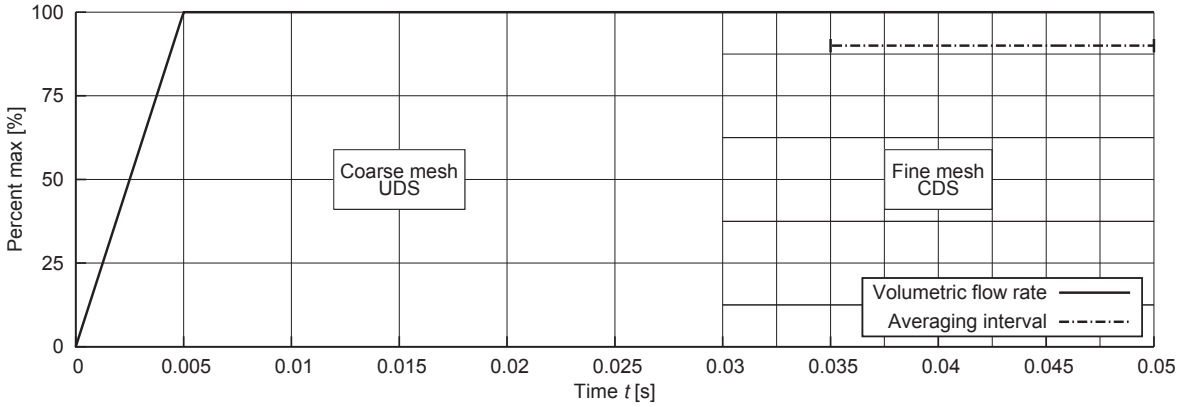

Figure 4.13: Timeline for simulations done for the *GrindBall* prototype

4.2.2 Reynolds and Mach numbers

Table 4.8 shows Reynolds numbers for each flow rate $\dot{V}_N$, where the Reynolds number is defined as

$$Re = \overline{U} h_d / \nu_S \tag{4.16}$$

with

$$\overline{U} = \dot{m} / \rho_S A_d, \tag{4.17}$$

the mean velocity of the flow determined by dividing the mass flow rate $\dot{m}$ by the density of air at room temperature $\rho_S \approx 1.2\,\mathrm{kg\,m^{-3}}$ and the cross-sectional area of the duct $A_d \approx 1.26 \cdot 10^{-5}\,\mathrm{m^2}$. $h_d = 0.004\,\mathrm{m}$ is the height of the duct and $\nu_S = 1.5 \cdot 10^{-5}\,\mathrm{m^2 s^{-1}}$ represents the kinematic viscosity of air at room temperature.

Flow rates [$\mathrm{m^3 h^{-1}}$]	1	2	3	4	5
Re	$6.30 \cdot 10^3$	$1.26 \cdot 10^4$	$1.89 \cdot 10^4$	$2.52 \cdot 10^4$	$3.15 \cdot 10^4$

Flow rates [$\mathrm{m^3 h^{-1}}$]	6	7	8	9	10
Re	$3.78 \cdot 10^4$	$4.41 \cdot 10^4$	$5.03 \cdot 10^4$	$5.66 \cdot 10^4$	$6.29 \cdot 10^4$

Table 4.8: Reynolds numbers Re for each flow rate

Table 4.9 shows maximum Mach numbers for each case. The flow becomes super-sonic for high rotation frequencies at $\dot{V}_N = 10\,\mathrm{m^3 h^{-1}}$. Super-sonic flow can lead to choking at the narrowest point in the system (the duct), i.e. it can lead to high pressure and density fluctuations which would cause heavy vibration and impair the transfer of the flow's momentum on to the sphere. Hence, only volumetric flow rates up to $9\,\mathrm{m^3 h^{-1}}$ are considered beyond this point. High Reynolds numbers in conjunction with a broad spectrum of Mach numbers justify the use of a compressible LES model.

Flow rates [$\mathrm{m^3 h^{-1}}$]	1	2	3	4	5	6	7	8	9	10
0 Hz	0.11	0.21	0.29	0.40	0.48	0.57	0.67	0.77	0.9	0.93
25 Hz			0.30							
50 Hz	0.10			0.41		0.58	0.65	0.78	0.87	
75 Hz		0.21			0.49					
100 Hz			0.30	0.40		0.6	0.69	0.74	0.87	
150 Hz					0.47					
200 Hz						0.65				0.93
250 Hz							0.68			
300 Hz								0.78		
350 Hz									0.87	
400 Hz										1.01

Table 4.9: Maximum Mach numbers Ma for each case

4.2.3 Temperature variation

Figure 4.14 shows the temperature distribution for the case $\dot{V}_N = 9\,\mathrm{m^3 h^{-1}}$ with $f = 100\,\mathrm{Hz}$.

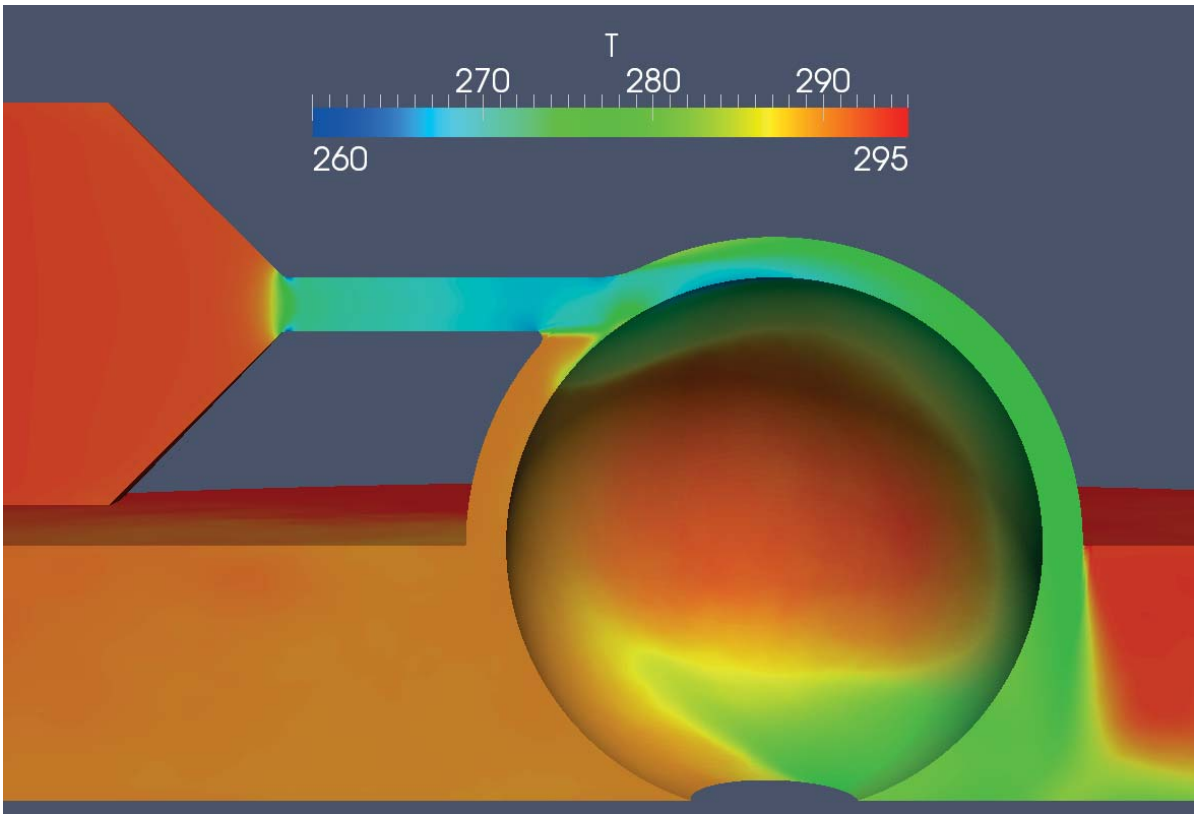

Figure 4.14: Temperature distribution in [K] for the case $\dot{V}_N = 9\,\mathrm{m^3\,h^{-1}}$, $f = 100\,\mathrm{Hz}$

Temperature values lie between 270 K and room temperature. Such low variation justifies the use of adiabatic walls.

4.2.4 Normal forces

Figure 4.15 shows forces F_x^p and F_z^p exerted on the sphere for each case listed in Table 4.6. Error bars are omitted for sake of clear visibility. F_y^p is also omitted as average forces in y-direction tend to zero over time due to symmetry. F_x^p displays somewhat constant behaviour for flow rates up to $\dot{V}_N = 5\,\mathrm{m^3 h^{-1}}$. For higher flow rates, F_x^p fluctuates about a mean and constant behaviour can no longer be observed. F_x^p seems to increase with increasing $\dot{V}_N$. Simulations for several more rotation frequencies per flow rate would be required before a general statement can be made as to how F_x^p behaves. This, however, is unnecessary because the magnetic control bearing responds to displacement of the sphere on the fly. Approximate values of acting forces are sufficient for programming the control element prior to use. F_z^p displays more consistent behaviour. Forces in z-direction seem to be fairly constant across rotation frequency for all flow rates while, just as with F_x^p, steadily increasing with increasing $\dot{V}_N$. Figure 4.16 shows forces averaged over rotation frequency for each constant $\dot{V}_N$. Magnitudes of $\overline{F}_x^p$ as well as their standard deviations increase with increasing $\dot{V}_N$. A similar observation can be made for $\overline{F}_z^p$ regarding both

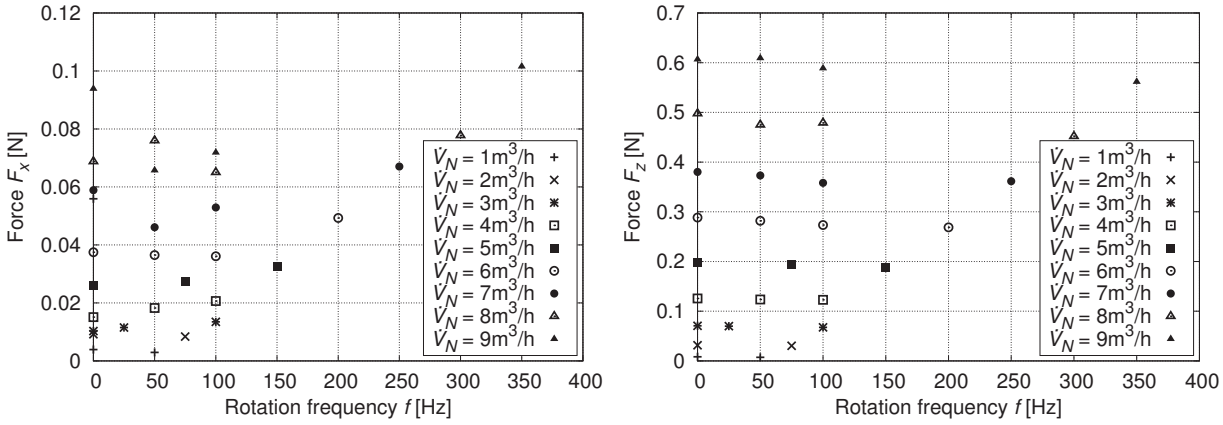

(i) Force exerted in x-direction F_x^p (ii) Force exerted in z-direction F_z^p

Figure 4.15: Forces F_x^p and F_z^p for all simulations conducted for the prototype

magnitude of $\overline{F}_z^p$ and standard deviations. Mean normal forces as a function of $\dot{V}_N$ are given by:

$$\overline{F}_x^p = \beta_1^p \dot{V}_N^{1.789} \tag{4.18}$$

$$\overline{F}_z^p = \beta_2^p \dot{V}_N^{1.912}. \tag{4.19}$$

Use of the tool is not impaired by upward force for high flow rates, as even with $max\left(\overline{F}_z^p + \sigma\left(\overline{F}_z^p\right)\right) \approx 0.8\,\mathrm{N}$ it still has $F_{n,\mathrm{tot}}^p = 1.7\,\mathrm{N}$ of downward force resulting from the weight of the sphere at its disposal. This means that the sphere will not be drawn toward the top of the gap in idle conditions.

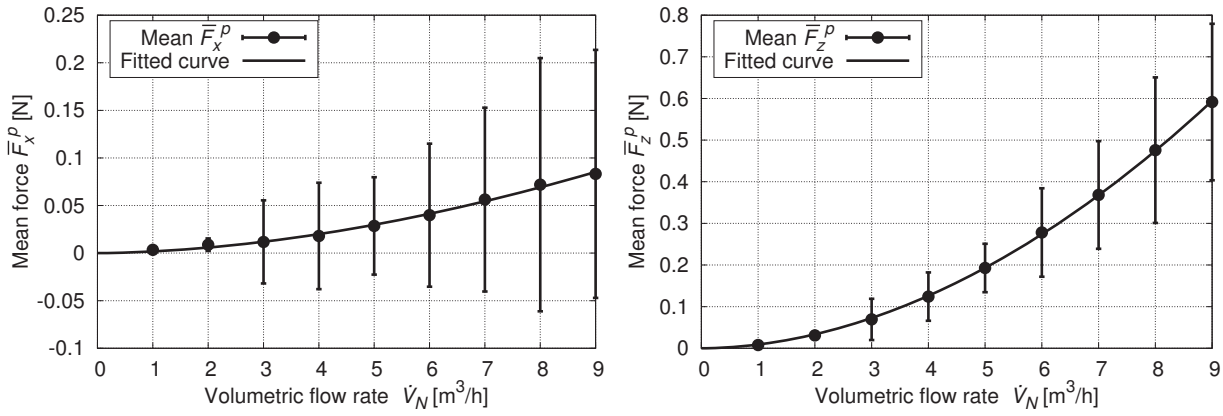

(i) Mean force $\overline{F}_x^p$ (ii) Mean force $\overline{F}_z^p$

Figure 4.16: Mean forces $\overline{F}_x^p$ and $\overline{F}_z^p$ averaged over rotation frequency f for the prototype

4.2.5 Tangential forces

As seen in Figure 4.17, tangential force for the prototype F_t^p displays a linear dependency on rotation rate f for constant standard volumetric flow rates $\dot{V}_N$. This allows for a linear regression line to be fitted to each constant $\dot{V}_N$, giving a mathematical approximation for the dependency of F_t^p on f.

As is to be expected, the slope of each regression line is negative since the velocity gradients (and thus the viscous forces) between the sphere's surface and the flow impacting the sphere become lower as rotation frequency increases (more on this is Section 4.2.6). The intercept of each regression line corresponds to the tangential force for a stationary sphere $F_{t,0}^p$, i.e. tangential force for $f = 0$. Each null point can be interpreted as the idle rotation frequency f_0^p for the corresponding flow rate due to the fact that if $F_t^p = 0$, the sphere can neither accelerate nor decelerate. Note for completeness that the trivial case in which both $F_t^p = 0$ and $f = 0$ implies the absence of flow, i.e. $\dot{V}_N = 0$. Figure 4.18.i shows the tangential force for a stationary sphere $F_{t,0}^p$ depending on volumetric flow rate $\dot{V}_N$. This relation can be given using the function governing the regression curve:

$$F_{t,0}^p = \alpha_1^p \dot{V}_N^{1.544}. \tag{4.20}$$

A similar analysis can be done for idle rotation frequencies which are extrapolated from the null points of the individual linear equations for constant standard volumetric flow rates. Figure 4.18.ii shows idle rotation frequencies f_0^p determined through extrapolation of the simulation results along with a fitted curve. See Appendix A for details on how the standard deviation is extrapolated for these values.

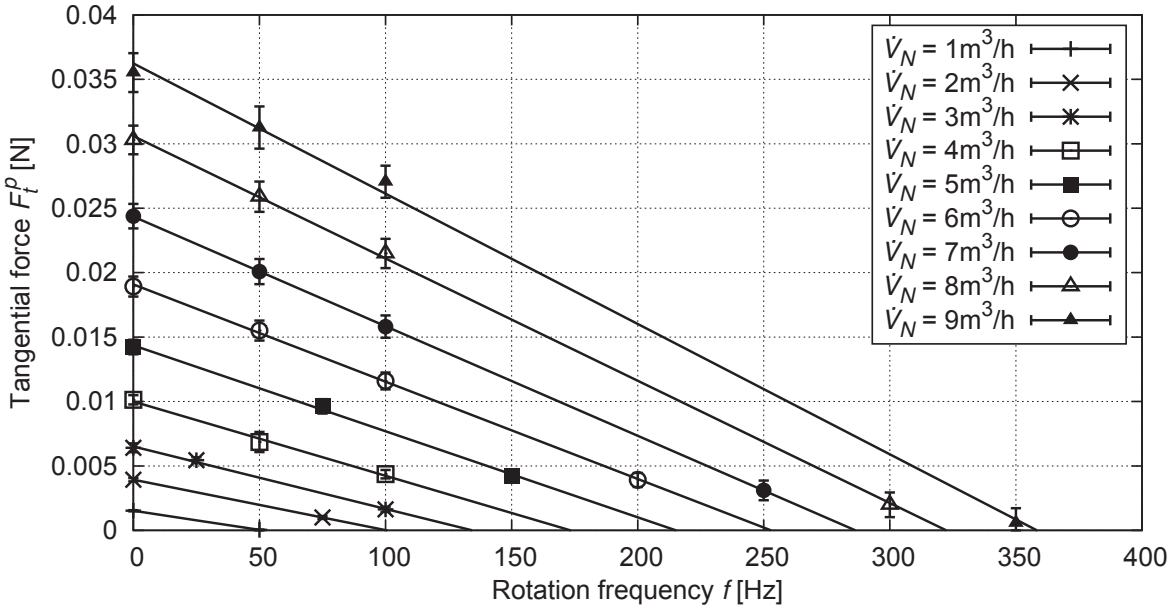

Figure 4.17: Tangential force F_t^p over rotation frequency f with fitted regression lines for each standard volumetric flow rate $\dot{V}_N$ for the *GrindBall* prototype

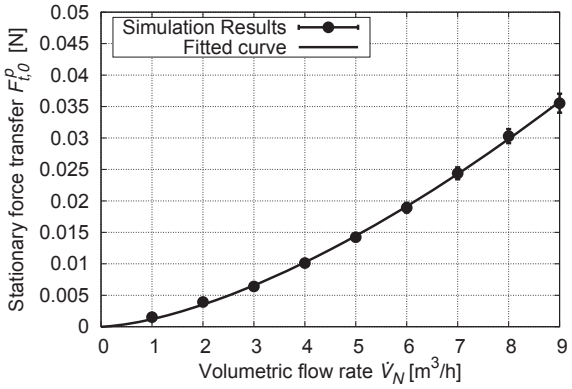

(i) Stationary force transfer $F_{t,0}^p$

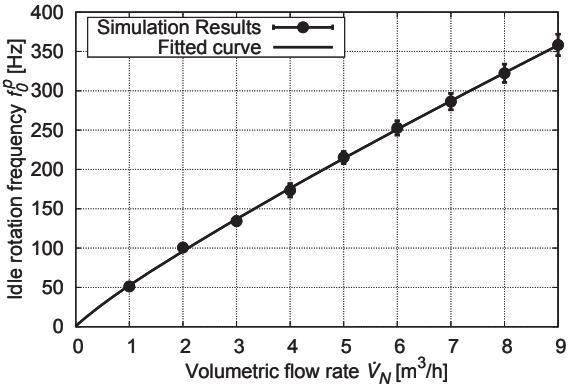

(ii) Idle rotation frequency f_0^p

Figure 4.18: Stationary force transfer $F_{t,0}^p$ and idle rotation frequency f_0^p over volumetric flow rate $\dot{V}_N$ for the *GrindBall* prototype

The fitted curve governing idle rotation frequency is a root function given by

$$f_0^p = \alpha_2^p \dot{V}_N^{0.875}. \tag{4.21}$$

Using the functions governing idle rotation frequency and stationary tangential force, a three dimensional relation may be obtained governing tangential force in terms of volumetric flow rate and rotation frequency.

4.2.6 Flow analysis

Before deriving this relation, a brief inspection of the flow will investigate the nature of momentum transfer and the resulting tangential force. High velocity gradients near the sphere are responsible for viscous forces that cause tangential stress on its surface. The higher these gradients, the more stress is caused and, thus, the more momentum is transferred on to the sphere. This is basically the statement made by eqn (4.7). Figure 4.17 shows a linear dependency of tangential force on rotation frequency for constant volumetric flow rates. The slopes of the functions governing this relation are negative, meaning that less grinding force is available with increasing rotation frequency. While this may seem intuitive, this section will take a closer look at the reason for this by considering the simulations conducted for $\dot{V}_N = 8\,\mathrm{m^3h^{-1}}$. The left hand side of Figure 4.19 shows a side view of the dimensionless mass flow rate

$$\hat{\dot{m}} = \frac{\overline{\rho}\overline{U}A_0}{\dot{m}}, \tag{4.22}$$

where $A_0 = 7.07 \cdot 10^{-6}\,\mathrm{m^2}$ is the cross-sectional area of the duct and $\dot{m} = 0.002874\,\mathrm{kg\,s^{-1}}$ is the mass flow rate corresponding to $\dot{V}_N = 8\,\mathrm{m^3h^{-1}}$. The right hand side shows velocity

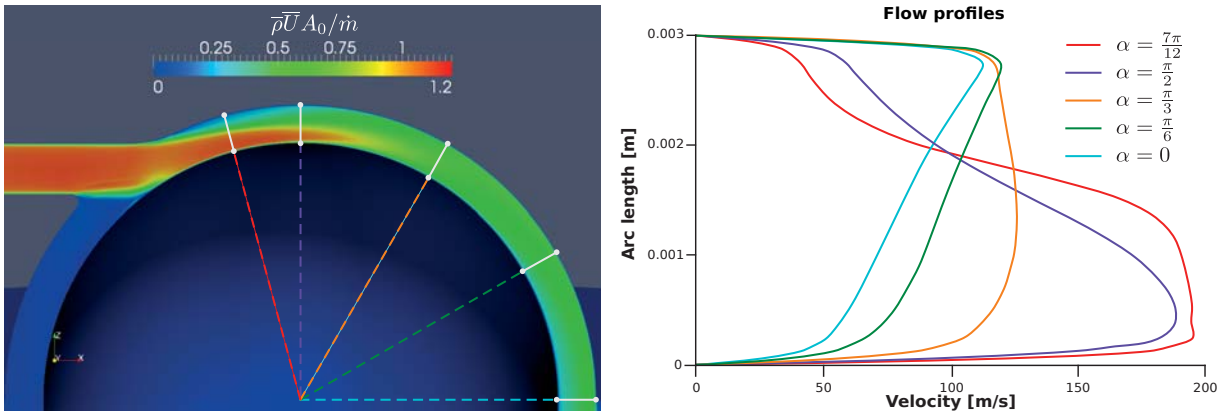

Figure 4.19: Flow profiles for $f = 0\,\mathrm{Hz}$, $\dot{V}_N = 8\,\mathrm{m^3h^{-1}}$

profiles plotted along the height of the gap for several angles α (the angle between the x-axis and the line over which velocity is plotted). Figure 4.20 shows the same for a rotation frequency of 50 Hz. Note how the magnitudes of velocities are practically unchanged, yet the gradients become smaller near the sphere at the bottom because its surface is moving at a velocity of approx. $6\,\mathrm{m\,s^{-1}}$. This becomes even more obvious in Figures 4.21 and 4.22. Increasing surface velocity of the sphere causes velocity gradients near the sphere to become smaller. Lower viscous moments M_v are a direct consequence.

Another interesting observation can be made upon considering the shape of the velocity profiles. Regardless of the rotation frequency, the peak velocity starts out very close to the sphere for $\alpha = 7\pi/12$. Similarly for $\alpha = \pi/2$, however, the peak moves slightly towards the center of the gap while also decreasing in magnitude. $\alpha = \pi/3$ sees a velocity profile almost symmetric along the height of the gap while $\alpha = \pi/6$ clearly shows that the flow impacts the top of the gap at this point. The exit point of the gap at $\alpha = 0$ displays little change. This is a clear indication that most of the flow's momentum is transferred

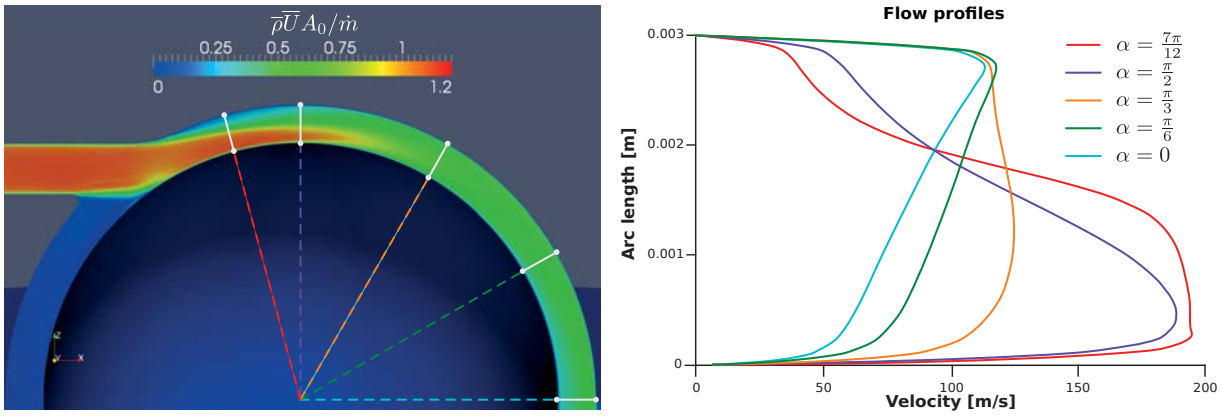

Figure 4.20: Flow profiles for $f = 50\,\mathrm{Hz}$, $\dot{V}_N = 8\,\mathrm{m^3h^{-1}}$

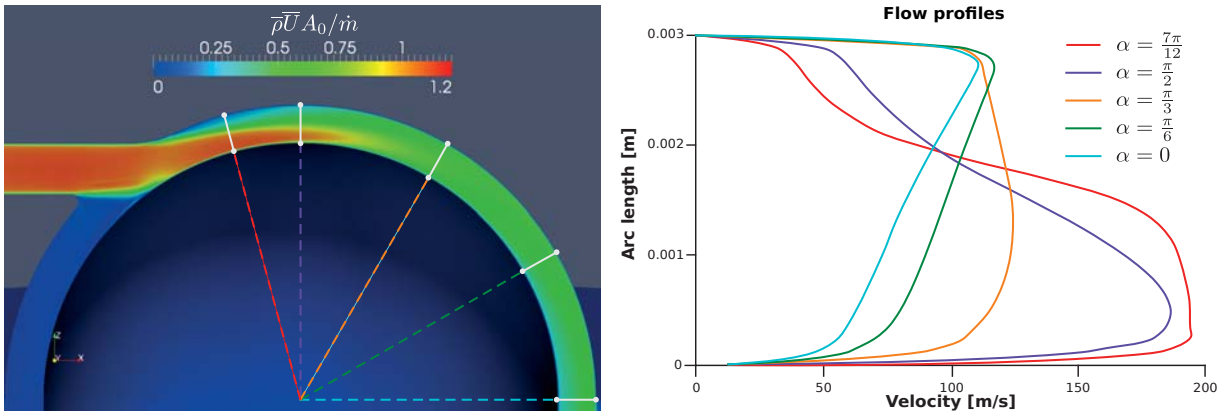

Figure 4.21: Flow profiles for $f = 100\,\mathrm{Hz}$, $\dot{V}_N = 8\,\mathrm{m^3h^{-1}}$

at and close to its point of impact on the sphere. Beyond $\alpha = \pi/3$ momentum transfer becomes negligible. This is a valuable insight for future development should the duct no longer be introduced horizontally, but vertically or at a specific angle. Care should be taken that there is an angle of no less than 45° between the flow's point of impact and the end of the spherical gap to ensure that momentum is not lost by letting the flow exit the gap prematurely.

4.2.7 Grinding force dependency

As previously seen, the relation between tangential force F_t^p and rotation frequency f is linear for constant volumetric flow rates $\dot{V}_N$. Furthermore, the 2D relations between $F_{t,0}^p$ and $\dot{V}_N$ for $f = 0$ and between f_0^p and $\dot{V}_N$ for $F_t^p = 0$ are known. A single equation

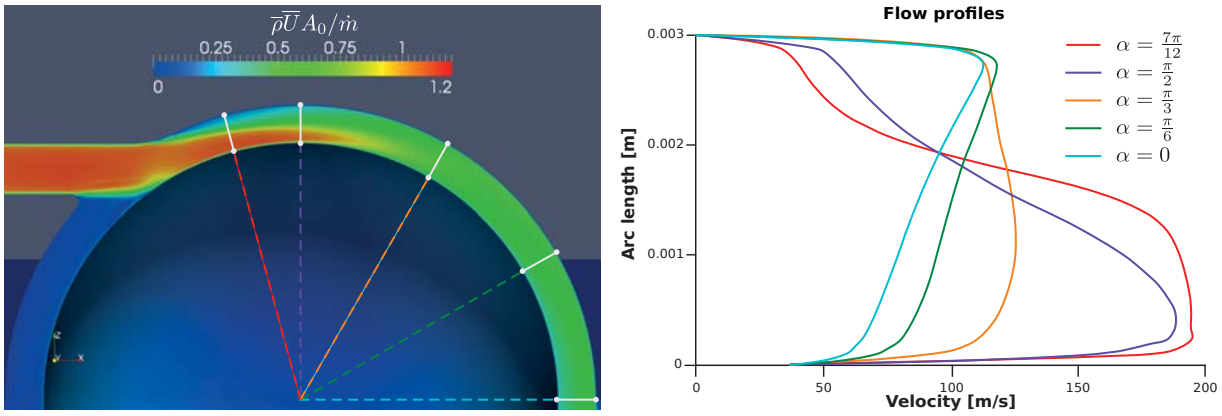

Figure 4.22: Flow profiles for $f = 300\,\mathrm{Hz}$, $\dot{V}_N = 8\,\mathrm{m^3h^{-1}}$

relating all three variables to one another can hence be obtained using $F_{t,0}^p$ as intercept, the ratio of $F_{t,0}^p$ to f_0^p as the slope, and f as the dependant variable:

$$F_t^p = F_{t,0}^p - \frac{F_{t,0}^p}{f_0^p} f = F_{t,0}^p \left(1 - \frac{f}{f_0^p}\right). \tag{4.23}$$

Hence, tangential force F_t^p is governed by

$$F_t^p \;=\; (\alpha_3^p \dot{V}_N^{1.544}) \left(\alpha_4^p - \alpha_5^p \dot{V}_N{}^{-0.875} f\right). \tag{4.24}$$

Figure 4.23 shows a three dimensional plot of eqn (4.24), with eqn (4.20) and eqn (4.21), as well as the linear regression curves from Figure 4.17 superimposed on to the surface.

Eqn (4.24) is of particular interest for the use of the *GrindBall*, as knowledge of F_t is required before commencing operation. Particular materials require certain amounts of force, which can simply be plugged into eqn (4.24), resulting in a 2D equation governing flow rate vs. rotation frequency. Thus, the flow rate can then be chosen to achieve a certain frequency for a given amount of force. Usually, higher rotation frequencies are desirable to achieve a smooth surface structure inside the cavity being ground [Bra].

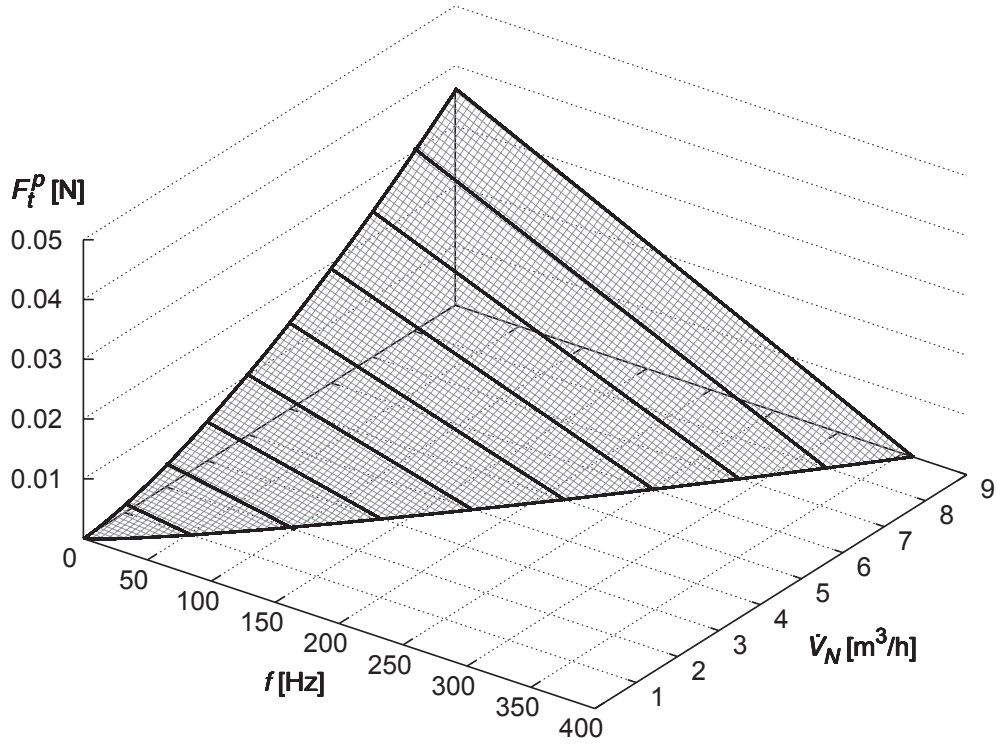

Figure 4.23: Tangential force F_t^p depending on rotation frequency f and standard volumetric flow rate $\dot{V}_N$ for the *GrindBall* prototype

4.2.8 Grinding power

One shortcoming of eqn (4.24) is that it does not give any indication as to optimum grinding conditions. Obviously one cannot grind at $f = 0$ where the force is largest since the sphere is not spinning. Grinding is equally impossible at f_0 where the rotation frequency is largest as there is no force being transferred. Hence, *grinding power* P_G is introduced to quantify performance. The physical quantity power P is a measure of work done per time, i.e.:

$$P = \frac{\mathrm{d}W}{\mathrm{d}t}. \tag{4.25}$$

For a tangential force F_t acting parallel to the path length s, one can use

$$W = \int_{s(t)} F_t \mathrm{d}s \tag{4.26}$$

and eqn (4.25) thus becomes

$$\begin{aligned} P &= \frac{\mathrm{d}}{\mathrm{d}t} \int_{s(t)} F_t \mathrm{d}s \\ &= \frac{\mathrm{d}}{\mathrm{d}t} \left(F_t s(t) \right) \\ &= F_t \dot{s}, \end{aligned} \tag{4.27}$$

where the force is treated as constant in space and time [GHSW96]. For the *GrindBall*, the force F_t is applied f times per second over the circumference of the sphere $2\pi r$, hence $\dot{s} = 2\pi r f$. Plugging into eqn (4.27), grinding power P_G is expressed as:

$$P_G = 2\pi r f F_t. \tag{4.28}$$

The functions governing the straight lines depicted in Figure 4.17 may be multiplied by $\dot{s}$ to obtain parabolic functions governing the prototype's grinding power P_G^p for each simulated flow rate $\dot{V}_N$. These are presented in Figure 4.24.

The maximum of each parabola indicates the highest attainable grinding power for that specific volumetric flow rate. It is thus possible to fit a curve through these maxima to get $P_{G,\max}^p$, the maximum grinding power:

$$P_{G,\max}^p = \alpha_6^p f^{2.798}. \tag{4.29}$$

Eqn (4.29) governs grinding power over rotation frequency. This is, however, not very useful as it does not include the flow rate. To incorporate $\dot{V}_N$, one must consider each of the parabola depicted in Figure 4.24. These have the general form

$$P_{G,n}^p = \left(a_n - b_n f \right) f, \tag{4.30}$$

where $P^p_{G,n} = P^p_G$ for $\dot{V}_N = n\,\mathrm{m}^3/\mathrm{h}$. The coefficients a_n and b_n are fitted over $\dot{V}_N$ yielding flow-rate-dependent coefficients $a(\dot{V}_N)$ and $b(\dot{V}_N)$. Plugging these back into eqn (4.30) results in a relation for grinding power depending on flow rate and rotation frequency:

$$P^p_G = \Big(a(\dot{V}_N) - b(\dot{V}_N) f\Big)\, f. \tag{4.31}$$

Note that alternatively, one could also plug eqn (4.24) into eqn (4.28) to obtain an expression for P^p_G.

For the 40 mm *GrindBall* prototype, this relation is given by:

$$P^p_G = \alpha^p_7 \dot{V}_N^{0.632} f^2 + \alpha^p_8 \dot{V}_N^{1.566} f. \tag{4.32}$$

A plot of eqn (4.32) can be seen in Figure 4.25. $P^p_{G,\max}(\xi)$ can now be given as a parametric curve in three-dimensional space for $\xi \in [0, 9]$:

$$f(\xi) = \alpha^p_9 \xi^{0.875} \tag{4.33}$$

$$\dot{V}_N(\xi) = \alpha^p_{10} \xi \tag{4.34}$$

$$P^p_{G,\max}(\xi) = \alpha^p_{11} \xi^{2.453} \tag{4.35}$$

leading to the operating point $\underline{\mathbf{P}}^p_{\mathrm{op}}(\xi)$, which parametrically describes $P^p_{G,\max}(\xi)$ as a vector in 3D space:

$$\underline{\mathbf{P}}^p_{\mathrm{op}}(\xi) = \left(\alpha^p_9 \xi^{0.875}, \alpha^p_{10} \xi, \alpha^p_{11} \xi^{2.453}\right). \tag{4.36}$$

Maximum grinding power is thus now determined. Using eqn (4.36) one can find the maximum power for each flow rate $\dot{V}_N$ along with a corresponding rotation frequency f.

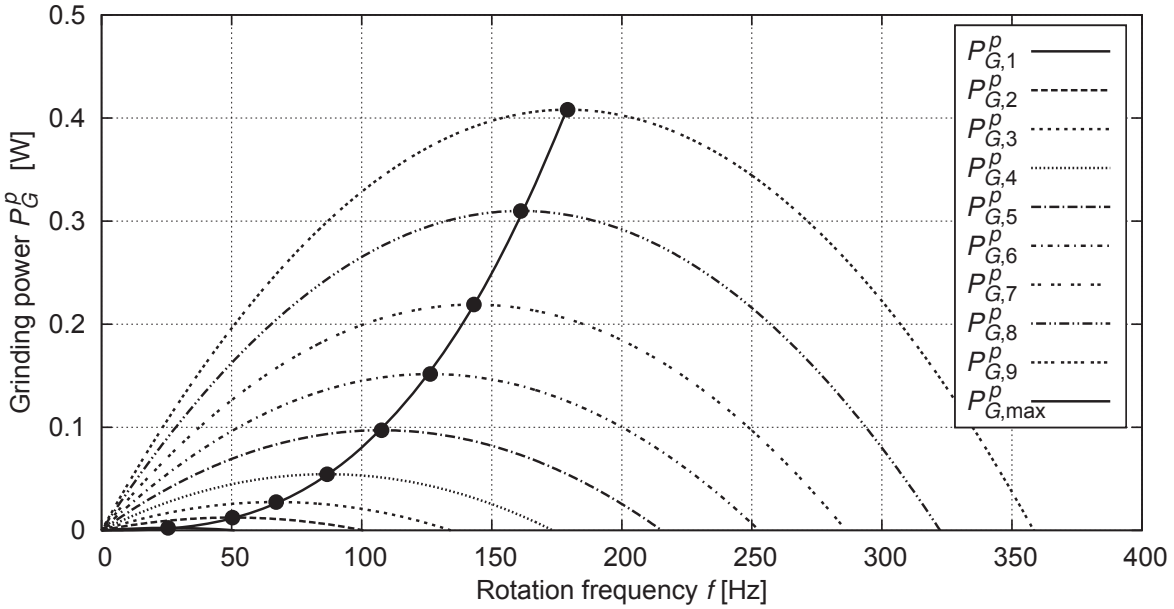

Figure 4.24: Grinding power P^p_G and $P^p_{G,\max}$ over rotation frequency f with fitted curves for each constant volumetric flow rate $\dot{V}_N$ for the *GrindBall* prototype

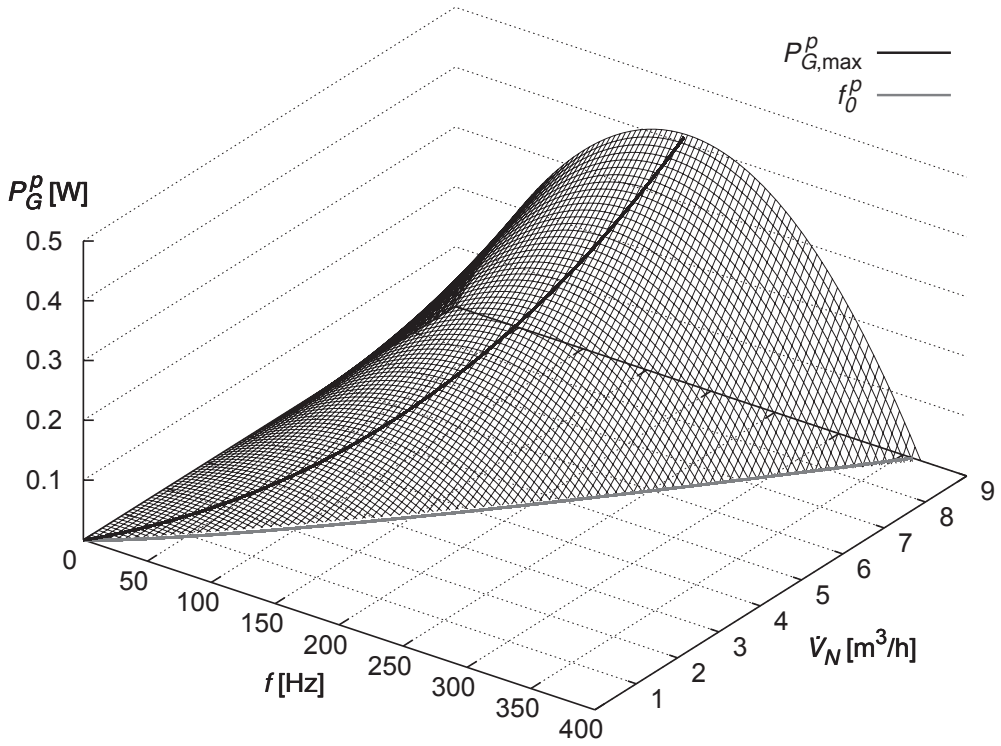

Figure 4.25: Grinding power P_G^p depending on rotation frequency f and volumetric flow rate $\dot{V}_N$ for the *GrindBall* prototype

Available grinding force and power are now both fully quantified for the 40 mm *GrindBall* prototype with eqns (4.24) and (4.32).

Chapter 5

Empirical validation of simulated data

Unforeseen difficulties in the development of the electro-magnetic bearing caused the practical portion of the project to fall behind schedule and development of a working prototype of the *GrindBall* was subsequently delayed. It is, however, of vital importance to validate numerical results, not only to show that formulae and methods are correctly implemented in the CFD code, but also to confirm that the employed mesh is fine enough and of sufficient quality to produce good results. To this end, a separate experiment was devised with which to validate the performed simulations, especially the process of fluid-to-solid force transfer.

Using a *Kistler MiniDyn 9256C2* Multicomponent Dynamometer, a device capable of accurately measuring all three Cartesian force components acting upon it, in combination

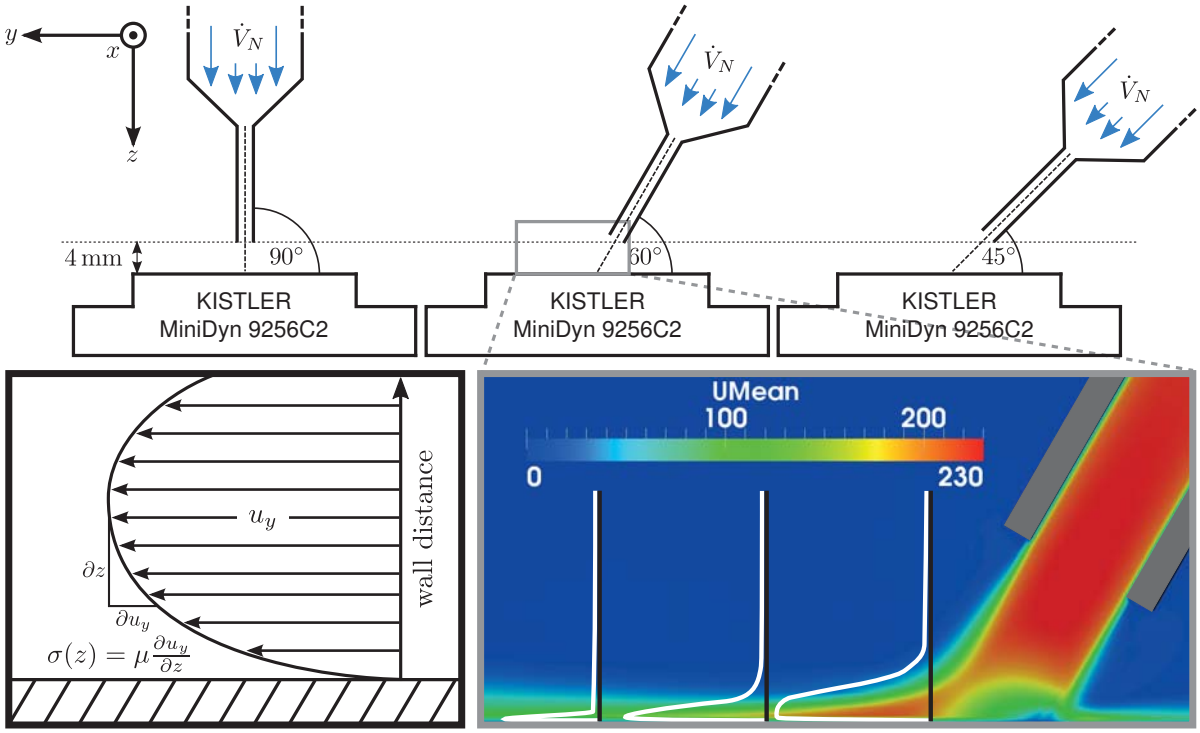

Figure 5.1: Experiment devised to validate fluid-to-solid force transfer

with a disconnected duct taken from the 40 mm *GrindBall*, experiments are conducted under a variety of flow rates and flow angles using air (Figure 5.1). These are then compared with analogous simulations using a simulation-setup as similar as possible to that used for the *GrindBall* prototype. With the process of fluid-solid interaction and the inherent transfer of forces and moments validated, past, present, and future simulations done for the *GrindBall* can thus also be considered valid. The flow angle γ is introduced to distinguish between normal and tangential forces. While $\gamma = 90°$ sees only normal forces, since tangential forces cancel each other out due to symmetry, flow angles of 60° and 45° introduce additional tangential forces. Thus, if all three simulated angles are in good agreement with the corresponding experiments, both normal and tangential forces can be considered valid. Validation of moments follows from this, as they are calculated simply by taking the cross product of tangential force with the lever arm (see eqns (4.5) and (4.7)).

5.1 Experimental setup

The experimental procedure uses much of the same hardware as is used for the *GrindBall* prototype: air is delivered from a 30 mm hose into a 4 mm duct. The hose, the funnel, and the duct are identical to those used for the the 40 mm GrindBall. Instead of leading into a spherical gap, however, the flow is expelled into open space before impacting on to the dynamometer as seen in Figure 5.2.

Hence, the duct's exit is straight and its length of 30 mm is the same on all sides. For all angles, the lowest point of the duct is positioned 4 mm above the plate and the duct's centre is aligned with the plate's mid-point (see Figure 5.1). Four standard volumetric flow rates $\dot{V}_N = 4, 6, 8$, and $10\,\mathrm{m}^3/\mathrm{h}$ are considered for each angle.

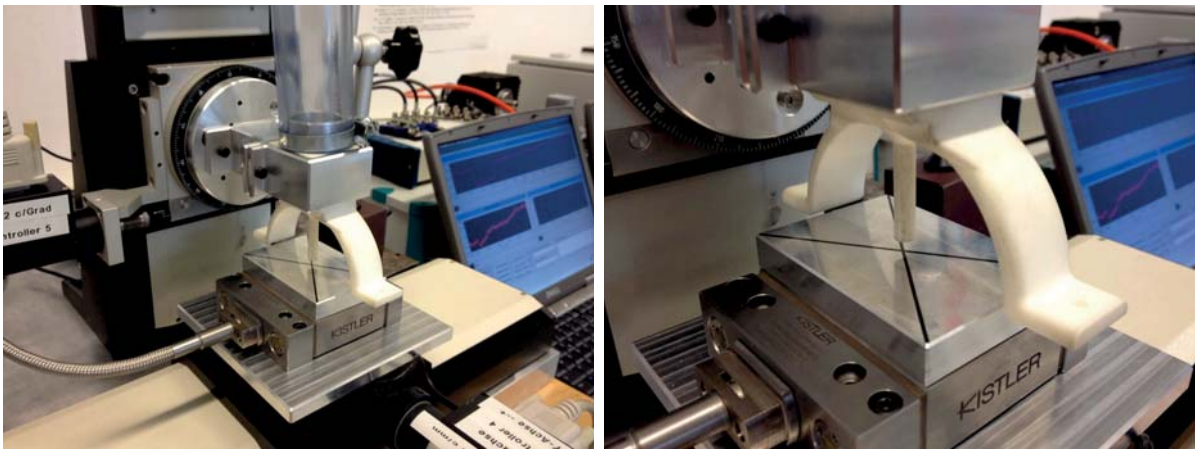

Figure 5.2: Experimental setup for the dynamometer validation

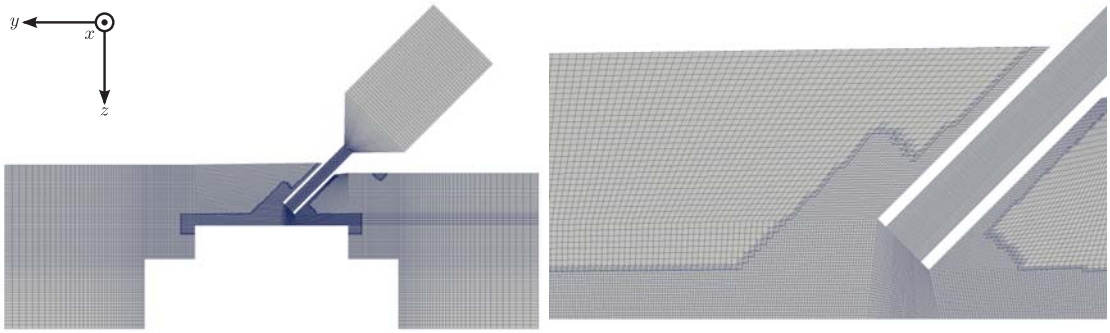

Figure 5.3: Computational grid for the dynamometer validation (2D slice)

5.2 Simulation setup

Experimental results are compared to analogous simulations conducted on a mesh consisting of approx. 9 million cells. The employed numerical methods and boundary conditions are identical to those used in the simulations conducted for the *GrindBall* prototype in Section 4.2 and can be seen in detail in Appendix D.2. The top of the plate has the same cell resolution as the *GrindBall* prototype does inside its spherical gap with about 8 cells per millimetre in each direction. Also, the cell resolution inside the duct is chosen such that it is in keeping with the prototype simulations. Local grid refinement (Appendix B.3) ensures that this resolution is achieved while maintaining an acceptable total number of cells. Figures 5.3 and 5.4 give an overview over the computational grid.

Furthermore, the simulation timeline is similar to that used for the *GrindBall* prototype (see Figure 4.13) apart from the fact that simulations are conducted on the ultimate mesh from the beginning. The flow is initialised until 0.005 s and results are averaged over the interval from 0.01 s to 0.02 s.

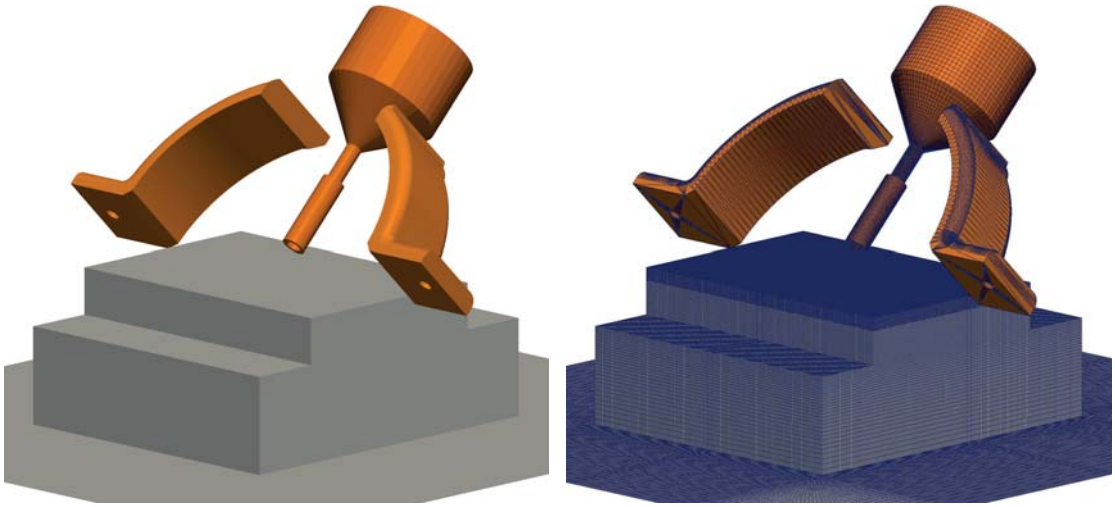

Figure 5.4: Computational grid for the dynamometer validation (3D view)

5.3 Empirical and computational results

Figure 5.5 shows isosurfaces of constant mean velocity magnitude $\overline{U} = 40\,\mathrm{m/s}$ for all three flow angles, coloured according to the standard deviation of the instantaneous velocity magnitude U. The left picture clearly shows the flow's point-symmetric behaviour in the xy-plane about the centre of the plate for $\gamma = 90°$. Furthermore, the standard deviation illustrates that turbulent fluctuations are distributed with symmetry equal to that of the mean velocity. Hence, it is safe to ignore forces tangential to the plate at $\gamma = 90°$ and only consider normal forces resulting from pressure acting downward on to the plate for this case. 60° and 45°, however, display a strong asymmetry about the x-axis. While F_x may still be neglected due to symmetry about the y-axis, F_y is of particular interest as this is where viscous forces acting tangentially to the plate come into play. Even though a measured F_y can not be considered a purely viscous force since regions of low pressure may form immediately behind the end of the plate and exert pressure force, the combination of first validating pure pressure forces for $\gamma = 90°$ and subsequently validating mixed pressure-viscous forces for $\gamma = 60°$ and $\gamma = 45°$ allows for forces of purely viscous nature to be considered valid as well.

Figure 5.6 shows the results for $\gamma = 90°$. Clearly, the simulations are in very good agreement with the experiments for 90°. The most noticeable discrepancy between simulated and measured data is observed for $\dot{V}_N = 4\,\mathrm{m^3/h}$, however, it is still well within an acceptable range and may be attributed to forces being slightly too low to be measured accurately by the dynamometer at this flow rate.

Figure 5.7 illustrates the results for $\gamma = 60°$. F_y sees a minor deviation between measured and simulated values again for $\dot{V}_N = 4\,\mathrm{m^3/h}$ while F_z slightly deviates for $\dot{V}_N = 8\,\mathrm{m^3/h}$. Both discrepancies, however, are again well within acceptable ranges and the agreement of measured and simulated values is very good.

Finally, results for $\gamma = 45°$ are seen in Figure 5.8. Simulated data and experimental values are in excellent agreement for both F_y and F_z.

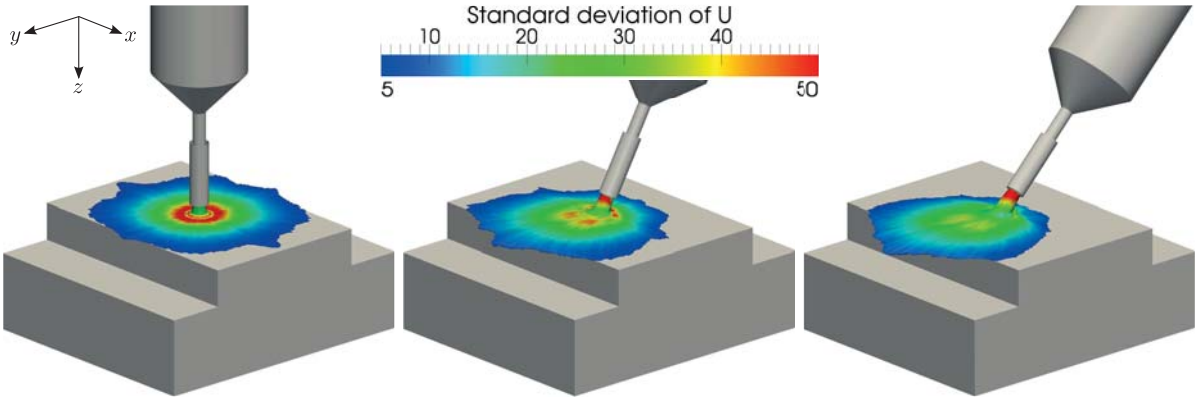

Figure 5.5: Isosurfaces with $\overline{U} = 40\,\mathrm{m/s}$ for flow angles γ (from left) 90°, 60°, and 45°

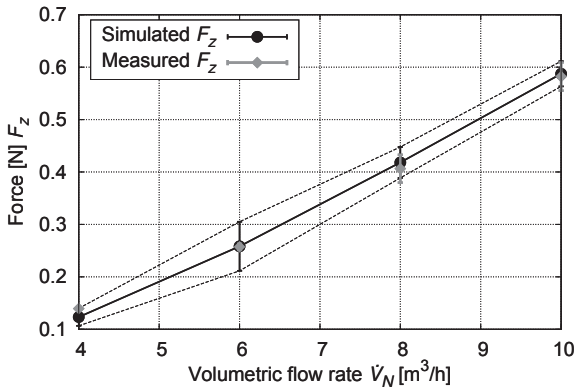

Figure 5.6: Normal forces for a flow angle of 90°

Simulated forces appear to coincide very well with measured data. Their standard deviations, however, do not agree as well. With the exception of $\sigma(F_y)$ for $\gamma = 45°$, standard deviation of measured forces seems fairly independent of the flow rate. Standard deviations of simulated forces, however, clearly increase with rising flow rate as has also been observed in all previous *GrindBall* related simulations. Actually, the latter result seems intuitively correct since increasing flow rate incorporates more intense turbulence and thus greater fluctuation about the mean. The question remains why this behaviour is not observed in measurements. Generally, the discrepancy in standard deviation of the simulated and measured value is much greater for low flow rates.

The higher the flow rate, the more the two begin to coincide. This leads to the possible conclusion that the standard deviation of measured results is strongly influenced by noise brought about by the dynamometer itself. This particular model can capture forces ranging from 0.002 N to 250 N so clearly the forces measured here are at the low end of the spectrum and a certain amount of noise is to be expected. Environmental effects of

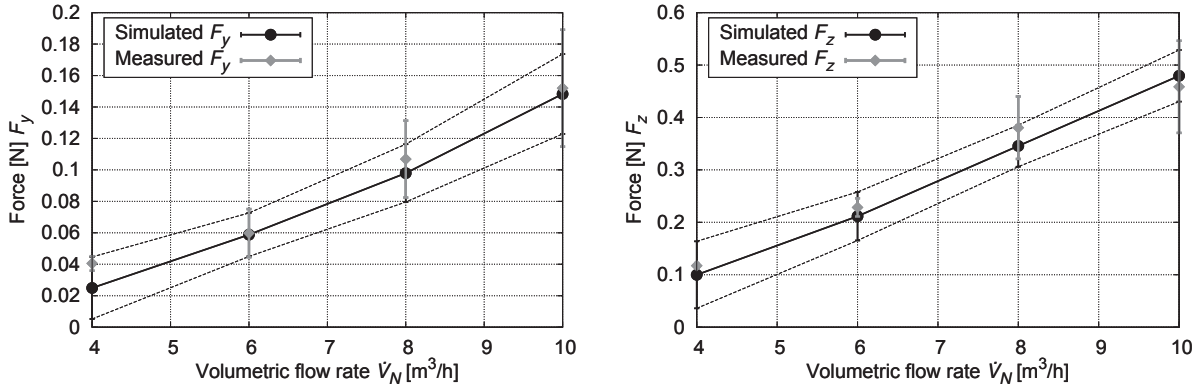

Figure 5.7: Normal and tangential forces for a flow angle of 60°

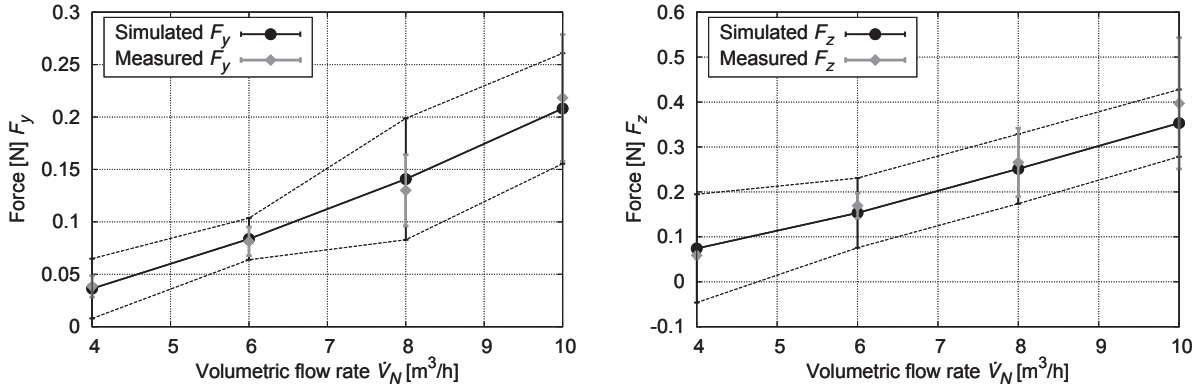

Figure 5.8: Normal and tangential forces for a flow angle of 45°

the surroundings may also induce this behaviour such as a draft or vibrations caused by machinery operating nearby. Regardless, the mean forces are clearly not influenced in a measurable way as has been demonstrated above and the overall result is extremely pleasing. The process of fluid to solid force transfer is now considered valid for previously conducted prototype simulations. Future simulations should have equal validity provided that the same simulation parameters are used and that the mesh resolution is not less than that which was used here.

Chapter 6

Developing a fully functional 8 mm grinding tool

With the 40 mm *GrindBall* prototype completed, the next step is to miniaturise it down to a tool incorporating an 8 mm grinding sphere. Several changes are made in order to improve upon the prototype. Firstly, two additional ducts are employed which introduce a higher total flow rate (relative to the spheres diameter of course), thus transferring more momentum from the flow on to the sphere. Secondly, all three ducts are aligned vertically and lead into the spherical gap from the top in order to make the tool more compact and to create downward contact force which assists the grinding sphere in penetrating the surfaces of workpieces.

6.1 Determination of an adequate propulsion fluid

The abrasion force depicted in Figure 4.23 is nowhere near enough to conduct grinding trials with the *GrindBall* prototype let alone use it to machine an actual work piece. The viscosity of air is simply too low to produce enough shear stress on the grinding sphere's surface to achieve the necessary force transfer. Initial simulations have shown that scaling down the tool even increases the gap between required and delivered tangential force. Thus, the propulsion medium must be changed in order to achieve satisfactory results. Switching to another gas is unlikely to induce the desired effect and so liquids - specifically oils - are studied instead.

6.1.1 Cavitation: limiting factor of liquids

Cavitation must almost always be considered when designing devices or machinery that handle liquids [Arn81]. It can affect performance and cause damage, even completely destroy machinery. The latter can range from minor damage over a long period of time to sudden catastrophic failure and complete destruction of components. Turbulent flows are especially susceptible to this phenomenon [MP97]. On a side note, even though cavitation

is usually considered a hindrance, it can also be useful, for example in the homogenisation of milk or the process of cleaning with ultrasonic cavitation [Arn81, MP97].

By definition, cavitation is the formation of vapour in a liquid. It is caused by a drop in local absolute pressure below the liquid's saturated vapour pressure p_v (note that conversely, boiling occurs when raising the liquids vapour pressure above local pressure). Bubbles form which then implode as soon as pressure increases again. The implosion releases energy in the form of acoustic waves and visible light. This can cause noise, vibration, and even severe damage through erosion and should thus be avoided or at least kept to a minimum when developing tools which employ liquid fluid flow. To quantify cavitation, the cavitation number Ca is defined according to

$$Ca = \frac{p - p_v}{\frac{1}{2}\rho U^2}. \tag{6.1}$$

It relates the difference between local absolute pressure and the vapour pressure to the flow's kinetic energy. The lower Ca, the greater the flow's potential of producing cavitation.

In designing the *GrindBall*, cavitation should be avoided for several reasons. Firstly, high noise levels are always undesirable when using a tool of any kind and should be avoided if it is possible and sensible to do so. Secondly, increased vibration causes the magnetic bearing to produce more heat while attempting to maintain the sphere's centred position, which in turn could not only inhibit prolonged use, but also decrease the viscosity of the propulsion fluid, thereby lowering F_t and making the tool less effective. Thirdly, the grinding spheres would erode more quickly if subjected to cavitation. Finally and most importantly, while the tool will consist mainly of high quality steel, its miniature nature is prone to damage due to small components and thin walls. Structural damage could lead to the tool's destruction, which obviously undesirable.

6.1.2 Oil viscosity study

Initial tests using water show that, while it can produce more grinding force, cavitation occurs even at low flow velocities and, more importantly, before a desirable level of grinding force can be reached. Propulsion media with higher viscosities must thus be considered. To this end, simulations are run using an initial version of the 8 mm *GrindBall*, comparing oils of varying viscosity grades with the goal of maximising grinding force while at the same time keeping the risk of cavitation to a minimum. Table 6.1 shows the viscosities of the oils considered here. EVO Fluid HLP is chosen, because these oils

ISO VG	5	7	10	15	22	32	46	68
ν [mm^2/s]	8.9	13	22	37	57	87	138	210
ρ [kg/m^3]	790	830	830	860	860	870	880	880
p_v [Pa]	< 10	< 10	< 10	< 10	< 0.5	< 0.5	< 0.5	< 0.5

Table 6.1: Kinematic viscosity, density, and vapour pressure of examined EVO Fluid HLP oils at room temperature $T = 293.15\,\mathrm{K}$

abide by ISO viscosity grade standards according to DIN 51519 [Deu98]. This guarantees that the oils' actual viscosities deviate no more that 10% from their stated values, thus ensuring consistent results. Furthermore, other physical properties such as density and vapour pressure are known and easily accessible.

Oils are compared using the following geometric parameters (cp. Figure 6.1): duct diameters of all three ducts are equal with $h_d = 1\,\mathrm{mm}$. Gap height is $h_g = 1\,\mathrm{mm}$. The offset of the main duct is $h_{o,1} = 0.8\,\mathrm{mm}$ and the offsets of the co-ducts are $h_{o,2} = 1.2\,\mathrm{mm}$. Note that for the 8 mm *GrindBall*, the offset, unlike for the prototype, is measured from the edge of the inlet basin. The angle of the imaginary lines connecting the centre of each co-duct with the centre of the inlet basin and the symmetry plane $y = 0$ is $\phi = 60°$. Furthermore, the inlet basin has a fixed diameter of 8 mm, which is the maximum diameter permitted due to spatial requirements of the magnetic bearing [Nor].

The simulations are conducted on a mesh consisting of approximately 4 million cells using `OpenFOAM-2.1.x`'s incompressible solver `pimpleFoam`. See Appendix D.4 for a detailed description of simulation parameters. Three runs are performed with varying volumetric flow rates resulting in mean flow velocities of 10 m/s, 20 m/s, and 30 m/s per duct ($\dot{V} = 3\overline{U}_d A$, where $\overline{U}_d$ is the mean velocity in each duct and A is the cross-sectional area of a single duct). Those oils that do not show signs of cavitation in the first run are re-examined in the second run. Similarly, those that do not cavitate in run 2 advance to the third run and so on. Unless stated otherwise, all simulations described in this and the following section incorporate a non-moving stationary sphere.

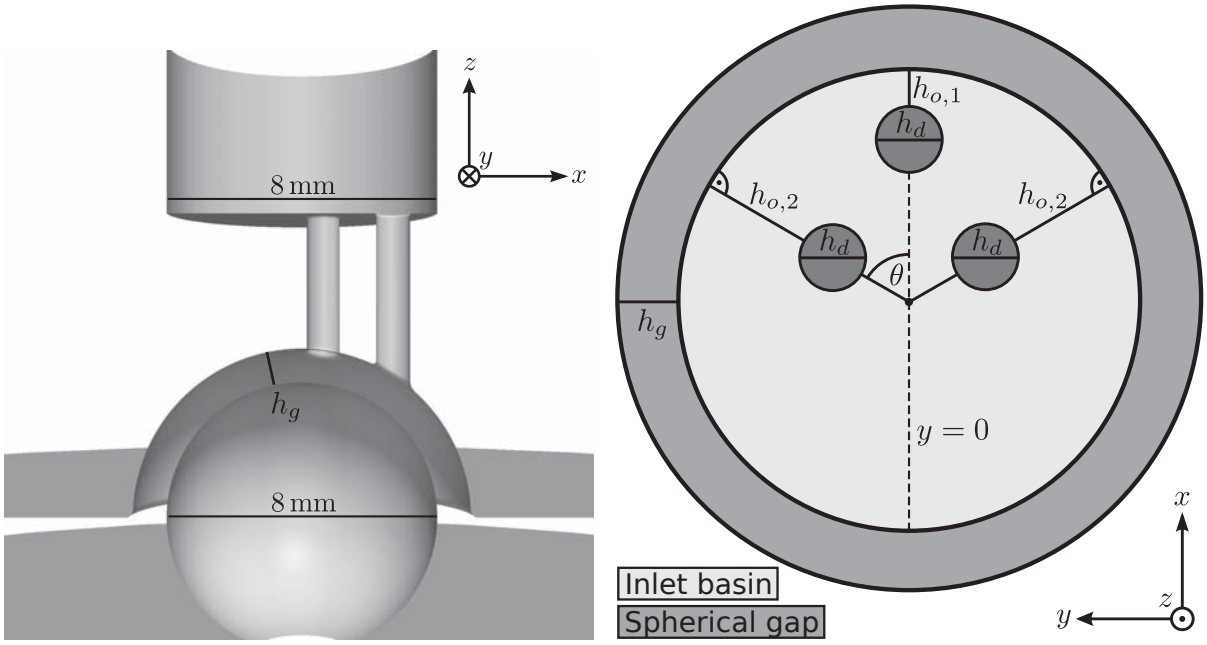

(i) Side view (ii) Top view

Figure 6.1: Geometric parameters for the 8 mm *GrindBall*

Note that for incompressible simulations, pressure values are relative and not absolute (although they are chosen to coincide with absolute values here). For this reason, it is possible to obtain negative values for pressure. Furthermore, despite the low vapour pressure of the oils tested in this study (see Table 6.1), to provide certainty the criterion for the occurrence of cavitation is defined as a drop of $p_{\min}$ below 10^4 Pa anywhere in the simulation domain. Table 6.2 and Figure 6.2 show the results of the oil study.

The first run shows a clear increase of force transfer F_t with increasing viscosity up to VG46, upon which it decreases slightly for VG68. Downward contact force F_n increases with viscosity across the board. The minimum pressure $p_{\min}$ observed inside the simulation domain stays within acceptable values except for VG15 and VG22 where $p_{\min}$ takes on negative values. It is not clear why this occurs.

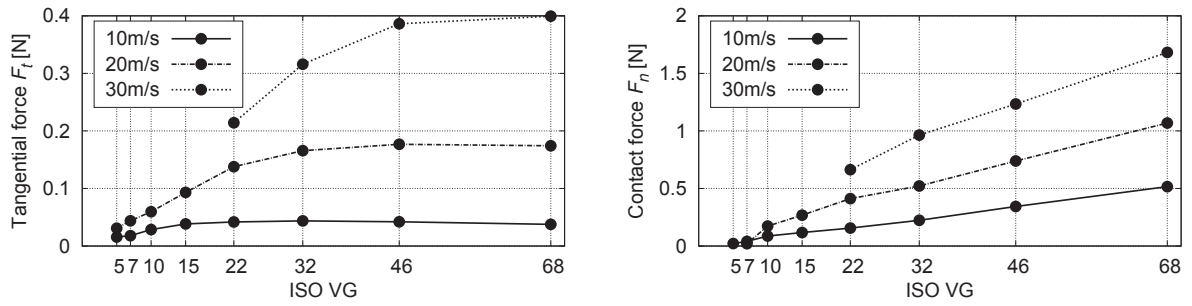

Figure 6.2: Tangential force and normal force plotted over viscosity for three test runs

$\overline{U}_d$		VG5	VG7	VG10	VG15	VG22	VG32	VG46	VG68
10 [m s^{-1}]	F_t [N]	0.016	0.018	0.029	0.038	0.042	0.044	0.042	0.038
	F_n [N]	0.022	0.040	0.087	0.117	0.156	0.223	0.344	0.516
	$p_{\min}$ [mbar]	580	580	898	-2130	-748	862	810	792
20 [m s^{-1}]	F_t [N]	0.031	0.044	0.060	0.093	0.138	0.166	0.177	0.174
	F_n [N]	-0.049	0.020	0.173	0.268	0.412	0.522	0.739	1.068
	$p_{\min}$ [mbar]	-968	-1003	-924	-308	493	493	378	264
30 [m s^{-1}]	F_t [N]					0.214	0.316	0.386	0.400
	F_n [N]					0.664	0.963	1.234	1.683
	$p_{\min}$ [mbar]					-1883	-176	-185	-405

Table 6.2: Results of the propulsion fluid study: Tangential force F_t, contact force F_n, and minimum pressure $p_{\min}$

In the second run, F_t displays the same behaviour as in run 1, peaking at VG46. Again, downward contact force increases in magnitude with viscosity, however, this time beginning with an upward force for VG5 resulting from low pressure zones at the top of the sphere where cavitation is most likely to occur. $p_{\min}$ shows that cavitation occurs for VG5 through VG15, hence these four oils do not advance to the third run.

In run 3, the remaining oils all show signs of cavitation and focus is drawn to VG46 and VG68 in run 2 as these display the highest momentum transfer. Although VG68 displays an F_t only less than 2% lower than that of VG46, its contact force is approximately 40% higher in magnitude. However, since the abrasion process requires only 0.5 N of downward contact force [Bra], VG46 is chosen over VG68 in order to maximise tangential force.

6.2 Optimisation of geometric parameters

Now that an adequate propulsion fluid has been determined, the next step is to optimise geometric parameters depicted in Figure 6.1. The goal is to maximise momentum transfer on to the sphere while maintaining a downward contact force of $F_n > 0.5$ N. Five steps lead up to the final geometry: investigation of gap height, optimising co-duct positions, examination of duct diameters, finding an optimal offset for the main duct, and performing final tweaks to the entire geometric layout.

6.2.1 Gap height

Height of the spherical gap h_g is investigated first. The aim here is to determine whether better results are achieved using $h_g < h_d$ (as was the case for the pneumatic prototype

in Section 4.1.4) for incompressible liquid flow. To this end, gap heights of 0.8 mm and 0.9 mm are compared to results from the reference case "VG46, run 2" in Table 6.2 where $h_g = 1\,\text{mm}$. Henceforth "VG46, run 2" is referred to as "case 0" in this section. Other geometric parameters remain identical to those used in case 0 as does the volumetric flow rate. Figure 6.3 shows the results.

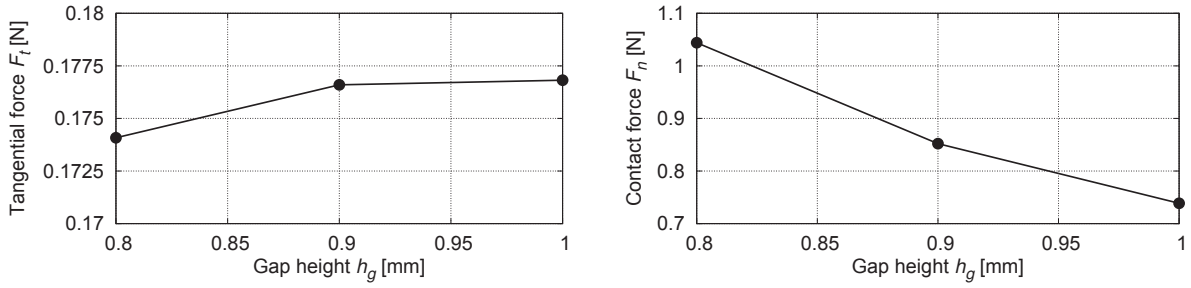

Figure 6.3: Tangential force and normal force plotted over gap height

F_t is highest for case 0 and it is clear that incompressible flow does not profit from $h_g < h_d$ in this regard. While contact force increases in magnitude with decreasing gap height, case 0 still provides a sufficient F_n. Furthermore, setting the gap height at exactly 1.0 mm makes the magnetic control element more efficient as it decreases response times [Nor]. Hence, h_g remains at 1 mm.

6.2.2 Co-duct position

Next, the effect of shifting the co-ducts' positions is investigated. The position of the main duct is held constant with $h_d = 0.8\,\text{mm}$ and the position of the co-ducts is varied to examine in which direction the co-ducts should be moved in order to maximise momentum transfer. Starting from case 0, the co-ducts are shifted a distance a in y-direction away from the symmetry plane $y = 0$, and a distance b in positive x-direction. Figure 6.4.i shows the four cases simulated and Figure 6.5 shows the results.

Comparing case 0 to case 2 shows that shifting the co-ducts along y has very little effect regarding momentum transfer. Comparing case 0 to case 1, however, shows that a shift in x-direction increases F_t substantially. Case 3 (the combination of cases 1 and 2) shows slight improvement over case 1. Finally, case 4 shows further improvement with an even larger displacement in positive x-direction. Consequently it becomes clear that shifting co-ducts away from the centre of the inlet basin results in higher momentum transfer. Shifts along the y-axis show minor improvements while shifting along the x-axis are more yielding. Also, improvements resulting from shifts along y are bound to be limited as the moment arm between the point of the flow's impact on the sphere and the axis of rotation becomes shorter with increasing a. In contrast, regarding contact force, the opposite can

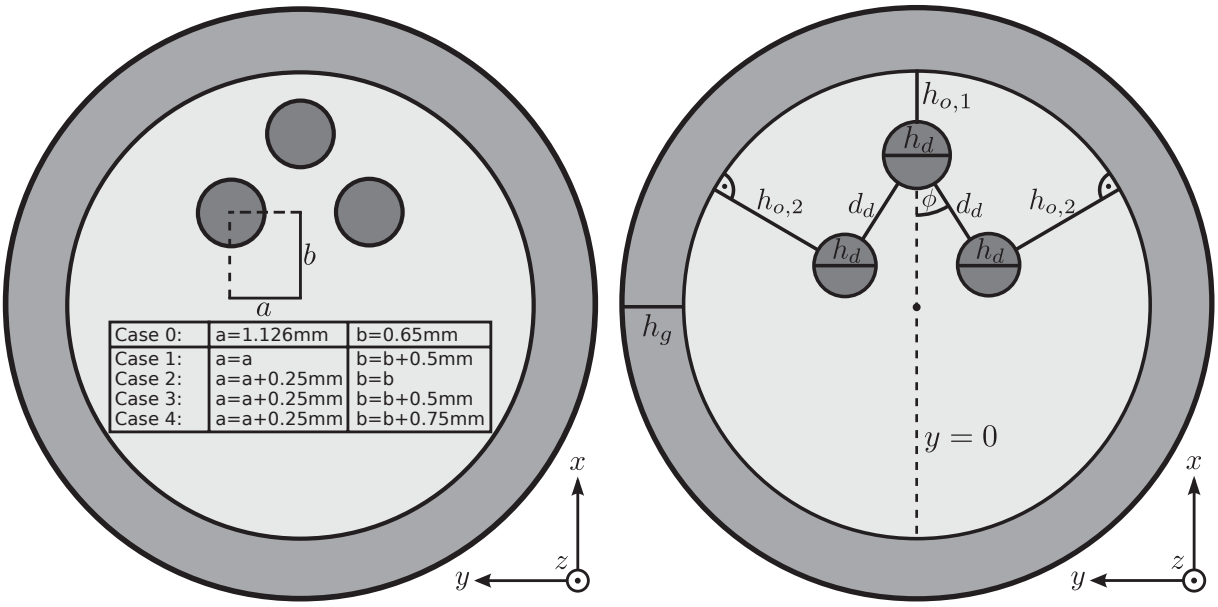

(i) Investigation of co-duct positions

(ii) Final part of the parametric study

Figure 6.4: Further geometric parameters for the 8 mm *GrindBall*

be observed. Moving co-ducts further away from the centre results in lower magnitudes of F_n.

While this may seem as an intuitive result, it is vital to ensure that $F_n > 0.5\,\mathrm{N}$ at all times [Bra]. This imposes a limitation for the geometry at this point which is dealt with in the following.

6.2.3 Duct diameter

While the investigation performed in Section 6.2.1 shows that decreasing gap height at a constant volumetric flow rate does not have a desired effect, increasing duct-diameter

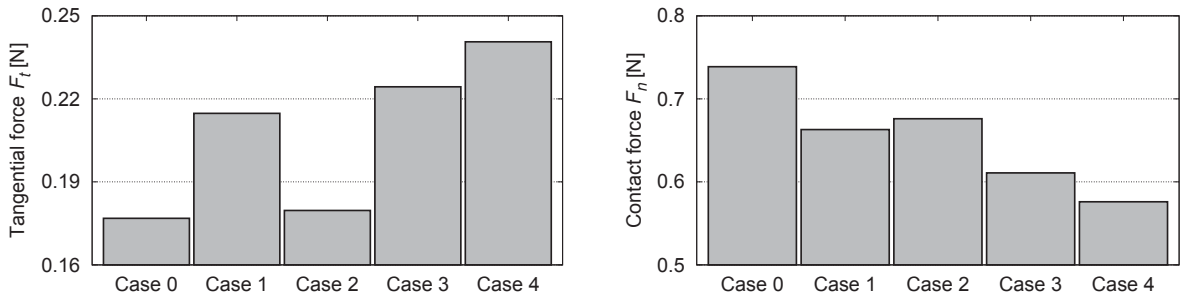

Figure 6.5: Tangential force and normal force for varying co-duct configurations

makes it possible to increase volumetric flow rate without exceeding $\overline{U} = 20\,[\mathrm{m/s}]$ per duct as the cross sectional area A also increases. The risk of cavitation occurring despite increasing the flow rate is kept low by doing so. Gap height cannot be increased beyond 1 mm due to the distance between magnets and grinding sphere becoming too large and so is held constant at 1 mm. Diameters of 1.1 mm, 1.2 mm, 1.3 mm, 1.4 mm, and 1.5 mm are compared to case 0. Rather than keeping offsets constant as well, the centre of each duct remains at the same spot relative to the sphere for each case, i.e. $h_{o,1} = 0.8\,\mathrm{mm} + 0.5\,\mathrm{mm} - h_d/2$ and $h_{o,2} = 1.2\,\mathrm{mm} + 0.5\,\mathrm{mm} - h_d/2$. This provides a better basis for comparison. Figure 6.6 shows the results.

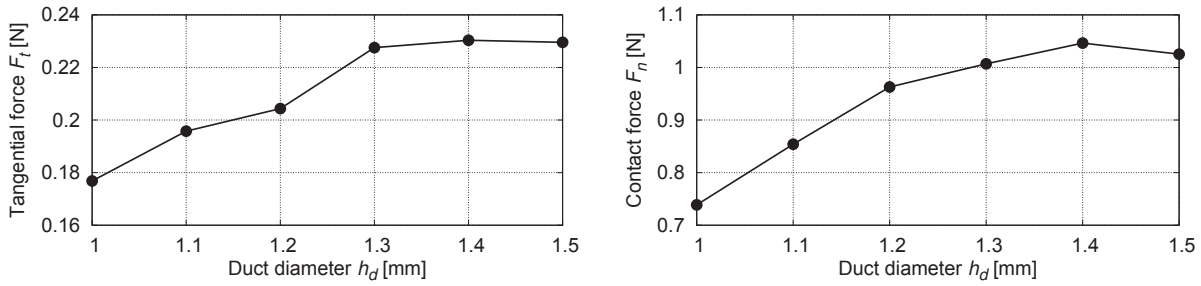

Figure 6.6: Tangential force and normal force plotted over duct diameter

Momentum transfer increases with duct diameter and peaks at 1.4 mm. Downward contact force F_n displays the same behaviour. Hence, the best choice here is clearly $h_d = 1.4\,\mathrm{mm}$.

6.2.4 Main duct offset

As an optimum value for the offset could not be determined for the prototype unequivocally due to spatial restrictions (see Section 4.1), the main offset $h_{o,1}$ is varied in the following. In order to maintain structural integrity under high pressure, the minimum distance permitted between the main duct and the wall of the inlet basin is 0.6 mm. Hence, the following offsets $h_{o,1}$ are considered: 0.6 mm, 0.7 mm, 0.8 mm (case 0), 0.9 mm, 1.0 mm, and 1.1 mm. To enable comparison with case 0, the co-ducts remain at the exact same position, i.e. $h_{o,2} = 1.2\,\mathrm{mm}$ and $\theta = 60°$, and duct diameters remain at $h_d = 1.0\,\mathrm{mm}$. Figure 6.7 shows the results.

F_t peaks at $h_{o,1} = 0.7\,\mathrm{mm}$ upon which it decreases with rising offset. As expected, F_n increases in magnitude with rising offset because the flow impacts the sphere's surface at a larger angle, resulting in more normal force and less tangential force.

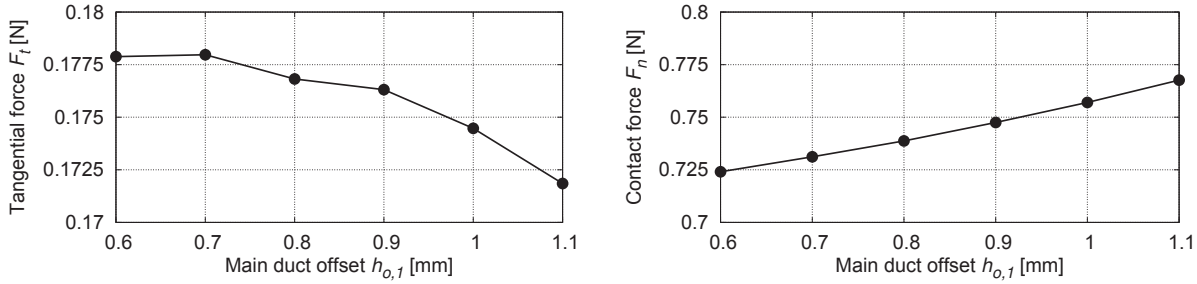

Figure 6.7: Tangential force and normal force plotted over main duct offset

6.2.5 Final adjustments

So far, parameters have been varied individually and compared to a reference case. Furthermore, it has been determined that shifting co-ducts in positive x-direction results in larger momentum transfer. Optimal positions for the co-ducts still need to be determined. Furthermore, it is not necessarily the case that the optimum values determined so far deliver in the best possible setup when combined with each other. This final study determines the best placement for the co-ducts and does some final tweaks to the geometry. Figure 6.4.ii shows the relevant parameters for this final part.

The distance between main duct and co-ducts is fixed at its minimum permitted value of $d_d = 0.6\,\text{mm}$. This seems prudent considering the results from Section 6.2.2. Duct diameters are $h_d = 1.4\,\text{mm}$, gap height is $h_g = 1.0\,\text{mm}$, and main offset is $h_{o,1} = 0.7\,\text{mm}$. First, the angle ϕ between the imaginary lines connecting the centre of the main duct with the centre of each co-duct and the symmetry plane $y = 0$ is varied. Simulations are performed for $\phi = 30°, 40°, 50°$, and $60°$ (see Figure 6.8).

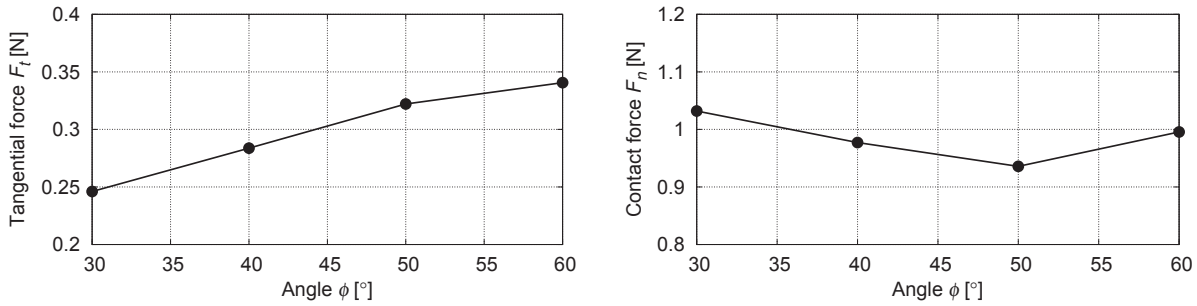

Figure 6.8: Tangential force and normal force plotted over the angle ϕ

F_t increases with increasing ϕ. F_n is well within acceptable values across the board. Next, the main offset $h_{o,1}$ is once again considered. Unlike in Section 6.2.4, co-duct positions are held fixed relative to the main duct with $\phi = 60°$ and $d_d = 0.6\,\text{mm}$.

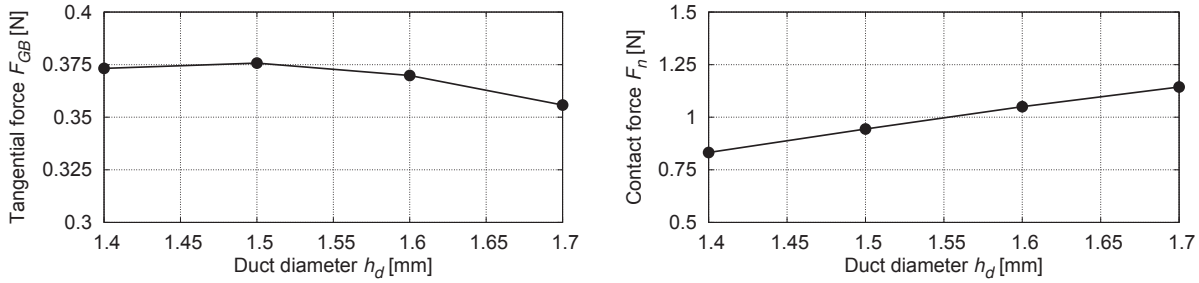

Figure 6.10: Tangential force and normal force plotted over duct diameter

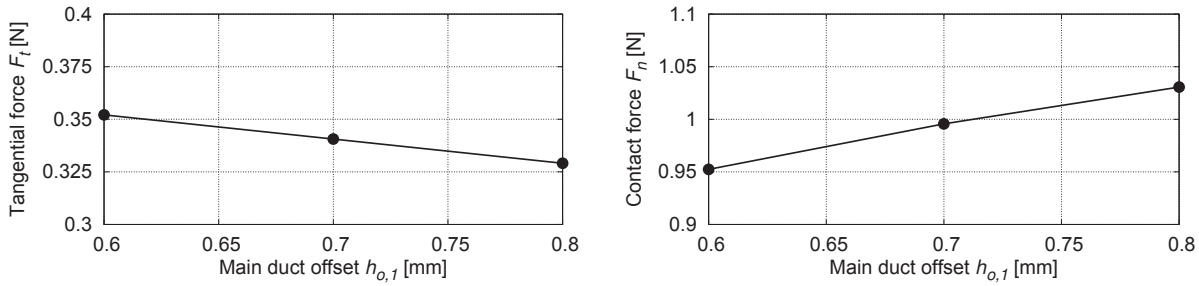

Figure 6.9: Tangential force and normal force plotted over main duct offset

The minimum permitted value of $h_{o,1} = 0.6\,\text{mm}$ delivers best results with the highest momentum transfer. Since a value of $\phi = 70°$ would result in $h_{o,2} < 0.6\,\text{mm}$ for this configuration, choosing ϕ is abandoned in favour of fixing $h_{o,2} = 0.6\,\text{mm}$ and $d_d = 0.6\,\text{mm}$ at this point. In the following, the described geometry is subjected to one final variation: duct diameter h_d, results of which can be seen in Figure 6.10.

The best result is achieved using $h_d = 1.5\,\text{mm}$. However, momentum transfer F_t for duct diameters of 1.4 mm and 1.6 mm is considerably close. Thus, Table 6.3 gives a more detailed perspective, incorporating not only simulations for a stationary sphere ($f = 0\,\text{Hz}$), but also simulations for $f = 250\,\text{Hz}$. Using the results from two rotation frequencies per case, a line can be fitted (cp. Section 4.2.5) allowing for conjectures to be

h_d [mm]	$F_{t,0}$ [N]	$F_{t,250}$ [N]	f_0 [Hz]	$f_{0.1}$ [Hz]
1.4	0.37246	0.10400	346.57	253.73
1.5	0.37574	0.11529	360.66	264.68
1.6	0.36985	0.12030	370.51	270.33
1.7	0.35579	0.11023	362.22	260.41

Table 6.3: Results of the final duct diameter study

made about the idle rotation frequency f_0, and the rotation rate at which an abrasion force of 0.1 N is achieved $f_{0.1}$.

Not only is $F_{t,250}$ highest for a diameter of 1.6 mm, f_0 and $f_{0.1}$ also show that the best performance is achieved using $h_d = 1.6\,\text{mm}$.

6.2.6 Summary

The final geometry for the 8 mm *GrindBall* is now determined. It is clear that moving main duct and co-ducts as far as possible toward the forward edge of the inlet basin (i.e. minimal offsets) maximises tangential force while maintaining acceptable values for contact force. Furthermore, co-ducts should remain close to the main duct to ensure that their flow impacts the sphere at a point at which the lever arm about the axis of rotation is long. Varying gap height shows little influence and an optimal duct diameter is found by considering simulations with two different spherical rotation frequencies per diameter.

Optimal values for geometric parameters are: a gap height of $h_g = 1.0\,\text{mm}$, a main duct offset of $h_{o,1} = 0.6\,\text{mm}$, a co-duct offset of $h_{o,2} = 0.6\,\text{mm}$, a distance of $d_d = 0.6\,\text{mm}$ between main and co-ducts, and a duct diameter of $h_d = 1.6\,\text{mm}$. Cavitation is not an issue with $p_{\min} > 10^4\,\text{Pa}$. This configuration delivers a tangential force of $F_t = 0.12030\,\text{N}$ at 250 Hz and yields a rotation frequency of $f_{0.1} = 270.33\,\text{Hz}$ at a tangential force of $F_t = 0.1\,\text{N}$. These tangential forces in combination with downward contact forces of $F_n > 1.0\,\text{N}$ allow the tool to be used efficiently for industrial grinding purposes.

Based on the findings presented in this section, a tangible 8 mm *GrindBall* module could be manufactured using rapid prototyping by the LFM and fitted with a magnetic bearing by the IALB. Figure 6.11 shows the actual module and two CAD images revealing its interior design.

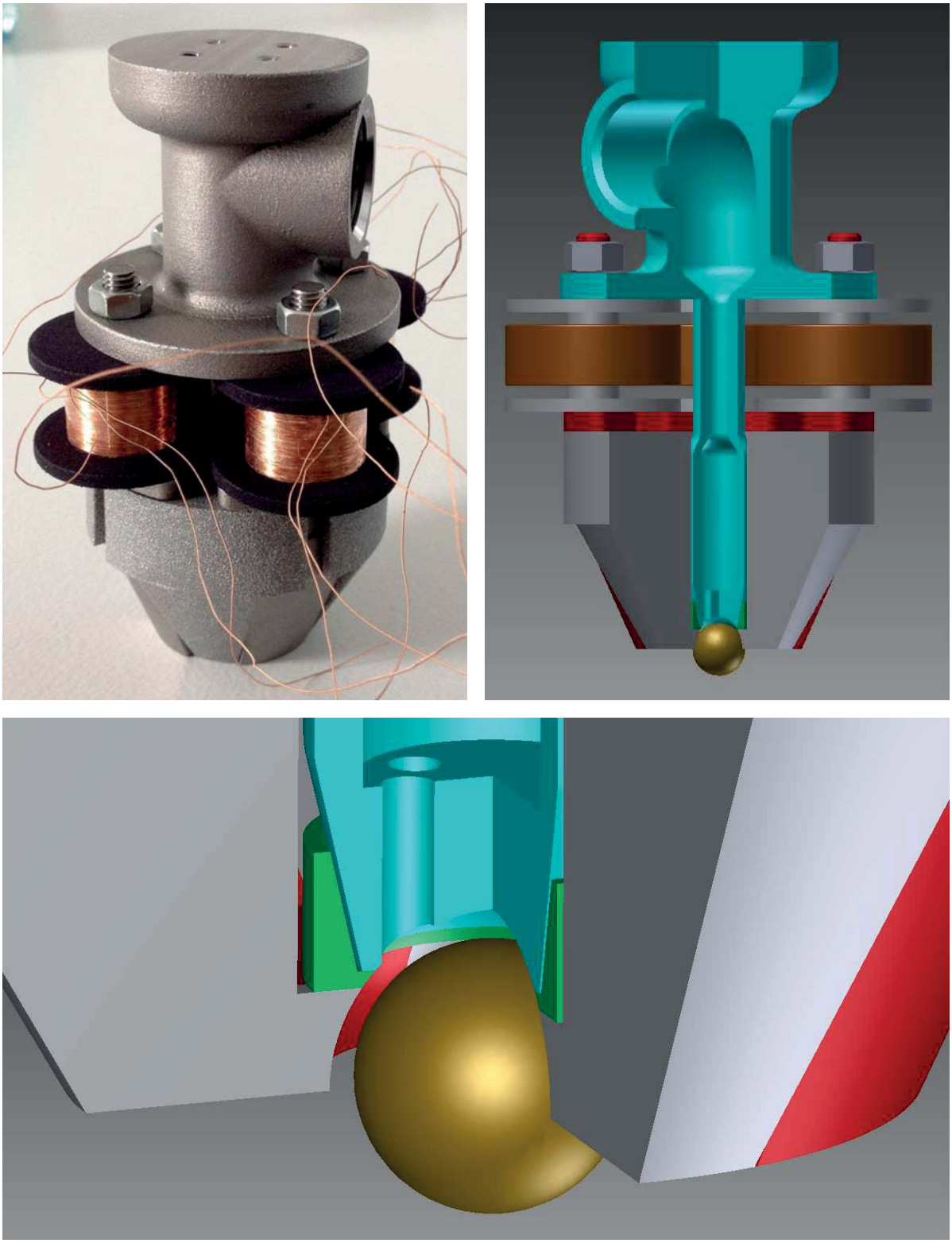

Figure 6.11: 8 mm *GrindBall* module (top left) and its interior represented by CAD imagery (top right and bottom)

6.3 Optimisation of the computational grid

Now that the geometric layout has been determined unequivocally, the computational grid needs to be tailored to it to deliver best possible results at a relatively low computational cost. To this end, several grids are tested and results are compared to an extremely fine grid - one which would result in too high a cost were it used throughout. This is done separately for two propulsion media - air and oil - as a further study using air is to be carried out later in Chapter 7.

Grid	$n_{\text{cells,gap}}$	$n_{\text{cells,total}}$	Description
base	15	$3.5 \cdot 10^6$	unmodified coarse mesh
mod 1	30	$9.50 \cdot 10^6$	gap refined
mod 2	30	$7.49 \cdot 10^6$	top half of gap and ducts refined
mod 3	30	$6.69 \cdot 10^6$	top half of gap refined
mod 4	30	$10.32 \cdot 10^6$	gap and ducts refined (reference mesh)
base 2	20	$7.06 \cdot 10^6$	finer base mesh

Table 6.4: Grids tested for the final *GrindBall* geometry. $n_{\text{cells,gap}}$ denotes the number of cells along the height of the top half of the spherical gap and $n_{\text{cells,total}}$ denotes the total number of cells in the grid

Table 6.4 lists the grids tested here. *Base* denotes a coarse base grid. *Mod 1-4* are modifications of the base grid with refinements implemented in various areas. See Appendix B.3 for details on refinement methods. *Base 2* is an alternative, finer base mesh which is used without additional refinement.

Figure 6.12 shows a clipped side view of the computational domain and Figure 6.13 the particular meshes. A notable difference to the prototype, apart from the obvious addition of two ducts and their vertical introduction into the spherical gap, is the fact that the sphere is no longer partially submerged in the bottom wall, i.e. in a workpiece, but hanging freely 3 mm above the floor. This is done for two reasons: firstly, the depth of penetration into the workpiece is neither known nor is it constant so that choosing an arbitrary constant depth would most certainly be incorrect. Secondly, validation experiments involving a functioning *GrindBall* would most likely be carried out by measuring idle rotation frequency and not by measuring F_t directly [Bra].

Mod 4 is used as a reference to which results from the other meshes are compared. It is not suited for further studies because its large number of cells and the required small time steps make it unsuitable for conducting analyses requiring many simulations. The grid that comes closest to the results attained on *mod 4* is then used for upcoming studies.

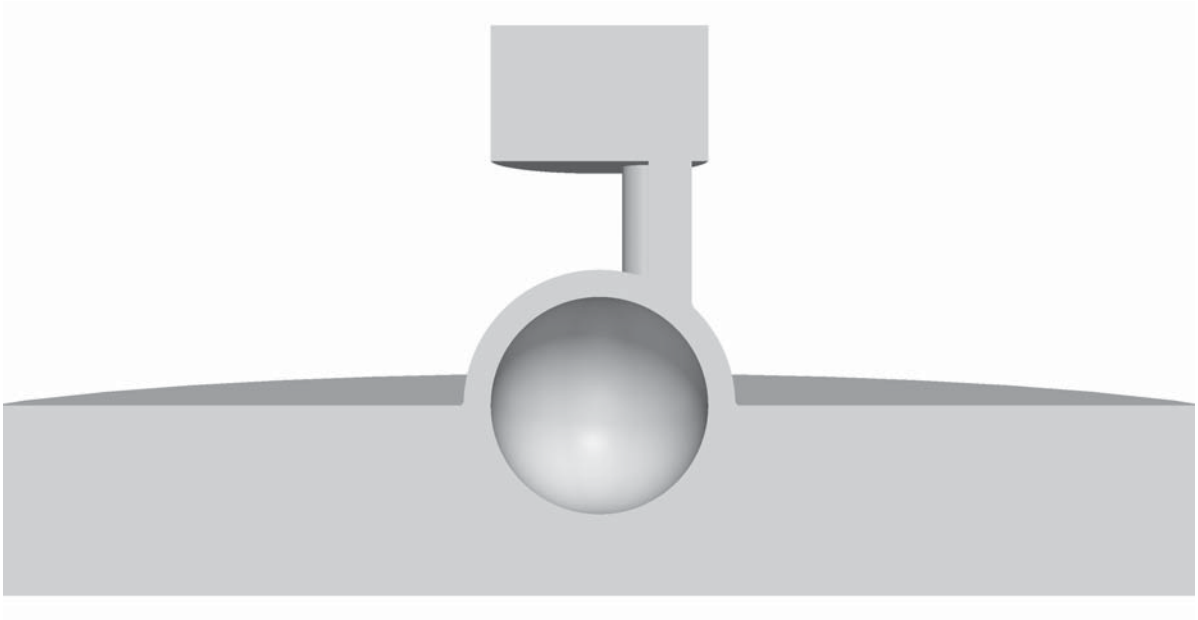

Figure 6.12: Computational domain for the final *GrindBall* geometry

6.3.1 Test setup

The tests are conducted for air and oil using the geometric parameters summarised in Section 6.2.6. The mass flow rate at the inlet is set to $\dot{V}_N = 3\,\mathrm{m}^3/\mathrm{h}$ for air while $\dot{V} = 7\,\mathrm{l}/\mathrm{min}$ for oil. The rotation frequency of the sphere is set to 100 Hz. See Appendix D.6 for a detailed description of simulation settings for the compressible case and Appendix D.5 for the incompressible case. The aim is to compute mean tangential and normal forces and see which of the meshes shows the best agreement with the mesh *mod 4*.

6.3.2 Results for air

Figure 6.14 shows the results for the various computational grids using air as the propulsion medium. It should be stated beforehand that *mod 1* could not achieve stable operation using CDS for spatial discretisation and had to be run using UDS. Hence, the results from *mod 1* can be ignored here as they cannot be compared to results obtained using CDS and will not be discussed any further.

Apart from *base*, all meshes show good agreement with *mod 4* in terms of momentum transfer with *mod 2* performing best. Considering pressure force in x-direction, all meshes are in good agreement, yet *mod 2* once again displays the result closest to *mod 4*. Contact force F_n sees *base* performing badly with a 50% discrepancy to *mod 4*, *mod 3* and *base 2* are below 20% deviation, and *mod 2* performs best yet again. Finally, the mean time-step

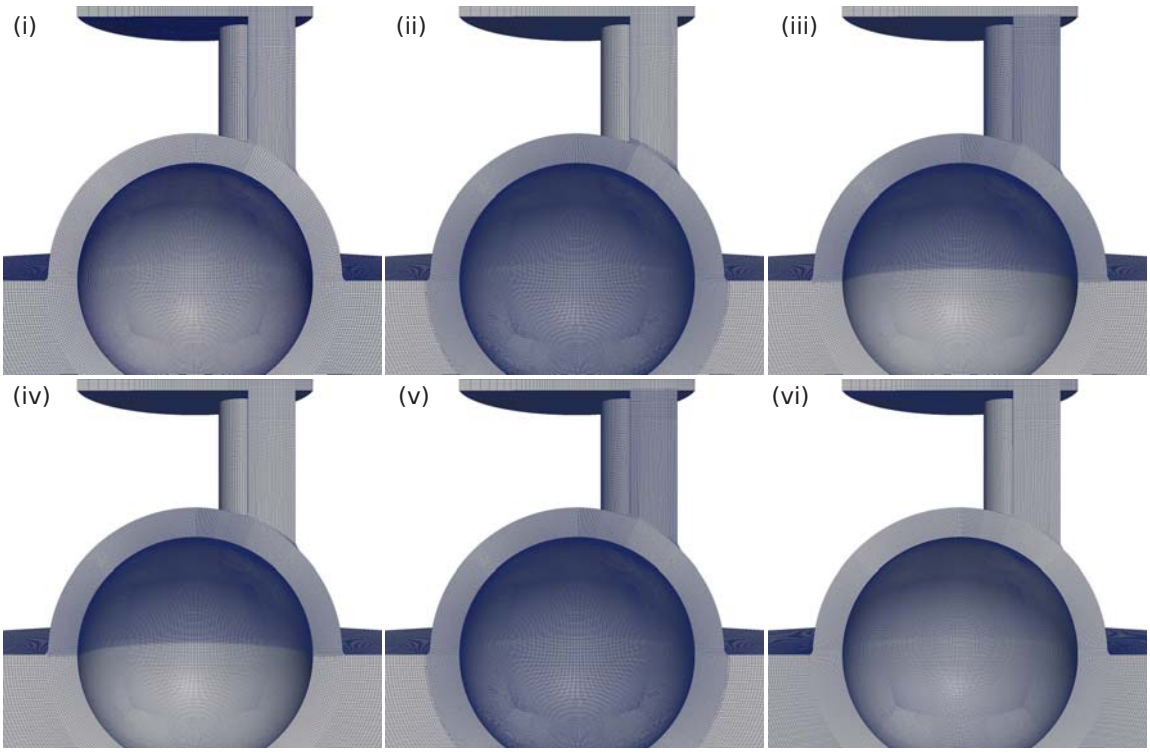

Figure 6.13: Grids tested for the final *GrindBall* geometry. (i) *base*, (ii) *mod 1*, (iii) *mod 2*, (iv) *mod 3*, (v) *mod 4*, (vi) *base 2*

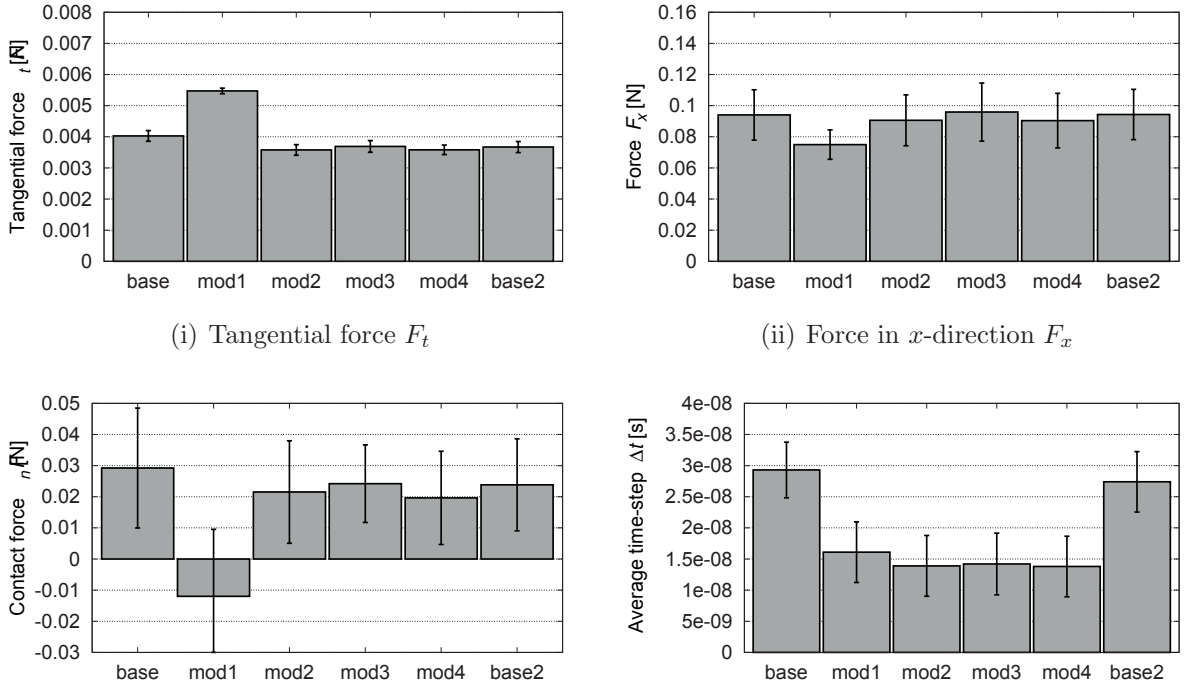

(i) Tangential force F_t

(ii) Force in x-direction F_x

(iii) Contact force F_n

(iv) Average time-step Δt

Figure 6.14: Results of the mesh test for air

size unsurprisingly shows both base meshes outperforming the others approximately by a factor of 2. Considering that a large number of simulations need to be performed on this grid, the time-step size is a very important factor. Although *mod 2* is clearly in best agreement with the finest mesh, the discrepancies between *base 2* and the fine mesh are small enough to consider *base 2* as the best choice because its computational cost amounts to far less than that required by *mod 2*.

6.3.3 Results for oil

The incompressible case is unable to run on meshes using local grid refinement because pressure correction fails to converge, most likely due to the high viscosity of the fluid. Hence, *base* and *base 2* are the only meshes considered for oil.

Figure 6.15 shows the results. F_t, F_x, and F_n are all in good agreement for both meshes with less than 10% discrepancy. The only big difference is the average time-step. Δt is larger on *base* by a factor of approximately 1.33 making *base* more efficient. However, results should later be comparable to those obtained for compressible simulations. This can be better achieved if the number of cells along the height of the gap are identical, e.g. to ensure that velocity gradients near walls do not differ based solely on differences in the mesh. For this reason *base 2* is also chosen for incompressible simulations.

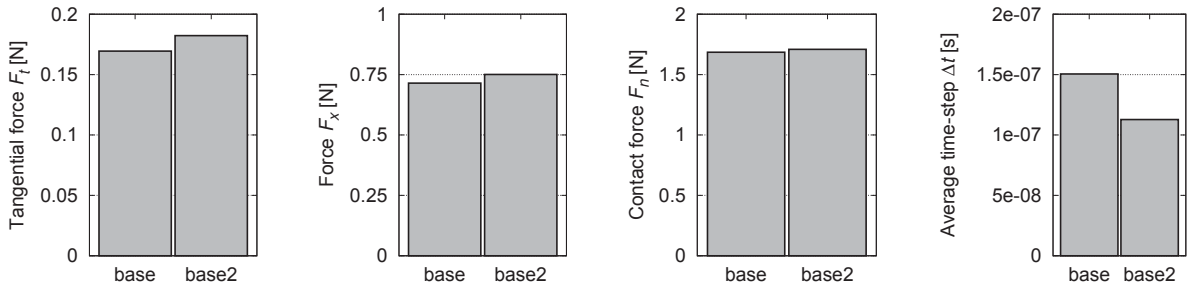

(i) Tangential force F_t (ii) Force in x-direction F_x (iii) Contact force F_n (iv) Average time-step Δt

Figure 6.15: Results of the mesh test for oil

6.4 Computational Results

This section discusses the computational results obtained from simulations conducted for the final 8 mm *GrindBall* using oil. Normal forces are briefly discussed upon which tangential force is analysed in detail. Finally, grinding power is determined and an operating point found.

6.4.1 Reynolds and Cavitation numbers

Table 6.5 shows Reynolds numbers for each flow rate $\dot{V}$, where the Reynolds number is defined as

$$Re = \frac{\overline{U} h_d}{\nu_{\text{oil}}} \tag{6.2}$$

with $\overline{U} = \dot{V}/3A_d$, the mean velocity of the flow determined by dividing a third of the volumetric flow rate $\dot{m}$ (because the flow is considered to be evenly distributed among the three ducts) by the cross-sectional area of the duct $A_d = (0.5h_d)^2\pi$. Note that $h_d = 0.4r$, $r = 0.004\,\text{m}$, and $\nu_{\text{oil}} = 1.38 \cdot 10^{-4}\,\text{m}^2\text{s}^{-1}$ at room temperature.

$\dot{V}$ [$\text{l}\,\text{min}^{-1}$]	1	2	3	4	5	6	7
Re	32	64	96	128	160	192	224
p_{min} [Pa]	$1.0 \cdot 10^5$	$9.3 \cdot 10^4$	$7.7 \cdot 10^4$	$5.4 \cdot 10^4$	$4.2 \cdot 10^4$	$2.4 \cdot 10^4$	$1.3 \cdot 10^4$
Ca_{min}	9	2.3	1.1	0.59	0.38	0.29	0.18

Table 6.5: Reynolds numbers and Cavitation numbers corresponding to each flow rate simulated for 8 mm oil

Clearly the flow is purely laminar due to the high viscosity of oil making modelling of turbulence redundant. Minimum pressure p_{min} and the minimum Cavitation number Ca_{min} (see eqn (6.1)) both decrease with increasing flow rate. While pressure is still at acceptable levels for $\dot{V} = 7\,\text{l}\,\text{min}^{-1}$ with $p_{\text{min}} = 1.3 \cdot 10^4\,\text{Pa}$, the Cavitation number drops dangerously low to $Ca_{\text{min}} = 0.18$. For this reason, simulations are conducted only until $\dot{V} = 7\,\text{l}\,\text{min}^{-1}$ and not beyond. Figure 6.16 shows p_{min} and Ca as well as velocity magnitude U for $\dot{V} = 7\,\text{l}\,\text{min}^{-1}$. The areas most prone to cavitation, i.e. areas of both low pressure and Cavitation number, are the near-wall regions where the ducts join into the spherical gap, and the regions in close proximity to the sphere slightly below the point of impact of the flow on to the sphere. Consequently, cavitation could damage both the structure of the magnetic bearing and the surface of the grinding sphere. While the latter can be easily replaced, damage to the former would require an entirely new tool to be manufactured. Volumetric flow rates should thus not exceed $\dot{V} = 7\,\text{l}\,\text{min}^{-1}$ in order to avoid damage.

6.4.2 Normal forces

Figure 6.17 shows the forces F_x^{oil} and F_n^{oil} for the 8 mm *GrindBall*. Unlike for the prototype, F_x^{oil} and F_n^{oil} are no longer independent of the rotation frequency f for constant $\dot{V}$. Instead, rising f causes a linear increase in both F_x^{oil} and F_n^{oil}. Moreover, there is no clear pattern as to how the slopes of these linear fits behave regarding $\dot{V}$. While they appear to become constant for $\dot{V} \geq 5\,\text{l}\,\text{min}^{-1}$, the behaviour at lower flow rates differs.

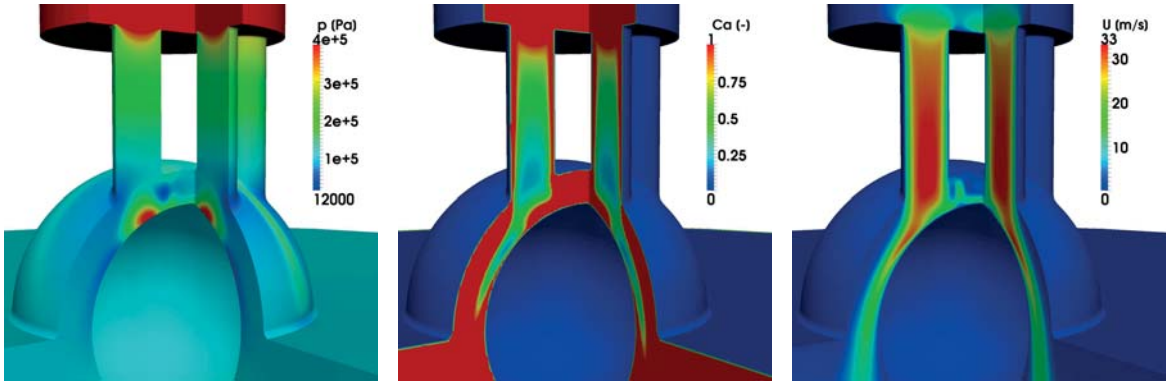

(i) Pressure p (ii) Cavitation number Ca (iii) Velocity magnitude U

Figure 6.16: Pressure and Cavitation number and velocity magnitude for $\dot{V} = 7\,\mathrm{l\,min^{-1}}$

F_x^{oil} starts with a flat slope for $1\,\mathrm{l\,min^{-1}}$, quickly increases before decreasing and converging to a constant. F_n^{oil} on the other hand starts with a flat slope which gradually increases and converges to a constant slope. Constructing a good 3D fit for such seemingly irregular data requires the use of high order polynomials. Fitting the coefficients of each straight line (each line of constant $\dot{V}$) over the volumetric flow rate, results in the following relations for F_x^{oil} and F_n^{oil}:

$$F_x^{\mathrm{oil}} = (\beta_1^{\mathrm{oil}}\dot{V}^4 + \beta_2^{\mathrm{oil}}\dot{V}^3 + \beta_3^{\mathrm{oil}}\dot{V}^2 + \beta_4^{\mathrm{oil}}\dot{V})f + \beta_5^{\mathrm{oil}}\dot{V}^2 + \beta_6^{\mathrm{oil}}\dot{V} \tag{6.3}$$

$$F_n^{\mathrm{oil}} = (\beta_7^{\mathrm{oil}}\dot{V}^5 + \beta_8^{\mathrm{oil}}\dot{V}^4 + \beta_9^{\mathrm{oil}}\dot{V}^3 + \beta_{10}^{\mathrm{oil}}\dot{V}^2 + \beta_{11}^{\mathrm{oil}}\dot{V})f + \beta_{12}^{\mathrm{oil}}\dot{V}^3 + \beta_{13}^{\mathrm{oil}}\dot{V}^2 + \beta_{14}^{\mathrm{oil}}\dot{V}. \tag{6.4}$$

Note that while these high order polynomials fit the present data very well, they are unlikely to provide a good basis for comparison to data obtained on other scales or using other propulsion media. Additionally, the fact that liquid propulsion, i.e. oil propulsion,

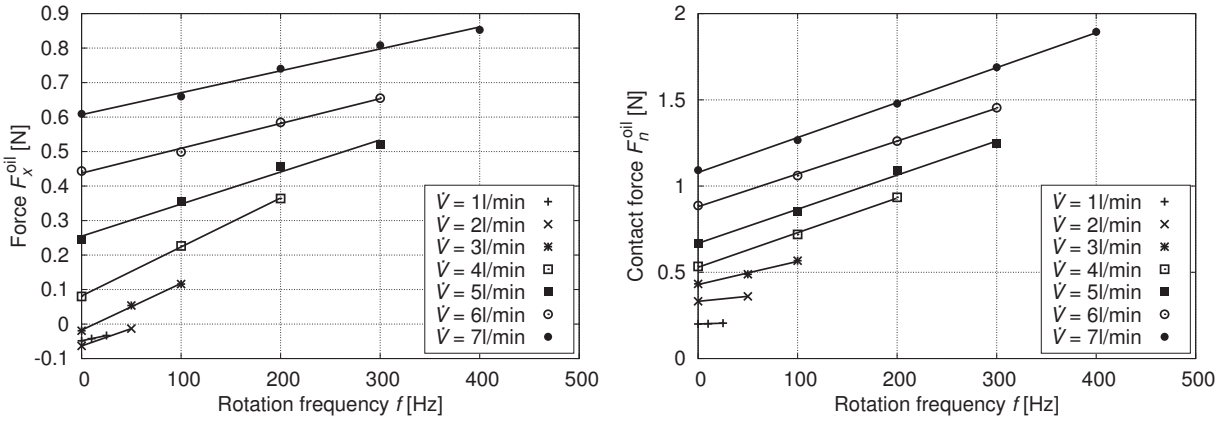

(i) Force exerted in x-direction F_x^{oil} (ii) Force exerted in $-z$-direction F_n^{oil}

Figure 6.17: Forces F_x^{oil} and F_n^{oil} for all simulations conducted for 8 mm oil

introduces rotation frequency dependence into normal forces makes a comparison even more problematic. Both 3D relations are plotted in Figure 6.18.

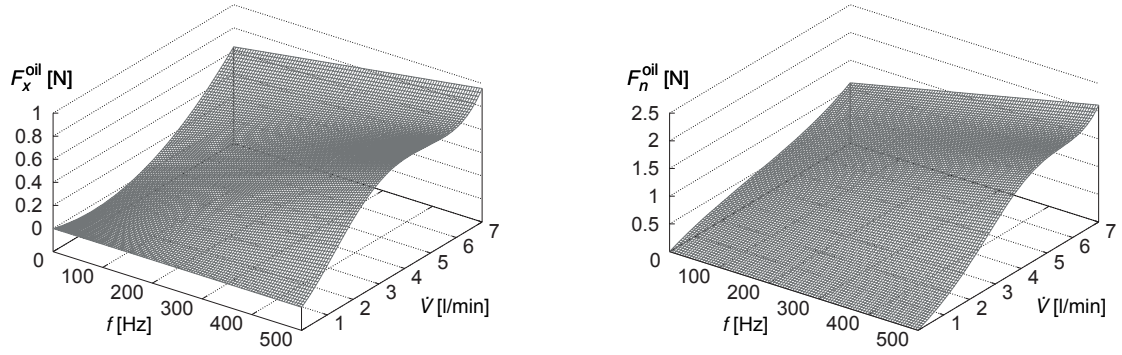

(i) Force F_x^{oil} (ii) Force F_n^{oil}

Figure 6.18: 3D forces F_x^{oil} and F_n^{oil} over rotation frequency f and flow rate $\dot{V}$

The question arises why hydraulic propulsion invokes a frequency dependence while pneumatic propulsion does not. Two possible reasons are the incompressibility and the much higher viscosity of oil. Figure 6.19 shows a comparison of oil propulsion at $\dot{V} = 7\,\text{l}\,\text{min}^{-1}$ for $f = 0\,\text{Hz}$ and $f = 400\,\text{Hz}$.

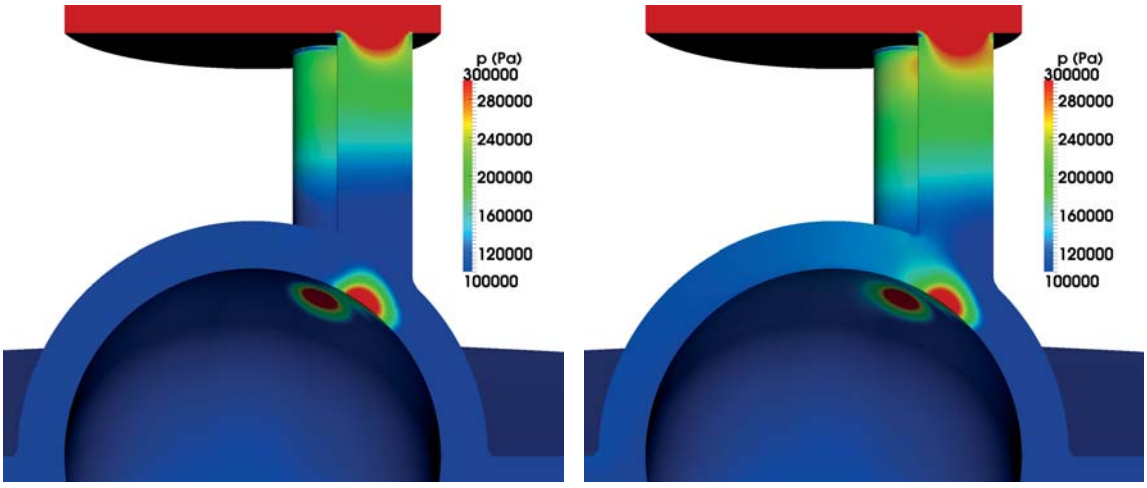

(i) $\dot{V} = 7\,\text{l}\,\text{min}^{-1}$, $f = 0\,\text{Hz}$ (ii) $\dot{V} = 7\,\text{l}\,\text{min}^{-1}$, $f = 400\,\text{Hz}$

Figure 6.19: Pressure distribution for two different rotation frequencies f at constant flow rate $\dot{V}$

Clearly, pressure for $f = 400\,\text{Hz}$ is higher inside the spherical gap both at the top of the sphere and on the left (-x-direction) which is made apparent by differences in F_x^{oil} and F_n^{oil} for constant $\dot{V}$. Rotation of the sphere causes surrounding fluid to be sucked into

the spherical gap on the left side. While this effect occurs regardless of the propulsion medium, the high viscosity of oil causes proportionally more fluid to be taken in, which consequently, due to the fluid being incompressible, leads to an immediate rise in pressure inside the gap both on the left and at the top. Hence, the effect is extremely noticeable for oil propulsion and negligible when using air. Also interesting to note is the fact that there is a visible difference in the pressure distribution at the very top of and inside the duct, i.e. the rotation of the sphere has a noteworthy effect on the flow upstream, effectively leading to a different pressure distribution inside the main parts of the tool.

6.4.3 Tangential forces

Tangential forces F_t^{oil} are plotted in Figure 6.20. Straight lines are fitted for each simulated constant $\dot{V}$. Close inspection of the data shows that the relation between F_t^{oil} and f are actually not linear, but slightly parabolic. This is made apparent by the fact that data points close to the intercepts and null points tend to lie below the fitted straight lines, and points in the mid field tend to lie above the fitted lines. In order to fit parabolae accurately, however, more data points, i.e. more simulations would be necessary. Since the deviation of the data points to the fitted lines is minor within the range discussed here ($F_t^{\text{oil}} > 0 \wedge f > 0$), straight lines provide an accurate enough representation of tangential force and are kept at this point.

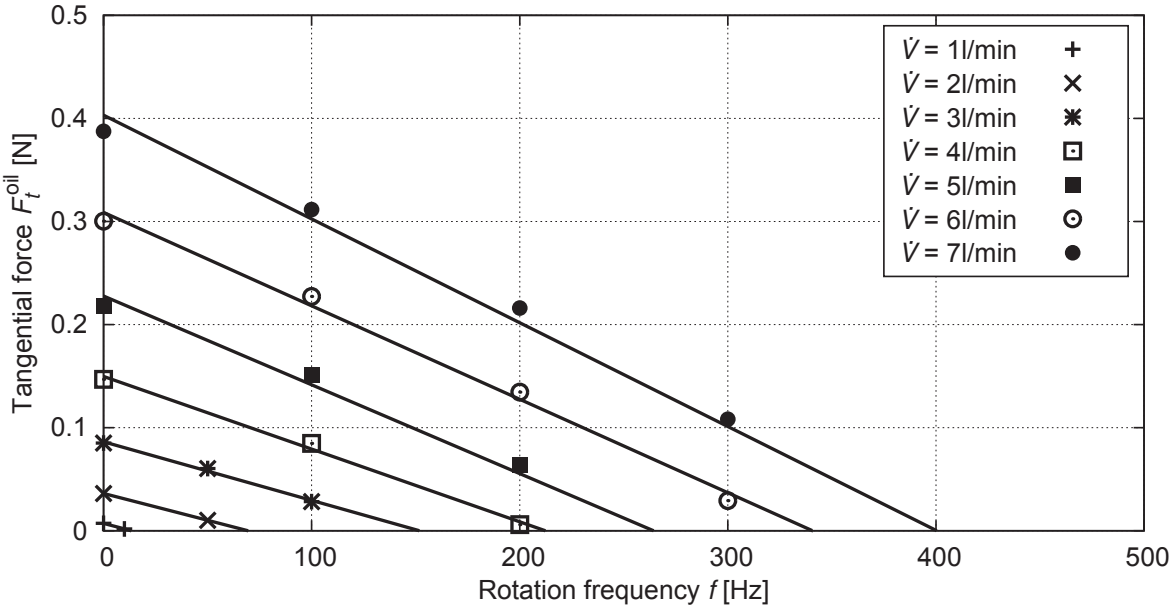

Figure 6.20: Tangential force F_t^{oil} over rotation frequency f with fitted regression lines for each volumetric flow rate $\dot{V}$ for 8 mm oil

Much in the same way as performed in Section 4.2.5 on tangential force for the 40 mm prototype, fitting the intercepts and null points of the straight lines portrayed in Figure 6.20

over volumetric flow rate yields the following equations for stationary force transfer $F_{t,0}^{\text{oil}}$ and idle rotation frequency f_0^{oil} (see Figure 6.21 for plots):

$$F_{t,0}^{\text{oil}} = \alpha_1^{\text{oil}} \dot{V}^{1.777} \tag{6.5}$$

$$f_0^{\text{oil}} = \alpha_2^{\text{oil}} \dot{V}^{1.270}. \tag{6.6}$$

The most notable difference to pneumatic propulsion at this point is that the exponent of $\dot{V}$ in eqn (6.6) is greater than 1, whereas it was less than one (0.875 to be exact) in eqn (4.21) for the idle rotation frequency in the case of the prototype. Taking a look at Figure 6.21 reveals that stationary force transfer has increased by a factor of 10 within examined flow rates compared to the prototype, despite the sphere having only one fifth the diameter. This fact demonstrates the positive effect of increasing both the number of ducts and the viscosity of the propulsion medium on tangential force transfer. Idle rotation frequencies are similar in magnitude for both oil and air. While higher frequencies are to be expected for a smaller sphere, oil propulsion requires lower flow speeds to avoid cavitation (Section 6.1.1).

Using eqn (4.23), the following relation governing tangential force is derived in the same way as was done in Chapter 4:

$$F_t^{\text{oil}} = (\alpha_3^{\text{oil}} \dot{V}^{1.777}) \left(\alpha_4^{\text{oil}} - \alpha_5^{\text{oil}} \dot{V}^{-1.270} f \right). \tag{6.7}$$

Figure 6.22 shows a plot of eqn (6.7). Tangential force of 0.1 N is achieved with approximately $f = 300\,\text{Hz}$ at the maximum flow rate of $\dot{V} = 7\,\text{l}\,\text{min}^{-1}$. Overall, tangential force has increased dramatically comparing to the pneumatic case while rotation frequencies have remained virtually identical (cp. Figure 4.23). This version of the tool with hydraulic propulsion and three ducts is capable of being used to conduct grinding trials and represents the first model of the *GrindBall* able to machine actual workpieces.

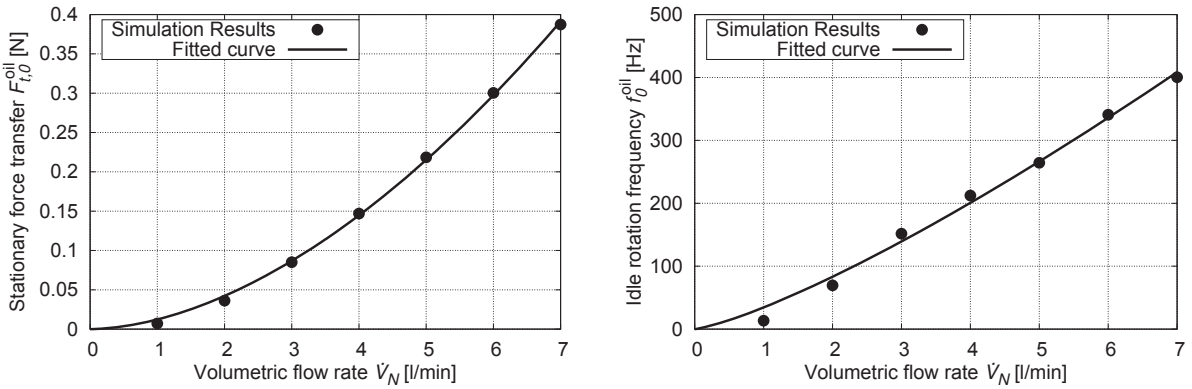

(i) Stationary force transfer $F_{t,0}^{\text{oil}}$

(ii) Idle rotation frequency f_0^{oil}

Figure 6.21: Stationary force transfer $F_{t,0}^{\text{oil}}$ and idle rotation frequency f_0^{oil} over volumetric flow rate $\dot{V}$ for 8 mm oil

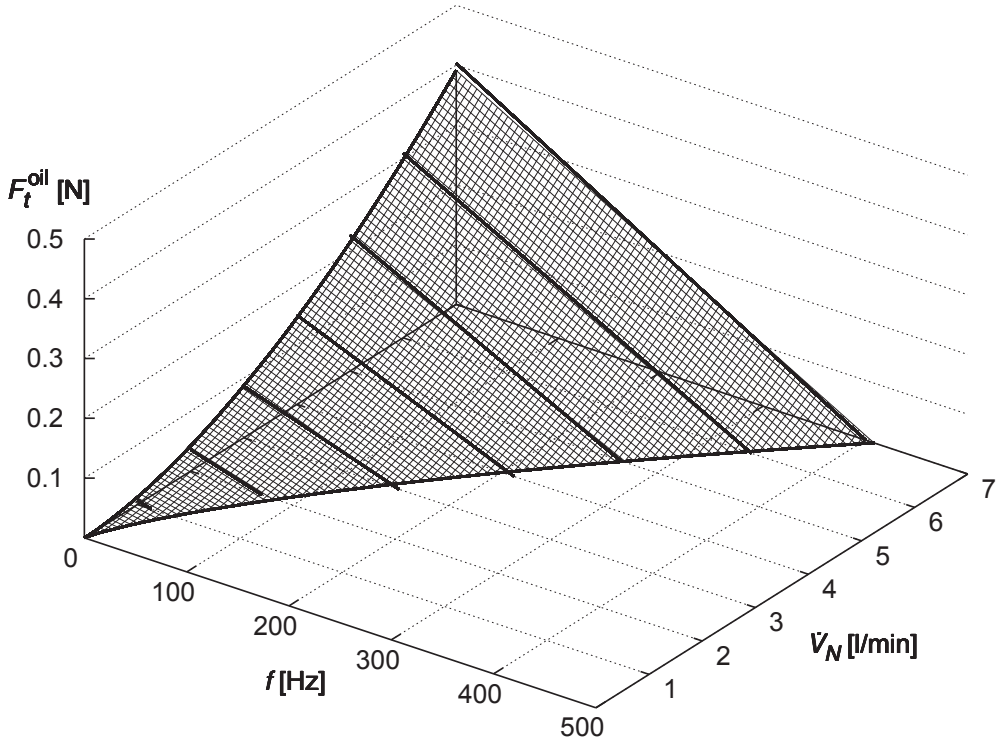

Figure 6.22: Tangential force F_t^{oil} depending on rotation frequency f and volumetric flow rate $\dot{V}$ for 8 mm oil

6.4.4 Grinding power

Grinding power is obtained by multiplying F_t^{oil} by $\dot{s} = 2\pi r f$ with $r = 0.004\,\text{m}$ (see Section 4.2.8 for details on how grinding power is derived). Each straight line from Figure 6.20 becomes parabolic as can be seen in Figure 6.23. Fitting a curve through the maxima of these parabolae results in

$$P_{G,\max}^{\text{oil}} = \alpha_6^{\text{oil}} f^{2.499}, \tag{6.8}$$

which needs to be made dependant on the volumetric flow rate $\dot{V}$.

Fitting the coefficients of each parabola in Figure 6.23 over the volumetric flow rate results in the following three-dimensional relation governing grinding power P_G^{oil} in terms of f and $\dot{V}$:

$$P_G^{\text{oil}} = \alpha_7^{\text{oil}} \dot{V}^{0.429} f^2 + \alpha_8^{\text{oil}} \dot{V}^{1.801} f. \tag{6.9}$$

Figure 6.24 shows a plot of eqn (6.9). Grinding power is roughly doubled compared to the pneumatic prototype. This makes sense considering that tangential force is increased ten-fold while the radius is reduced to one fifth, leaving a factor of 2.

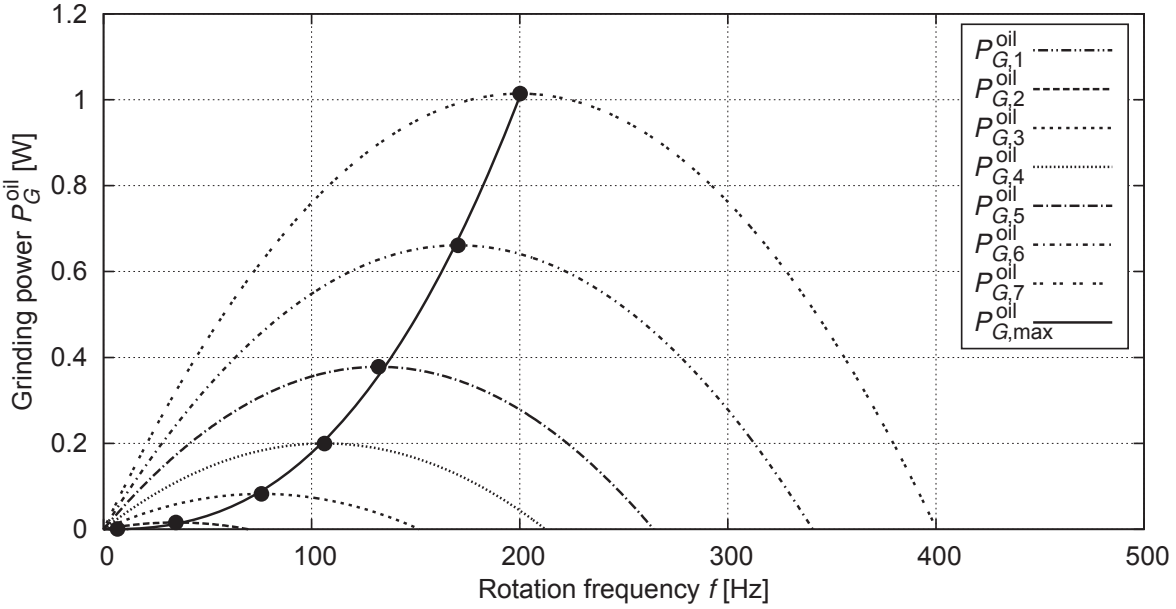

Figure 6.23: Grinding power P_G^{oil} and $P_{G,\max}^{\text{oil}}$ over rotation frequency f with fitted curves for each constant volumetric flow rate $\dot{V}$ for 8 mm oil

As was also done for the prototype, $P_{G,\max}^{\text{oil}}(\xi)$ is now given as a parametric curve in 3D space for $\xi \in [0, 7]$:

$$f(\xi) = \alpha_9^{\text{oil}} \xi^{1.270} \tag{6.10}$$

$$\dot{V}(\xi) = \alpha_{10}^{\text{oil}} \xi \tag{6.11}$$

$$P_{G,\max}^{\text{oil}}(\xi) = \alpha_{11}^{\text{oil}} \xi^{2.916} \tag{6.12}$$

leading to the operating point $\underline{\mathbf{P}}_{\text{op}}^{\text{oil}}(\xi)$, which parametrically describes $P_{\max}^{\text{oil}}(\xi)$ as a vector in 3D space:

$$\underline{\mathbf{P}}_{\text{op}}^{\text{oil}}(\xi) = \left(\alpha_9^{\text{oil}} \xi^{1.270}, \alpha_{10}^{\text{oil}} \xi, \alpha_{11}^{\text{oil}} \xi^{2.916}\right). \tag{6.13}$$

$\underline{\mathbf{P}}_{\text{op}}^{\text{oil}}(\xi)$ can be seen in Figure 6.24 along with P_G^{oil}.

Grinding power is now fully determined for the 8 mm *GrindBall* with oil propulsion. Using eqn (6.13) one can find the maximum power for each flow rate $\dot{V}$ along with a corresponding rotation frequency f. Overall, the improvements made in comparison with the prototype are very auspicious. In terms of design, the addition of two co-ducts improve tangential force transfer while vertical arrangement of the ducts provide sufficient contact force required to penetrate into workpieces. Similarly, the use of high-viscosity oil as a means of propulsion increases tangential and normal forces while also eliminating the problem of upward lift acting on the sphere. Normal forces described by eqns (6.3) and (6.4) provide a basis for designing and calibrating the electro-magnetic bearing. Furthermore, having fully quantified both grinding force and power with eqns (6.7) and (6.9), the tool is now ready for production and subsequent operation.

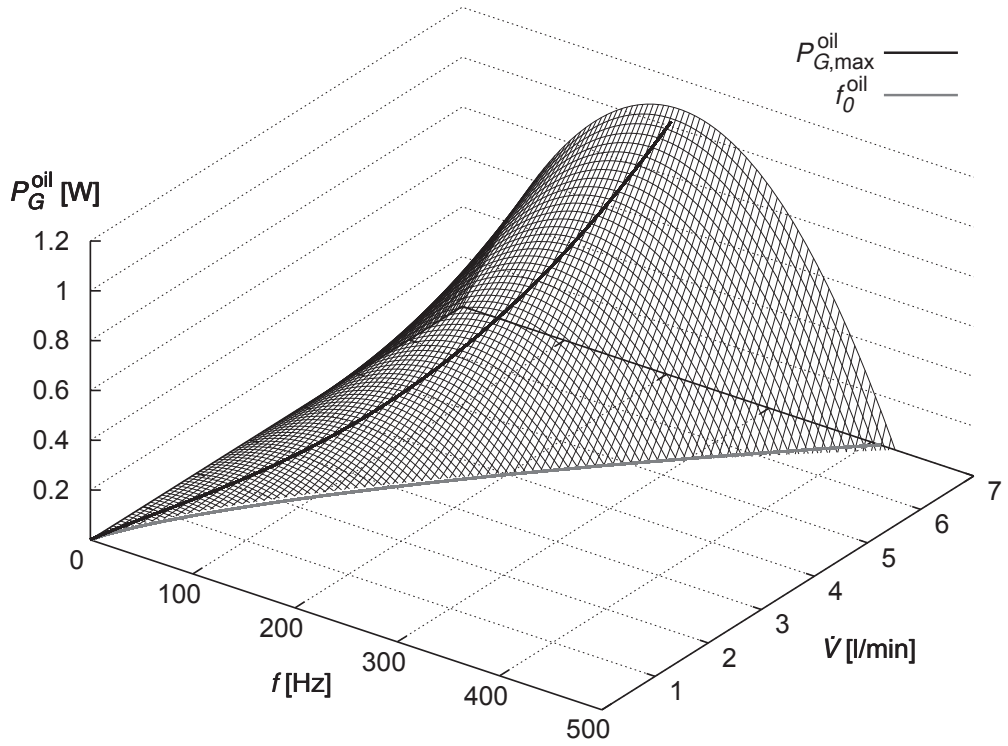

Figure 6.24: Grinding power P_G^{oil} depending on rotation frequency f and volumetric flow rate $\dot{V}$ for 8 mm oil

Chapter 7

Modelling force transfer across multiple scales

This chapter focuses on the process of force transfer for compressible turbulent flow in boundary layers of moving walls and investigates whether it can be made independent of the length scale. To this end, the vertical triple duct *GrindBall* geometry discussed in Chapter 6 is examined using three different spherical diameters: 40 mm, 8 mm, and 1 mm. Relations for normal forces, tangential force, stationary force transfer, idle rotation frequency, and grinding power are obtained. These are then made dimensionless and compared to each other across the three different scales. Finally, the results are compared to those found for the single duct geometry and for the triple duct setup using hydraulic propulsion.

7.1 Simulation Setup

The setup is identical to the ones used for previous compressible simulations. See Appendix D.6 for a complete overview of settings and boundary conditions.

Mesh

The mesh used is the *base 2* mesh described in Section 6.3.

Simulation timeline

Unlike for the prototype, the simulations are run on the ultimate mesh from the beginning. Instead of switching meshes to save computational cost, each flow rate is first run with a stationary sphere. Once complete, the final result is copied and the velocity boundary condition for the sphere adjusted upon which the simulation is continued for each desired rotation frequency. Computational cost is greatly reduced since the flow only needs to develop for a stationary sphere. Following cases start with an already fully developed

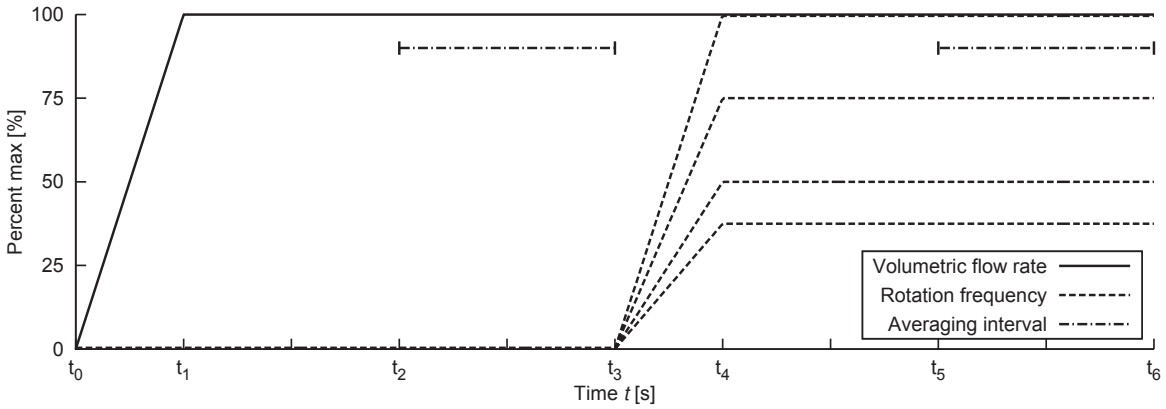

Figure 7.1: Timeline for simulations done for the *GrindBall* prototype

flow which only needs to adapt to the change in rotation frequency. Figure 7.1 gives an overview.

Table 7.1 shows the time intervals used for different length scales.

	t_0	t_1	t_2	t_3	t_4	t_5	t_6
40 mm sphere [s]	0	0.005	0.035	0.05	0.054	0.065	0.08
8 mm sphere [s]	0	0.0005	0.003	0.009	0.0095	0.01	0.016
1 mm sphere [s]	0	0.000015	0.0001	0.0003	0.000315	0.0004	0.0006

Table 7.1: Time details for simulations done across all length scales

Cases

Table 7.2 shows cases simulated for 40 mm, 8 mm, and 1 mm using pneumatic propulsion.

40 mm											
Flow rates [m^3h^{-1}]	9	18	27	36	45	54	63	72	81	90	99
Frequencies [Hz]	0 50	0 100	0 100	0 100 200	0 100 250	0 200 300	0 200 400	0 200 400	0 200 500	0 200 400 500	0 200 400 600
8 mm											
Flow rates [m^3h^{-1}]			0.5	1.0	1.5	2.0	2.5	3.0	3.5		
Frequencies [Hz]			0 400	0 500	0 500 1000	0 1000 1500	0 10 0 2000	0 1000 2000 2400	0 1000 2000 2500		

1 mm							
Flow rates [m^3h^{-1}]	0.01	0.02	0.03	0.04	0.05	0.06	0.07
Frequencies [Hz]	0	0	0	0	0	0	0
	2000	2000	5000	5000	5000	5000	5000
	4000	5000	10000	10000	10000	10000	10000
	5000	7500	15000	15000	15000	15000	15000
		10000		20000	20000	20000	20000
					30000	25000	25000
							30000

Table 7.2: Case configurations simulated for the triple duct geometry using pneumatic propulsion

Reynolds and Mach numbers

The Reynolds numbers for each flow rate for 40 mm, 8 mm, and 1 mm can be seen in Table 7.3. Re is defined as in Section 4.2.2, yet assuming that the volumetric flow rate is distributed evenly among the three ducts:

$$Re = \overline{U} h_d / \nu \tag{7.1}$$

with

$$\overline{U} = \dot{m} / 3 \rho_S A_d. \tag{7.2}$$

40 mm							
Flow rates [$m^3\,h^{-1}$]	9	18	27	36	45	54	
Re	$9.52{\cdot}10^3$	$1.91{\cdot}10^4$	$2.86{\cdot}10^4$	$3.81{\cdot}10^4$	$4.76{\cdot}10^4$	$5.72{\cdot}10^4$	
Flow rates [$m^3\,h^{-1}$]	63	72	81	90	99		
Re	$6.67{\cdot}10^4$	$7.62{\cdot}10^4$	$8.57{\cdot}10^4$	$9.53{\cdot}10^4$	$1.04{\cdot}10^5$		

8 mm							
Flow rates [$m^3\,h^{-1}$]	0.5	1.0	1.5	2.0	2.5	3.0	3.5
Re	2646	5293	7939	10586	13232	15879	18525

1 mm							
Flow rates [$m^3\,h^{-1}$]	0.01	0.02	0.03	0.04	0.05	0.06	0.07
Re	423	847	1270	1694	2117	2541	2964

Table 7.3: Reynolds numbers Re for each flow rate for 40 mm air

Turbulence ($Re > 5000$) is observed for all flow rates at 40 mm. The flow becomes transitional ($3000 < Re < 5000$) at 8 mm only for $\dot{V}_N = 0.5\,\mathrm{m^3\,h^{-1}}$ and remains turbulent at higher flow rates. 1 mm is entirely laminar ($Re < 3000$). Maximum Mach numbers for 40 mm, 8 mm, and 1 mm can be seen in Table 7.4. Flow rates for which the flow becomes super-sonic ($Ma > 1$) are not considered beyond this point.

High Reynolds numbers justify the use of an LES model for 40 mm and 8 mm. While the flow is mostly laminar for 1 mm, transitional flow is also observed for some cases and, hence, the LES model is used here as well. Employing the LES model on laminar flow does not distort the results as subgrid scale quantities simply tend to zero. Mach numbers ranging up to ∼1.0 justify performing compressible simulations for all three scales.

40 mm

Flow rates [$\mathrm{m^3\,h^{-1}}$]	9	18	27	36	45	54	63	72	81	90	99
0 Hz	0.09	0.17	0.28	0.36	0.47	0.56	0.67	0.74	0.86	0.97	1.05
50 Hz	0.09										
100 Hz		0.18	0.26	0.37	0.44						
200 Hz				0.36		0.57	0.63	0.73	0.84	0.92	1.05
250 Hz					0.48						
300 Hz						0.60					
400 Hz							0.68	0.76		0.94	1.13
500 Hz									0.84	0.98	
600 Hz											1.06

8 mm

Flow rates [$\mathrm{m^3\,h^{-1}}$]	0.5	1.0	1.5	2.0	2.5	3.0	3.5
0 Hz	0.38	0.26	0.38	0.48	0.62	0.75	0.88
400 Hz	0.26						
500 Hz		0.24	0.38				
1000 Hz			0.37	0.51	0.65	0.73	0.91
1500 Hz				0.50			
2000 Hz					0.66	0.75	0.94
2400 Hz						0.74	
2500 Hz							0.92

1 mm

Flow rates [$\mathrm{m^3\,h^{-1}}$]	0.01	0.02	0.03	0.04	0.05	0.06	0.07
0 Hz	0.30	0.28	0.43	0.58	0.79	0.86	0.99
2000 Hz	0.16	0.27					
4000 Hz	0.23						
5000 Hz	0.34	0.28	0.41	0.58		0.86	1.05

7500 Hz	0.28					
10000 Hz	0.28	0.43	0.58	0.75	0.87	1.11
15000 Hz		0.43	0.57	0.70	0.84	0.99
20000 Hz			0.57	0.73	0.88	1.01
25000 Hz					0.86	0.98
30000 Hz				0.74		1.10

Table 7.4: Maximum Mach Ma numbers for each case at 40 mm

7.2 Computational results

Results obtained on the vertical three-duct geometry using three different grinding sphere diameters (40 mm, 8 mm, and 1 mm) are discussed in this section and comparisons drawn to the pneumatic prototype in Chapter 4 and the hydraulic tool from Chapter 6. Dimensioned coefficients are again represented by $\alpha_n^{d\text{mm}}$ and $\beta_n^{d\text{mm}}$ where d is the diameter of the sphere and n is an enumerating integer. Their actual values can be seen in Table C.15, Table C.16, and Table C.17 in Appendix C.

7.2.1 Normal forces

Forces in x and z-direction for each case simulated are shown for individual diameters in Figure 7.3. The first thing to note is that there appears to be no clear dependence of force on rotation frequency at constant flow rate for any of the three diameters. While this was also the case for the prototype, hydraulic propulsion showed an obvious dependence. This strengthens the assumptions made in Section 6.4.2 that attribute this dependence to the fluid's incompressibility and high viscosity, since covering such a large spectrum of Reynolds numbers with air shows no apparent change in this matter. Independence of rotation frequency allows for normal forces to be averaged over f so that a single value is assigned to each $\dot{V}_N$ thereby making the analysis more straightforward.

Figure 7.4 shows mean normal forces plotted over flow rate for each individual diameter. Comparing $\overline{F}_x$ across the three scales shows similar behaviour throughout: the sphere is "pulled" in positive x-direction by the flow and this force increases with rising flow rate. This makes sense considering the upward lift that was observed for the prototype. Vertical arrangement of the ducts translates this effect into force in x-direction. The dependence of $\overline{F}_x$ on $\dot{V}_N$ is roughly quadratic for 40 mm and 8 mm (see eqns (7.3) and (7.4)) but bears an exponent of 2.473 for 1 mm (eqn (7.5)). There are distinct differences in magnitude between the three scales. Normal forces are dominated by pressure effects which are defined as force acting on a surface. Since the sphere's surface decreases according to r^2, it stands to reason that normal forces do the same. $\overline{F}_x$ decreases by a factor of approx. 25 from 40 mm to 8 mm, supporting the hypothesis. From 8 mm to 1 mm, however, it

decreases by a factor of approx. 80, possibly due to the absence of turbulence. Again the 1 mm case is slightly out of line.

Now looking at $\overline{F}_z$ across scales in Figure 7.4, rather inconsistent behaviour can be observed. For 40 mm and 8 mm there is still upward lift acting on the sphere, i.e. despite the flow being introduced vertically from the top, low pressure zones at the top of the spherical gap outweigh the downward force exerted by the flow's impact on to the sphere. This phenomenon can be seen in Figure 7.2, as can the 1 mm case in which the sphere is in fact pushed downward. At 1 mm the Reynolds numbers are so low that the flow cannot generate enough lift on the sphere, however, Figure 7.4.vi clearly shows a turning point at $\dot{V}_N \approx 0.055\,\mathrm{m}^3/\mathrm{h}$, corresponding to $Re \approx 2300$ beyond which lift forces begin to become apparent and start to counter downward force. Magnitudes of $\overline{F}_z$ decrease by a factor of approx. 30 going from 40 mm to 8 mm, and by a factor of around 64 going from 8 mm to 1 mm. While the former, much like for $\overline{F}_x$, is roughly in keeping with a decrease according to r^2, the latter is dead on, albeit acting in the opposing direction. $\overline{F}_z$ shows an approximately quadratic dependence on $\dot{V}_N$ for 40 mm and 8 mm in eqns (7.6) and (7.7) respectively. For 1 mm, however, $\overline{F}_z$ obeys a cubic function of flow rate. The relation in eqn (7.8) provides the best match to the 1 mm data in the given range considering that a minimum and a turning point is required to provide an adequate fit.

$$\overline{F}_x^{40\mathrm{mm}} = \beta_1^{40\mathrm{mm}} \dot{V}_N^{2.053} \tag{7.3}$$
$$\overline{F}_x^{8\mathrm{mm}} = \beta_1^{8\mathrm{mm}} \dot{V}_N^{2.038} \tag{7.4}$$
$$\overline{F}_x^{1\mathrm{mm}} = \beta_1^{1\mathrm{mm}} \dot{V}_N^{2.473} \tag{7.5}$$
$$\overline{F}_z^{40\mathrm{mm}} = \beta_2^{40\mathrm{mm}} \dot{V}_N^{2.078} \tag{7.6}$$
$$\overline{F}_z^{8\mathrm{mm}} = \beta_2^{8\mathrm{mm}} \dot{V}_N^{2.216} \tag{7.7}$$
$$\overline{F}_z^{1\mathrm{mm}} = \beta_2^{1\mathrm{mm}} \dot{V}_N^{3} + \beta_3^{1\mathrm{mm}} \dot{V}_N^{2} + \beta_4^{1\mathrm{mm}} \dot{V}_N. \tag{7.8}$$

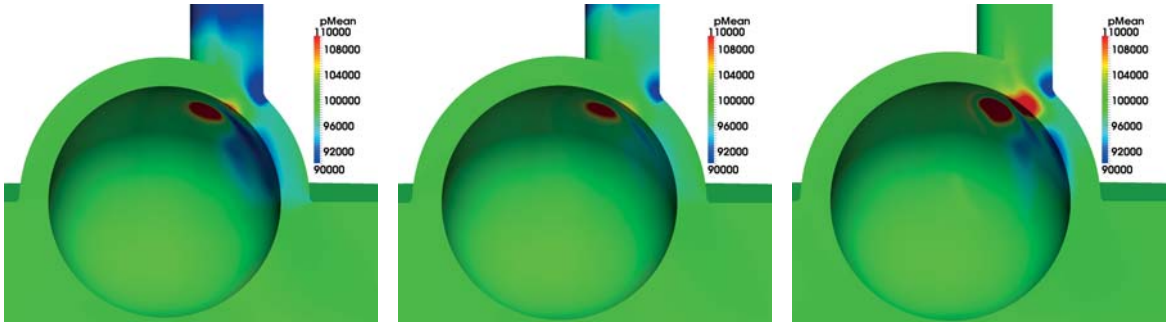

(i) 40 mm spherical diameter, $\dot{V}_N = 90\,\mathrm{m}^3/\mathrm{h}$, $f = 500\,\mathrm{Hz}$

(ii) 8 mm spherical diameter, $\dot{V}_N = 3\,\mathrm{m}^3/\mathrm{h}$, $f = 2400\,\mathrm{Hz}$

(iii) 1 mm spherical diameter, $\dot{V}_N = 0.06\,\mathrm{m}^3/\mathrm{h}$, $f = 25000\,\mathrm{Hz}$

Figure 7.2: Mean pressure distribution inside the spherical gap across three scales

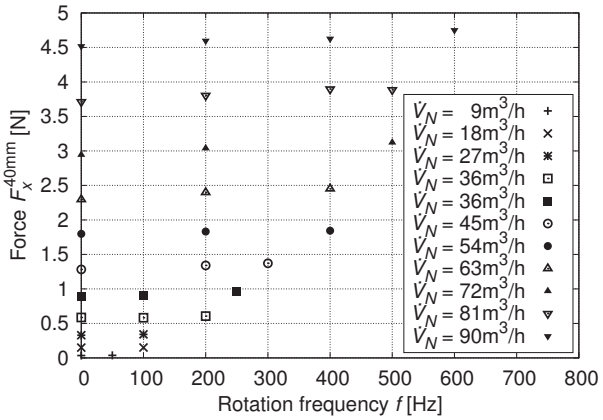

(i) Force exerted in x-direction $F_x^{40\text{mm}}$

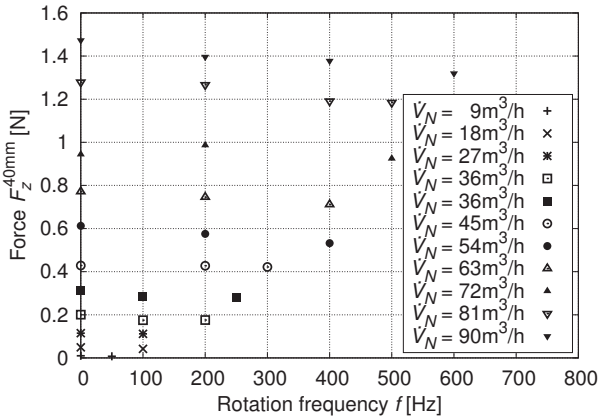

(ii) Force exerted in z-direction $F_z^{40\text{mm}}$

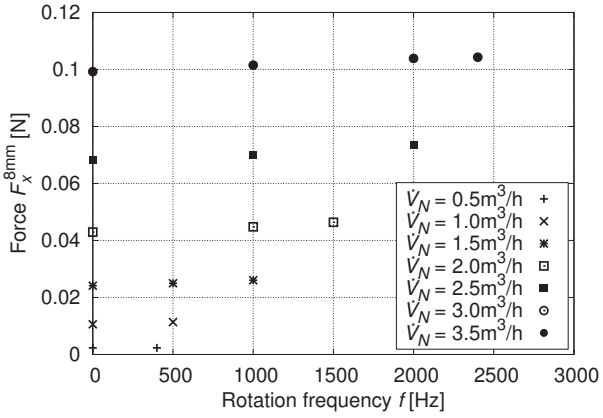

(iii) Force exerted in x-direction $F_x^{8\text{mm}}$

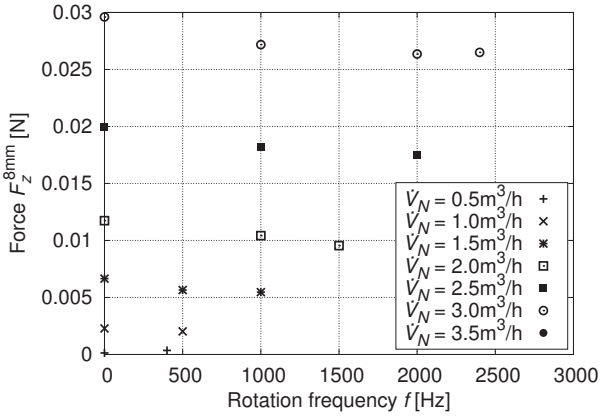

(iv) Force exerted in z-direction $F_z^{8\text{mm}}$

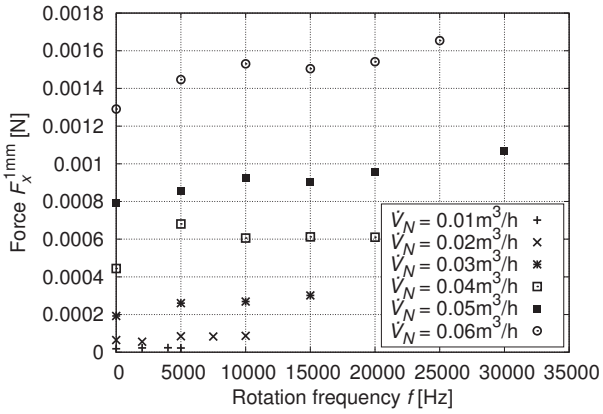

(v) Force exerted in x-direction $F_x^{1\text{mm}}$

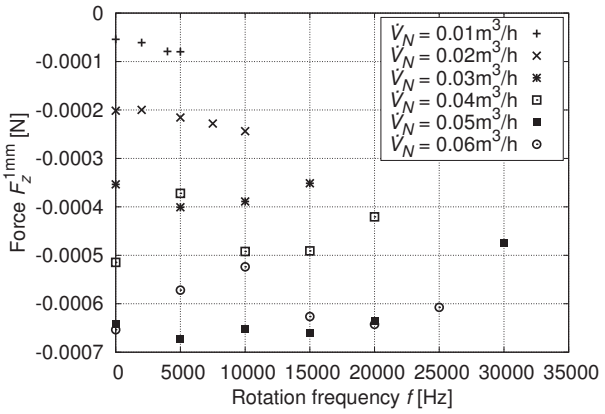

(vi) Force exerted in z-direction $F_z^{1\text{mm}}$

Figure 7.3: Forces F_x and F_z for all simulations conducted for 40 mm, 8 mm, and 1 mm

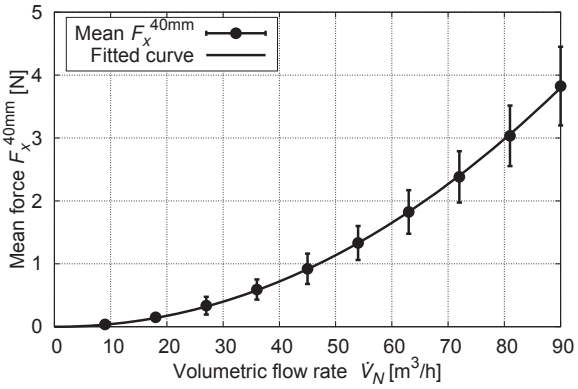

(i) Mean force $\overline{F}_x^{40\mathrm{mm}}$

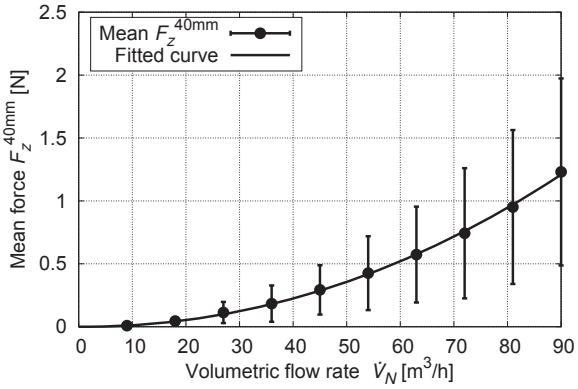

(ii) Mean force $\overline{F}_z^{40\mathrm{mm}}$

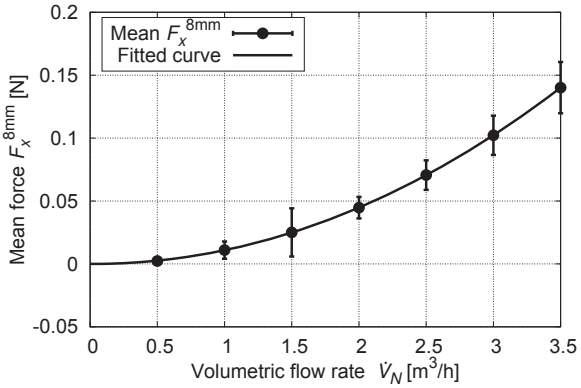

(iii) Mean force $\overline{F}_x^{8\mathrm{mm}}$

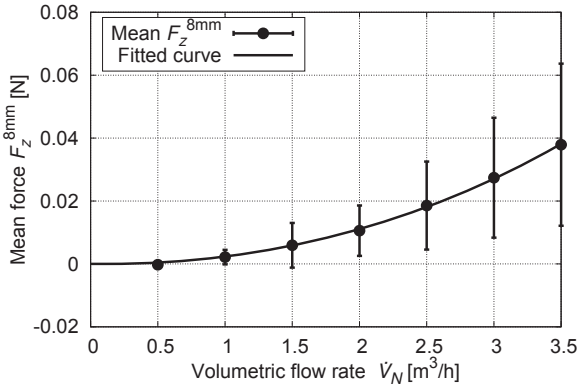

(iv) Mean force $\overline{F}_z^{8\mathrm{mm}}$

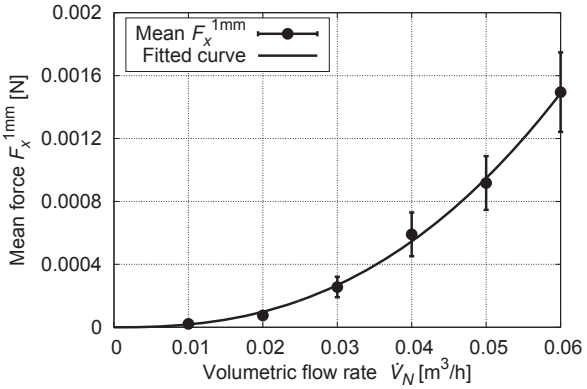

(v) Mean force $\overline{F}_x^{1\mathrm{mm}}$

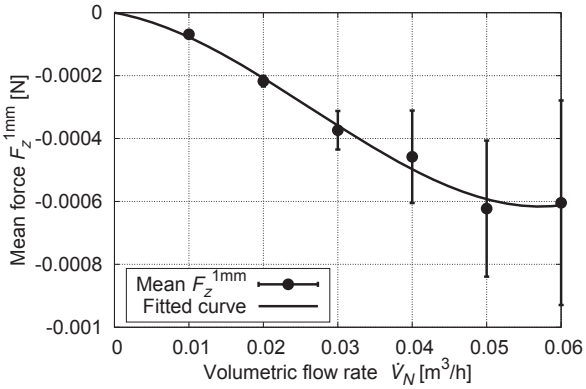

(vi) Mean force $\overline{F}_z^{1\mathrm{mm}}$

Figure 7.4: Mean forces $\overline{F}_x$ and $\overline{F}_z$ averaged over rotation frequency f for 40 mm, 8 mm, and 1 mm

7.2.2 Tangential force

Tangential forces are analysed and compared across three scales in this section. Stationary force transfer and idle rotation frequencies are then extrapolated and discussed. Finally, three-dimensional relations governing tangential force in terms of flow rate and rotation frequency are established.

Figure 7.5 shows the simulation results for tangential force $F_t^{40\text{mm}}$ with a fitted regression line for each flow rate. $F_t^{40\text{mm}}$ displays a linear dependence on rotation frequency for constant flow rates as is the case for the *GrindBall* prototype in Section 4. Extrapolated from the intercepts and null points are the stationary force transfer $F_{t,0}^{40\text{mm}}$ and the idle rotation frequency $f_0^{40\text{mm}}$ depicted in Figure 7.8.i and Figure 7.8.ii respectively. Stationary force transfer is nearly tripled in magnitude compared to the prototype. A gain is to be expected because of the increase in duct diameter and the addition of two supplementary ducts, both of which cause a higher flow rate and thereby raise the potential amount of momentum available for transfer on to the sphere. Vertical alignment of the ducts causes no loss in tangential force transfer due to the fact that the flow's point of impact lies more than 45° above the end of the spherical gap (cp. Section 4.2.6). Rotation frequencies are only increased by a factor of about 1.5 compared to the prototype, i.e. tangential forces are subject to diminishing returns when increasing the rotation frequency using the vertical three-duct model.

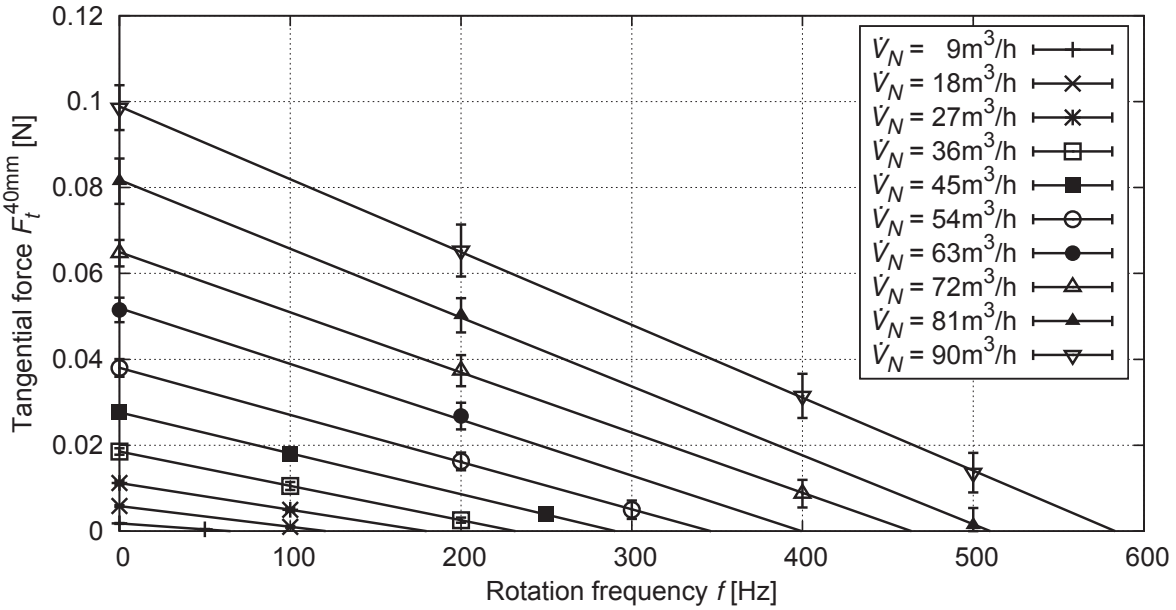

Figure 7.5: Tangential force $F_t^{40\text{mm}}$ over rotation frequency f with fitted regression lines for each standard volumetric flow rate $\dot{V}_N$ for 40 mm air

Tangential force $F_t^{8\text{mm}}$ again displays a linear dependence on rotation frequency for constant flow rates at 8 mm. Figure 7.6 shows the simulation results with a fitted regression

line for each flow rate. Close inspection reveals that a linear fit is no longer accurate at 8 mm. Looking at individual flow rates, the linear fit lies slightly above simulation results both near the horizontal and the vertical axis, whereas it lies slightly below simulation results within the middle range. Thus, a parabolic fit seems more appropriate, however, there are not enough data points to accurately fit parabolae. Furthermore, the deviation between the linear fit and the data is so minute that it provides an accurate result despite being of lower order. The results for hydraulic propulsion in Section 6.4.3 also show a somewhat parabolic behaviour at 8 mm. Stationary force transfer for 8 mm shown in Figure 7.8.iii drops in magnitude by a factor of approx. 18 compared to $F_{t,0}^{40\text{mm}}$. This factor lies between a quadratic drop (25) and a linear drop (5) and can be attributed to the way in which force is transferred on to the sphere: the majority of force is transferred at the spot at which the flow impacts on to the sphere and this spot's area decreases according to r^2. Force is also transferred, however, between the point of impact and the exit of the spherical gap as discussed in Section 4.2.6. This length decreases linearly according to r. Hence, approximately 65% of force transfer takes places at the point of impact, while the remaining 35% occur thereafter. This implies that since the area used to grind workpieces on the bottom of the sphere decreases quadratically - as does the amount of required tangential force - the tool becomes more efficient the smaller its grinding sphere. Idle rotation frequency, on the other hand, increases by a factor of 5 (Figure 7.8.iv). This is because the speed of the flow is kept constant across scales and rotation frequency of the sphere must increase linearly in order to maintain the same surface velocity. This also means that the diminishing returns observed for 40 mm compared to the prototype are maintained at smaller scales.

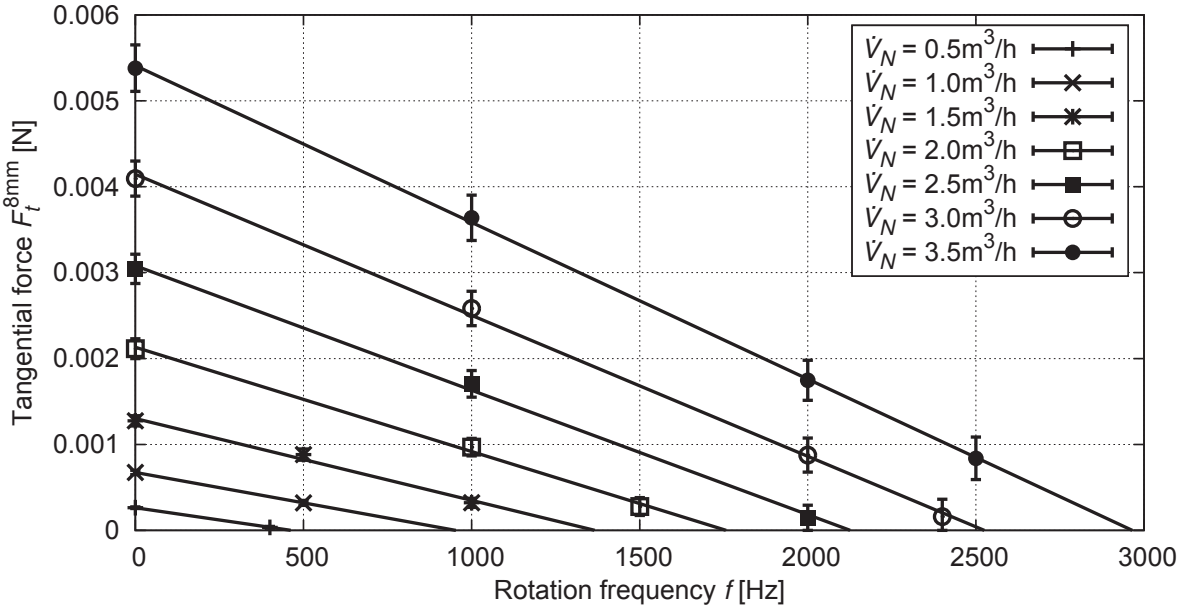

Figure 7.6: Tangential force $F_t^{8\text{mm}}$ over rotation frequency f with fitted regression lines for each standard volumetric flow rate $\dot{V}_N$ for 8 mm air

The results for tangential force $F_t^{1\text{mm}}$ in Figure 7.7 show strong parabolic behaviour. For this reason more simulations are performed per flow rate in order to be able to accurately fit parabolae to the data. Considering also tangential forces for 8 mm above and for the hydraulic propelled tool in Section 6.4.3, it would appear that smaller scales promote parabolic behaviour independent of fluid properties and the Reynolds number. Stationary force transfer $F_{t,0}^{1\text{mm}}$ depicted in Figure 7.8.v drops by a factor of approx. 22 from 8 mm down to 1 mm. This implies that tangential force transfer for laminar flow is dominated by linear effects, i.e. momentum transfer along the gap dominates over momentum transfer at the flow's point of impact. Furthermore, the tool becomes even more efficient at this very small 1 mm scale. Idle rotation frequency $f_0^{1\text{mm}}$ shown in Figure 7.8.vi increases by a factor of around 9.5, implying that there are slightly less diminishing returns resulting from spherical rotation at this scale.

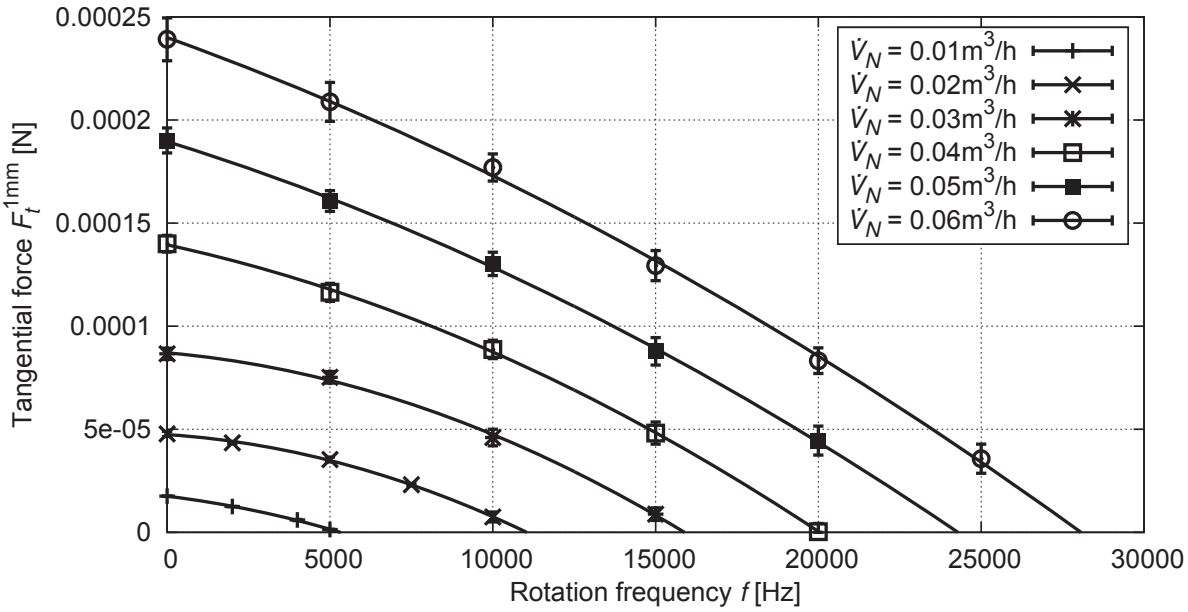

Figure 7.7: Tangential force $F_t^{1\text{mm}}$ over rotation frequency f with fitted regression curves for each standard volumetric flow rate $\dot{V}_N$ for 1 mm air

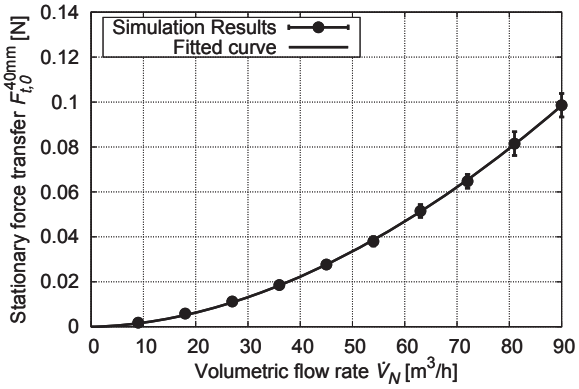

(i) Stationary force transfer $F_{t,0}^{40\mathrm{mm}}$

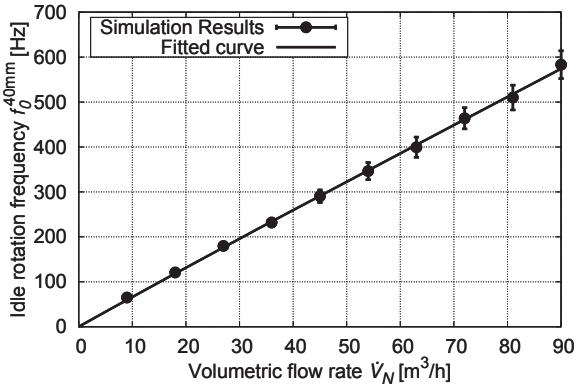

(ii) Idle rotation frequency $f_0^{40\mathrm{mm}}$

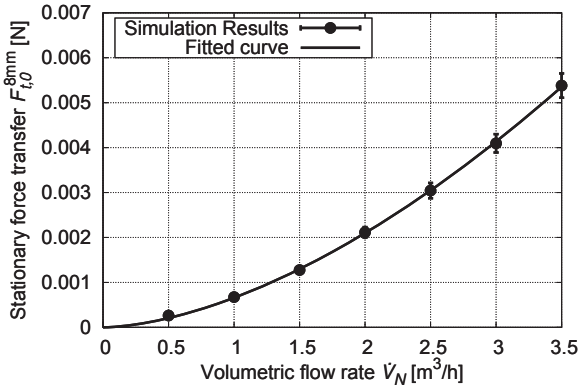

(iii) Stationary force transfer $F_{t,0}^{8\mathrm{mm}}$

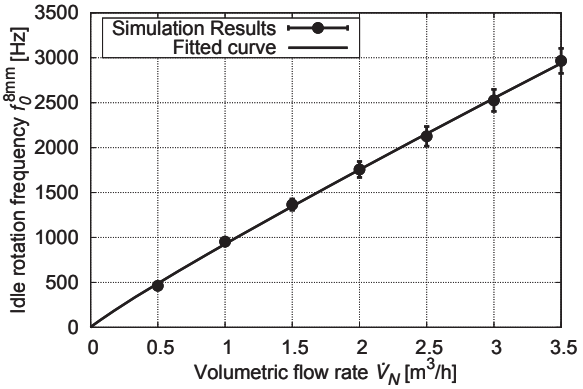

(iv) Idle rotation frequency $f_0^{8\mathrm{mm}}$

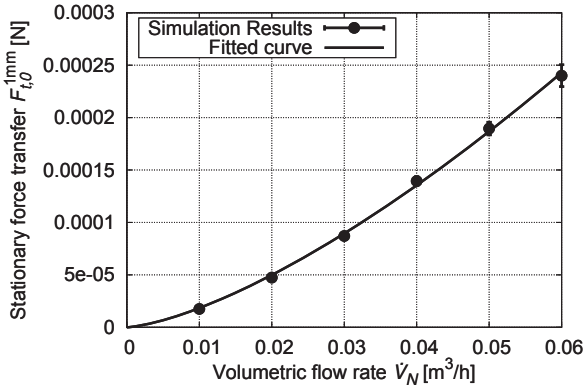

(v) Stationary force transfer $F_{t,0}^{1\mathrm{mm}}$

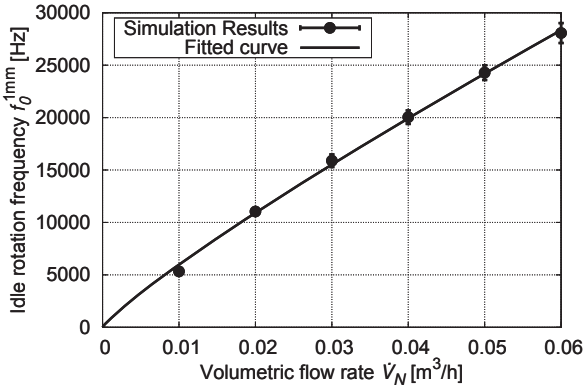

(vi) Idle rotation frequency $f_0^{1\mathrm{mm}}$

Figure 7.8: Stationary force transfer $F_{t,0}^{40\mathrm{mm}}$ and idle rotation frequency $f_0^{40\mathrm{mm}}$ over volumetric flow rate $\dot{V}_N$ for 40 mm, 8 mm, and 1 mm

Eqns (7.9) through (7.11) state the relations between stationary force transfer $F_{t,0}$ and volumetric flow rate $\dot{V}_N$ across the three scales. The exponent of $\dot{V}_N$ starts at 1.833 for 40 mm and decreases with scale: 1.673 for 8 mm and 1.441 for 1 mm, i.e. the dependence of $F_{t,0}$ on $\dot{V}_N$ moves away from a quadratic relation towards a linear one with decreasing scale. Eqns (7.12) through (7.14) give the relations between idle rotation frequency f_0 and volumetric flow rate $\dot{V}_N$ across the three scales. Here, the relation starts off almost linear with an exponent 0.985 for $\dot{V}_N$ and continues to decrease with scale: 0.921 for 8 mm and 0.869 for 1 mm.

$$F_{t,0}^{40\text{mm}} = \alpha_1^{40\text{mm}} \dot{V}_N^{1.833} \tag{7.9}$$
$$F_{t,0}^{8\text{mm}} = \alpha_1^{8\text{mm}} \dot{V}_N^{1.673} \tag{7.10}$$
$$F_{t,0}^{1\text{mm}} = \alpha_1^{1\text{mm}} \dot{V}_N^{1.441} \tag{7.11}$$
$$f_0^{40\text{mm}} = \alpha_2^{40\text{mm}} \dot{V}_N^{0.985} \tag{7.12}$$
$$f_0^{8\text{mm}} = \alpha_2^{8\text{mm}} \dot{V}_N^{0.921} \tag{7.13}$$
$$f_0^{1\text{mm}} = \alpha_2^{1\text{mm}} \dot{V}_N^{0.869} \tag{7.14}$$

Obtaining a three-dimensional relation governing tangential forces in terms of flow rates and rotation frequencies is done in the same way as for the prototype and the hydraulic 8 mm tool according to

$$F_t = F_{t,0} \left(1 - \frac{f}{f_0}\right) \tag{4.23}$$

for 40 mm and 8 mm since tangential forces are linearly dependent on rotation frequencies at constant flow rates. For 1 mm, however, tangential force can not be obtained using eqn (4.23) because $F_t^{1\text{mm}}$ depends on f parabolically. Instead, the coefficients of the parabolae governing tangential force over rotation frequency must be made dependent on the flow rate by fitting a curve in a similar fashion as was previously done for grinding power. The result is that each parabola of the form

$$F_{t,n} = a_n \left(b_n + f\right)^2 + c_n, \tag{7.15}$$

where n represents a specific volumetric flow rate, is combined into a 3D equation of the form

$$F_t = a(\dot{V}_N) \left(b(\dot{V}_N) + f\right)^2 + c(\dot{V}_N). \tag{7.16}$$

Tangential forces for 40 mm, 8 mm, and 1 mm are thus given by the following relations:

$$F_t^{40\text{mm}} = (\alpha_3^{40\text{mm}} \dot{V}_N^{1.833})(\alpha_4^{40\text{mm}} - \alpha_5^{40\text{mm}} f \dot{V}_N^{-0.985}) \tag{7.17}$$
$$F_t^{8\text{mm}} = (\alpha_3^{8\text{mm}} \dot{V}_N^{1.673})(\alpha_4^{8\text{mm}} - \alpha_5^{8\text{mm}} f \dot{V}_N^{-0.921}) \tag{7.18}$$
$$F_t^{1\text{mm}} = (\alpha_3^{1\text{mm}} \dot{V}_N^{1.829} + \alpha_4^{1\text{mm}}) f^2 + (\alpha_5^{1\text{mm}} \dot{V}_N^{1.369}) f + \alpha_6^{1\text{mm}} \dot{V}_N^{1.441}, \tag{7.19}$$

which are plotted in Figure 7.9, Figure 7.10, and Figure 7.11 respectively. These equations fully describe tangential forces for all three simulated scales and a more detailed analysis of tangential force behaviour is performed in Section 7.3.2

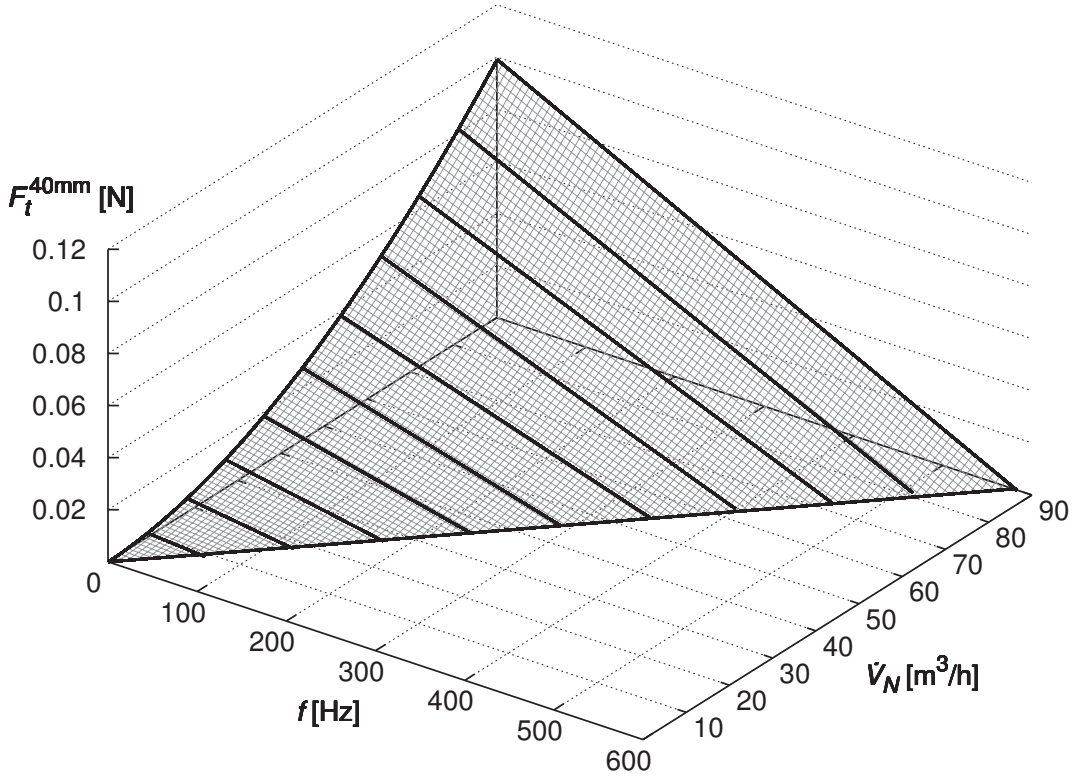

Figure 7.9: Tangential force $F_t^{40\mathrm{mm}}$ for a 40 mm pneumatic sphere

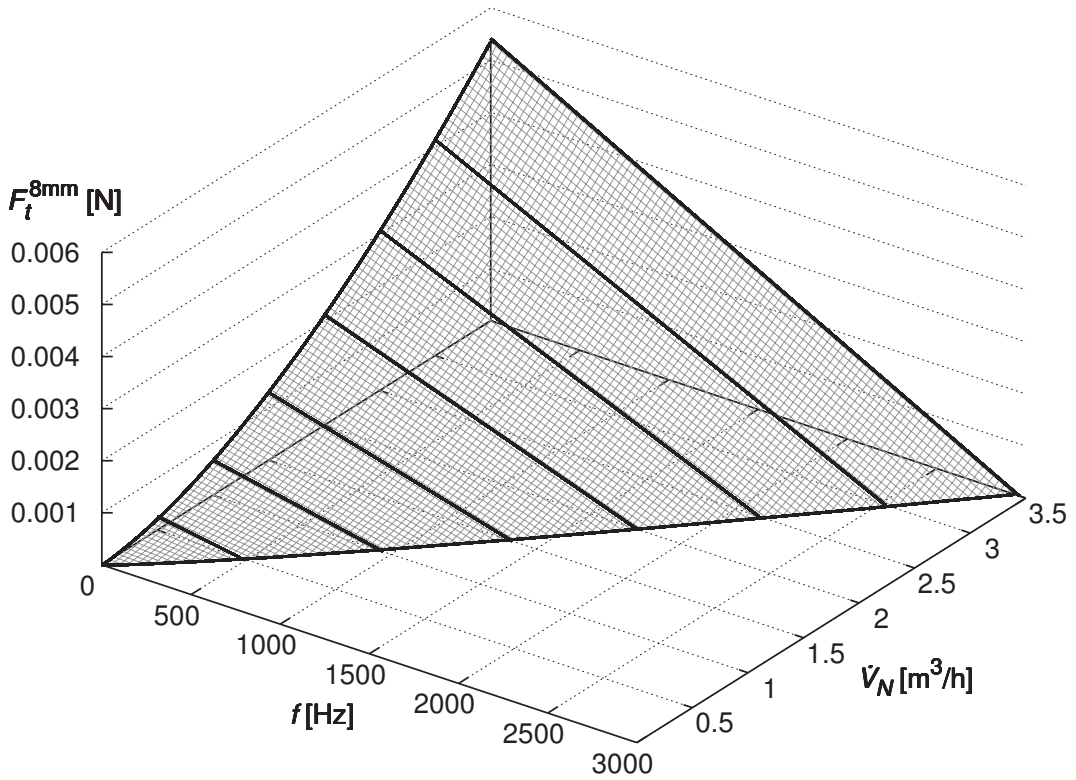

Figure 7.10: Tangential force $F_t^{8\mathrm{mm}}$ for an 8 mm pneumatic sphere

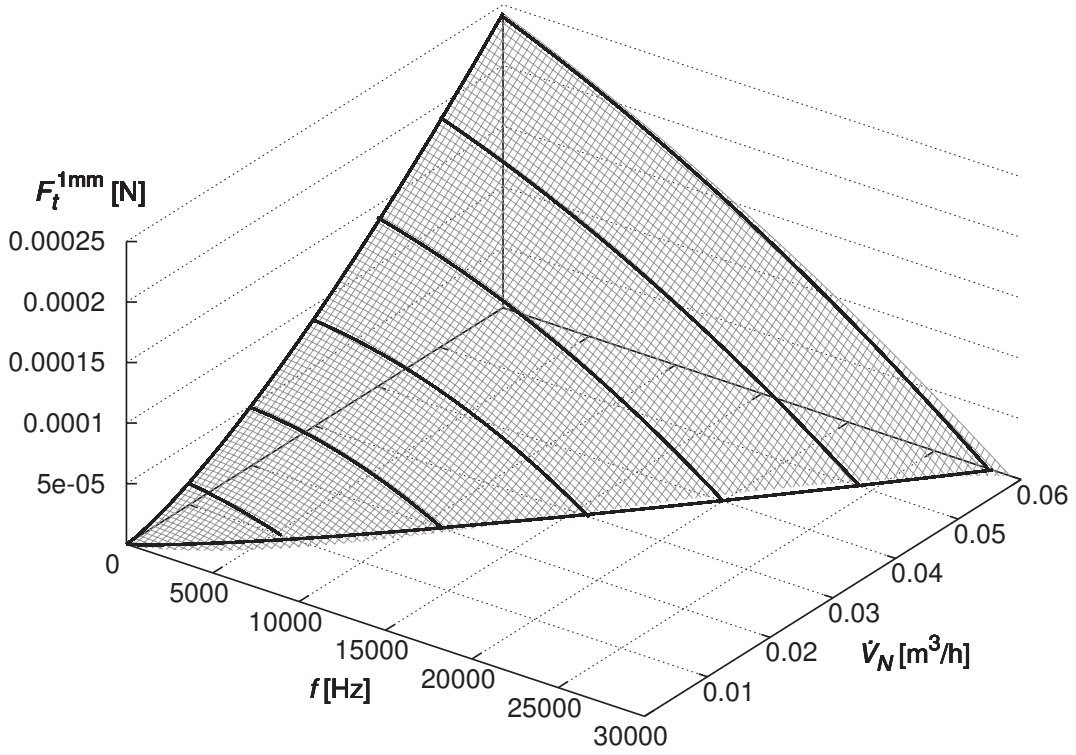

Figure 7.11: Tangential force $F_t^{1\text{mm}}$ for a 1 mm pneumatic sphere

7.2.3 Grinding power

Grinding power is now extrapolated from tangential force as described in Section 4.2.8. For 40 mm and 8 mm the procedure is the same as in previous cases. In a similar way, grinding power for 1 mm is obtained by multiplying each parabola for $F_{t,n}^{1\text{mm}}$ by $s = 2\pi r f$ with $r = 0.0005$ m resulting in cubic equations. These cubics each have a single maximum within the considered domain between $f = 0$ and $f = f_0$, and hence serve the purpose of this analysis just as well. The results for 40 mm, 8 mm, and 1 mm are illustrated in Figure 7.12, Figure 7.13, and Figure 7.14 respectively, along with curves fitted through the maxima of the parabolae, which obey the following relations:

$$P_{G,\max}^{40\text{mm}} = \alpha_6^{40\text{mm}} f^{2.782} \tag{7.20}$$

$$P_{G,\max}^{8\text{mm}} = \alpha_6^{8\text{mm}} f^{2.751} \tag{7.21}$$

$$P_{G,\max}^{1\text{mm}} = \alpha_7^{1\text{mm}} f^{2.662}. \tag{7.22}$$

The exponents of f in eqns (7.20) through (7.22) are very similar to each other bearing only a slight decrease with scale. Comparing the magnitude of $P_{G,\max}^{40\text{mm}}$ with the prototype, grinding power increases by a factor of around 4.5. Note that tangential force only increases by a factor less than 3, indicating that the slight increase in rotation frequency toward the prototype has a positive effect on grinding power. $P_{G,\max}$ drops by a factor of ~ 18 going from 40 mm to 8 mm. This is not surprising considering that $\dot{s} = 2\pi r f$ is

unaffected by scale as r decreases by a factor of 5 and f increases by roughly the same amount, while tangential force is reduced by a factor of approx. 18 (see the previous section). Going from 8 mm to 1 mm, $P_{G,\max}$ drops by a factor of around 16, although rotation frequency increases by a factor slightly bigger than the radius of the sphere decreases, while stationary tangential force decreases by a factor of ~ 22. The reason for this is that the parabolic shape of $F_t^{1\text{mm}}$ causes the maxima of $P_{G,\max}^{1\text{mm}}$ to be shifted toward the right due to larger rotation frequencies. Much like tangential force, grinding power's decrease with scale moves away from quadratic effects and more towards linear ones as the tool gets smaller. This again affirms, that the tool becomes more and more efficient through miniaturisation.

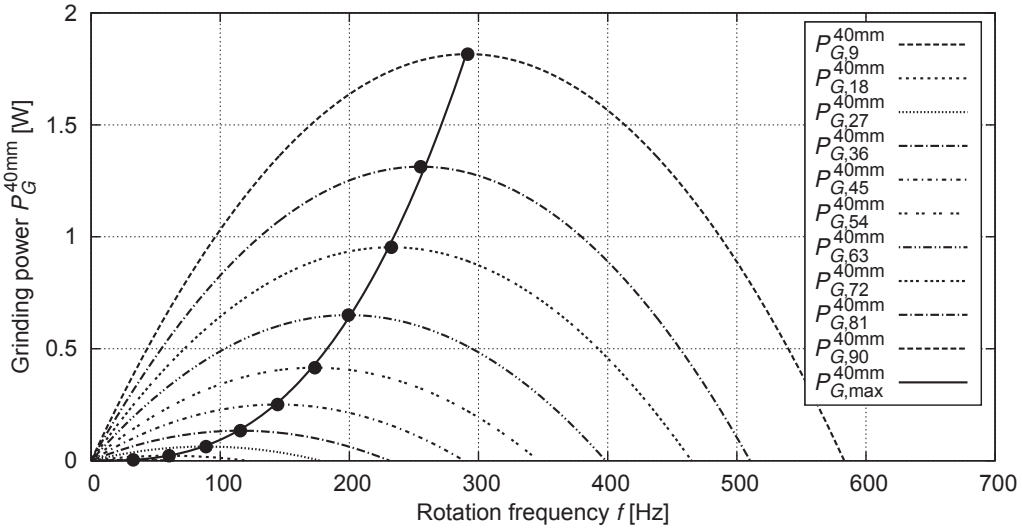

Figure 7.12: Grinding power $P_G^{40\text{mm}}$ and $P_{G,\max}^{40\text{mm}}$ for a 40 mm pneumatic sphere

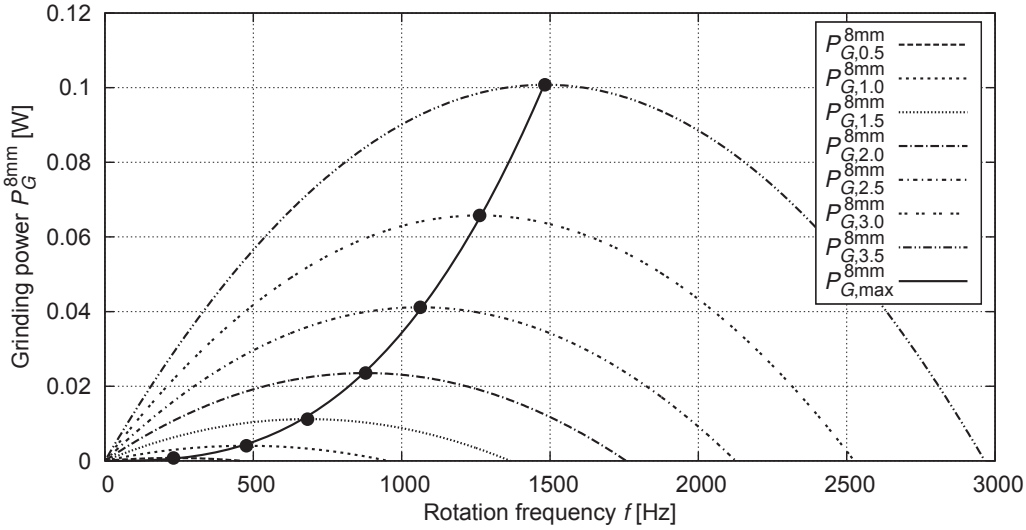

Figure 7.13: Grinding power $P_G^{8\text{mm}}$ and $P_{G,\max}^{8\text{mm}}$ for an 8 mm pneumatic sphere

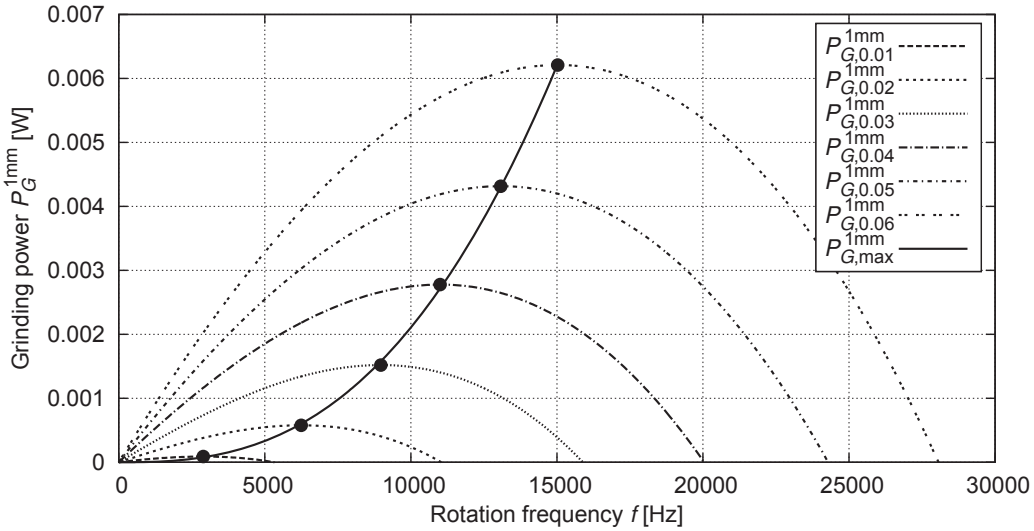

Figure 7.14: Grinding power $P_G^{1\text{mm}}$ and $P_{G,\max}^{1\text{mm}}$ for a 1 mm pneumatic sphere

Now to introduce the dependence of grinding power on volumetric flow rate. Again, the procedure for 40 mm and 8 mm are the same as for the prototype and the hydraulic tool. With tangential force being parabolic for 1 mm, however, grinding power at this scale is no longer of the form presented in eqn (4.31), but obeys a third order polynomial in f:

$$P_G^{1\text{mm}} = a(\dot{V}_N)f^3 + b(\dot{V}_N)f^2 + c(\dot{V}_N)f, \tag{7.23}$$

where the coefficients a, b, and c of the cubics presented in Figure 7.14 are fitted over volumetric flow rate in order to introduce the additional dependence on $\dot{V}_N$. The resulting three-dimensional relations governing grinding power over rotation frequency and flow rate for all three scales are thus given by:

$$P_G^{40\text{mm}} = \alpha_7^{40\text{mm}}\dot{V}_N^{0.815}f^2 + \alpha_8^{40\text{mm}}\dot{V}_N^{1.833}f \tag{7.24}$$

$$P_G^{8\text{mm}} = \alpha_7^{8\text{mm}}\dot{V}_N^{0.696}f^2 + \alpha_8^{8\text{mm}}\dot{V}_N^{1.664}f \tag{7.25}$$

$$P_G^{1\text{mm}} = (\alpha_8^{1\text{mm}}\dot{V}_N^{1.813} + \alpha_9^{1\text{mm}})f^3 + \alpha_{10}^{1\text{mm}}\dot{V}_N^{1.588}f^2 + \alpha_{11}^{1\text{mm}}\dot{V}_N^{1.441}f. \tag{7.26}$$

Finally, the additional variable $\dot{V}_N$ is also introduced into $P_{G,\max}$. For 40 mm, $P_{G,\max}^{40\text{mm}}$ is given as a parametric curve in three-dimensional space using the parameter $\zeta \in [0, 90]$:

$$f(\zeta) = \alpha_9^{40\text{mm}}\zeta^{0.985} \tag{7.27}$$

$$\dot{V}_N(\zeta) = \alpha_{10}^{40\text{mm}}\zeta \tag{7.28}$$

$$P_{G,\max}^{40\text{mm}}(\zeta) = \alpha_{11}^{40\text{mm}}\zeta^{2.872}. \tag{7.29}$$

For 8 mm, $P_{G,\max}^{8\text{mm}}$ is given parametrically for $\eta \in [0, 3.5]$:

$$f(\eta) = \alpha_9^{8\text{mm}}\eta^{0.921} \tag{7.30}$$

$$\dot{V}_N(\eta) = \alpha_{10}^{8\text{mm}}\eta \tag{7.31}$$

$$P_{G,\max}^{8\text{mm}}(\eta) = \alpha_{11}^{8\text{mm}}\eta^{2.634}. \tag{7.32}$$

For 1 mm, $P^{1\mathrm{mm}}_{G,\max}$ is given parametrically for $\xi \in [0, 0.06]$:

$$f(\xi) = \alpha^{1\mathrm{mm}}_{12}\xi^{0.827} \tag{7.33}$$
$$\dot{V}_N(\xi) = \alpha^{1\mathrm{mm}}_{13}\xi \tag{7.34}$$
$$P^{1\mathrm{mm}}_{G,\max}(\xi) = \alpha^{1\mathrm{mm}}_{14}\xi^{2.043}. \tag{7.35}$$

Eqns (7.27) through (7.35) determine the operating point $\underline{\mathbf{P}}_{\mathrm{op}}$ for each scale, describing $P_{G,\max}$ as vectors in 3D space:

$$\underline{\mathbf{P}}^{40\mathrm{mm}}_{\mathrm{op}}(\zeta) = \left(\alpha^{40\mathrm{mm}}_{9}\zeta^{0.985}, \alpha^{40\mathrm{mm}}_{10}\zeta, \alpha^{40\mathrm{mm}}_{11}\zeta^{2.872}\right) \tag{7.36}$$
$$\underline{\mathbf{P}}^{8\mathrm{mm}}_{\mathrm{op}}(\eta) = \left(\alpha^{8\mathrm{mm}}_{9}\eta^{0.921}, \alpha^{8\mathrm{mm}}_{10}\eta, \alpha^{8\mathrm{mm}}_{11}\eta^{2.634}\right) \tag{7.37}$$
$$\underline{\mathbf{P}}^{1\mathrm{mm}}_{\mathrm{op}}(\xi) = \left(\alpha^{1\mathrm{mm}}_{12}\xi^{0.827}, \alpha^{1\mathrm{mm}}_{13}\xi, \alpha^{1\mathrm{mm}}_{14}\xi^{2.043}\right). \tag{7.38}$$

Eqns (7.24) through (7.26) governing grinding power are plotted in Figure 7.15, Figure 7.16, and Figure 7.17 respectively, along with $\underline{\mathbf{P}}_{\mathrm{op}}$ for each case given in eqns (7.36) through (7.38).

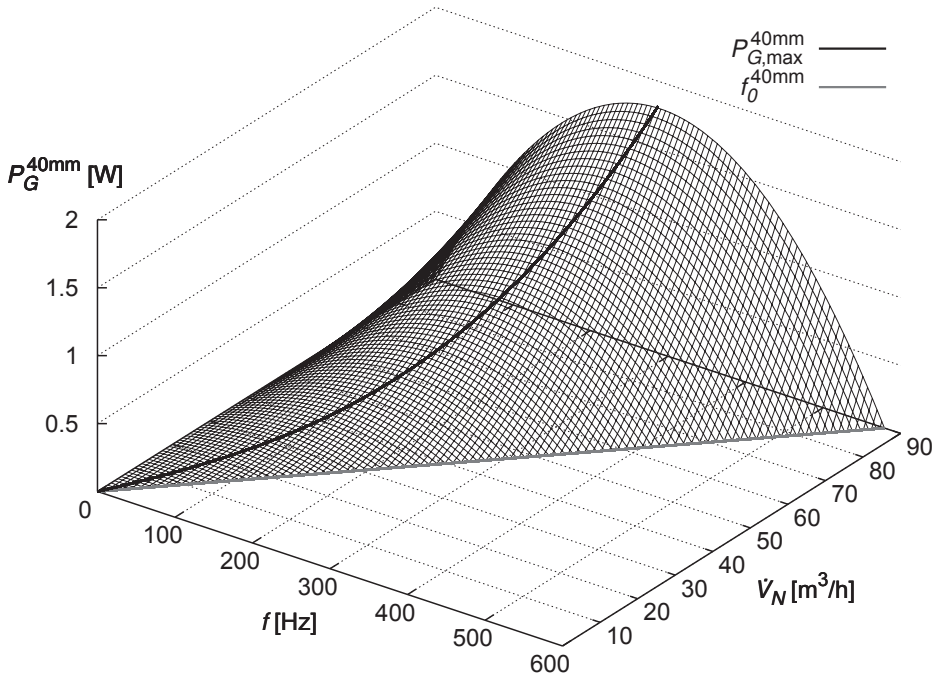

Figure 7.15: Grinding power $P^{40\mathrm{mm}}_{G}$ for a 40 mm pneumatic sphere

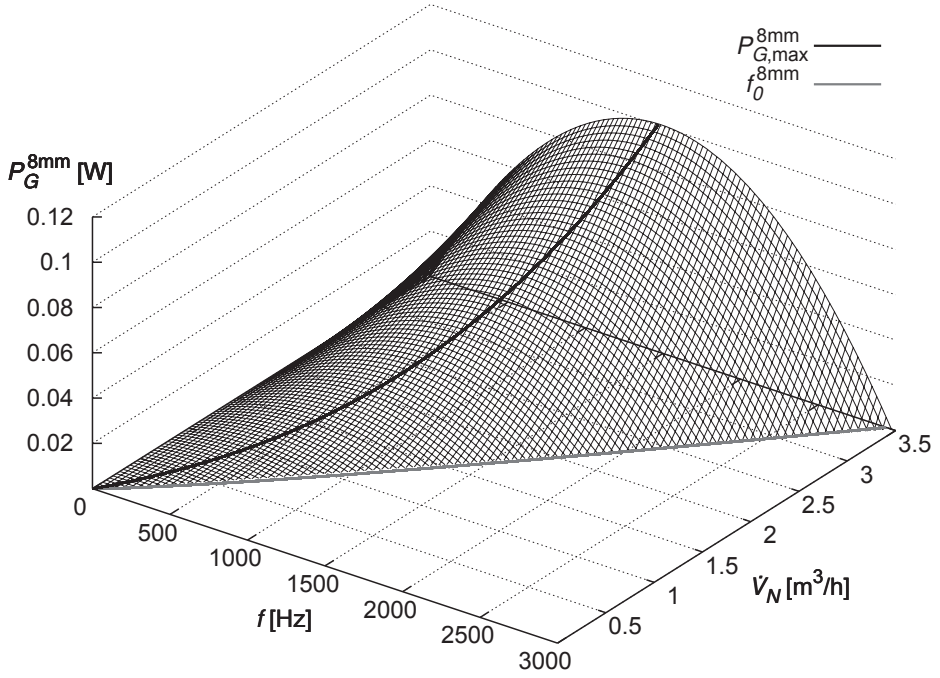

Figure 7.16: Grinding power $P_G^{40\mathrm{mm}}$ for an 8 mm pneumatic sphere

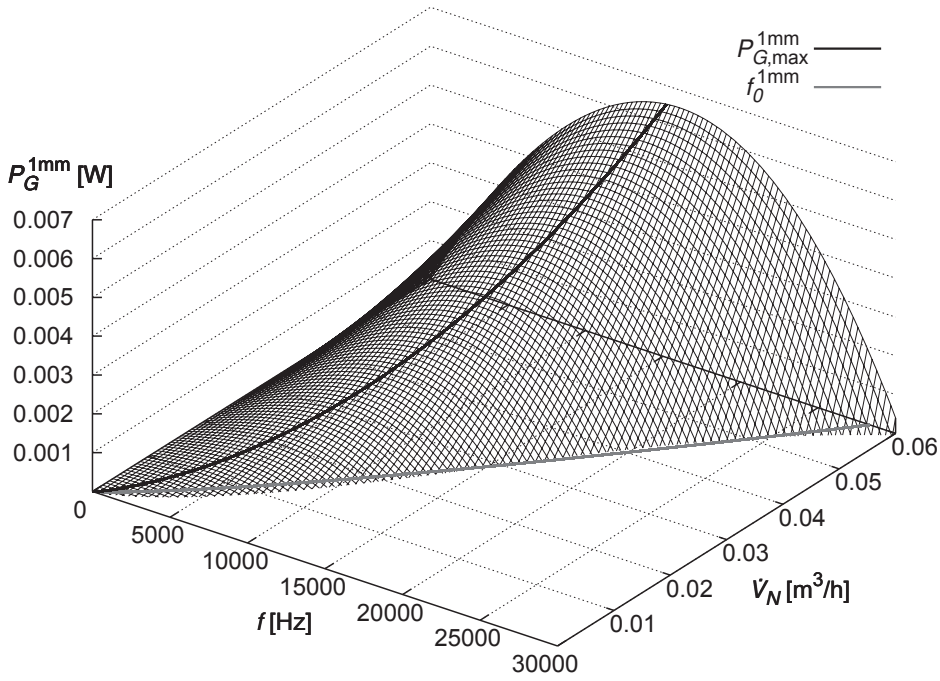

Figure 7.17: Grinding power $P_G^{40\mathrm{mm}}$ for a 1 mm pneumatic sphere

Unlike the dependence of $P_{G,\max}$ on f in 2D, which was barely influenced by decreasing the scale, the dependence on $\dot{V}_N$ (i.e. on the parameter) does display a notable decrease with scale. While it starts off with an almost cubic relation in eqn (7.29) at 40 mm, the exponent is only 2.634 in eqn (7.32) at 8 mm, and becomes quadratic in eqn (7.35) at 1 mm. This implies that increasing returns from rising flow rates are amplified at higher Reynolds numbers, i.e. larger turbulent effects. While this effect negatively influences miniaturisation, overall the sheer magnitude of grinding power profits greatly by decreasing the size of the tool.

Having fully described tangential forces and grinding power across three scales covering turbulent, transitional, and laminar flow, the next section deals with making these results independent of scale and aims at providing a better suited basis for comparison.

7.3 Non-dimensional analysis

In the previous section, results are presented for three different scales which cover laminar, transitional, and fully turbulent flow. While the results do seem very similar regarding the resulting relations, an appropriate comparison requires non-dimensionalisation in order to measure properties across various scales and be able to reach conclusions about arbitrary scales without having to conduct new sets of simulations. Non-dimensionalisation is performed using the radius of the sphere r, the standard kinematic viscosity of air $\nu_N = 1.33 \cdot 10^{-5}\,\mathrm{m^2\,s^{-1}}$, and the standard density of air $\rho_N = 1.293\,\mathrm{kg\,m^{-3}}$. The resulting dimensionless variables are:

$$P^D = \frac{P}{\nu_N^3 \rho_N r^{-1}} \tag{7.39}$$

$$F^D = \frac{F}{\nu_N^2 \rho_N} \tag{7.40}$$

$$f^D = \frac{f}{\nu_N r^{-2}} \tag{7.41}$$

$$\dot{V}_N^D = \frac{\dot{V}_N}{\nu_N r}, \tag{7.42}$$

where the exponent D denotes a dimensionless quantity. Furthermore, $Re \propto \dot{V}_N^D$, i.e. the Reynolds number is proportional to the dimensionless flow rate:

$$Re = \frac{10\nu_N\rho_N}{3\pi\nu_S\rho_S}\dot{V}_N^D = \frac{3.1846\overline{1}}{\pi}\dot{V}_N^D. \tag{7.43}$$

Noting the similarity between the numerator and denominator of the coefficient, it can be said that

$$Re \approx \dot{V}_N^D. \tag{7.44}$$

Using these new variables, simulation results obtained on different scales may now be compared to each other without bias resulting from different geometric proportions. Furthermore, four additional simulations are conducted for a 400 mm sphere with $\dot{V}_N = 7200\,\mathrm{m}^3/\mathrm{h}$ and rotation frequencies $f = 0$, 20, 30, and 50 Hz to provide reference values at a larger scale which are used to test the validity of the relations derived using the data from the three smaller spherical diameters.

7.3.1 Normal forces

Dimensionless mean force acting on the grinding sphere in x-direction $\overline{F}_x^D$ can be seen in Figure 7.18.

Figure 7.18.i shows varying behaviour between data sets for Reynolds numbers below and above 5000. A function governing the full range of Reynolds numbers is thus defined in a piecewise manner and is not continuously differentiable:

$$\overline{F}_x^D = \begin{cases} 1{,}029{,}470\,(\exp(4.152 \cdot 10^{-6} Re^{1.681}) - 1) & \text{for } Re < 5000 \\ 1.052 Re^{2.051} & \text{for } Re \geq 5000. \end{cases} \tag{7.45}$$

Note that the data point for 400 mm is not included in the fitting process and is used merely to check whether the fitted curves still provide a good estimate at larger scales. This is clearly the case for F_x^D. To make eqn (7.45) continuously differentiable, a sigmoid function (see Appendix A.6 for details)

$$\sigma_{F_x}(Re) = \frac{1}{1 + \exp(-(Re - 2775.5)/200)} \tag{7.46}$$

is used to smoothly combine the two sub-functions with $Re_0 = 2775.5$, the point at which

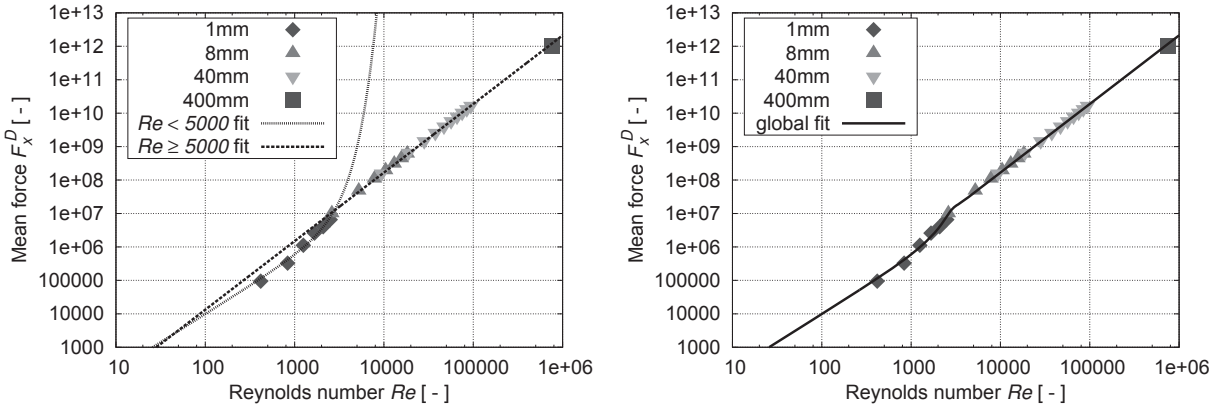

(i) Mean force $\overline{F}_x^D$ with individual fits

(ii) Mean force $\overline{F}_x^D$ with single global fit

Figure 7.18: Mean force in x-direction $\overline{F}_x^D$ over Reynolds number Re (log-log)

both sub-functions intersect. The result is plotted in Figure 7.18.ii and obeys the function

$$\begin{aligned} \overline{F}_x^D &= 1{,}029{,}470\left(\exp(4.152\cdot 10^{-6}Re^{1.681})-1\right)\left(1-\sigma_{F_x}(Re)\right) \\ &\quad + 1.052Re^{2.051}\,\sigma_{F_x}(Re). \end{aligned} \tag{7.47}$$

$\overline{F}_z^D$, the dimensionless mean force acting in z-direction, is plotted in Figure 7.19.i for $Re < 10^5$. Recalling that $F_z^{1\text{mm}}$ is negative, only the horizontal axis is presented in the logarithmic scale. A quadratic polynomial is chosen to fit the data in order to incorporate negative values for low Reynolds numbers by making use of its parabolic shape, yielding

$$\overline{F}_z^D = 0.618Re^2 - 2095.751Re. \tag{7.48}$$

Figure 7.19.ii shows a log-log representation incorporating only larger scales. Not only does eqn (7.48) fit the data very well for all scales, it also agrees very well with the 400 mm reference value.

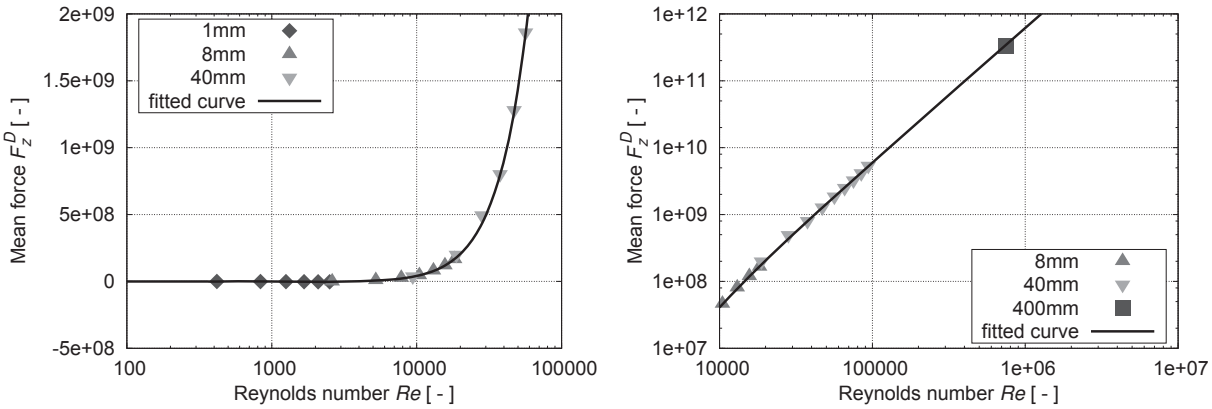

(i) Mean force $\overline{F}_z^D$ (log Re)

(ii) Mean force $\overline{F}_z^D$ (log-log)

Figure 7.19: Mean force in z-direction $\overline{F}_z^D$ over Reynolds number Re

Normal forces are now quantified across a variety of scales and can subsequently be calculated for arbitrary scales without the need for additional simulations.

7.3.2 Tangential forces

Figure 7.20 shows the tangential forces for all the simulated scales plotted in one graph. Despite non-dimensionalisation, there is still large variation among scales and it is difficult to illustrate all data points simultaneously. Using a log-log scale would also be problematic because the behaviour on and near the axes cannot be depicted.

Instead, non-dimensional stationary force transfer $F_{t,0}^D$ and idle rotation frequency f_0^D are considered separately. Figure 7.21 shows both variables with curves fitted to each

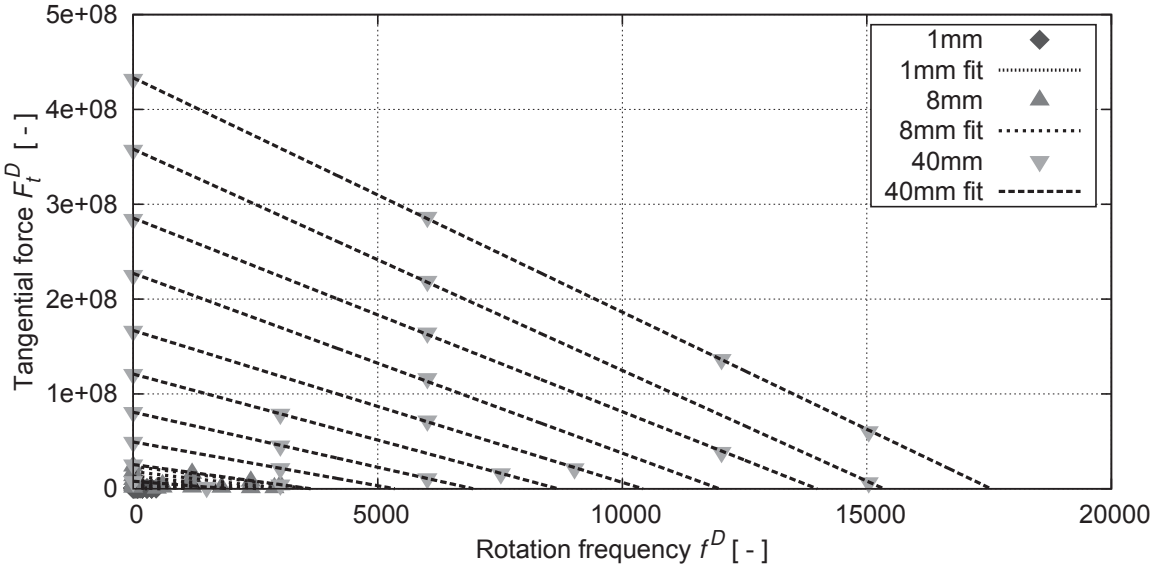

Figure 7.20: Tangential force F_t^D over rotation frequency f^D with fitted regression curves for constant Reynolds numbers Re

individual scale. Regarding $F_{t,0}^D$, the three fitted curves obviously do not agree well with each other. Use of the log-log scale portrays these curves as straight lines and there are easily visible discrepancies between their "slopes". Hence, a global fit encompassing all scales is unlikely to be of the form aRe^b, but rather obeys an exponential function. Furthermore, the question arises whether an exponential fit can be used across all scales, or if it is merely useful for either laminar or turbulent flow. Idle rotation frequency f_0^D shows slightly better agreement among the individually fitted curves. Differences between the three fitted curves are smaller, yet they still do not allow for a global fit.

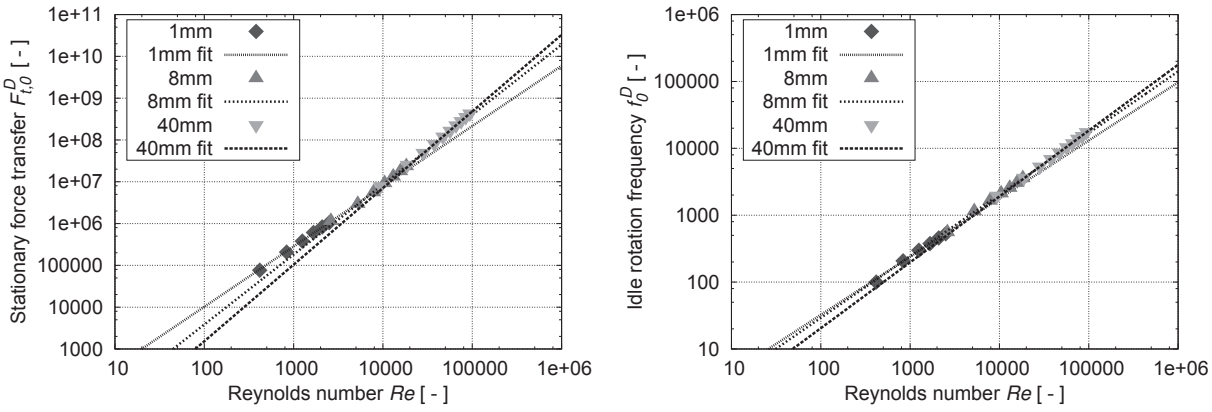

(i) Stationary force transfer $F_{t,0}^D$

(ii) Idle rotation frequency f_0^D

Figure 7.21: Stationary force transfer $F_{t,0}^D$ and idle rotation frequency f_0^D over Reynolds number Re (log-log) with individual fits per scale

Figure 7.22.i illustrates $F_{t,0}^D$ wherein it is fitted with an exponential for $Re < 10^5$ and a regular curve for $Re \geq 10^4$ - again excluding the large 400 mm scale. Close examination of the two fitted curves shows that while the exponential fits the simulated data very well for $Re < 10^5$, the larger 400 mm scale lies almost exactly on the curve fitted only to $Re \geq 10^4$. Hence, $F_{t,0}^D$ shows exponential behaviour only until a certain Reynolds number upon which it follows a regular curve, giving

$$F_{t,0}^D = \begin{cases} 1.323 \cdot 10^{-4} \left(\exp(13.653 Re^{0.065}) - 1\right) & \text{for } Re < 10^5 \\ 0.354 Re^{1.827} & \text{for } Re \geq 10^4. \end{cases} \tag{7.49}$$

Obviously, the overlap in the domain between $10^4 \leq Re < 10^5$ is not ideal. To make the function unambiguously defined and continuously differentiable, a sigmoid function is once again employed. Equating the two sub-functions shows that they intersect at $Re_0 = 42{,}772$. Hence, using a sigmoid with $Re_0 = 42{,}772$, i.e.

$$\sigma_{F_{t,0}}(Re) = \frac{1}{1 + \exp(-(Re - 42{,}772)/200)}, \tag{7.50}$$

stationary force transfer is governed by:

$$\begin{aligned} F_{t,0}^D &= 1.323 \cdot 10^{-4} \left(\exp(13.653 Re^{0.065}) - 1\right) \left(1 - \sigma_{F_{t,0}}\right) \\ &\quad + 0.354 Re^{1.827} \sigma_{F_{t,0}}. \end{aligned} \tag{7.51}$$

Returning to Figure 7.21 and considering f_0^D shows that while the three individual fitted curves differ less than they do for $F_{t,0}^D$, a clear difference in slope can still be observed.

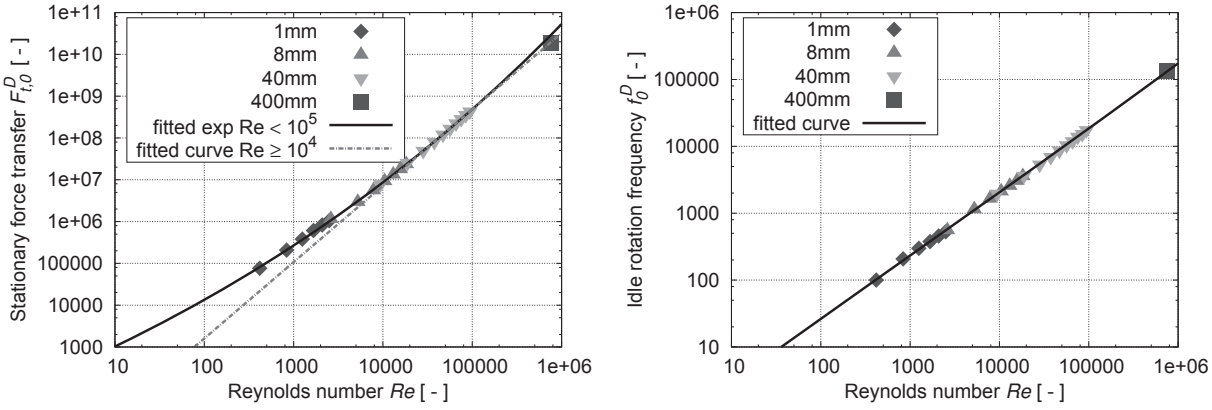

(i) Stationary force transfer $F_{t,0}^D$

(ii) Idle rotation frequency f_0^D

Figure 7.22: Stationary force transfer $F_{t,0}^D$ and idle rotation frequency f_0^D over Reynolds number Re (log-log) with global fit

The three curves intercept each other in the vicinity of $Re \approx 10^4$. Thus, two separate fits are performed, one for $Re < 10^4$ and another for $Re \geq 10^4$, resulting in

$$f_0^D = \begin{cases} 0.335Re^{0.947} & \text{for } Re < 10^4 \\ 0.240Re^{0.977} & \text{for } Re \geq 10^4. \end{cases} \tag{7.52}$$

Making use of the sigmoid function

$$\sigma_{f_0}(Re) = \frac{1}{1 + \exp(-(Re - 82{,}301)/200)} \tag{7.53}$$

smoothly combines the two sub-functions about their point of intersection $Re_0 = 82{,}301$ using $\lambda = 200$ into the following relation (Figure 7.22.ii):

$$f_0^D = 0.335Re^{0.947}\left(1 - \sigma_{f_0}\right) + 0.240Re^{0.977}\sigma_{f_0}. \tag{7.54}$$

A three dimensional relation governing tangential force F_t^D in terms of rotation frequency f^D and Reynolds number Re may now be constructed using the relation in eqn(7.51) as well as eqn (7.52). It has already been established that the dependence of tangential force upon rotation frequency can be considered linear for spherical diameters of 40 mm and 8 mm. For 1 mm, however, i.e. for laminar flow, this dependence is no longer linear but quadratic. Hence, the approximation

$$F_t^D = F_{t,0}^D\left(1 - \frac{f^D}{f_0^D}\right) \tag{7.55}$$

bears an error inversely proportional to the Reynolds number. At this point it may be pointed out that with the present state of technology, it is not possible to construct a *GrindBall* with a radius of less than 4 mm [Nor, Bra]. With this in mind and also considering that the error is still within an acceptable range were the data in Figure 7.7 fitted with straight lines instead of parabolae, eqn (7.55) is used to derive the following relation governing non-dimensional tangential force (Figure 7.23):

$$\begin{aligned} F_t^D \;=\; & \left(1.323 \cdot 10^{-4}\left(\exp\left(13.653Re^{0.065}\right) - 1\right)\left(1 - \sigma_{F_{t,0}}\right) + 0.354Re^{1.827}\sigma_{F_{t,0}}\right) \\ & \cdot \left(1 - \left(0.335Re^{0.947}\left(1 - \sigma_{f_0}\right) + 0.240Re^{0.977}\sigma_{f_0}\right)^{-1} f^D\right). \end{aligned} \tag{7.56}$$

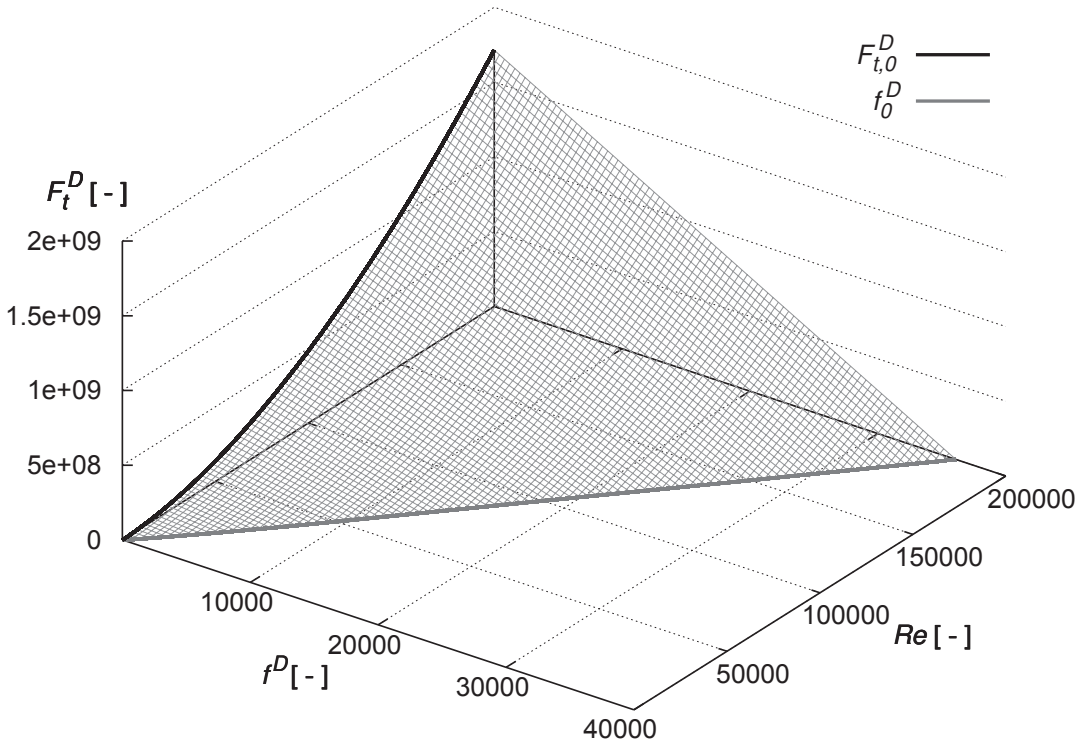

Figure 7.23: Tangential force F_t^D depending on rotation frequency f^D and Reynolds number Re

7.3.3 Grinding power

Non-dimensional grinding power P_G^D is calculated according to

$$P_G^D = F_t^D \dot{s}^D \tag{7.57}$$

using the dimensionless grinding velocity $\dot{s}^D = 2\pi f^D$, giving the relation

$$\begin{aligned} P_G^D &= \left(1.323 \cdot 10^{-4} \left(\exp\left(13.653 Re^{0.065}\right) - 1\right)\left(1 - \sigma_{F_{t,0}}\right) + 0.354 Re^{1.827} \sigma_{F_{t,0}}\right) \\ &\quad \cdot \left(1 - \left(0.335 Re^{0.947}\left(1 - \sigma_{f_0}\right) + 0.240 Re^{0.977} \sigma_{f_0}\right)^{-1} f^D\right) 2\pi f^D. \end{aligned} \tag{7.58}$$

$P_{G,\max}^D(\xi)$ is calculated by fitting a curve through the maxima of $P_G^D\big|_{Re=\text{const}}$, resulting in the following parametric representation:

$$f^D(\xi) = 0.167\,\xi^{0.947} \tag{7.59}$$

$$Re(\xi) = \xi \tag{7.60}$$

$$P_{G,\max}^D(\xi) = 0.186\,\xi^{2.774} \tag{7.61}$$

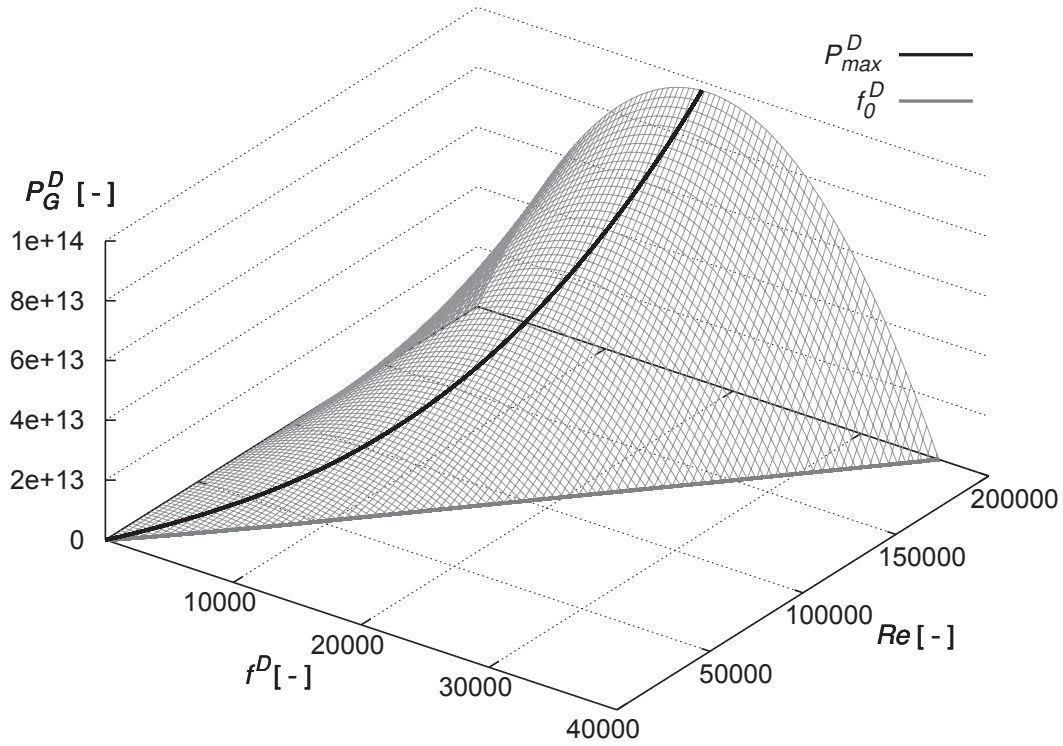

Figure 7.24: Grinding power P_G^D depending on rotation frequency f^D and Reynolds number Re

and yielding the operating point $\underline{\mathbf{P}}^D_{\mathrm{op}}(\xi)$:

$$\underline{\mathbf{P}}^D_{\mathrm{op}}(\xi) = \left(0.167\,\xi^{0.947}, \xi, 0.186\,\xi^{2.774}\right). \tag{7.62}$$

Eqn (7.58) is plotted in Figure 7.24 along with $P^D_{G,\max}(\xi)$.

7.4 Single duct vs. triple duct geometry

In the following, a comparison is made between the single duct geometry devised in Chapter 4 and the improved triple duct geometry from Chapter 6. Note that the relation between Reynolds number and dimensionless volumetric flow rate is different for the single duct geometry due to the different ratio of duct diameter h_d to the spherical diameter r, and the fact that there is only one duct:

$$Re = \frac{20\nu_N\rho_N}{\pi\nu_S\rho_S}\dot{V}^D \approx 6\dot{V}^D. \tag{7.63}$$

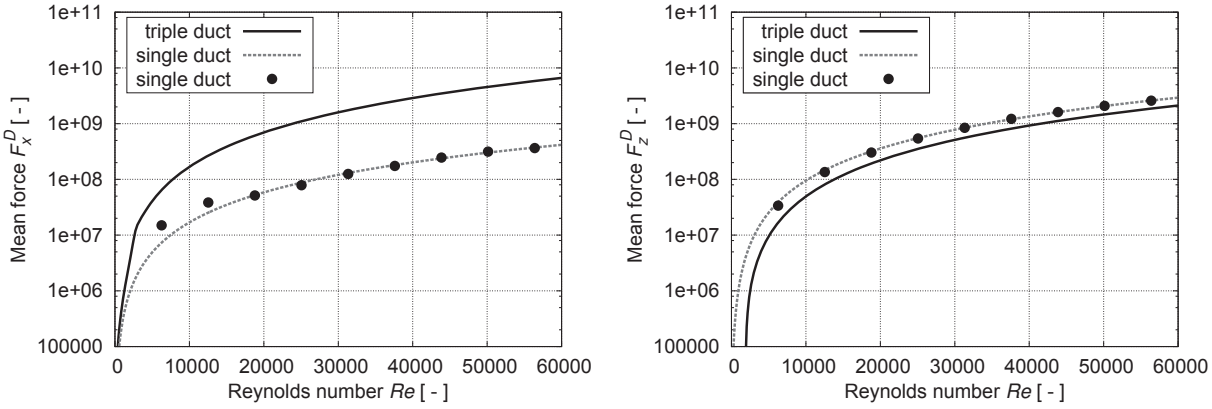

(i) Mean normal force $\overline{F}_x^D$

(ii) Mean normal force $\overline{F}_z^D$

Figure 7.25: Mean normal forces $\overline{F}_x^D$ and $\overline{F}_z^D$ over Reynolds number Re using air for single and triple duct geometries

Mean dimensionless forces $\overline{F}_x^D$ and $\overline{F}_z^D$ for both cases are governed by

$$\begin{aligned}
\overline{F}_x^{D,\text{triple}} &= 1{,}029{,}470\left(\exp(4.152\cdot 10^{-6}Re^{1.681})-1\right)\left(1-\sigma_{F_x}(Re)\right) \\
&\quad + 1.052Re^{2.051}\,\sigma_{F_x}(Re). && (7.64)\\
\overline{F}_x^{D,\text{single}} &= 1.181Re^{1.789} && (7.65)\\
\overline{F}_z^{D,\text{triple}} &= 0.618Re^2 - 2095.751Re && (7.66)\\
\overline{F}_z^{D,\text{single}} &= 2.141Re^{1.912}, && (7.67)
\end{aligned}$$

which are plotted in Figure 7.25. As is to be expected, they do not agree very well. Forces in x-direction show a large disparity. The reason for this is that while the single duct geometry introduces the duct into the spherical gap horizontally, the triple duct geometry does so vertically. Consequently, the flow pushes the grinding sphere in a different direction making a sensible comparison between the two geometries regarding this force impractical. Force in z-direction does show some agreement with a certain offset in the logarithmic representation. This suggests that the lift on the sphere behaves similarly regardless of the direction from which the flow is introduced.

Force transfer on to a stationary sphere $F_{t,0}^D$ for both cases are governed by

$$\begin{aligned}
F_{t,0}^{D,\text{triple}} &= 1.323\cdot 10^{-4}\left(\exp(13.653Re^{0.065})-1\right)\left(1-\sigma_{F_{t,0}}\right) \\
&\quad + 0.354Re^{1.827}\sigma_{F_{t,0}} && (7.68)\\
F_{t,0}^{D,\text{single}} &= 7.218Re^{1.544} && (7.69)
\end{aligned}$$

and idle rotation frequencies obey

$$\begin{aligned}
f_0^{D,triple} &= 0.335Re^{0.947}\left(1-\sigma_{f_0}\right) + 0.240Re^{0.977}\sigma_{f_0} && (7.70)\\
f_0^{D,\text{single}} &= 0.750Re^{0.875}, && (7.71)
\end{aligned}$$

which are both plotted in Figure 7.26.

$F_{t,0}^{D,\text{triple}}$ and $F_{t,0}^{D,\text{single}}$ agree extremely well for Reynolds numbers below 75,000. However, beyond this point the two curves begin to increasingly drift apart (not shown in the plot). $f_0^{D,triple}$ and $f_0^{D,\text{oil}}$ show equally pleasing agreement, yet start to slowly drift apart for Reynolds numbers beyond $2 \cdot 10^5$. The most probable reason for this Re-dependant discrepancy is accuracy. Note that the data used to derive eqns 7.68 and 7.70 covers a spectrum of Reynolds numbers ranging from $423 \leq Re \leq 1.04 \cdot 10^5$, while the data used to generate eqns 7.69 and 7.71 is limited to $6.30 \cdot 10^3 \leq Re \leq 6.29 \cdot 10^4$. It stands to reason that the equations derived for the single duct geometry do not produce good accuracy outside of their range of Reynolds numbers. This is supported by the fact that agreement between single and triple duct equations is highly satisfactory within the region of overlapping Reynolds numbers and gets increasingly worse with increasing distance from the overlap. The linear relation between $F_{t,0}^D$ and f_0^D implies that the same is true for tangential force F_t^D. All in all this shows that the non-dimensional relations derived in Section 7.3 are not only applicable to the triple duct geometry, but are also valid for variations of the *GrindBall*'s geometry, provided of course that the changes are not too radical. Furthermore, this implicitly shows that the full potential of the flow's momentum is still utilised by arranging the ducts vertically, as tangential force is not reduced by the fact that the flow has proportionally less distance to travel inside the spherical gap.

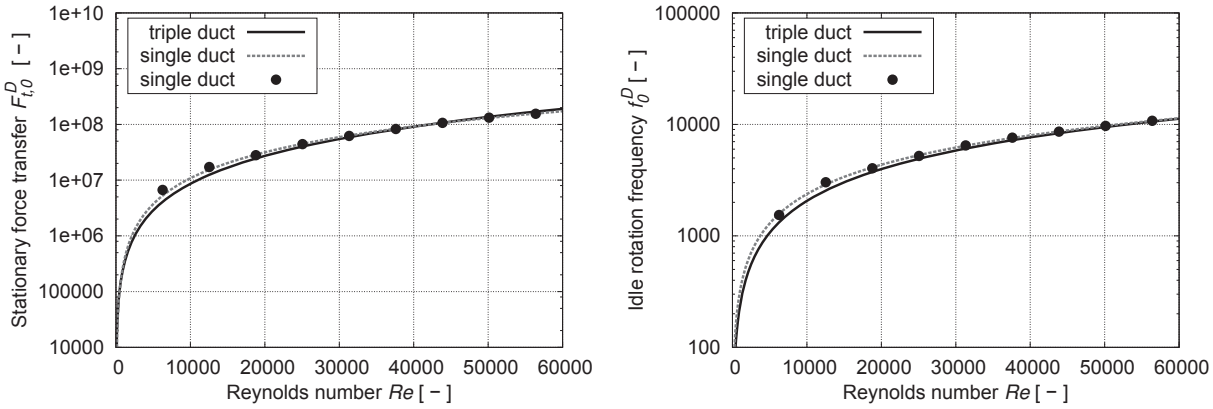

(i) Stationary force transfer $F_{t,0}^D$

(ii) Idle rotation frequency f_0^D

Figure 7.26: Stationary force transfer $F_{t,0}^D$ and idle rotation frequency f_0^D over Reynolds number Re for single and triple duct geometries using air

7.5 Air vs. oil propulsion

In the previous sections, non-dimensional equations are derived in order to compare simulations done on various length scales or geometries. Remembering the role of the kinematic viscosity in eqns (7.39) through (7.42), the same analysis can be used not only to compare varying parameters depending on the radius r, but also different fluid viscosities ν. Data from Section 7.3 using pneumatic propulsion can thus be compared to results obtained for hydraulic propulsion in Section 6.4. Non-dimensionalisation is performed for oil with ν_{oil} instead of ν_N and ρ_{oil} instead of ρ_N, both of which are constant. Also, for incompressible cases

$$Re = \frac{10}{3\pi}\dot{V}^D. \tag{7.72}$$

Normal forces are difficult to compare since they cannot be considered independent of rotation frequency for compressible cases and are omitted here. The two functions governing force transfer for air and oil on a stationary sphere in their non-dimensional forms are

$$\begin{aligned} F_{t,0}^{D,\text{air}} &= 1.323 \cdot 10^{-4} \left(\exp(13.653 Re^{0.065}) - 1\right)\left(1 - \sigma_{F_{t,0}}\right) \\ &\quad + 0.354 Re^{1.827}\sigma_{F_{t,0}} \qquad (7.73) \\ F_{t,0}^{D,\text{oil}} &= 1.551 Re^{1.777}, \qquad (7.74) \end{aligned}$$

while idle rotation frequencies are given by

$$\begin{aligned} f_0^{D,\text{air}} &= 0.335 Re^{0.947}\left(1 - \sigma_{f_0}\right) + 0.240 Re^{0.977}\sigma_{f_0} \qquad (7.75) \\ f_0^{D,\text{oil}} &= 4.917 \cdot 10^{-2} Re^{1.270}. \qquad (7.76) \end{aligned}$$

Both quantities are plotted in Figure 7.27.

Most notably, the exponents in the relations governing idle rotation frequency are > 1 for oil while they are < 1 for air. This implies that oil does not give diminishing returns when increasing the flow rate at high rotation frequencies. The relations for stationary force transfer are in keeping with air as they show a proportional increase with increasing Reynolds number.

Looking at the plots, similar behaviour is observed for both quantities. Agreement between oil and air, while poor for $Re < 100$, becomes increasingly better with rising Reynolds numbers. Again, the linear relation between $F_{t,0}^D$ and f_0^D implies that the same is true for tangential force F_t^D. The most likely reason for the discrepancies below $Re = 100$ is accuracy. The data used to derive eqns 7.74 and 7.76 covers $32 \leq Re \leq 224$, while the data used to derive eqns 7.73 and 7.75 has a minimum Reynolds number of 423. Hence, the two curves diverge for very low Re due to lack of overlapping data. Similarly, the curves diverge for large, turbulent Re (not shown). This is acceptable since a turbulent oil propulsion scenario is not a realistic method of operation due to cavitation occurring.

Arguably, the relations for non-dimensional tangential forces in Section 7.3 are applicable not only to the triple duct *GrindBall* using pneumatic propulsion, but are also valid for geometric variations and other propulsion media. The same is true for grinding power because of the simplistic way in which it is calculated based on tangential force.

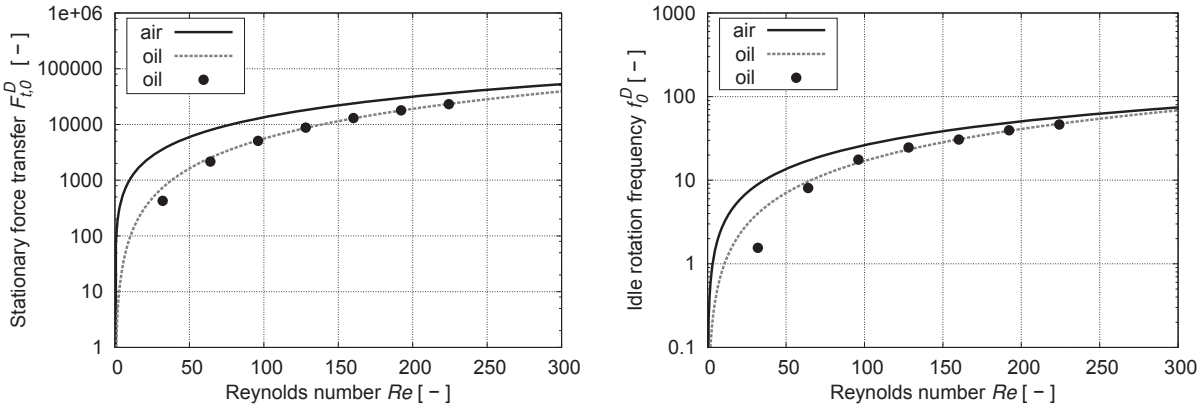

(i) Stationary force transfer $F_{t,0}^D$

(ii) Idle rotation frequency f_0^D

Figure 7.27: Stationary force transfer $F_{t,0}^D$ and idle rotation frequency f_0^D over Reynolds number Re for pneumatic and hydraulic propulsion

Chapter 8

Conclusion

The findings in this thesis are summarised and discussed in the following. Limitations are stated along with the implications that these limitations may have. Finally, future research possibilities are presented which may prove to elaborate or improve upon what was produced within the scope of this project.

8.1 Summary

The aim of this thesis has been to investigate forces transferred by turbulent compressible and incompressible fluid flows on to moving walls of smooth solid objects. It did so by conducting CFD simulations with `OpenFOAM` of a novel micro-grinding tool, which was introduced in Chapter 1. This tool utilises a grinding sphere set in rotational motion using fluid-dynamic propulsion and is controlled by an electro-magnetic bearing. The aptly named *GrindBall* presents an innovative way of maximising grinding force by keeping its axis of rotation parallel to the workpiece at all times.

Chapter 2 discussed the equations relevant to the simulations performed here, most importantly the compressible and incompressible Navier-Stokes equations. Chapter 3 gave an overview as to how the equations derived in Chapter 2 can be made discrete and applied to CFD simulations. Furthermore, the notion of Large Eddy Simulation was introduced, which provides an elegant way of achieving a sophisticated level of accuracy at relatively adequate computational cost.

Chapter 4 saw the first step in the development of the *GrindBall* by conducting parametric studies on geometrical parameters leading up to a pneumatically propelled prototype with a 40 mm grinding sphere. This prototype was subsequently examined through simulations with varying flow rates as well as spherical rotation frequencies. Relations were found which govern normal forces acting on the grinding sphere, tangential forces equivalent to the force available to the grinding process, as well as grinding power for which the tool behaves optimally. Tangential forces display a linear dependence on rotation frequency for constant volumetric flow rates and a 3D relation governing tangential force as a function

of rotation frequency and flow rate could be derived. Contrary to prior expectations, it was discovered that air delivers grinding forces of $F_t < 0.04\,\mathrm{N}$, which is not enough to make viable use of the tool, and that the propulsion medium had to be changed to one with higher viscosity in order to achieve sufficient results. It stands to reason that miniaturisation of the tool will not provide any improvement in this regard. Furthermore, the horizontal arrangement of the duct introducing the flow into the spherical gap in which the sphere is mounted causes lift, which is a hindrance considering that the tool also requires downward contact force to machine a workpiece.

In order to test the validity of the results presented within this thesis, a separate experiment was devised in Chapter 5: a dynamometer measures forces transferred by air pneumatically propelled through a duct from the *GrindBall* prototype on to an even plate. Analogous simulations were conducted which showed good agreement with the experimental data. Thus, it could be shown that the performed simulations provide trustworthy results in terms of fluid-to-solid force transfer.

Based on the findings of Chapter 4, Chapter 6 investigated how to turn the *GrindBall* into a functioning grinding tool with a smaller 8 mm sphere. Two additional ducts were introduced in order to achieve proportionally higher flow rates to further increase tangential force. All three ducts were introduced vertically from the top, increasing downward force and making the tool more compact. Several hydraulic propulsion media of varying viscosities were examined with the aim of finding a viable means of propulsion. It was found that EVO Fluid HLP VG46 oil with a kinematic viscosity of $\nu = 1.38 \cdot 10^{-4}\,\mathrm{m^2\,s^{-1}}$ at room temperature delivers the best results regarding tangential force in combination with contact force. Geometric parameters were optimised in a series of parametric studies and the best values for duct diameters, duct positions, and gap height determined. Thus, the tool's final geometric layout has been conceived. Similarly to the approach used in Chapter 4, this layout was subsequently simulated under a variety of flow rates and spherical rotation frequencies to examine the behaviour of acting forces in detail. Unlike for the prototype, tangential force shows slightly parabolic behaviour depending on rotation frequency at constant flow rates. A linear fit nonetheless still provided a sufficiently accurate approximation. It has been shown that conditions for productive use of the *GrindBall* are met by this particular combination of oil and geometry with maximum contact force F_n in the range of 1-2 N, and tangential force $F_t = 0.1\,\mathrm{N}$ at a rotation frequency of $f \approx 300\,\mathrm{Hz}$. Grinding power has been determined and an operating point $\underline{\mathbf{P}}_{\mathrm{op}}$ found at which the tool operates with maximum efficiency. The outcome is that the *GrindBall* presents not only a viable alternative to existing grinding tools, it in fact revolutionises the field of micro-grinding by presenting a compact, versatile, and highly efficient product capable of being used in industrial applications. It is unfortunate that efficient propulsion must resort to the use of oil because it not only makes handling the tool more elaborate and costly, but also pollutes the workpieces being machined and requires a laborious cleaning process. It does presently seem, however, to be the only effective means of propulsion for the *GrindBall*.

Finally, Chapter 7 conducted a scale analysis of the triple-duct geometry devised in Chapter 6 using pneumatic propulsion. The scales investigated covered 40 mm, 8 mm, and 1 mm. Normal forces, tangential force, and grinding power were determined for each scale, followed by a non-dimensional analysis of said quantities. It was found that the dependence of tangential force on rotation frequency at constant flow rates becomes increasingly parabolic with decreasing scale. Concluding from these and the afore mentioned results, it can be speculated that the form of dependence between the two quantities is dependent on the Reynolds number and fluid properties. Lower Reynolds numbers and higher viscosities seem to promote an increasingly parabolic relation. Furthermore, it has been shown that employing an appropriate method of non-dimensionalisation leads to a single relation for each quantity which is valid across all scales - including arbitrary ones. This implies that no further simulations are necessary to investigate scales which may be of future interest, e.g. 4 mm or 2 mm. It was also discovered that the behaviour of forces is dependant on the Reynolds number and the thereby implied degree of turbulence. In some cases this led to piecewise functions that needed to be smoothly combined using a sigmoid. Additionally, non-dimensional relations for grinding force and power were shown to be valid both across different geometries by drawing a comparison to the prototype results from Chapter 4, as well as other propulsion media by comparing them to hydraulic propulsion from Chapter 6. This is an extremely pleasing result since future versions of the tool, versions in which the geometry may have changed so radically that the results presented here no longer apply, now require far less simulations in order to fully describe tangential forces and grinding power. Instead of focussing on a multitude of flow rates per scale and subsequently varying the scale, one simply needs to cover a large enough spectrum of Reynolds numbers by scaling the tool and can then derive non-dimension relations valid for arbitrary scales and propulsion media.

8.2 Limitations

Certain limitations do apply to the results presented in this thesis. Compressible simulations have throughout been restricted entirely to sub-sonic flow and hence all results are valid only for $Ma < 1$. This needs to be considered when conducting future simulations on other geometries. Achieving higher Reynolds numbers cannot be done solely by increasing the flow rate because, at some point, this would result in super-sonic flow. Instead, the scale of the geometry must be increased to keep the Mach number below 1. Analogously to the Mach number, the Cavitation number Ca presented a limiting factor for incompressible flow. The solver used is not capable of modelling cavitation bubbles and instead produces negative values for pressure. This unrealistic behaviour needed to be avoided and so flow rates are limited to those that do not produce cavitation. This of course needs to be considered when using the herein derived non-dimensional relations to determine the behaviour of forces at arbitrary scales or for other propulsion media.

Normal forces could not be compared among different geometries or propulsion media. While the former case presented discrepancies obviously resulting from changing the arrangement of the duct, oil showed entirely different behaviour compared to air. While normal forces for pneumatic propulsion seemed to be dependant only on flow rate, hydraulic propulsion introduced an additional dependence on spherical rotation frequency. Supplementary studies into this matter would be required to be able to quantify these forces definitively, however, tangential forces were regarded as a much higher priority and so they were not investigated any further.

Temperature is another issue. Adiabatic walls were assumed for compressible simulations, while temperature variation was neglected entirely for incompressible ones. Practical use of the tool will see two major sources of temperature fluctuation: heat generated by the magnets used to keep the sphere centred at its location and heat generated by the process of grinding. The main reasons why these sources of heat were neglected is that not only is the amount of generated heat unknown, it is also not known how this heat is distributed. It is open to question what temperature the magnets will reach as this depends mainly on the work the bearing has to carry out, which in turn depends on the duration of use and the material being ground. Also, how much of this heat will be transferred on to the propulsion fluid and into the spherical gap remains to be seen. Temperature distribution across the sphere requires the nature of the sphere's rotation to be determined. Should there be slight fluctuations in the axis of rotation, the sphere would tumble resulting in a uniform temperature across the sphere. A steady axis of rotation on the other hand would cause a temperature gradient along said axis. These issues need to be addressed by conducting grinding trials using the actual tool. Incorporating such quantities into simulations before they have been examined experimentally would have most likely reduced the accuracy of the results.

Finally, the penetration depth of the sphere into the workpiece presents an issue. This depth depends entirely on the type of cavity being ground and covers a large range of values, starting from close to zero and ending with the radius of the sphere. This additional parameter increases the simulation effort immensely. While an arbitrary value was chosen for the prototype, later simulations disregarded penetration entirely. Chapter 4 showed that tangential force transfer on to the sphere takes place almost entirely inside the spherical gap. Thus, no discrepancy is to be expected by neglecting this parameter regarding F_t or P_G. Normal forces, however, may be affected especially for high rotation frequencies. Flow induced by rotation of the sphere in close proximity to the cavity may cause local pressure variations, which could affect normal forces in all three directions.

8.3 Future research possibilities

Should empirical studies show that super-sonic flow presents a means of stable operation, this field could provide an interesting research opportunity. Higher flow rates would increase force transfer on to the sphere and may prove to make air a viable propulsion medium. It would be interesting to see whether the derived equations still hold, or if super-sonic flow behaves in a different manner. Additionally, pre-heating the air would increase the speed of sound and provide a way of increasing flow rates even further. Regarding incompressible flow, should operation of the tool with cavitation occurring prove to be only of minor concern, i.e. little to no damage being done to the tool, this could also be considered as a means of increasing grinding forces.

Another way of improving the tool's efficiency may be offered by considering other gap shapes. The spherical gap could, for example, be replaced by an oval-shaped gap which is narrower along the axis of rotation and wider along the intended direction of the flow. This would force the flow to increasingly propagate in the direction of the sphere's surface's direction of motion, thereby increasing tangential force transferred on to the sphere.

Oil presents a more viable propulsion medium compared to air because of its high viscosity. This high viscosity, however, also bears a disadvantage: those parts of the sphere which are not influenced directly by the flow exiting the ducts are also submersed in oil and hence exposed to increased friction as the high viscosity of the fluid slows down the grinding sphere's rotation frequency. This could be countered by two-phase operation: while propulsion is still realised with oil, the tool need not be submersed in it entirely, but used in atmospheric surroundings. This would not only increase the efficiency of the tool, but also make it far more practical to use. Analogously, operating the *GrindBall* inside a vacuum chamber would have a similar effect on pneumatic propulsion. This, of course, does not exactly increase practicality, but may prove to improve the effectiveness of air as a propulsion fluid.

Overall, it was very enjoyable to be a part of project *GrindBall* and to be able to conduct research in this interdisciplinary venture. I hope this thesis inspires others to perform further research in the field of micro-grinding, especially concerning innovative and efficient propulsion methods and the simulation thereof.

Appendix A

Theorems & formulae

A.1 Divergence theorem

Let V be a three-dimensional closed volume bounded by a piecewise smooth surface S. Then for a finitely smooth vector field $\underline{\boldsymbol{\psi}}$ defined on V, the following must hold:

$$\iiint_V \left(\nabla \cdot \underline{\boldsymbol{\psi}}\right) \mathrm{d}V = \oiint_{\delta V} \left(\underline{\boldsymbol{\psi}} \cdot \underline{\hat{\mathbf{n}}}\right) \mathrm{d}S,$$

where $\underline{\hat{\mathbf{n}}}$ is the unit normal surface vector pointing outward of V. This can be interpreted physically as the sources of $\underline{\boldsymbol{\psi}}$ within V being equal to the flow across the boundary δV.

A.2 Leibnitz integral rule

Leibnitz integral rule for fixed limits of integration states that for an integral of the form

$$\int_a^b \psi(x, y)\mathrm{d}y,$$

the derivative w.r.t. x may be expressed as

$$\frac{\mathrm{d}}{\mathrm{d}x} \int_a^b \psi(x, y)\mathrm{d}y = \int_a^b \frac{\partial}{\partial x}\psi(x, y)\mathrm{d}y$$

given that ψ is continuous and continuously differentiable w.r.t. x.
For variable limits of integration, the rule takes the form

$$\frac{\mathrm{d}}{\mathrm{d}x} \int_{a(x)}^{b(x)} \psi(x, y)\mathrm{d}y = \frac{\mathrm{d}b(x)}{\mathrm{d}x}\psi(x, b(x)) - \frac{\mathrm{d}a(x)}{\mathrm{d}x}\psi(x, a(x)) + \int_{a(x)}^{b(x)} \frac{\partial}{\partial x}\psi(x, y)\mathrm{d}y.$$

A.3 Reynolds transport theorem

Leibnitz integral rule is extended to the 3D case in Reynolds transport theorem. The function $\underline{\boldsymbol{\psi}} = \psi(\underline{\mathbf{x}}, t)$ is integrated over a time dependant volume $\Omega(t)$ with corresponding boundary $\delta\Omega(t)$ and then differentiated w.r.t. t:

$$\frac{\mathrm{d}}{\mathrm{d}t}\int\limits_{\Omega(t)} \underline{\boldsymbol{\psi}}\mathrm{d}V = \int\limits_{\Omega(t)} \frac{\partial \underline{\boldsymbol{\psi}}}{\partial t}\mathrm{d}V + \int\limits_{\delta\Omega(t)} (\underline{\mathbf{u}}_b \cdot \underline{\hat{\mathbf{n}}})\underline{\boldsymbol{\psi}}\mathrm{d}S,$$

where $\underline{\hat{\mathbf{n}}}(\underline{\mathbf{x}}, t)$ is the unit normal surface vector and $\underline{\mathbf{u}}_b(\underline{\mathbf{x}}, t)$ is the velocity of the corresponding boundary element.
For the particular case of a continuous material volume, particles immediately adjacent to the boundary move with the boundary elements, hence

$$\underline{\mathbf{u}}_b \cdot \underline{\hat{\mathbf{n}}} = \underline{\mathbf{u}} \cdot \underline{\hat{\mathbf{n}}}.$$

Substituting this into the above yields

$$\frac{\mathrm{d}}{\mathrm{d}t}\int\limits_{\Omega(t)} \underline{\boldsymbol{\psi}}\mathrm{d}V = \int\limits_{\Omega(t)} \frac{\partial \underline{\boldsymbol{\psi}}}{\partial t}\mathrm{d}V + \int\limits_{\delta\Omega(t)} (\underline{\mathbf{u}} \cdot \underline{\hat{\mathbf{n}}})\underline{\boldsymbol{\psi}}\mathrm{d}S.$$

Or, applying the divergence theorem:

$$\frac{\mathrm{d}}{\mathrm{d}t}\int\limits_{\Omega(t)} \underline{\boldsymbol{\psi}}\mathrm{d}V = \int\limits_{\Omega(t)} \frac{\partial \underline{\boldsymbol{\psi}}}{\partial t}\mathrm{d}V + \int\limits_{\Omega(t)} \nabla \cdot (\underline{\boldsymbol{\psi}} \otimes \underline{\mathbf{u}})\mathrm{d}V.$$

Similarly, considering a scalar ψ instead of a vector:

$$\frac{\mathrm{d}}{\mathrm{d}t}\int\limits_{\Omega(t)} \psi\mathrm{d}V = \int\limits_{\Omega(t)} \frac{\partial \psi}{\partial t}\mathrm{d}V + \int\limits_{\Omega(t)} \nabla \cdot (\psi\underline{\mathbf{u}})\mathrm{d}V.$$

A.4 Grinding angle and corresponding abrasion force

In practise, F_t can be calculated without error as the grinding angle is chosen prior to the use of the tool and can be used to calculate the average distance to the axis of rotation, i.e. the average length of the moment arm:

$$\overline{r}_y = \frac{r}{2}\left(\frac{\alpha}{\sin\alpha} + \cos\alpha\right) \qquad 0 < \alpha \leq \frac{\pi}{2},$$

where α is half the grinding angle. This average distance is then used to calculate available abrasion force exactly using

$$F_t = \frac{M_y}{\overline{r}_y}.$$

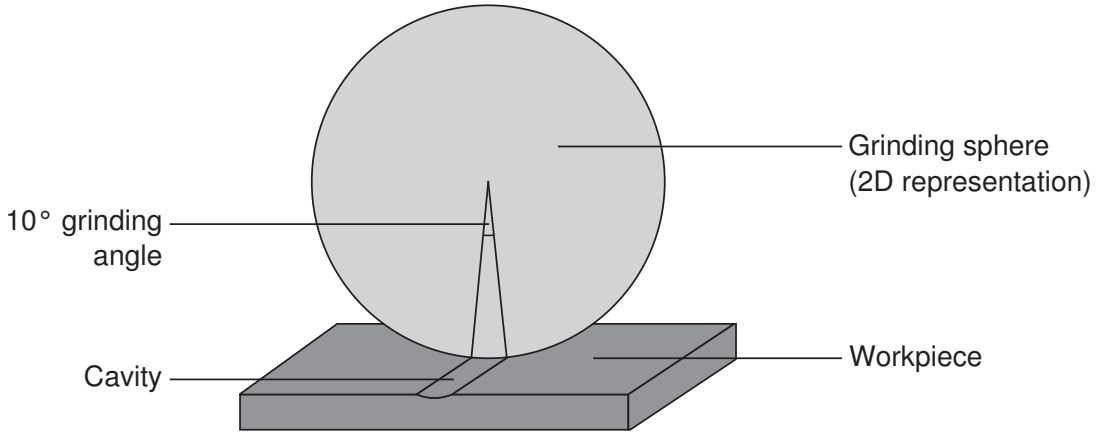

Figure A.1: Grinding angle of 10°

A.5 Extrapolation of standard deviation

Since the results for f_0 stem from extrapolation, no explicit standard deviations exist for these values. Error bars are thus determined using the standard deviations of the values obtained through simulation using a mean standard deviation:

$$\overline{\sigma} = \frac{1}{n}\sqrt{\sum_{i=1}^{n}\sigma_i^2},$$

where n is the number of simulation results for a given $\dot{V}_N$. The error $\overline{\epsilon}$ is then obtained using the angle α between the linear regression curve for the particular flow rate and the f-axis:

$$\overline{\epsilon} = \frac{\overline{\sigma}}{\tan\alpha}.$$

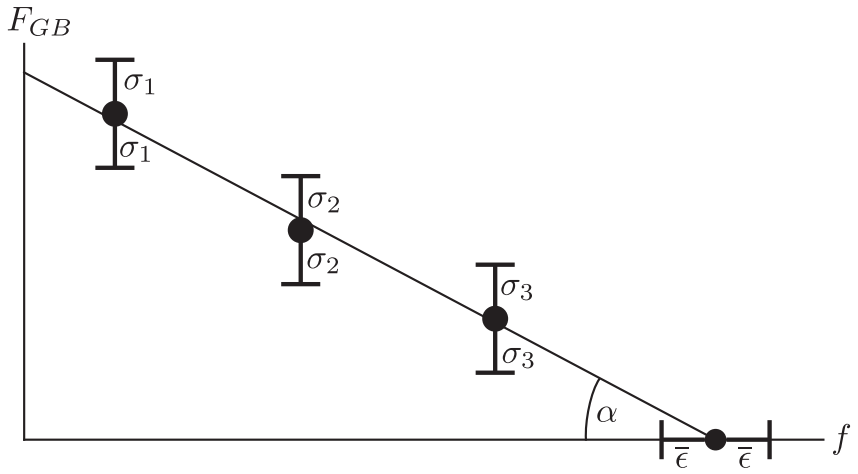

Figure A.2: Extrapolation of standard deviation for f_0

A.6 Sigmoid function

The sigmoid function [Wei] is an S-shaped mathematical function which initially grows exponentially and then saturates for large values of x. It has a variety of uses in applications which present fast growth initially and eventually stagnate, e.g. a type of learning curve. It can be defined as

$$\sigma(x) = \frac{1}{1 + \exp(-(x - x_0)/\lambda)},$$

where x_0 is a displacement relative to the origin and λ is used to influence the "transition width". Here, the sigmoid is used to smoothly combine discontinuous or non-continuously differentiable functions with each other.

Consider two functions

$$\begin{aligned} f(x) &= x \\ g(x) &= -x + 10 \end{aligned}$$

which intersect at $(5, 5)$ and are plotted in Figure A.3.

The piecewise function amalgamating $f(x)$ and $g(x)$

$$h(x) = \begin{cases} x & \text{for } x < 5 \\ -x + 10 & \text{for } x \geq 5 \end{cases}$$

is not continuously differentiable as its derivative jumps at $x = 5$. Using the sigmoid function with $x_0 = 5$, $h(x)$ can be made continuously differentiable by defining

$$H(x) = (1 - \sigma(x))f(x) + \sigma(x)g(x).$$

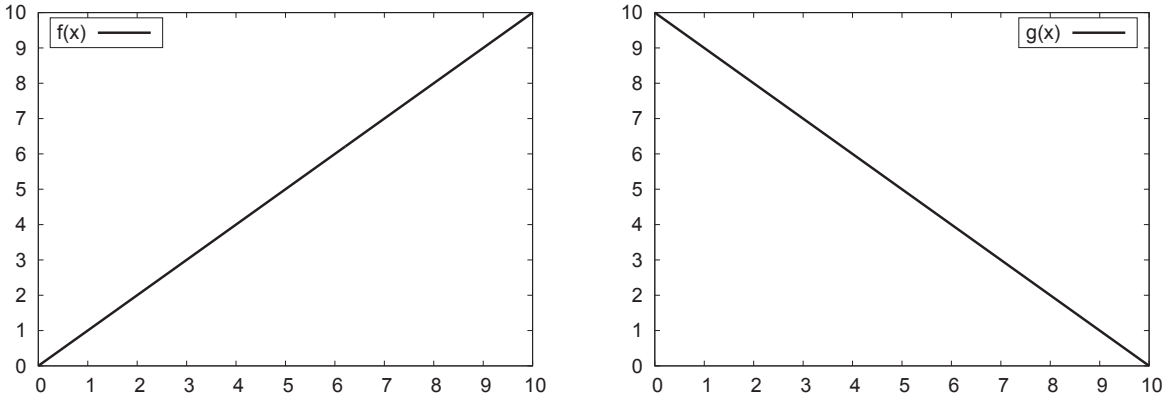

Figure A.3: Functions $f(x)$ and $g(x)$

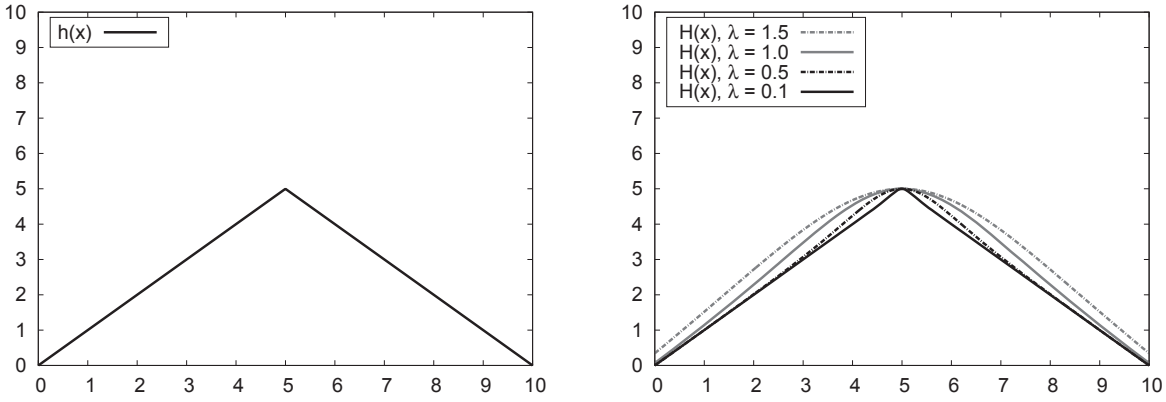

Figure A.4: Functions $h(x)$ (left) and $H(x)$ (right) with $x_0 = 5$ and $\lambda = 0.1, 0.5, 1.0, 1.5$

Figure A.4 shows $h(x)$ as well as $H(x)$ for different values of λ.

The transition from $f(x)$ to $g(x)$ becomes smoother with rising λ. Too large values of λ can, however, lead to unwanted behaviour further away from the point transition, as is the case for $\lambda = 2$ which does not intersect the y-axis close to the origin.

Appendix B

Advanced Meshing Techniques

B.1 Meshing a cylinder with hexahedra

Constructing computational grids purely with hexahedra provides the best basis for running simulations using the Finite Volume Method described in Section 3.1.2. Results are obtained with a good combination of accuracy and low computational cost. Meshing complex geometries purely with hexahedra, however, does not always present an easy task. In order to construct a mesh consisting only of hexagonal cells, each enclosed volume must be defined by six surfaces, which in turn must each consist of 4 enclosing lines.

Cylindrical shapes, i.e. pipes, are highly relevant to this project and present something of a challenge when aiming to construct a high-quality hexahedral mesh. Figure B.1 illustrates the problem presented by meshing a cylinder in this way. While the mesh is of decent quality in the inner regions of the cylinder, the outer region possesses bad quality cells near the "corners" (i.e. where the curves enclosing the surface meet).

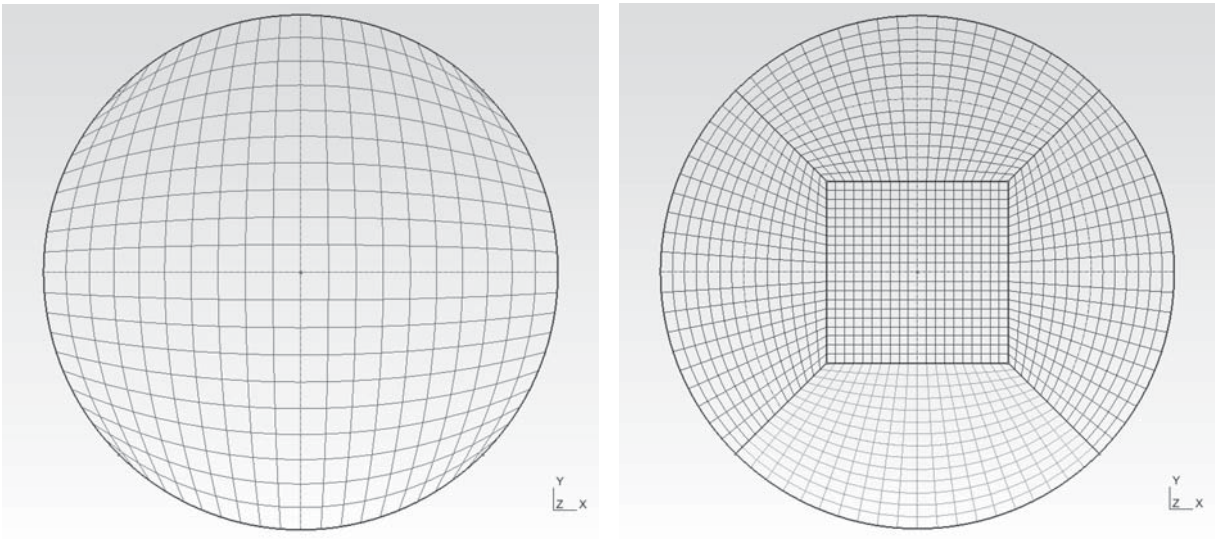

Figure B.1: 2D slices of a cylinder mesh. Crude mesh (left) and butterfly mesh (right)

A so-called *butterfly mesh* can solve this issue by dividing the circular cross-section of the pipe into five separate surfaces (see Figure B.1 on the right). Naturally, the question arises in what way the circle should be divided in order to achieve best results. This problem is outlined in Figure B.2.

The point **P** must be chosen such that the cells are evenly distributed and their sizes do not vary a great deal. Regarding only the outer region of the circle and considering only the distribution of points along r_o and a_o, optimum quality is reached when they are of equal length, i.e. $r_o/a_o = 1$. This condition, however, implies **P** be located at the origin. Considering again the outer region but this time considering the distribution of points along a_i and the cylinder wall, optimal distribution is achieved when they are both of equal length, i.e. $4a_i/r\pi = 1$. This condition implies **P** be located on the cylinder wall. Note that the inner region need not be considered because the cells are always squares.

It should be clear that placing **P** at the origin or on the cylinder wall is an unrealistic and purely hypothetical result. To determine an optimal position for **P**, both ratios are equated so that they can be maximised according to one another:

$$\frac{r_o}{a_o} = \frac{4a_i}{r\pi}. \tag{B.1}$$

Note that $r_o = r - r_i$ and $a_i = r_i \cos(\pi/4)$ and so eqn B.1 becomes

$$\frac{r - r_i}{r - r_i \cos(\pi/4)} = \frac{4r_i \cos(\pi/4)}{r\pi}. \tag{B.2}$$

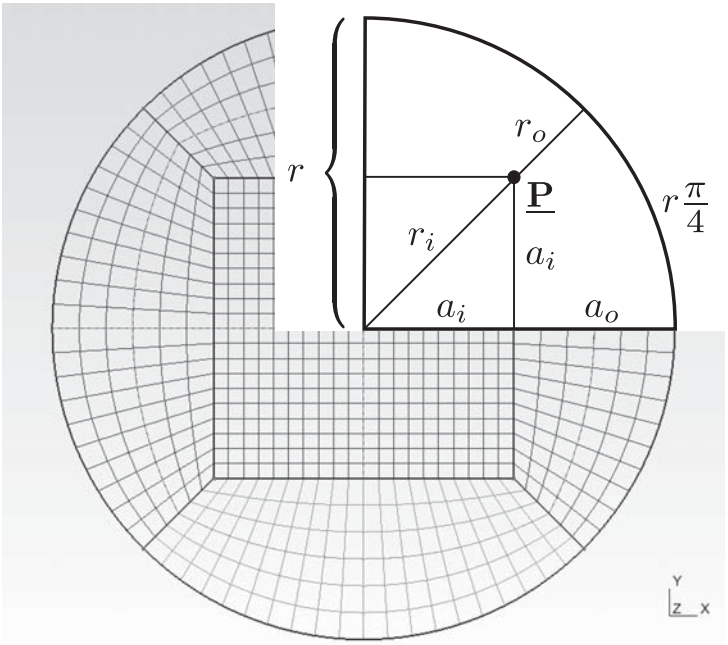

Figure B.2: Optimising butterfly mesh parameters

Eqn B.2 is dependent only on r and r_i and so it can be solved to express r_i in terms of r:

$$r_{i,1} \approx 0.682r \quad \text{and} \quad r_{i,2} \approx 2.303. \tag{B.3}$$

Obviously, $r_{i,2}$ is not applicable in this case and a purely mathematical solution. Hence, it can be said that an optimum hexahedral mesh is achieved when

$$r_i \approx 0.7r, \tag{B.4}$$

which implies

$$a_i \approx 0.5r \tag{B.5}$$

and so

$$\underline{\mathbf{P}} \approx (0.5r, 0.5r). \tag{B.6}$$

One final issue that needs to be addressed is the inner square. Since it takes up almost one third of the circle's area, there is not much room for the mesh to gradually adopt a circular shape as it approaches the cylinder's walls (see Figure B.2). In order to counter this, the inner body need not actually be a square. Instead, the four lines can be slightly convex so that the approximation of the circular shape of the wall is more gradual and consistent. The convexity and the number of cells in the inner and outer parts need to be carefully chosen so that the cells remain of similar shape and size throughout the cross section of the cylinder. As a general rule, the number of cells along r_o should make up between 30% and 50% of the total number cells along r.

Figure B.3 shows the final result with a coarse and a fine version of the finished butterfly mesh. Note how the cross-sectional area shows that the individual cells are virtually equilateral. They do increase somewhat in size toward the cylinder walls because equilaterality is favoured over equal sizes in this example. This is especially important when using isotropic turbulence modelling (see the Smagorinsky Model in Section 3.6.2).

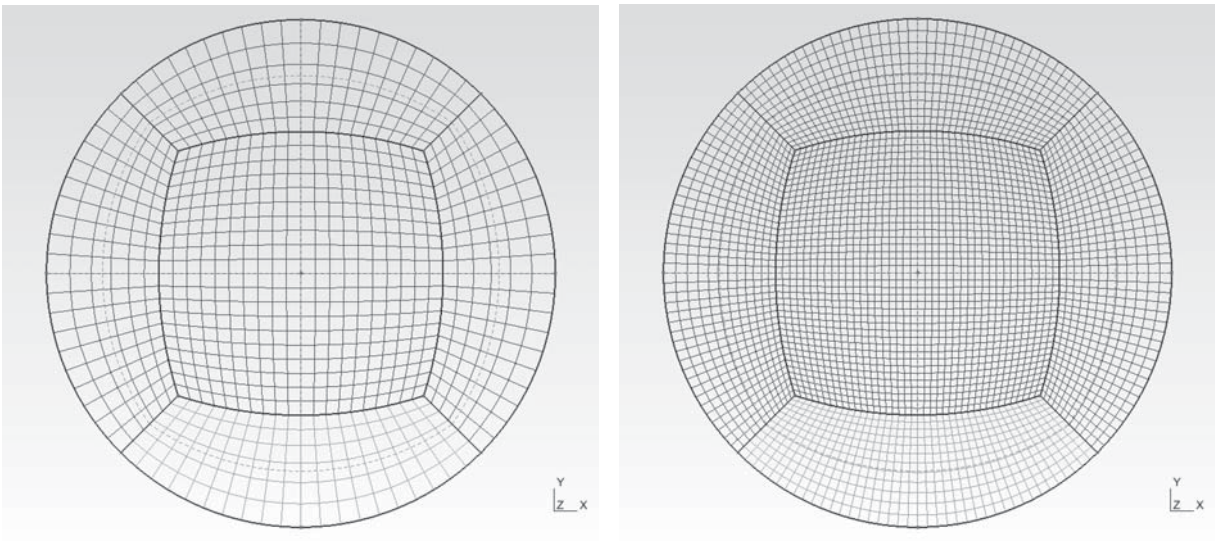

Figure B.3: Optimal butterfly mesh setup in coarse (left) and fine (right) variations

B.2 Automatic Mesh Generation

Conducting parametric studies in which geometric parameters vary implies the need to generate a new mesh for each considered case. Since the *GrindBall*'s geometry is extremely complicated, it would be profoundly time consuming to generate a new mesh from scratch every time a new parameter is investigated. Instead, the computational grid is generated with the help of a script which computes the grid points automatically based on given geometric parameter input. This script defines the coordinates of every single point in the *GrindBall*'s geometry based on a given spherical radius, gap height, duct diameter, duct position, et cetera. It then outputs a list of points with corresponding coordinates that are inserted into a `gmsh` [GR09] file which goes on to create the computational grid. Using this technique, the grid needs only to be manually constructed once, i.e. lines, curves, surfaces, and volumes are defined the first time the mesh is built. For each subsequent mesh the script generates a new set of points and replaces the previous list of points in the `gmsh` script, thereby drastically reducing the time needed for mesh generation.

Maplesoft `Maple 14` [Map10] is used to generate the script. While it would be also possible to handle the scripting part with `gmsh`, `Maple` provides greater functionality and ease of use, e.g. by providing while-loops and the ability to solve equations directly. The following example is the script used to generate the meshes for the 8 mm vertical three-duct *GrindBall*'s geometric parametric study discussed in Section 6.2. It computes the coordinates of a total of 1751 points in 0.95 seconds on a regular desktop computer.

Table B.1 provides an overview over the variables used followed by the actual `Maple` script, which includes annotations and graphic representations of the mesh in order to provide an idea of which segment of the grid is being generated by the according lines of code.

The following script is the one used to create the computational grid for the vertical triple-duct *GrindBall* geometry including pre-defined workpiece penetration as seen in Chapter 6.

Index of Variables

Variable	Description
kugelR, r	Spherical radius
R	Spherical gap radius
spalt	Gap height
zulauf, d	Main duct diameter
zulauf2, $d2$	Co-duct diameters
offset, os	Main duct offset
offset2, $os2$	Co-duct offset
winkel, θ	Angle between ducts
Krümmungsradius, kr	Radius of curvature
Eindringtiefe, Ae	Penetration depth
Ap	Penetration width
$scaleme$	Subroutine to scale a point from one sphere's surface to another
$PList$	List containing relevant points
$PArray$	Array containing relevant points
$tmpList$	Temporary list containing relevant points
x, y, z	Spatial coordinates
ex, ey, ez	Spatial coordinates
n, i	Running indices
$md, md2, md3$	Coordinates of main and co-ducts
mz	z-coordinate of duct entry points
$mz2$	z-coordinate of duct entry points including curvature
ir	Radius of inlet basin
iz	Height of inlet basin
Or	Radius of outlet basin
h	Height of outlet basin
$\alpha, \beta, \gamma, \delta, \epsilon, \zeta, \eta$	Outlet basin segment angles
aL	List of outlet basin segment angles
$radii, cmd, cd$	Variables for smooth duct/gap intersection
a, b, c	Dummy variables
tx, m, ur	Dummy variables
fx, nfx	Dummy coordinates
nx, ny, nz	Dummy coordinates
$r1, r2, r3, r4$	Dummy radii
$\phi, alph, bet$	Dummy angles

Table B.1: Input parameters (standard font) and variables (italic font) used in the Maple script to create the *GrindBall* mesh

```
> restart :
  createmesh := proc(kugelR, spalt, zulauf, Eindringtiefe, Krümmungsradius, offset, winkel, offset2, zulauf2)
  local r, R, d, os, PList, scaleme, Ae, Ap, tmpList, n, md, mz, Or, kr, mz2, α, β, γ, δ, ϵ, radii, x, y, z, ϑ, d2, os2,
        md2, md3, ir, iz, h, f, lr, ur, ϕ, a, b, c, tx, θ, i, cmd, cd, ζ, η, L, L2, aL, r1, r2, r3, r4, m;
  Digits := 20;

  # an internal procedure that scales point coordinates from one sphere's surface to
      another's
  scaleme := proc(ex, ey, ez, er2)
  local alph, bet, fx, nfx, nx, ny, nz, r1, x, y, z, r2 ;
   Digits := 20;
   x := evalf(ex, 20) :
   y := evalf(ey, 20) :
   z := evalf(ez, 20) :
   r2 := evalf(er2, 20) :
   fx := sqrt(x^2 + y^2) :
   r1 := sqrt(x^2 + y^2 + z^2) :
   alph := arccos(fx / r1) :
  if x ≠ 0 then bet := arctan(abs(y) / abs(x)) : else bet := π / 2 : end if:
  nfx := r2 · cos(alph) :
  if x ≥ 0 then nx := nfx · cos(bet) : else nx := −nfx · cos(bet) : end if:
  if y ≥ 0 then ny := nfx · sin(bet) : else ny := −nfx · sin(bet) : end if:
  if z ≥ 0 then nz := r2 · sin(alph) : else nz := −r2 · sin(alph) : end if:
  return(nx, ny, nz);
  end proc:

  # begin by defining basic parameters
  r := kugelR;
  R := r + spalt;
  d := zulauf :
  d2 := zulauf2 :
  os := offset;
  os2 := offset2 :
  Ae := Eindringtiefe;
  Ap := fsolve(r^2 = (r − Ae)^2 + Ap^2, Ap)[2];
  kr := Krümmungsradius;
  ϑ := winkel :
  md := R − os − d / 2 ;
  mz := r / 0.004 · 0.005 + r :
  mz2 := evalf(mz − kr · cos(Pi / 4), 20);
  md2 := evalf([[R − os2 − d2 / 2) · cos(ϑ), (R − os2 − d2 / 2) · sin(ϑ), mz], 20) :
  md3 := md2 + [0, 0, 0.008 − mz] :

  ir := 0.004 :
  iz := mz + 0.005 · r / 0.004 :
  PList := [[0, 0, 0]];
  Or := 6 · r :
  aL := [α, β, γ, δ, ϵ, ζ, η] :
  for n from 1 to nops(aL) do
   aL[n] := (n − 0.5) / 7 · 1 / 2 · Pi :
  end do:
```

$h := 3 \cdot kr \cdot \cos\left(\mathrm{Pi} - \frac{\mathrm{Pi}}{2} - \frac{\mathrm{Pi}}{3}\right)$:
$y := \mathrm{sqrt}((R + 3 \cdot kr)^2 - h^2)$:
$r1 := y$;
$m := \mathrm{sqrt}(9 \cdot kr^2 - h^2)$:
$tmpList := [\,]$:

 # define the sphere and the spherical gap on the plane z=0
for n **from** 1 **to** $nops(aL)$ **do**
$tmpList := [op(tmpList), [r \cdot \sin(aL[n]), r \cdot \cos(aL[n]), 0]]$;
end do:
for n **from** 1 **to** $nops(tmpList)$**do**
$tmpList := [op(tmpList), [-tmpList[\mathrm{n}][1], tmpList[\mathrm{n}][2], tmpList[\mathrm{n}][3]]]$;
end do:
for n **from** 1 **to** $nops(tmpList)$**do**
$tmpList := [op(tmpList), [tmpList[\mathrm{n}][1], -tmpList[\mathrm{n}][2], tmpList[\mathrm{n}][3]]]$;
end do:
for n **from** 1 **to** $nops(tmpList)$**do**
$tmpList := [op(tmpList), [scaleme(tmpList[n][1], tmpList[n][2], 0, y - m)]]$;
end do;
$tmpList := evalf(tmpList)$;
$PList := [op(PList), op(tmpList)]$;
$tmpList := [\,]$:

 # create the outlet basin with a radius of 6r
for n **from** 1 **to** $nops(aL)$ **do**
$tmpList := [op(tmpList), [\mathrm{scaleme}(r \cdot \sin(aL[n]), r \cdot \cos(aL[n]), 0, Or)]]$;
end do:
for n **from** 1 **to** $nops(tmpList)$**do**
$tmpList := [op(tmpList), [-tmpList[\mathrm{n}][1], tmpList[\mathrm{n}][2], tmpList[\mathrm{n}][3]]]$;
end do:
for n **from** 1 **to** $nops(tmpList)$**do**
$tmpList := [op(tmpList), [tmpList[\mathrm{n}][1], -tmpList[\mathrm{n}][2], tmpList[\mathrm{n}][3]]]$;
end do:
for n **from** 1 **to** $nops(tmpList)$**do**
$tmpList := [op(tmpList), [tmpList[\mathrm{n}][1], tmpList[\mathrm{n}][2], -(r - Ae)]]$;
end do:
$tmpList := evalf(tmpList)$;
$PList := [op(PList), op(tmpList)]$;
$tmpList := [\,]$:

 # create a rounded off edge at the gap- exit
for n **from** 1 **to** $nops(aL)$ **do**
$tmpList := [op(tmpList), [y \cdot \sin(\mathrm{aL[n]}), \mathrm{y} \cdot \cos(\mathrm{aL[n]}), h]]$;
end do:
for n **from** 1 **to** $nops(tmpList)$**do**
$tmpList := [op(tmpList), [-tmpList[\mathrm{n}][1], tmpList[\mathrm{n}][2], tmpList[\mathrm{n}][3]]]$;
end do:
for n **from** 1 **to** $nops(tmpList)$**do**
$tmpList := [op(tmpList), [tmpList[\mathrm{n}][1], -tmpList[\mathrm{n}][2], tmpList[\mathrm{n}][3]]]$;
end do:
for n **from** 1 **to** $nops(tmpList)$**do**
$tmpList := [op(tmpList), [scaleme(tmpList[n][1], tmpList[n][2], tmpList[n][3], R)]]$;
end do:
$h := tmpList[-1][-1]$;
$tmpList := [op(tmpList), [0, 0, h]]$;
$tmpList := evalf(tmpList)$;
$PList := [op(PList), op(tmpList), [0, 0, -(r - Ae)]]$;
$tmpList := [\,]$:

```
y := fsolve(b^2 + h^2 = r^2, b)[2];
for n from 1 to nops(aL) do
 tmpList := [op(tmpList), [y·sin(aL[n]), y·cos(aL[n]), h]];
end do:
for n from 1 to nops(tmpList)do
 tmpList := [op(tmpList), [ −tmpList[n][1], tmpList[n][2], tmpList[n][3]]];
end do:
for n from 1 to nops(tmpList)do
 tmpList := [op(tmpList), [tmpList[n][1], −tmpList[n][2], tmpList[n][3]]];
end do:
tmpList := evalf(tmpList) :
PList := [op(PList), op(tmpList)] :
tmpList := [ ] :

# define corresponding points at the bottom of the domain
h := fsolve((r − Ae)^2 + x^2 = (r1 − m)^2, x)[2];
for n from 1 to nops(aL) do
 tmpList := [op(tmpList), [Ap·sin(aL[n]), Ap·cos(aL[n]), −(r − Ae)]];
 tmpList := [op(tmpList), [h·sin(aL[n]), h·cos(aL[n]), −(r − Ae)]] :
end do:
for n from 1 to nops(tmpList)do
 tmpList := [op(tmpList), [ −tmpList[n][1], tmpList[n][2], tmpList[n][3]]];
end do:
for n from 1 to nops(tmpList)do
 tmpList := [op(tmpList), [tmpList[n][1], −tmpList[n][2], tmpList[n][3]]];
end do:
tmpList := evalf(tmpList);
PList := [op(PList), op(tmpList)];

# define the inlet basin
tmpList := [[ir·cos(Pi/10), ir·sin(Pi/10), mz], [ir·cos(Pi/6.5), ir·sin(Pi/6.5), mz], [ir·cos(Pi/4), ir·sin(Pi/4),
    mz], [ir·cos(Pi/2.8), ir·sin(Pi/2.8), mz], [ir·cos(Pi/2), ir·sin(Pi/2), mz], [ir·cos(Pi/2 + Pi/8), ir
    ·sin(Pi/2 + Pi/8), mz], [ir·cos(Pi/2 + Pi/4), ir·sin(Pi/2 + Pi/4), mz], [ir·cos(Pi/2 + Pi/2.5), ir·sin(Pi/2
    + Pi/2.5), mz], [0.85·ir·cos(Pi/8), 0.85·ir·sin(Pi/8), mz], [0.7·ir·cos(Pi/5.2), 0.7·ir·sin(Pi/5.2), mz],
    [0.5·ir·cos(Pi/2), 0.5·ir·sin(Pi/2), mz], [0.575·ir·cos(Pi/2 + Pi/2.5), 0.575·ir·sin(Pi/2 + Pi/2.5), mz],
    [0.6·ir·cos(Pi/2 + Pi/4), 0.6 ir·sin(Pi/2 + Pi/4), mz], [0.25·ir·cos(Pi/2), 0.25·ir·sin(Pi/2), mz]] :
for n from 1 to nops(tmpList) do
 tmpList := [op(tmpList), [tmpList[n][1], −tmpList[n][2], tmpList[n][3]]] :
end do:
for n from 1 to nops(tmpList) do
 tmpList := [op(tmpList), [tmpList[n][1], tmpList[n][2], iz]] :
end do:
tmpList := evalf(tmpList);
PList := [op(PList), op(tmpList)] :

# implement main and co- ducts to connect the inlet basin and the spherical gap
tmpList := [[md, 0, mz], [md, 0, 0.008], [md, 0, iz], [md + d/2·cos(Pi/4), d/2·cos(Pi/4), 0.008], [md − d/2
    ·cos(Pi/4), d/2·cos(Pi/4), 0.008], [md + 0.7·d/2·cos(Pi/4), 0.7·d/2·cos(Pi/4), 0.008], [md − 0.7·d/2
    ·cos(Pi/4), 0.7·d/2·cos(Pi/4), 0.008]] :
```

for n **from** 3 **to** $nops(tmpList)$ **do**
$tmpList := [op(tmpList), [tmpList[n][1], -tmpList[n][2], tmpList[n][3]]]$;
end do:

$$tmpList := \left[op(tmpList), [R - os, 0, 0.008], [R - os - d, 0, 0.008], \left[\mathrm{md}, \frac{\mathrm{d}}{2}, 0.008\right], \left[\mathrm{md}, -\frac{\mathrm{d}}{2}, 0.008\right]\right];$$

for n **from** 0 **to** 7 **do**

$$tmpList := \left[op(tmpList), \left[\mathrm{md} + \cos\left(\frac{n\cdot \mathrm{Pi}}{4}\right)\cdot\left(\frac{d}{2} + kr\right), \sin\left(\frac{n\cdot \mathrm{Pi}}{4}\right)\cdot\left(\frac{d}{2} + kr\right), 0.008\right], \left[\mathrm{md} + \cos\left(\frac{n\cdot \mathrm{Pi}}{4}\right)\cdot\left(\frac{d}{2}\right), \sin\left(\frac{n\cdot \mathrm{Pi}}{4}\right)\cdot\left(\frac{d}{2}\right), mz\right], \left[\mathrm{md} + \cos\left(\frac{n\cdot \mathrm{Pi}}{4}\right)\cdot\left(\frac{d}{2}\right), \sin\left(\frac{n\cdot \mathrm{Pi}}{4}\right)\cdot\left(\frac{d}{2}\right), iz\right]\right]:$$

end do:

$$f := \left(\frac{d}{2} + kr - 0.7\cdot\frac{d}{2}\right)\cdot\cos\left(\arcsin\left(\frac{mz - mz2}{\frac{d}{2} + kr - 0.7\cdot\frac{d}{2}}\right)\right):$$

for n **from** 1 **to** 7 **by** 2 **do**

$$tmpList := \left[op(tmpList), \left[\mathrm{md} + \left(\frac{\mathrm{d}}{2} + kr - f\right)\cdot\cos\left(\frac{n\cdot \mathrm{Pi}}{4}\right), \left(\frac{\mathrm{d}}{2} + kr - f\right)\cdot\sin\left(\frac{n\cdot \mathrm{Pi}}{4}\right), mz\right], \left[\mathrm{md} + \left(\frac{\mathrm{d}}{2} + kr - f\right)\cdot\cos\left(\frac{n\cdot \mathrm{Pi}}{4}\right), \left(\frac{\mathrm{d}}{2} + kr - f\right)\cdot\sin\left(\frac{n\cdot \mathrm{Pi}}{4}\right), iz\right]\right];$$

end do:

$tmpList := evalf(tmpList)$;
$PList := [op(PList), op(tmpList)]$:
$tmpList := [md2, md3, md2 + [0, 0, iz - mz]]$:

for n **from** 0 **to** 7 **do**

$$tmpList := \left[op(tmpList), md3 + \left[\frac{d2}{2}\cdot\cos\left(\frac{n\cdot \mathrm{Pi}}{4}\right), \frac{d2}{2}\cdot\sin\left(\frac{n\cdot \mathrm{Pi}}{4}\right), 0\right], md3 + \left[\left(\frac{d2}{2} + kr\right)\cdot\cos\left(\frac{n\cdot \mathrm{Pi}}{4}\right), \left(\frac{d2}{2} + kr\right)\cdot\sin\left(\frac{n\cdot \mathrm{Pi}}{4}\right), 0\right], md2 + \left[\left(\frac{d2}{2}\right)\cdot\cos\left(\frac{n\cdot \mathrm{Pi}}{4}\right), \left(\frac{d2}{2}\right)\cdot\sin\left(\frac{n\cdot \mathrm{Pi}}{4}\right), 0\right], md2 + \left[\left(\frac{d2}{2}\right)\cdot\cos\left(\frac{n\cdot \mathrm{Pi}}{4}\right), \left(\frac{d2}{2}\right)\cdot\sin\left(\frac{n\cdot \mathrm{Pi}}{4}\right), \mathrm{iz} - \mathrm{mz}\right]\right]:$$

end do:
for n **from** 1 **to** 7 **by** 2 **do**

$$tmpList := \left[op(tmpList), md3 + \left[0.7\cdot\frac{d2}{2}\cdot\cos\left(\frac{n\cdot \mathrm{Pi}}{4}\right), 0.7\cdot\frac{d2}{2}\cdot\sin\left(\frac{n\cdot \mathrm{Pi}}{4}\right), 0\right]\right]:$$

end do:

$$f := \left(\frac{d2}{2} + kr - 0.7\cdot\frac{d2}{2}\right)\cdot\cos\left(\arcsin\left(\frac{mz - mz2}{\frac{d2}{2} + kr - 0.7\cdot\frac{d2}{2}}\right)\right):$$

for n **from** 1 **to** 7 **by** 2 **do**

$$tmpList := \left[op(tmpList), \mathrm{md2} + \left[\left(\frac{\mathrm{d2}}{2} + kr - f\right)\cdot\cos\left(\frac{n\cdot \mathrm{Pi}}{4}\right), \left(\frac{\mathrm{d2}}{2} + kr - f\right)\cdot\sin\left(\frac{n\cdot \mathrm{Pi}}{4}\right), 0\right], \mathrm{md2} + \left[\left(\frac{\mathrm{d2}}{2} + kr - f\right)\cdot\cos\left(\frac{n\cdot \mathrm{Pi}}{4}\right), \left(\frac{\mathrm{d2}}{2} + kr - f\right)\cdot\sin\left(\frac{n\cdot \mathrm{Pi}}{4}\right), \mathrm{iz} - \mathrm{mz}\right]\right];$$

end do:
for n **from** 1 **to** $nops(tmpList)$ **do**
$tmpList := [op(tmpList), [\mathrm{tmpList[n][1]}, -tmpList[n][2], tmpList[n][3]]]$:
end do:
$tmpList := evalf(tmpList)$;
$PList := [op(PList), op(tmpList)]$:
$tmpList := [\,]$:

 # make smooth transitions ("trumpets") from the ducts into the spherical gap

$$lr := \left[md - \frac{d}{2} - kr, 0, \mathrm{sqrt}\left((R + kr)^2 - \left(\mathrm{md} - \frac{d}{2} - kr\right)^2\right)\right]:$$

$radii := [\mathrm{sqrt}((lr[1] + kr)^2 + lr[3]^2)]$:

$\phi := \mathrm{Pi} - \arctan\left(\frac{lr[3]}{lr[1]}\right):$
$a := md + \frac{d}{2}:$
$b := fsolve(a^2 + s^2 = radii[1]^2, s)[2]:$
$c := radii[1]:$
$tx := -\frac{1}{2} \cdot \frac{R^2 - a^2 - b^2}{R - a}:$
$ur := [a + tx, 0, b]:$
$\theta := \arctan\left(\frac{ur[3]}{ur[1]}\right):$
$r1 := [scaleme(ur[1], ur[2], ur[3], R)]:$
$r2 := [scaleme(lr[1], lr[2], lr[3], R)]:$
$radii := [\,]:$
for i **from** 0 **to** 5 **do**
if i $\neq$ 4 **then**
$radii := \left[op(radii), \mathrm{sqrt}\left(\left(lr[3] - kr \cdot \sin\left(\frac{i \cdot \phi}{5}\right)\right)^2 + \left(lr[1] + kr \cdot \cos\left(\frac{i \cdot \phi}{5}\right)\right)^2\right)\right]:$
$cmd := \frac{1}{2} \cdot \left(ur[1] - tx \cdot \cos\left(\frac{i \cdot \theta}{5}\right) + lr[1] + kr \cdot \cos\left(\frac{i \cdot \phi}{5}\right)\right):$
$cd := ur[1] - tx \cdot \cos\left(\frac{i \cdot \theta}{5}\right) - \mathrm{lr}[1] - \mathrm{kr} \cdot \cos\left(\frac{i \cdot \phi}{5}\right):$
for n **from** 0 **to** 31 **do**
$x := cmd + \frac{cd}{2} \cdot \cos\left(\frac{n \cdot 2 \cdot \mathrm{Pi}}{32}\right):$
$y := \frac{cd}{2} \cdot \sin\left(\frac{n \cdot 2 \cdot \mathrm{Pi}}{32}\right):$
$z := fsolve(x^2 + y^2 + s^2 = radii[\mathrm{i} + 1]^2, s)[2]:$
$tmpList := [op(tmpList), [\mathrm{x}, \mathrm{y}, \mathrm{z}]]:$
if $i = 5$ **then**
$tmpList := [op(tmpList), [\mathrm{scaleme}(\mathrm{evalf}(\mathrm{x}, 20), \mathrm{evalf}(\mathrm{y}, 20), \mathrm{evalf}(\mathrm{z}, 20), \mathrm{r})]]:$
end if:
if $evalb(n \in [0, 1, 2, 3, 4, 12, 13, 14, 15, 16, 17, 18, 19, 20, 28, 29, 30, 31])$ **then**
$x := cmd + \left(0.6 + 0.2 \cdot \sin\left(\frac{n \cdot 2 \cdot \mathrm{Pi}}{32}\right)^2\right) \cdot \frac{cd}{2} \cdot \cos\left(\frac{n \cdot 2 \cdot \mathrm{Pi}}{32}\right):$
$y := \left(0.6 + 0.2 \cdot \sin\left(\frac{n \cdot 2 \cdot \mathrm{Pi}}{32}\right)^2\right) \cdot \frac{cd}{2} \cdot \sin\left(\frac{n \cdot 2 \cdot \mathrm{Pi}}{32}\right):$
$z := fsolve(x^2 + y^2 + s^2 = radii[\mathrm{i} + 1]^2, s)[2]:$
$tmpList := [op(tmpList), [\mathrm{x}, \mathrm{y}, \mathrm{z}]]:$
else
$x := cmd + \left(0.8 - 0.2 \cdot \sin\left(\frac{n \cdot 2 \cdot \mathrm{Pi}}{32}\right)^2\right) \cdot \frac{cd}{2} \cdot \cos\left(\frac{n \cdot 2 \cdot \mathrm{Pi}}{32}\right):$
$y := \left(0.8 - 0.2 \cdot \sin\left(\frac{n \cdot 2 \cdot \mathrm{Pi}}{32}\right)^2\right) \cdot \frac{cd}{2} \cdot \sin\left(\frac{n \cdot 2 \cdot \mathrm{Pi}}{32}\right):$
$z := fsolve(x^2 + y^2 + s^2 - radii[\mathrm{i} + 1]^2, s)[2]:$
$tmpList := [op(tmpList), [\mathrm{x}, \mathrm{y}, \mathrm{z}]]:$
end if:
if $i = 5$ **then**
$tmpList := [op(tmpList), [\mathrm{scaleme}(\mathrm{evalf}(\mathrm{x}, 20), \mathrm{evalf}(\mathrm{y}, 20), \mathrm{evalf}(\mathrm{z}, 20), \mathrm{r})]]:$
end if:
end do:
else $radii := \left[op(radii), \mathrm{sqrt}\left(\left(lr[3] - kr \cdot \sin\left(\frac{i \cdot \phi}{5}\right)\right)^2 + \left(R - os2 - d2 - kr + kr \cdot \cos\left(\frac{i \cdot \phi}{5}\right)\right)^2\right)\right]:$
end if:
end do:
$tmpList := evalf(tmpList);$
$PList := [op(PList), op(tmpList)]:$

```
tmpList := [ ]:
lr := (R − os2 − d2 − kr)/(R − os2 − d2/2) · [md2[1], md2[2], 0]:
lr[3] := sqrt((R + kr)^2 − sqrt(lr[1]^2 + lr[2]^2)^2):
radii := [sqrt((R − os2 − d2)^2 + lr[3]^2)]:
ϕ := Pi − arctan(lr[3]/sqrt(lr[1]^2 + lr[2]^2)):
a := R − os2:
b := fsolve(a^2 + s^2 = radii[1]^2, s)[2]:
c := radii[1]:
tx := −1/2 · (R^2 − a^2 − b^2)/(R − a):
ur := [(a + tx)·cos(ϑ), (a + tx)·sin(ϑ), b]:
θ := arctan(b/(a + tx)):
r3 := [scaleme(ur[1], ur[2], ur[3], R)]:
r4 := [scaleme(lr[1], lr[2], lr[3], R)]:
radii := [ ]:
for i from 0 to 5 do
 if i ≠ 4 then
  radii := [op(radii), sqrt((lr[3] − kr·sin(i·ϕ/5))^2 + (R − os2 − d2 − kr + kr·cos(i·ϕ/5))^2)]:
  cmd := 1/2 · (sqrt(ur[1]^2 + ur[2]^2) − tx·cos(i·θ/5) + sqrt(lr[1]^2 + lr[2]^2) + kr·cos(i·ϕ/5)):
  cd := sqrt(ur[1]^2 + ur[2]^2) − tx·cos(i·θ/5) − sqrt(lr[1]^2 + lr[2]^2) − kr·cos(i·ϕ/5):
  for n from 0 to 31 do
   x := cmd·cos(ϑ) + cd/2 · cos(n·2·Pi/32):
   y := cmd·sin(ϑ) + cd/2 · sin(n·2·Pi/32):
   z := fsolve(x^2 + y^2 + s^2 = radii[i + 1]^2, s)[2]:
   tmpList := [op(tmpList), [x, y, z]]:
   if i = 5 then
    tmpList := [op(tmpList), [scaleme(evalf(x, 20), evalf(y, 20), evalf(z, 20), r)]]:
   end if:
   if evalb(n ∈ [0, 1, 2, 3, 4, 12, 13, 14, 15, 16, 17, 18, 19, 20, 28, 29, 30, 31]) then
    x := cmd·cos(ϑ) + (0.6 + 0.2·sin(n·2·Pi/32)^2) · cd/2 · cos(n·2·Pi/32):
    y := cmd·sin(ϑ) + (0.6 + 0.2·sin(n·2·Pi/32)^2) · cd/2 · sin(n·2·Pi/32):
    z := fsolve(x^2 + y^2 + s^2 = radii[i + 1]^2, s)[2]:
    tmpList := [op(tmpList), [x, y, z]]:
   else
    x := cmd·cos(ϑ) + (0.8 − 0.2·sin(n·2·Pi/32)^2) · cd/2 · cos(n·2·Pi/32):
    y := cmd·sin(ϑ) + (0.8 − 0.2·sin(n·2·Pi/32)^2) · cd/2 · sin(n·2·Pi/32):
    z := fsolve(x^2 + y^2 + s^2 = radii[i + 1]^2, s)[2]:
    tmpList := [op(tmpList), [x, y, z]]:
   end if:
   if i = 5 then
    tmpList := [op(tmpList), [scaleme(evalf(x, 20), evalf(y, 20), evalf(z, 20), r)]]:
   end if:
 end do:
```

```
 else radii := [op(radii), sqrt(((lr[3] - kr·sin(i·ϕ/5))^2 + (R - os2 - d2 - kr + kr·cos(i·ϕ/5))^2))]:
end if:
end do:
for n from 1 to nops(tmpList) do
 tmpList := [op(tmpList), [tmpList[n][1], -tmpList[n][2], tmpList[n][3]]]:
end do:
tmpList := evalf(tmpList);
PList := [op(PList), op(tmpList)]:
tmpList := []:

# form the top of the sphere and spherical gap
L := [4, 12, 20, 28];
L2 := [0.2·r, 0.4·r, 0.8·r, 1.15·r];
for n from 1 to nops(L) do
 for i from 0 to L[n] - 1 do
  if evalf(cos(2· Pi/L[n] + 2·i·2· Pi/L[n])) ≥ 0 then
   x := (0.8 + 0.2·sin(Pi/L[n] + i·2· Pi/L[n])^2)·L2[n]·cos(Pi/L[n] + i·2· Pi/L[n]):
   y := (0.8 + 0.2·sin(Pi/L[n] + i·2· Pi/L[n])^2)·L2[n]·sin(Pi/L[n] + i·2· Pi/L[n]):
   z := fsolve(x^2 + y^2 + s^2 = R^2, s)[2]:

   tmpList := [op(tmpList), [x, y, z], [scaleme(evalf(x, 20), evalf(y, 20), evalf(z, 20), r)]]:
  else
   x := (1-0.2·sin(Pi/L[n] + i·2· Pi/L[n])^2)·L2[n]·cos(Pi/L[n] + i·2· Pi/L[n]):
   y := (1-0.2·sin(Pi/L[n] + i·2· Pi/L[n])^2)·L2[n]·sin(Pi/L[n] + i·2· Pi/L[n]):
   z := fsolve(x^2 + y^2 + s^2 = R^2, s)[2]:
   tmpList := [op(tmpList), [x, y, z], [scaleme(evalf(x, 20), evalf(y, 20), evalf(z, 20), r)]]:
  end if:
 end do:
end do:
tmpList := [op(tmpList), [0, 0, mz], [0, 0, iz]]:
tmpList := evalf(tmpList);
PList := [op(PList), op(tmpList)]:

# some finishing touches to the inlet basin
tmpList := [[[0.25·ir·cos(Pi/6), 0.25·ir·sin(Pi/6), mz], [0.1·ir·cos(Pi/2), 0.1·ir·sin(Pi/2), mz], [0.55·ir
      ·cos(27·Pi/28), 0.55·ir·sin(27·Pi/28), mz], [ir·cos(27·Pi/28), ir·sin(27·Pi/28), mz]]:
for n from 1 to nops(tmpList) do
 tmpList := [op(tmpList), [tmpList[n][1], -tmpList[n][2], tmpList[n][3]]]:
end do:
for n from 1 to nops(tmpList) do
 tmpList := [op(tmpList), [tmpList[n][1], tmpList[n][2], iz]]:
end do:
tmpList := evalf(tmpList);
PList := [op(PList), op(tmpList)]:

return(PList);
end proc:
> # finally, execute the procedure and output the points in a way that gmsh can understand
#PList:=createmesh(kugelR, spalt, zulauf, Eindringtiefe, Krümmungsradius, offset, winkel, offset2, zulauf2):
PList := createmesh(0.004, 0.001, 0.0016, 0.0002, 0.0001, 0.0016, 0.873676900, 0.0016, 0.0016):
```

```
PArray := Array(1 ..nops(PList), 1 ..3) :
for n from 1 to nops(PList) do
 PArray[n, 1] := PList[n][1] :
 PArray[n, 2] := PList[n][2] :
 PArray[n, 3] := PList[n][3] :
end do:
for n from 1 to nops(PList) do
 printf("\nPoint(%d) = {%a, %a, %a};", n, PArray[n][1], PArray[n][2], PArray[n][3]);
end do:
```

```
Point(1) = {0, 0, 0};
Point(2) = {.44785790441323143388e-3, .39748488395729703341e-2, 0.};
Point(3) = {.13211162478206683270e-2, .37755333212334702516e-2, 0.};
.
.
Point(1750) = {-.21861668617651336838e-2, -.24632184742727728866e-3, .14000000000000000000e-1};
Point(1751) = {-.39748488395729703341e-2, -.44785790441323143392e-3, .14000000000000000000e-1};
```

B.3 Selective Grid Refinement

Selective grid refinement refines the computational grid in certain areas based on predefined criteria. The advantage of this is that the grid need only to be fine in close proximity to particular areas of interest and not in the entire domain. Doing so keeps both the number of cells and the computational cost low while the accuracy of obtained results remains comparable to that achieved on an entirely refined mesh. Two particular refinement methods are described here: adaptive grid refinement during the simulation and local grid refinement prior to the simulation.

For *adaptive grid refinement* the solver `rhoPimpleFoam` [Ope13a] is modified to be able to refine the mesh based on user defined criteria. More specifically, every 10 time steps the solver checks the mesh for cells with $\mu_{sgs} > 10^{-5}$. Each of these cells is split equidistantly into eight smaller cells. Also, previously refined cells are checked for cell clusters in which $\mu_{sgs} < 10^{-7}$ in which case they revert back to a coarser cell. Hence, areas with high shear stress, i.e. near-wall regions and areas with heavy turbulence are resolved with greater precision, thereby increasing overall accuracy of the flow's characteristics (see Figure B.4).

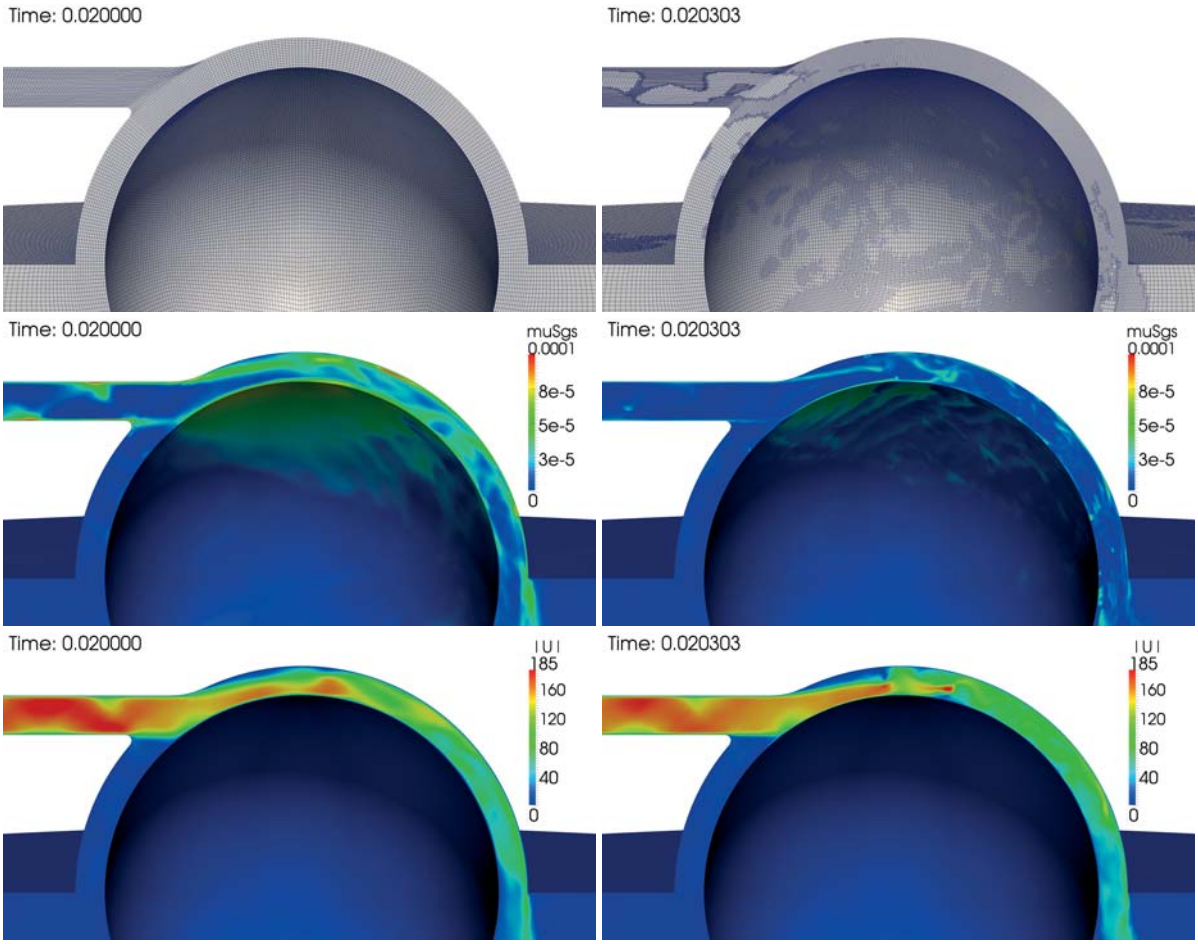

Figure B.4: Adaptive grid refinement for the *GrindBall*

The advantage of this method is that the number of cells and thus the computational cost is matched perfectly to the geometry, the flow, and the requirements of the user. However, computational cost is added each time the grid is refined. Although the refinement frequency can be defined by the user, too low a frequency will reduce accuracy and make this method less effective. Adaptive grid refinement is especially effective for simulations in which the area of interest is in motion, such as the phase interface in multiphase flow or the transition from sub to supersonic speeds in high-speed compressible flows. For simulations involving the *GrindBall*, however, this method is not favourable as the area of interest, i.e. the area adjacent to the sphere is not in motion. Furthermore, the solver does not distinguish between patches. Thus the criteria for refinement cannot be limited to close proximity to the sphere, but are applied in the entire domain. The number of cells are thereby unnecessarily increased, e.g. because of refinements being made on the work piece or near the outlet.

Local grid refinement is applied in the pre-processing stage. Using `snappyHexMesh` - a tool in `OpenFOAM` capable of modifying meshes - the grid is refined in a spatially defined area. While this may incur a larger number of cells, the refinement is permanent and no further computational cost arises from modifications during the simulation. This is the method used for the 40 mm *GrindBall* discussed in Section 4.2. Figure 4.12 shows an unrefined mesh as well as a refined mesh with all cells within 3 mm of the sphere refined once. The level of refinement is not limited to 1. Figure B.5 shows the mesh used for simulation of a submarine under water. The grid becomes finer with increasing proximity to the hull of the vehicle.

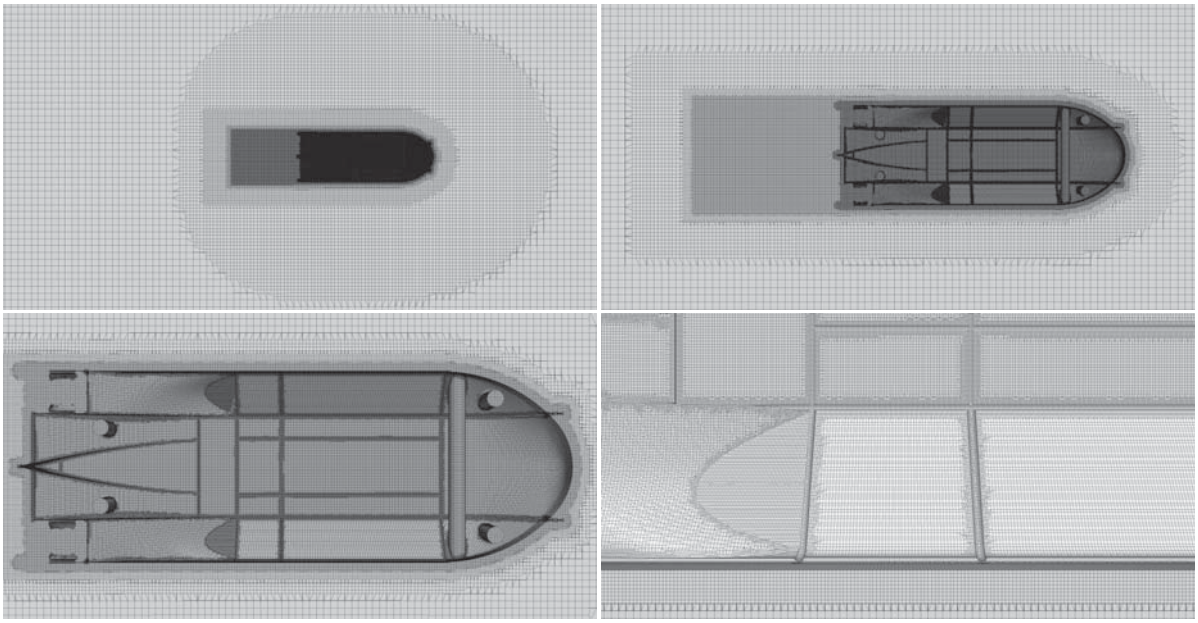

Figure B.5: Local grid refinement for a submarine

Appendix C

Supplemental results

This chapter contains supplemental results that are instrumental to the analyses conducted in this thesis. Results are sorted in order of appearance of the different cases in the main body of the thesis:

- 40 mm *GrindBall* prototype
- Dynamometer validation experiments
- 8 mm hydraulic grinding tool
- Scalability analysis

Dimensioned coefficients are presented with their actual values and dimensions. The corresponding equations are also given for the purpose of quick association as well as their non-dimensional form according to eqns (7.39)-(7.42). Furthermore, data used to generate plots and figures are given in the form of tables containing numeric values for reference.

Quick Reference Guide

The following provides a brief summary of relevant variables and their variations.

Variables

F_t	Tangential force
$F_{t,0}$	Stationary tangential force
F_x, F_y, F_z, F_n	Normal forces
f	Rotation frequency
f_0	Idle rotation frequency
h	Height/length
P_G	Grinding power
$P_{\max}$	Maximum grinding power

$\underline{\mathbf{P}}_{\text{op}}$	Operating point vector for grinding power
p	Pressure
$\dot{V}_N$	Standard volumetric flow rate
α, β	Dimensioned coefficients
$\zeta, \eta.\xi$	Parametric values
σ	Standard deviation

Superscripts

p	*GrindBall* prototype
oil	8 mm pneumatic grinding tool
40 mm	40 mm triple duct hydraulic tool
8 mm	8 mm triple duct hydraulic tool
1 mm	1 mm triple duct hydraulic tool
D	Dimensionless parameter

C.1 40mm GrindBall prototype (Chapter 4)

The following equations are relevant to the analysis conducted in Chapter 4 regarding the 40 mm pneumatic *GrindBall* prototype. In their dimensioned forms they read:

Relevant equations

$$\overline{F}_x^p = \beta_1^p \dot{V}_N^{1.789} \tag{4.18}$$
$$\overline{F}_z^p = \beta_2^p \dot{V}_N^{1.912} \tag{4.19}$$
$$F_{t,0}^p = \alpha_1^p \dot{V}_N^{1.544} \tag{4.20}$$
$$f_0^p = \alpha_2^p \dot{V}_N^{0.875} \tag{4.21}$$
$$F_t^p = (\alpha_3^p \dot{V}_N^{1.544}) \left(\alpha_4^p - \alpha_5^p \dot{V}_N{}^{-0.875} f\right) \tag{4.24}$$
$$P_{\max}^p = \alpha_6^p f^{2.798} \tag{4.29}$$
$$P_G^p = \alpha_7^p \dot{V}_N^{0.632} f^2 + \alpha_8^p \dot{V}_N^{1.566} f \tag{4.32}$$
$$\underline{\mathbf{P}}_{\text{op}}^p(\xi) = \left(\alpha_9^p \xi^{0.875}, \alpha_{10}^p \xi, \alpha_{11}^p \xi^{2.453}\right). \tag{4.36}$$

These equations contain dimensioned coefficients α_n^p and β_n^p, which are given in the following table:

Coefficients

function	coefficients	unit
$\overline{F}_x^p$	$\beta_1^p = 1.674 \cdot 10^{-3}$	$\mathrm{N\,h^{1.789}\,m^{-3\cdot 1.789}}$
$\overline{F}_z^p$	$\beta_2^p = 8.901 \cdot 10^{-3}$	$\mathrm{N\,h^{1.912}\,m^{-3\cdot 1.912}}$
$F_{t,0}^p$	$\alpha_1^p = 1.203 \cdot 10^{-3}$	$\mathrm{N\,h^{1.544}\,m^{-3\cdot 1.544}}$
f_0^p	$\alpha_2^p = 52.384$	$\mathrm{Hz\,h^{0.875}\,m^{-3\cdot 0.875}}$
F_t^p	$\alpha_3^p = 1.203 \cdot 10^{-3}$	$\mathrm{N^{0.5}\,h^{1.544}\,m^{-3\cdot 1.544}}$
	$\alpha_4^p = 1$	$\mathrm{N^{0.5}}$
	$\alpha_5^p = 1.909 \cdot 10^{-2}$	$\mathrm{N^{0.5}\,h^{\text{-}0.875}\,m^{3\cdot 0.875}\,s}$
$P_{\max}^p$	$\alpha_6^p = 2.029 \cdot 10^{-7}$	$\mathrm{W\,s^{2.798}}$
P_G^p	$\alpha_7^p = -3.129 \cdot 10^{-6}$	$\mathrm{W\,h^{0.632}\,m^{-3\cdot 0.632}\,s^2}$
	$\alpha_8^p = 1.463 \cdot 10^{-4}$	$\mathrm{W\,h^{1.566}\,m^{-3\cdot 1.566}\,s}$
$\underline{\mathbf{P}}_{\mathrm{op}}^p(\xi)$	$\alpha_9^p = 26.192$	Hz
	$\alpha_{10}^p = 1$	$\mathrm{m^3\,h^{\text{-}1}}$
	$\alpha_{11}^p = 1.867 \cdot 10^{-3}$	W

Table C.3: Coefficients for the 40 mm *GrindBall* prototype

Using the non-dimensionalisation technique introduced in Chapter 7 by eqns (7.39)-(7.42), dimensionless equations can be derived for each quantity presented above:

Relevant non-dimensional equations

$$
\begin{aligned}
\overline{F}_x^{D,p} &= 29.093 \dot{V}_N^{D1.789} \\
\overline{F}_z^{D,p} &= 65.790 \dot{V}_N^{D1.912} \\
F_{t,0}^{D,p} &= 114.792 \dot{V}_N^{D1.544} \\
f_0^{D,p} &= 3.597 \dot{V}_N^{D0.875} \\
F_t^{D,p} &= (1.736 \cdot 10^{-3} \dot{V}_N^{D1.544}) \left(66122.474 - 18382.753 \dot{V}_N^{D-0.875} f^D\right) \\
P_{\max}^{D,p} &= 97.529 f^{D2.798} \\
P_G^{D,p} &= -281.173 \dot{V}_N^{D0.632} f^{D2} + 599.028 \dot{V}_N^{D1.566} f^D \\
\underline{\mathbf{P}}_{\mathrm{op}}^{D,p}(\xi) &= \left(787.729 \xi^{0.875}, 1044.277 \xi, 1.227 \cdot 10^{10} \xi^{2.453}\right).
\end{aligned}
$$

C.2 Dynamometer validation (Chapter 5)

The results obtained while performing the validation experiments described in Chapter 5 are given here in detail. The experimental data used to generate the plots in Figure 5.6 and 5.7 are presented in Table C.4:

$\dot{V}_N$ [m^3/h]	$F_y^{45°}$	$\sigma(F_y^{45°})$	$F_z^{45°}$	$\sigma(F_z^{45°})$	$F_y^{60°}$	$\sigma(F_y^{60°})$	$F_z^{60°}$	$\sigma(F_z^{60°})$	$F_z^{90°}$	$\sigma(F_z^{90°})$
4	0.038	0.010	0.059	0.007	0.040	0.005	0.117	0.005	0.139	0.003
6	0.081	0.014	0.170	0.028	0.060	0.015	0.228	0.017	0.257	0.006
8	0.130	0.034	0.265	0.076	0.107	0.024	0.380	0.060	0.406	0.027
10	0.218	0.060	0.397	0.146	0.152	0.037	0.458	0.088	0.5827	0.027

Table C.4: Dynamometer validation: experimental results

Figure 5.6 and 5.7 also contain data from simulation results. This data is given in Table C.5:

$\dot{V}_N$ [m^3/h]	$F_y^{45°}$	$\sigma(F_y^{45°})$	$F_z^{45°}$	$\sigma(F_z^{45°})$	$F_y^{60°}$	$\sigma(F_y^{60°})$	$F_z^{60°}$	$\sigma(F_z^{60°})$	$F_z^{90°}$	$\sigma(F_z^{90°})$
4	-0.036	0.028	0.074	0.120	-0.025	0.020	0.100	0.064	0.123	0.017
6	-0.084	0.020	0.153	0.077	-0.059	0.014	0.212	0.046	0.258	0.047
8	-0.141	0.058	0.251	0.077	-0.099	0.018	0.346	0.040	0.418	0.029
10	-0.208	0.053	0.353	0.074	-0.148	0.025	0.479	0.049	0.587	0.024

Table C.5: Dynamometer validation: simulation results

See Chapter 5 for details on the dynamometer validation.

C.3 8mm hydraulic grinding tool (Chapter 6)

This section presents results supplemental to the 8 mm hydraulic grinding tool discussed in Chapter 6. Raw data used to generate plots for the propulsion media study and the study of geometric parameters are given, followed by the listing of dimensioned coefficients used in the results section of this chapter.

Parametric study (propulsion media)

Table C.6 shows the data used to generate the plot in Figure 6.2. See Section 6.1.2 for details on the execution of this study.

$\overline{U}_d$		VG5	VG7	VG10	VG15	VG22	VG32	VG46	VG68
10 [m s^{-1}]	F_t [N]	0.016	0.018	0.029	0.038	0.042	0.044	0.042	0.038
	F_n [N]	0.022	0.040	0.087	0.117	0.156	0.223	0.344	0.516
	$p_{\min}$ [mbar]	580	580	898	-2130	-748	862	810	792
20 [m s^{-1}]	F_t [N]	0.031	0.044	0.060	0.093	0.138	0.166	0.177	0.174
	F_n [N]	-0.049	0.020	0.173	0.268	0.412	0.522	0.739	1.068
	$p_{\min}$ [mbar]	-968	-1003	-924	-308	493	493	378	264
30 [m s^{-1}]	F_t [N]					0.214	0.316	0.386	0.400
	F_n [N]					0.664	0.963	1.234	1.683
	$p_{\min}$ [mbar]					-1883	-176	-185	-405

Table C.6: Results of the propulsion fluid study: Tangential force F_t, contact force F_n, and minimum pressure $p_{\min}$

Parametric study (geometric parameters)

The following lists the data obtained in the study of geometric parameters for the hydraulic 8 mm grinding tool discussed in Section 6.2.

Table C.7 shows the data used to generate the plot depicted in Figure 6.3 in Section 6.2.1.

h_g [mm]	F_t	$\sigma(F_t)$	F_x	$\sigma(F_x)$	F_z	$\sigma(F_z)$
1.0	0.17682	$5.50{\cdot}10^{-7}$	0.02251	$1.58{\cdot}10^{-5}$	0.73874	$1.19{\cdot}10^{-6}$
0.9	0.17660	$4.76{\cdot}10^{-8}$	0.00238	$4.64{\cdot}10^{-7}$	0.85214	$2.14{\cdot}10^{-5}$
0.8	0.17408	$5.14{\cdot}10^{-8}$	-0.03704	$1.71{\cdot}10^{-8}$	1.04408	$6.59{\cdot}10^{-9}$

Table C.7: Results of the gap height study. All forces in [N]

The study of the co-duct positions performed in Section 6.2.2 bases its results on the data in Table C.8, which is also used to generate the plot in Figure 6.5.

Case	F_t	$\sigma(F_t)$	F_x	$\sigma(F_x)$	F_z	$\sigma(F_z)$
Case 0	0.17682	$5.50{\cdot}10^{-7}$	0.02251	$1.58{\cdot}10^{-5}$	0.73874	$1.19{\cdot}10^{-6}$
Case 1	0.21476	$5.76{\cdot}10^{-8}$	0.01309	$1.31{\cdot}10^{-6}$	0.66300	$2.18{\cdot}10^{-5}$
Case 2	0.17967	$2.08{\cdot}10^{-8}$	0.01646	$2.63{\cdot}10^{-7}$	0.67602	$1.21{\cdot}10^{-8}$
Case 3	0.22436	$6.56{\cdot}10^{-9}$	0.00474	$1.79{\cdot}10^{-7}$	0.61082	$7.55{\cdot}10^{-7}$
Case 4	0.24060	$1.46{\cdot}10^{-9}$	-0.00379	$7.40{\cdot}10^{-8}$	0.57603	$3.04{\cdot}10^{-8}$

Table C.8: Results of the co-duct position study. All forces in [N]

An optimal value for the duct diameter is derived in Section 6.2.3. The data used to generate the plot in Figure 6.6 is presented in Table C.9:

h_d [mm]	F_t	$\sigma(F_t)$	F_x	$\sigma(F_x)$	F_z	$\sigma(F_z)$
1.0	0.17682	$5.50{\cdot}10^{-7}$	0.02251	$1.58{\cdot}10^{-5}$	0.73874	$1.19{\cdot}10^{-6}$
1.1	0.19578	$2.31{\cdot}10^{-7}$	0.07013	$1.36{\cdot}10^{-6}$	0.85399	$3.61{\cdot}10^{-7}$
1.2	0.20437	$2.46{\cdot}10^{-7}$	0.11612	$9.48{\cdot}10^{-7}$	0.96286	$4.69{\cdot}10^{-7}$
1.3	0.22754	$4.92{\cdot}10^{-8}$	0.16176	$1.30{\cdot}10^{-5}$	1.00692	$1.71{\cdot}10^{-6}$
1.4	0.23034	$3.04{\cdot}10^{-8}$	0.21721	$4.88{\cdot}10^{-5}$	1.04630	$7.24{\cdot}10^{-7}$
1.5	0.22957	$3.98{\cdot}10^{-8}$	0.29598	$6.97{\cdot}10^{-5}$	1.02532	$3.22{\cdot}10^{-6}$

Table C.9: Results of the duct diameter study. All forces in [N]

Section 6.2.4 sees the investigation of an optimal value for the main duct offset. The results, including the data used to generate the plot in Figure 6.7, is presented in Table C.10:

$h_{o,1}$ [mm]	F_t	$\sigma(F_t)$	F_x	$\sigma(F_x)$	F_z	$\sigma(F_z)$
0.6	0.17788	$1.10{\cdot}10^{-7}$	0.03534	$8.61{\cdot}10^{-7}$	0.72407	$1.96{\cdot}10^{-8}$
0.7	0.17797	$7.88{\cdot}10^{-8}$	0.03161	$9.22{\cdot}10^{-7}$	0.73117	$3.19{\cdot}10^{-8}$
0.8	0.17682	$5.50{\cdot}10^{-7}$	0.02251	$1.58{\cdot}10^{-5}$	0.73874	$1.19{\cdot}10^{-6}$
0.9	0.17631	$3.30{\cdot}10^{-8}$	0.02119	$5.30{\cdot}10^{-7}$	0.74750	$3.48{\cdot}10^{-8}$
1.0	0.17447	$1.51{\cdot}10^{-8}$	0.01408	$2.74{\cdot}10^{-7}$	0.75703	$4.28{\cdot}10^{-8}$
1.1	0.17185	$6.51{\cdot}10^{-9}$	0.00631	$5.69{\cdot}10^{-8}$	0.76762	$3.19{\cdot}10^{-8}$

Table C.10: Results of the main duct offset study. All forces in [N]

Final optimisations are performed for certain geometric parameters in Section 6.2.5.

The angle ϕ (see Figure 6.4) is optimised using the results presented in Table C.11, which are also used to generate the plot in Figure 6.8.

ϕ	F_t	$\sigma(F_t)$	F_x	$\sigma(F_x)$	F_z	$\sigma(F_z)$
30°	0.24607	$1.44{\cdot}10^{-5}$	0.20734	$8.42{\cdot}10^{-4}$	1.03194	$1.29{\cdot}10^{-3}$
40°	0.28374	$3.45{\cdot}10^{-8}$	0.17919	$1.06{\cdot}10^{-5}$	0.97726	$4.83{\cdot}10^{-7}$
50°	0.32209	$7.13{\cdot}10^{-8}$	0.09779	$3.70{\cdot}10^{-6}$	0.93580	$4.67{\cdot}10^{-5}$
60°	0.34064	$4.28{\cdot}10^{-9}$	-0.01085	$1.01{\cdot}10^{-5}$	0.99565	$1.08{\cdot}10^{-4}$

Table C.11: Results of the angle ϕ study. All forces in [N]

The main duct offset is revisited and optimised based on the data given in Table C.12. This data is also used for the plot in Figure 6.9.

$h_{o,1}$ [mm]	F_t	$\sigma(F_t)$	F_x	$\sigma(F_x)$	F_z	$\sigma(F_z)$
0.6	0.35209	$4.71{\cdot}10^{-9}$	-0.01008	$1.25{\cdot}10^{-6}$	0.95237	$1.40{\cdot}10^{-6}$
0.7	0.34064	$4.28{\cdot}10^{-9}$	-0.01085	$1.01{\cdot}10^{-5}$	0.99565	$1.08{\cdot}10^{-4}$
0.8	0.32910	$2.77{\cdot}10^{-9}$	-0.00800	$1.30{\cdot}10^{-6}$	1.03060	$2.38{\cdot}10^{-7}$

Table C.12: Results of the second main duct offset study. All forces in [N]

Duct diameter is investigated a second time. The results are listed in Table C.13 which is also the basis for the plots in Figure 6.10

h_d [mm]	F_t	$\sigma(F_t)$	F_x	$\sigma(F_x)$	F_z	$\sigma(F_z)$
1.4	0.37323	$8.45{\cdot}10^{-10}$	0.02902	$1.91{\cdot}10^{-6}$	0.83215	$1.81{\cdot}10^{-7}$
1.5	0.37574	$1.61{\cdot}10^{-8}$	0.03758	$2.21{\cdot}10^{-6}$	0.94400	$2.66{\cdot}10^{-7}$
1.6	0.36985	$1.17{\cdot}10^{-7}$	0.04579	$1.36{\cdot}10^{-6}$	1.04997	$3.53{\cdot}10^{-7}$
1.7	0.35579	$3.52{\cdot}10^{-7}$	0.05278	$1.79{\cdot}10^{-6}$	1.14356	$3.16{\cdot}10^{-7}$

Table C.13: Results of the second duct diameter study. All forces in [N]

Relevant equations

The following equations are relevant to the analysis conducted in Chapter 6 regarding the 8 mm hydraulic grinding tool. In their dimensioned forms they read:

$$F_x^{\text{oil}} = (\beta_1^{\text{oil}}\dot{V}^4 + \beta_2^{\text{oil}}\dot{V}^3 + \beta_3^{\text{oil}}\dot{V}^2 + \beta_4^{\text{oil}}\dot{V})f + \beta_5^{\text{oil}}\dot{V}^2 + \beta_6^{\text{oil}}\dot{V} \tag{6.3}$$

$$F_n^{\text{oil}} = (\beta_7^{\text{oil}}\dot{V}^5 + \beta_8^{\text{oil}}\dot{V}^4 + \beta_9^{\text{oil}}\dot{V}^3 + \beta_{10}^{\text{oil}}\dot{V}^2 + \beta_{11}^{\text{oil}}\dot{V})f + \beta_{12}^{\text{oil}}\dot{V}^3 + \beta_{13}^{\text{oil}}\dot{V}^2 + \beta_{14}^{\text{oil}}\dot{V} \tag{6.4}$$

$$F_{t,0}^{\text{oil}} = \alpha_1^{\text{oil}}\dot{V}^{1.777} \tag{6.5}$$

$$f_0^{\text{oil}} = \alpha_2^{\text{oil}}\dot{V}^{1.270} \tag{6.6}$$

$$F_t^{\text{oil}} = (\alpha_3^{\text{oil}}\dot{V}^{1.777})\left(\alpha_4^{\text{oil}} - \alpha_5^{\text{oil}}\dot{V}^{-1.270}f\right) \tag{6.7}$$

$$P_{\max}^{\text{oil}} = \alpha_6^{\text{oil}} f^{2.499} \tag{6.8}$$

$$P_G^{\text{oil}} = \alpha_7^{\text{oil}}\dot{V}^{0.429}f^2 + \alpha_8^{\text{oil}}\dot{V}^{1.801}f \tag{6.9}$$

$$\underline{\mathbf{P}}_{\text{op}}^{\text{oil}}(\xi) = \left(\alpha_9^{\text{oil}}\xi^{1.270}, \alpha_{10}^{\text{oil}}\xi, \alpha_{11}^{\text{oil}}\xi^{2.916}\right). \tag{6.13}$$

These equations contain dimensioned coefficients α_n^{oil} and β_n^{oil}, which are given in the following table.

Coefficients

function	coefficients	unit
F_x^{oil}	$\beta_1^{\text{oil}} = 5.920 \cdot 10^{-6}$	$\text{N}\,\text{min}^4\,\text{l}^{-4}\,\text{s}$
	$\beta_2^{\text{oil}} = 7.202 \cdot 10^{-5}$	$\text{N}\,\text{min}^3\,\text{l}^{-3}\,\text{s}$
	$\beta_3^{\text{oil}} = 1.620 \cdot 10^{-4}$	$\text{N}\,\text{min}^2\,\text{l}^{-2}\,\text{s}$
	$\beta_4^{\text{oil}} = 4.554 \cdot 10^{-4}$	$\text{N}\,\text{min}\,\text{l}^{-1}\,\text{s}$
	$\beta_5^{\text{oil}} = 2.286 \cdot 10^{-2}$	$\text{N}\,\text{min}^2\,\text{l}^{-2}$
	$\beta_6^{\text{oil}} = 6.912 \cdot 10^{-2}$	$\text{N}\,\text{min}\,\text{l}^{-1}$
F_z^{oil}	$\beta_7^{\text{oil}} = 2.833 \cdot 10^{-6}$	$\text{N}\,\text{min}^5\,\text{l}^{-5}\,\text{s}$
	$\beta_8^{\text{oil}} = -4.075 \cdot 10^{-5}$	$\text{N}\,\text{min}^4\,\text{l}^{-4}\,\text{s}$
	$\beta_9^{\text{oil}} = 1.632 \cdot 10^{-4}$	$\text{N}\,\text{min}^3\,\text{l}^{-3}\,\text{s}$
	$\beta_{10}^{\text{oil}} = -9.427 \cdot 10^{-5}$	$\text{N}\,\text{min}^2\,\text{l}^{-2}\,\text{s}$
	$\beta_{11}^{\text{oil}} = 1.303 \cdot 10^{-4}$	$\text{N}\,\text{min}\,\text{l}^{-1}\,\text{s}$
	$\beta_{12}^{\text{oil}} = 3.925 \cdot 10^{-3}$	$\text{N}\,\text{min}^3\,\text{l}^{-3}$
	$\beta_{13}^{\text{oil}} = -3.656 \cdot 10^{-2}$	$\text{N}\,\text{min}^2\,\text{l}^{-2}$
	$\beta_{14}^{\text{oil}} = 0.220$	$\text{N}\,\text{min}\,\text{l}^{-1}$
$F_{t,0}^{\text{oil}}$	$\alpha_1^{\text{oil}} = 1.231 \cdot 10^{-2}$	$\text{N}\,\text{min}^{1.777}\,\text{l}^{-1.777}$
f_0^{oil}	$\alpha_2^{\text{oil}} = 34.518$	$\text{Hz}\,\text{min}^{1.270}\,\text{l}^{-1.270}$
F_t^{oil}	$\alpha_3^{\text{oil}} = 1.231 \cdot 10^{-2}$	$\text{N}^{0.5}\,\text{min}^{1.777}\,\text{l}^{-1.777}$
	$\alpha_4^{\text{oil}} = 1$	$\text{N}^{0.5}$
	$\alpha_5^{\text{oil}} = 2.897 \cdot 10^{-2}$	$\text{N}^{0.5}\,\text{min}^{-1.270}\,\text{l}^{1.270}\,\text{s}$
$P_{\max}^{\text{oil}}$	$\alpha_6^{\text{oil}} = 1.791 \cdot 10^{-6}$	$\text{W}\,\text{s}^{2.499}$
P_G^{oil}	$\alpha_7^{\text{oil}} = -1.047 \cdot 10^{-5}$	$\text{W}\,\text{min}^{0.429}\,\text{l}^{-0.429}\,\text{s}^2$
	$\alpha_8^{\text{oil}} = 3.069 \cdot 10^{-4}$	$\text{W}\,\text{min}^{1.801}\,\text{l}^{-1.801}\,\text{s}$
$\underline{\mathbf{P}}_{\text{op}}^{\text{oil}}(t)$	$\alpha_9^{\text{oil}} = 17.259$	Hz
	$\alpha_{10}^{\text{oil}} = 1$	$\text{l}\,\text{min}^{-1}$
	$\alpha_{11}^{\text{oil}} = 3.498 \cdot 10^{-3}$	W

Table C.14: Coefficients for the 8 mm *GrindBall* using oil

Relevant non-dimensional equations

Using the non-dimensionalisation technique introduced in Chapter 7 by eqns (7.39)-(7.42), dimensionless equations can be derived for each quantity presented above:

$$
\begin{aligned}
F_x^{D,\text{oil}} &= \left(3.666 \cdot 10^{-6}\dot{V}^{D4} + 1.347 \cdot 10^{-3}\dot{V}^{D3} + 9.146 \cdot 10^{-2}\dot{V}^{D2} + 7.762\dot{V}^{D}\right) f^D \\
&\quad +1.496\dot{V}^{D2} + 136.601\dot{V}^{D} \\
F_z^{D,\text{oil}} &= \Big(5.811 \cdot 10^{-8}\dot{V}^{D5} - 2.524 \cdot 10^{-5}\dot{V}^{D4} + 3.051 \cdot 10^{-3}\dot{V}^{D3} \\
&\quad -5.322 \cdot 10^{-2}\dot{V}^{D2} + 2.221\dot{V}^{D}\Big) f^D \\
&\quad + 8.509 \cdot 10^{-3}\dot{V}^{D3} - 2.393\dot{V}^{D2} + 434.783\dot{V}^{D} \\
F_{t,0}^{D,\text{oil}} &= 1.723\dot{V}^{D1.777} \\
f_0^{D,\text{oil}} &= 5.282 \cdot 10^{-2}\dot{V}^{D1.270} \\
F_t^{D,\text{oil}} &= \left(7.052 \cdot 10^{-3}\dot{V}^{D1.777}\right)\left(244.275 - 4624.582\dot{V}^{D-1.270} f^D\right) \\
P_{\max}^{D,\text{oil}} &= 675.301 f^{D2.499} \\
P_G^{D,\text{oil}} &= -312.265\dot{V}^{D0.429} f^{D2} + 9.894\dot{V}^{D1.801} f^D \\
\underline{\mathbf{P}}_{\text{op}}^{D,\text{oil}}(\xi) &= \left(2.001\xi^{1.270}, 30.193\xi, 6050.063\xi^{2.916}\right).
\end{aligned}
$$

C.4 Scale Analysis (Chapter 7)

The following equations are relevant to the analysis conducted in Chapter 7 regarding the scalability analysis conducted for pneumatic propulsion at 40 mm, 8 mm, and 1 mm.

Relevant equations

In their dimensioned forms these equations read:

$$\overline{F}_x^{40\text{mm}} = \beta_1^{40\text{mm}}\dot{V}_N^{2.053} \tag{7.3}$$
$$\overline{F}_x^{8\text{mm}} = \beta_1^{8\text{mm}}\dot{V}_N^{2.038} \tag{7.4}$$
$$\overline{F}_x^{1\text{mm}} = \beta_1^{1\text{mm}}\dot{V}_N^{2.473} \tag{7.5}$$
$$\overline{F}_z^{40\text{mm}} = \beta_2^{40\text{mm}}\dot{V}_N^{2.078} \tag{7.6}$$
$$\overline{F}_z^{8\text{mm}} = \beta_2^{8\text{mm}}\dot{V}_N^{2.216} \tag{7.7}$$
$$\overline{F}_z^{1\text{mm}} = \beta_2^{1\text{mm}}\dot{V}_N^{3} + \beta_3^{1\text{mm}}\dot{V}_N^{2} + \beta_4^{1\text{mm}}\dot{V}_N \tag{7.8}$$
$$F_{0,t}^{40\text{mm}} = \alpha_1^{40\text{mm}}\dot{V}_N^{1.833} \tag{7.9}$$
$$F_{0,t}^{8\text{mm}} = \alpha_1^{8\text{mm}}\dot{V}_N^{1.673} \tag{7.10}$$
$$F_{0,t}^{1\text{mm}} = \alpha_1^{1\text{mm}}\dot{V}_N^{1.441} \tag{7.11}$$
$$f_0^{40\text{mm}} = \alpha_2^{40\text{mm}}\dot{V}_N^{0.985} \tag{7.12}$$
$$f_0^{8\text{mm}} = \alpha_2^{8\text{mm}}\dot{V}_N^{0.921} \tag{7.13}$$
$$f_0^{1\text{mm}} = \alpha_2^{1\text{mm}}\dot{V}_N^{0.869} \tag{7.14}$$

$$F_t^{40\mathrm{mm}} = (\alpha_3^{40\mathrm{mm}} \dot{V}_N^{1.833})(\alpha_4^{40\mathrm{mm}} - \alpha_5^{40\mathrm{mm}} f \dot{V}_N^{-0.985}) \tag{7.17}$$

$$F_t^{8\mathrm{mm}} = (\alpha_3^{8\mathrm{mm}} \dot{V}_N^{1.673})(\alpha_4^{8\mathrm{mm}} - \alpha_5^{8\mathrm{mm}} f \dot{V}_N^{-0.921}) \tag{7.18}$$

$$F_t^{1\mathrm{mm}} = (\alpha_3^{1\mathrm{mm}} \dot{V}_N^{1.829} + \alpha_4^{1\mathrm{mm}}) f^2 + (\alpha_5^{1\mathrm{mm}} \dot{V}_N^{1.369}) f) + \alpha_6^{1\mathrm{mm}} \dot{V}_N^{1.441} \tag{7.19}$$

$$P_{\max}^{40\mathrm{mm}} = \alpha_6^{40\mathrm{mm}} f^{2.782} \tag{7.20}$$

$$P_{\max}^{8\mathrm{mm}} = \alpha_6^{8\mathrm{mm}} f^{2.751} \tag{7.21}$$

$$P_{\max}^{1\mathrm{mm}} = \alpha_7^{1\mathrm{mm}} f^{2.662} \tag{7.22}$$

$$P_G^{40\mathrm{mm}} = \alpha_7^{40\mathrm{mm}} \dot{V}_N^{0.815} f^2 + \alpha_8^{40\mathrm{mm}} \dot{V}_N^{1.833} f \tag{7.24}$$

$$P_G^{8\mathrm{mm}} = \alpha_7^{8\mathrm{mm}} \dot{V}_N^{0.696} f^2 + \alpha_8^{8\mathrm{mm}} \dot{V}_N^{1.664} f \tag{7.25}$$

$$P_G^{1\mathrm{mm}} = (\alpha_8^{1\mathrm{mm}} \dot{V}_N^{1.813} + \alpha_9^{1\mathrm{mm}}) f^3 + \alpha_{10}^{1\mathrm{mm}} \dot{V}_N^{1.588} f^2 + \alpha_{11}^{1\mathrm{mm}} \dot{V}_N^{1.441} f \tag{7.26}$$

$$\underline{\mathbf{P}}_{\mathrm{op}}^{40\mathrm{mm}}(\zeta) = \left(\alpha_9^{40\mathrm{mm}} \zeta^{0.985}, \alpha_{10}^{40\mathrm{mm}} \zeta, \alpha_{11}^{40\mathrm{mm}} \zeta^{2.872}\right) \tag{7.36}$$

$$\underline{\mathbf{P}}_{\mathrm{op}}^{8\mathrm{mm}}(\eta) = \left(\alpha_9^{8\mathrm{mm}} \eta^{0.921}, \alpha_{10}^{8\mathrm{mm}} \eta, \alpha_{11}^{8\mathrm{mm}} \eta^{2.634}\right) \tag{7.37}$$

$$\underline{\mathbf{P}}_{\mathrm{op}}^{1\mathrm{mm}}(\xi) = \left(\alpha_{12}^{1\mathrm{mm}} \xi^{0.827}, \alpha_{13}^{1\mathrm{mm}} \xi, \alpha_{14}^{1\mathrm{mm}} \xi^{2.043}\right). \tag{7.38}$$

These equations contain dimensioned coefficients α_n and β_n, which are given in the following tables.

Coefficients 40 mm

function	coefficients	unit
$\overline{F}_x^{40\mathrm{mm}}$	$\beta_1^{40\mathrm{mm}} = 3.690 \cdot 10^{-4}$	$\mathrm{N\,h^{2.053}\,m^{-3 \cdot 2.053}}$
$\overline{F}_z^{40\mathrm{mm}}$	$\beta_2^{40\mathrm{mm}} = 1.051 \cdot 10^{-4}$	$\mathrm{N\,h^{2.078}\,m^{-3 \cdot 2.078}}$
$F_{t,0}$	$\alpha_1^{40\mathrm{mm}} = 2.582 \cdot 10^{-5}$	$\mathrm{N\,h^{1.833}\,m^{-3 \cdot 1.833}}$
f_0	$\alpha_2^{40\mathrm{mm}} = 6.836$	$\mathrm{Hz\,h^{0.985}\,m^{-3 \cdot 0.985}}$
F_t	$\alpha_3^{40\mathrm{mm}} = 2.582 \cdot 10^{-5}$ $\alpha_4^{40\mathrm{mm}} = 1$ $\alpha_5^{40\mathrm{mm}} = 0.146$	$\mathrm{N^{0.5}\,h^{1.833}\,m^{-3 \cdot 1.833}}$ $\mathrm{N^{0.5}}$ $\mathrm{N^{0.5}\,h^{-0.985}m^{3 \cdot 0.985}\,s}$
$P_{\max}$	$\alpha_6^{40\mathrm{mm}} = 2.553 \cdot 10^{-7}$	$\mathrm{W\,s^{2.782}}$
P_G	$\alpha_7^{40\mathrm{mm}} = -5.495 \cdot 10^{-7}$ $\alpha_8^{40\mathrm{mm}} = 3.253 \cdot 10^{-6}$	$\mathrm{W\,h^{0.815}\,m^{-3 \cdot 0.815}\,s^2}$ $\mathrm{W\,h^{1.833}\,m^{-3 \cdot 1.833}\,s}$
$\underline{\mathbf{P}}_{\mathrm{op}}(t)$	$\alpha_9^{40\mathrm{mm}} = 3.418$ $\alpha_{10}^{40\mathrm{mm}} = 1$ $\alpha_{11}^{40\mathrm{mm}} = 4.409 \cdot 10^{-6}$	Hz $\mathrm{m^3\,h^{-1}}$ W

Table C.15: Coefficients for the 40 mm *GrindBall* using air

Coefficients 8 mm

function	coefficients	unit
$\overline{F}_x^{8\text{mm}}$	$\beta_1^{8\text{mm}} = 1.091 \cdot 10^{-2}$	$\text{N}\,\text{h}^{2.038}\,\text{m}^{-3\cdot 2.038}$
$\overline{F}_z^{8\text{mm}}$	$\beta_2^{8\text{mm}} = 2.376 \cdot 10^{-3}$	$\text{N}\,\text{h}^{2.216}\,\text{m}^{-3\cdot 2.216}$
$F_{t,0}^{8\text{mm}}$	$\alpha_1^{8\text{mm}} = 6.582 \cdot 10^{-4}$	$\text{N}\,\text{h}^{1.673}\,\text{m}^{-3\cdot 1.673}$
$f_0^{8\text{mm}}$	$\alpha_2^{8\text{mm}} = 926.510$	$\text{Hz}\,\text{h}^{0.921}\,\text{m}^{-3\cdot 0.921}$
$F_t^{8\text{mm}}$	$\alpha_3^{8\text{mm}} = 6.582 \cdot 10^{-4}$ $\alpha_4^{8\text{mm}} = 1$ $\alpha_5^{8\text{mm}} = 1.079 \cdot 10^{-3}$	$\text{N}^{0.5}\,\text{h}^{1.673}\,\text{m}^{-3\cdot 1.673}$ $\text{N}^{0.5}$ $\text{N}^{0.5}\,\text{h}^{\text{-}0.921}\,\text{m}^{3\cdot 0.921}\,\text{s}$
$P_{\max}^{8\text{mm}}$	$\alpha_6^{8\text{mm}} = 1.920 \cdot 10^{-10}$	$\text{W}\,\text{s}^{2.751}$
$P_G^{8\text{mm}}$	$\alpha_7^{8\text{mm}} = -1.906 \cdot 10^{-8}$ $\alpha_8^{8\text{mm}} = 1.686 \cdot 10^{-5}$	$\text{W}\,\text{h}^{0.696}\,\text{m}^{-3\cdot 0.696}\,\text{s}^2$ $\text{W}\,\text{h}^{1.664}\,\text{m}^{-3\cdot 1.664}\,\text{s}$
$\underline{\mathbf{P}}_{\text{op}}^{8\text{mm}}(t)$	$\alpha_9^{8\text{mm}} = 463.255$ $\alpha_{10}^{8\text{mm}} = 1$ $\alpha_{11}^{8\text{mm}} = 3.700 \cdot 10^{-3}$	Hz $\text{m}^3\text{h}^{\text{-}1}$ W

Table C.16: Coefficients for the 8 mm *GrindBall* using air

Coefficients 1 mm

function	coefficients	unit
$\overline{F}_x^{1\text{mm}}$	$\beta_1^{1\text{mm}} = 1.566$	$\text{N}\,\text{h}^{2.473}\,\text{m}^{-3\cdot 2.473}$
$\overline{F}_z^{1\text{mm}}$	$\beta_2^{1\text{mm}} = 5.341$ $\beta_3^{1\text{mm}} = -0.422$ $\beta_4^{1\text{mm}} = -4.094 \cdot 10^{-3}$	$\text{N}\,\text{h}^3\,\text{m}^{-9}$ $\text{N}\,\text{h}^2\,\text{m}^{-6}$ $\text{N}\,\text{h}\,\text{m}^{-3}$
$F_{t,0}^{1\text{mm}}$	$\alpha_1^{1\text{mm}} = 1.399 \cdot 10^{-2}$	$\text{N}\,\text{h}^{1.441}\text{m}^{-3\cdot 1.441}$
$f_0^{1\text{mm}}$	$\alpha_2^{1\text{mm}} = 326497.586$	$\text{Hz}\,\text{h}^{0.869}\text{m}^{-3\cdot 0.869}$
$F_t^{1\text{mm}}$	$\alpha_3^{1\text{mm}} = 3.599 \cdot 10^{-11}$ $\alpha_4^{1\text{mm}} = -2.946 \cdot 10^{-13}$ $\alpha_5^{1\text{mm}} = -2.723 \cdot 10^{-7}$ $\alpha_6^{1\text{mm}} = 1.399 \cdot 10^{-2}$	$\text{N}\,\text{h}^{1.829}\text{m}^{-3\cdot 1.829}\,\text{s}^2$ $\text{N}\,\text{s}^2$ $\text{N}\,\text{h}^{1.369}\text{m}^{-3\cdot 1.369}\,\text{s}$ $\text{N}\,\text{h}^{1.441}\text{m}^{-3\cdot 1.441}$
$P_{\max}^{1\text{mm}}$	$\alpha_7^{1\text{mm}} = 4.734 \cdot 10^{-14}$	$\text{Ws}^{2.662}$
$P_G^{1\text{mm}}$	$\alpha_8^{1\text{mm}} = 1.269 \cdot 10^{-13}$ $\alpha_9^{1\text{mm}} = -9.775 \cdot 10^{-16}$	$\text{Wh}^{1.813}\text{m}^{-3\cdot 1.813}\,\text{s}^3$ $\text{W}\,\text{s}^3$

	$\alpha_{10}^{1\text{mm}} = -1.643 \cdot 10^{-9}$	$\text{W h}^{1.588}\,\text{m}^{-3\,\cdot\,1.588}\,\text{s}^2$
	$\alpha_{11}^{1\text{mm}} = 4.394 \cdot 10^{-5}$	$\text{W h}^{1.441}\,\text{m}^{-3\,\cdot\,1.441}\,\text{s}$
	$\alpha_{9}^{1\text{mm}} = 156033.408$	Hz
$\underline{\mathbf{P}}_{\text{op}}^{1\text{mm}}(t)$	$\alpha_{10}^{1\text{mm}} = 1$	m^3h^{-1}
	$\alpha_{11}^{1\text{mm}} = 1.958$	W

Table C.17: Coefficients for the 1 mm *GrindBall* using air

Relevant non-dimensional equations

Using the non-dimensionalisation technique introduced in Chapter 7 by eqns (7.39)-(7.42), dimensionless equations can be derived for each quantity presented above:

$$
\begin{aligned}
\overline{F}_x^{D,40\text{mm}} &= 1.024\dot{V}_N^{D2.053} \\
\overline{F}_x^{D,8\text{mm}} &= 1.264\dot{V}_N^{D2.038} \\
\overline{F}_x^{D,1\text{mm}} &= 2.559 \cdot 10^{-2}\dot{V}_N^{2.473} \\
\overline{F}_z^{D,40\text{mm}} &= 0.245\dot{V}_N^{D2.078} \\
\overline{F}_z^{D,8\text{mm}} &= 5.997 \cdot 10^{-2}\dot{V}_N^{D2.216} \\
\overline{F}_z^{D,1\text{mm}} &= 3.204 \cdot 10^{-4}\dot{V}_N^{3} - 1.057\dot{V}_N^{2} - 428.519\dot{V}_N \\
F_{0,t}^{D,40\text{mm}} &= 0.330\dot{V}_N^{D1.833} \\
F_{0,t}^{D,8\text{mm}} &= 1.735\dot{V}_N^{D1.673} \\
F_{0,t}^{D,1\text{mm}} &= 13.423\dot{V}_N^{D1.441} \\
f_0^{D,40\text{mm}} &= 0.219\dot{V}_N^{D0.985} \\
f_0^{D,8\text{mm}} &= 0.420\dot{V}_N^{D0.921} \\
f_0^{D,1\text{mm}} &= 0.592\dot{V}_N^{D0.869} \\
F_t^{D,40\text{mm}} &= (4.998 \cdot 10^{-6}\dot{V}_N^{D1.833})(66122.474 - 3.020 \cdot 10^{5}\dot{V}_N^{D-0.985} f^{*}) \\
F_t^{D,8\text{mm}} &= (2.623 \cdot 10^{-5}\dot{V}_N^{D1.673})(66122.474 - 1.575 \cdot 10^{5} f^{D}\dot{V}_N^{D-0.921}) \\
F_t^{D,1\text{mm}} &= (1.574 \cdot 10^{-6}\dot{V}_N^{D1.829} - 3.645) f^{D2} - 2.990 \cdot 10^{-2}\dot{V}_N^{D1.369} f^{D} + 13.423\dot{V}_N^{D1.441} \\
P_{\max}^{D,40\text{mm}} &= 128.569 f^{D2.782} \\
P_{\max}^{D,8\text{mm}} &= 151.841 f^{D2.751} \\
P_{\max}^{D,1\text{mm}} &= 305.789 f^{D2.662} \\
P_G^{D,40\text{mm}} &= -13.839\dot{V}_N^{D0.815} f^{D2} + 2.082\dot{V}_N^{D1.833} f^{D} \\
P_G^{D,8\text{mm}} &= -44.762\dot{V}_N^{D0.696} f^{D2} + 11.998\dot{V}_N^{D1.664} f^{D} \\
P_G^{D,1\text{mm}} &= (1.316 \cdot 10^{-5}\dot{V}_N^{D1.813} - 24.192) f^{D3} - 3.510 \cdot 10^{-2}\dot{V}_N^{D1.588} f^{D2} + 84.315\dot{V}_N^{D1.441} f^{D} \\
\underline{\mathbf{P}}_{\text{op}}^{D,40\text{mm}}(\zeta) &= \left(102.797\zeta^{0.985}, 1044.277\zeta, 2.899 \cdot 10^{7}\zeta^{2.872}\right) \\
\underline{\mathbf{P}}_{\text{op}}^{D,8\text{mm}}(\eta) &= \left(557.299\eta^{0.921}, 5221.387\eta, 4.865 \cdot 10^{9}\eta^{2.634}\right) \\
\underline{\mathbf{P}}_{\text{op}}^{D,1\text{mm}}(\xi) &= \left(2932.959\xi^{0.827}, 41771.094\xi, 3.218 \cdot 10^{11}\xi^{2.043}\right).
\end{aligned}
$$

Appendix D

OpenFOAM settings

A wide variety of simulations are performed throughout this thesis with varying setups: the *GrindBall* prototype (Chapter 4) and the scale analysis (Chapter 7), for example, are simulated using a compressible medium and turbulence modelling on meshes of different sizes, scales and refinement levels. Hydraulic propulsion (Chapter 6) is simulated mostly without modelling turbulence on differing meshes.

Each set of simulations has a distinct setup ranging from specific solver settings, over employed numerical methods, to different computational grids and simulation timelines. The following lists all settings as they appear in `OpenFOAM` [Ope13a]. The stated methods and variables are discussed in Chapter 3. For further reading see the `OpenFOAM` user guide [Ope13c]. Furthermore, brief quantitative statements are made about the computational grid and the simulation timeline is given.

D.1 40mm GrindBall parametric study (Chapter 4)

General settings	
Solver	`rhoPimpleFoam`
Fluid	Air
Density	Compressible
Algorithm	PIMPLE
Method	Finite Volume Method (FVM)
Turbulence properties	
Turbulence model	Large Eddy Simulation (LES)
Subgrid model	Compressible Smagorinsky
Δ	cubeRootVol
C_k	0.02
C_e	1.048
Pr_{sgs}	0.9
y^+	$5 \leq y^+ \leq 100$

Thermophysical properties		
nMoles		1
molWeight [kg kmol^{-1}]		28.96
C_p [J kg^{-1} K^{-1}]		1007
Hf [J kg^{-1}]		0
Pressure-density dependence		Ideal gas law
Viscosity properties		
Transport model		Sutherland
A_s [kg m^{-1} s^{-1} K$^{-0.5}$]		$1.4963 \cdot 10^{-6}$
T_s [K]		120
Discretisation		
Spatial		Gauss linear (CDS)
Temporal		Euler
Boundary Conditions		
Inlet	$\underline{\mathbf{u}}$	timeVaryingFlowRateInletVelocity
	p	zeroGradient
	T	fixedValue 293.15 K
	μ_{sgs}	zeroGradient
	α_{sgs}	zeroGradient
Outlet	$\underline{\mathbf{u}}$	zeroGradient
	p	totalPressure 101,325 Pa
	T	zeroGradient
	μ_{sgs}	zeroGradient
	α_{sgs}	zeroGradient
Stationary walls	$\underline{\mathbf{u}}$	fixedValue {0,0,0} m/s
	p	zeroGradient
	T	zeroGradient
	μ_{sgs}	muSgsSpaldingWallFunction
	α_{sgs}	alphaSgsSpaldingWallFunction
Mesh details		
Total cells		∼900,000
Cells along gap height		4 per mm
Simulation timeline		
Total time [s]		0.04
Mass flow initialisation [s]		0 - 0.005
Averaging interval [s]		0.025 - 0.04

D.2 40mm GrindBall prototype (Chapter 4)

General settings		
Solver		`rhoPimpleFoam`
Fluid		Air
Density		Compressible
Algorithm		PIMPLE
Method		Finite Volume Method (FVM)
Turbulence properties		
Turbulence model		Large Eddy Simulation (LES)
Subgrid model		Compressible Smagorinsky
Δ		cubeRootVol
C_k		0.02
C_e		1.048
Pr_{sgs}		0.9
y^+		$5 \leq y^+ \leq 100$
Thermophysical properties		
nMoles		1
molWeight [kg kmol^{-1}]		28.96
C_p [J kg^{-1} K^{-1}]		1007
Hf [J kg^{-1}]		0
Pressure-density dependence		Ideal gas law
Viscosity properties		
Transport model		Sutherland
A_s [kg m^{-1} s^{-1} K$^{-0.5}$]		$1.4963 \cdot 10^{-6}$
T_s [K]		120
Discretisation		
Spatial		Linear upwind (LUDS)
Temporal		Crank Nicolson 0.5
Boundary Conditions		
Inlet	$\underline{\mathbf{u}}$	timeVaryingFlowRateInletVelocity
	p	zeroGradient
	T	fixedValue 293.15 K
	μ_{sgs}	zeroGradient
	α_{sgs}	zeroGradient

Outlet	$\underline{\mathbf{u}}$	zeroGradient
	p	totalPressure 101,325 Pa
	T	zeroGradient
	μ_{sgs}	zeroGradient
	α_{sgs}	zeroGradient
Stationary walls	$\underline{\mathbf{u}}$	fixedValue {0,0,0} m/s
	p	zeroGradient
	T	zeroGradient
	μ_{sgs}	muSgsSpaldingWallFunction
	α_{sgs}	alphaSgsSpaldingWallFunction
Rotating wall	$\underline{\mathbf{u}}$	rotatingWallVelocity
	p	zeroGradient
	T	zeroGradient
	μ_{sgs}	muSgsSpaldingWallFunction
	α_{sgs}	alphaSgsSpaldingWallFunction
Mesh details		
Coarse mesh total cells		∼1,800,000
Fine mesh total cells		∼4,500,000
Coarse cells along gap height		12
Fine cells along gap height		24
Simulation timeline		
Total time [s]		0.05
Coarse mesh [s]		0 - 0.03
Fine mesh [s]		0.03 - 0.05
Mass flow initialisation [s]		0 - 0.005
Averaging interval [s]		0.035 - 0.05

D.3 Dynamometer validation (Chapter 5)

General settings	
Solver	`rhoPimpleFoam`
Fluid	Air
Density	Compressible
Algorithm	PIMPLE
Method	Finite Volume Method (FVM)
Turbulence properties	
Turbulence model	Large Eddy Simulation (LES)
Subgrid model	Compressible Smagorinsky

Δ		cubeRootVol
C_k		0.02
C_e		1.048
Pr_{sgs}		0.9
y^+		$5 \leq y^+ \leq 100$
Thermophysical properties		
nMoles		1
molWeight [kg kmol^{-1}]		28.96
C_p [J kg^{-1} K^{-1}]		1007
Hf [J kg^{-1}]		0
Pressure-density dependence		Ideal gas law
Viscosity properties		
Transport model		Sutherland
A_s [kg m^{-1} s^{-1} K$^{-0.5}$]		$1.4963 \cdot 10^{-6}$
T_s [K]		120
Discretisation		
Spatial		Linear upwind (LUDS)
Temporal		Crank Nicolson 0.5
Boundary Conditions		
Inlet	$\underline{\mathbf{u}}$	timeVaryingFlowRateInletVelocity
	p	zeroGradient
	T	fixedValue 293.15 K
	μ_{sgs}	zeroGradient
	α_{sgs}	zeroGradient
Outlet	$\underline{\mathbf{u}}$	zeroGradient
	p	totalPressure 101,325 Pa
	T	zeroGradient
	μ_{sgs}	zeroGradient
	α_{sgs}	zeroGradient
Stationary walls	$\underline{\mathbf{u}}$	fixedValue {0,0,0} m/s
	p	zeroGradient
	T	zeroGradient
	μ_{sgs}	muSgsSpaldingWallFunction
	α_{sgs}	alphaSgsSpaldingWallFunction
Mesh details		
Total cells		∼9,000,000
Coarse cells along gap height		12
Equiv. cells along gap height		32

Simulation timeline	
Total time [s]	0.02
Mass flow initialisation [s]	0 - 0.005
Averaging interval [s]	0.01 - 0.02

D.4 Propulsion fluid study (Chapter 6)

General settings		
Solver		`pimpleFoam`
Fluid		Oil (ISO VG5-64)
Density		Incompressible
Algorithm		PIMPLE
Method		Finite Volume Method (FVM)
Turbulence properties		
Turbulence model		Large Eddy Simulation (LES)
Subgrid model		Dynamic Smagorinsky
Δ		cubeRootVol
Filter		simple
y^+		$5 \leq y^+ \leq 100$
Viscosity properties		
Transport model		Constant
ν [$\mathrm{m^2\,s^{-1}}$]		$1.38 \cdot 10^{-4}$
Discretisation		
Spatial		Linear upwind (LUDS)
Temporal		Euler
Boundary Conditions		
Inlet	$\underline{\mathbf{u}}$	timeVaryingUniformFixedValue
	p	zeroGradient
	ν_{sgs}	zeroGradient
Outlet	$\underline{\mathbf{u}}$	zeroGradient
	p	totalPressure 101,325 Pa/ρ_{fluid}
	ν_{sgs}	zeroGradient
Stationary walls	$\underline{\mathbf{u}}$	fixedValue {0,0,0} m/s
	p	zeroGradient
	ν_{sgs}	nuSgsWallFunction
Rotating wall	$\underline{\mathbf{u}}$	rotatingWallVelocity
	p	zeroGradient
	ν_{sgs}	nuSgsWallFunction

Mesh details	
Total cells	∼7,000,000
Cells along gap height	20
Simulation timeline	
Total time [s]	0.008
Mass flow initialisation [s]	0 - 0.002
Averaging interval [s]	0.007 - 0.008

D.5 Simulations using ISO VG46 oil (Chapter 6)

General settings		
Solver		`pimpleFoam`
Fluid		Oil (ISO VG46)
Density		Incompressible
Algorithm		PIMPLE
Method		Finite Volume Method (FVM)
Turbulence properties		
Turbulence model		laminar
Viscosity properties		
Transport model		Constant
ν [$m^2 s^{-1}$]		$1.38 \cdot 10^{-4}$
Discretisation		
Spatial		Linear upwind (LUDS)
Temporal		Euler
Boundary Conditions		
Inlet	$\underline{\mathbf{u}}$	timeVaryingUniformFixedValue
	p	zeroGradient
Outlet	$\underline{\mathbf{u}}$	zeroGradient
	p	totalPressure 115.142 $m^2 s^{-2}$
Stationary walls	$\underline{\mathbf{u}}$	fixedValue {0,0,0} m/s
	p	zeroGradient
Rotating wall	$\underline{\mathbf{u}}$	rotatingWallVelocity
	p	zeroGradient
Mesh details		
Total cells		∼7,000,000
Cells along gap height		20

Simulation timeline	
Total time [s]	0.008
Mass flow initialisation [s]	0 - 0.002
Averaging interval [s]	0.007 - 0.008

D.6 Scale Analysis (Chapter 7)

General settings	
Solver	`rhoPimpleFoam`
Fluid	Air
Density	Compressible
Algorithm	PIMPLE
Method	Finite Volume Method (FVM)
Turbulence properties	
Turbulence model	Large Eddy Simulation (LES)
Subgrid model	Compressible Smagorinsky
Δ	cubeRootVol
C_k	0.02
C_e	1.048
Pr_{sgs}	0.9
y^+	$5 \leq y^+ \leq 100$
Thermophysical properties	
nMoles	1
molWeight [kg kmol^{-1}]	28.96
C_p [J kg^{-1} K^{-1}]	1007
Hf [J kg^{-1}]	0
Pressure-density dependence	Ideal gas law
Viscosity properties	
Transport model	Sutherland
A_s [kg m^{-1} s^{-1} K$^{-0.5}$]	$1.4963 \cdot 10^{-6}$
T_s [K]	120
Discretisation	
Spatial	Linear upwind (LUDS)
Temporal	Crank Nicolson 0.5

Boundary Conditions		
Inlet	$\underline{\mathbf{u}}$	timeVaryingFlowRateInletVelocity
	p	zeroGradient
	T	fixedValue 293.15 K
	μ_{sgs}	zeroGradient
	α_{sgs}	zeroGradient
Outlet	$\underline{\mathbf{u}}$	zeroGradient
	p	totalPressure 101,325 Pa
	T	zeroGradient
	μ_{sgs}	zeroGradient
	α_{sgs}	zeroGradient
Stationary walls	$\underline{\mathbf{u}}$	fixedValue {0,0,0} m/s
	p	zeroGradient
	T	zeroGradient
	μ_{sgs}	muSgsSpaldingWallFunction
	α_{sgs}	alphaSgsSpaldingWallFunction
Rotating wall	$\underline{\mathbf{u}}$	rotatingWallVelocity
	p	zeroGradient
	T	zeroGradient
	μ_{sgs}	muSgsSpaldingWallFunction
	α_{sgs}	alphaSgsSpaldingWallFunction
Mesh details		
Total cells		∼7,000,000
Cells along gap height		20
Simulation timeline		
40 mm	Total time [s]	0.05
	Mass flow initialisation [s]	0 - 0.005
	Averaging interval [s]	0.035 - 0.05
8 mm	Total time [s]	0.009
	Mass flow initialisation [s]	0 - 0.0005
	Averaging interval [s]	0.003 - 0.009
1 mm	Total time [s]	0.0005
	Mass flow initialisation [s]	0 - 0.000015
	Averaging interval [s]	0.0003 - 0.0005

Bibliography

[Arn81] R.E.A. Arndt. Cavitation in fluid machinery and hydraulic structures. *Annual Review of Fluid Mechanics*, 13(1):273–326, 1981.

[ASB10] D.A. Axinte, S. Abdul Shukor, and A.T. Bozdana. An analysis of the functional capability of an in-house developed miniature 4-axis machine tool. *International Journal of Machine Tools & Manufacture*, 50(1):191–203, 2010.

[Bal07] P. Balachandran. *Fundamentals of Compressible Fluid Dynamics*. Prentice-Hall of India Pvt.Ltd, New Delhi, India, 2007.

[BGB12] E. Brinksmeier, R. Gläbe, and C. Brandao. GrindBall - Ein innovatives Konzept zum achsenlosen Mikroschleifen. *wt Werkstattstechnik online*, 102(6):370–376, 2012.

[Bir45] R.T. Birge. The 1944 values of certain atomic constants with particular reference to the electronic charge. *American Journal of Physics*, 13(2):63–73, 1945.

[BOG+13] E. Brinksmeier, B. Orlik, R. Groll, A. Norbach, C. Brandao, and K. Leach. Grindball: an advanced micro-grinding tool. *Production Engineering*, 7(5):469–476, 2013.

[Bra] C. Brandao. Private communication. Research Assistant, Laboratory for Precision Machining (LFM).

[BRB+13] E. Brinksmeier, O. Riemer, C. Brandao, A. Meier, and F. Böhmermann. Potenziale der Mikrofertigung - Neue Wege der Bearbeitung und innovative Maschienenkonzepte. *Industrie Management*, 29(2):20–24, 2013.

[Bre01] N.W. Bressloff. A parallel pressure implicit splitting of operators algorithm applied to flows at all speeds. *International Journal for Numerical Methods in Fluids*, 36(5):497–518, 2001.

[BRKB13] E. Brinksmeier, O. Riemer, S. Kirchberg, and C. Brandao. Injection molded spherical grinding tools: manufacture and application of a novel tool concept for micro grinding. *Production Engineering*, 7(4):383–389, 2013.

[CFL28] H. Courant, K. Friedrichs, and H. Lewy. Über die partiellen Differenzengleichungen der mathematischen Physik. *Mathematische Annalen*, 100(1):32–74, 1928.

[Cla50] R. Clausius. Über die bewegende Kraft der Wärme und die Gesetze, welche sich daraus für die Wärmelehre selbst ableiten lassen. *Annalen der Physik und Chemie*, 155(3):368–394, 1850.

[CN47] J. Crank and P. Nicolson. A practical method for numerical evaluation of solutions of partial differential equations of the heat-conduction type. *Mathematical Proceedings of the Cambridge Philosophical Society*, 43(1):50–67, 1947.

[Deu98] Deutsches Institut für Normung e.V. DIN 51519 viscosity table. Website, 1998. `http://www.widman.biz/English/Tables/DIN%2051519.html`.

[DLP93] I. Demirdžić, Ž. Lilek, and M. Perić. A collocated finite volume method for predicting flows at all speeds. *International Journal for Numerical Methods in Fluids*, 16(12):1029–1050, 1993.

[DMK12] B. Denkena, H.C. Möhring, and H. Kayapinar. Design of a compact fluidic xy-stage for precise positioning. *7th International Conference on MicroManufacturing (ICOMM2012)*, pages 345–349, 2012.

[DMT06] D. Dornfeld, S. Min, and Y. Takeuchi. Recent advances in mechanical micromachining. *Annals of the CIRP*, 55(2):754–768, 2006.

[Fav83] A. Favre. Turbulence: space-time statistical properties and behavior in supersonic flows. *Physics of Fluids*, 26(10):2851–2863, 1983.

[FP96] J.H. Ferziger and M. Perić. *Computational Methods for Fluid Dynamics*. Springer Verlag, Heidelberg, Germany, 1996.

[Frö06] J. Fröhlich. *Large Eddy Simulation turbulenter Strömungen*. Teubner Verlag, Wiesbaden, Germany, 2006.

[Fur96] C. Fureby. On subgrid scale modeling in large eddy simulations of compressible fluid flow. *Physics of Fluids*, 8(5):1301–1311, 1996.

[Ger92] M. Germano. Turbulence, the filtering approach. *Journal of Fluid Mechanics*, 238(1):325–336, 1992.

[GHSW96] D. Gross, W. Hauger, J. Schröder, and W.A. Wall. *Technische Mechanik 3*. Springer Verlag, Heidelberg, Germany, 1996.

[GR09] C. Geuzaine and J.-F. Remacle. Gmsh: a three-dimensional finite element mesh generator with built-in pre- and post-processing facilities. *International Journal for Numerical Methods in Engineering*, 79(11):1309–1331, 2009.

[Gra01] W. Graebel. *Engineering Fluid Mechanics*. Taylor & Francis, New York, USA, 2001.

[Kü01] W. Kümmel. *Technische Strömungsmechanik: Theorie und Praxis*. Teubner Verlag, Stuttgart, Germany, 2001.

[Les08] M. Lesieur. *Turbulence in Fluids*. Springer, Dordrecht, The Netherlands, 2008.

[Lil92] D.K. Lilly. A proposed modification of the germano subgrid-scale closure method. *Physics of Fluids*, 4(3):633–635, 1992.

[LMC05] M. Lesieur, O. Métais, and Pierre Comte. *Large-Eddy Simulations of Turbulence*. Cambridge University Press, Cambridge, England, 2005.

[LR02] J.P. Le Roux. An integrated law of the wall for hydrodynamically transitional flow over plane beds. *Sedimentary Geology*, 163(3-4):311–321, 2002.

[Map10] Maplesoft. Maple 14. Software, 2010. `http://www.maplesoft.com`.

[MP97] Vijayanand S. Moholkar and Aniruddha B. Pandit. Bubble behavior in hydrodynamic cavitation: Effect of turbulence. *AIChE Journal*, 43(6):1641–1648, 1997.

[Nol93] B. Noll. *Numerische Strömungsmechanik*. Springer Verlag, Heidelberg, Germany, 1993.

[Nor] A. Norbach. Private communication. Research Assistant, Institute for Electrical Drives, Power Electronics and Devices (IALB).

[Nor12] A. Norbach. Magnetic bearing for grindball. *PCIM Proceedings*, 2012.

[Ope13a] OpenFOAM Foundation. OpenFOAM-2.1.x. Software, 2011-2013. `http://www.openfoam.org/download`.

[Ope13b] OpenFOAM Foundation. OpenFOAM Source Code. Website, 2011-2013. `http://www.openfoam.org/download`.

[Ope13c] OpenFOAM Foundation. OpenFOAM User Guide. Website, 2011-2013. `http://www.openfoam.org/docs/user/index.php`.

[Sag98] P. Sagaut. *Large Eddy Simulation for Incompressible Flows*. Springer Verlag, Heidelberg, Germany, 1998.

[Spu06] J.H. Spurk. *Strömungslehre*. Springer Verlag, Heidelberg, Germany, 2006.

[Sut93] W. Sutherland. The viscosity of gases and molecular force. *Philosophical Magazine Series 5*, 36(223):507–531, 1893.

[VM07] H.K. Versteeg and W. Malalasekera. *An Introduction to Computational Fluid Dynamics - The Finite Volume Method*. Pearson Education Limited, Essex, England, 2007.

[Wei] E.W. Weisstein. Sigmoid function. MathWorld-A Wolfram Web Resource. `http://mathworld.wolfram.com/SigmoidFunction.html`.

[WGKK12] J.P. Wulfsberg, S. Grimske, P. Kohrs, and N. Kong. Kleine werkzeugmaschinen für kleine werkstücke. *wt Werkstattstechnik online*, 100(11/12):886–891, 2012.

[Whi05] F.M. White. *Viscous Fluid Flow*. McGraw-Hill, New York, USA, 2005.

[Whi09] F.M. White. *Fluid Mechanics*. McGraw-Hill, New York, USA, 2009.

[WRK10] J.P. Wulfsberg, T. Redlich, and P. Kohrs. Square foot manufacturing: a new production concept for micro manufacturing. *Production Engineering*, 4(1):75–83, 2010.